UNIVERSITY OF CALIFORNIA
Los Angeles

Design, Construction, and Testing of a Radiofrequency Electron Photoinjector for the Next Generation Linear Collider

A dissertation submitted in partial satisfaction
of the requirements for the degree
Doctor of Philosophy in Physics

by

Eric Ralph Colby

1997

The dissertation of Eric Ralph Colby is approved.

Gerald P. Jackson

Claudio Pellegrini

Eli Yablonovitch

James B. Rosenzweig, Committee Chair

University of California, Los Angeles

1997

To my parents, with profound gratitude

Contents

1 Introduction **1**
- 1.1 Applications of High Brightness Electron Beams . . . 1
- 1.2 The TESLA Project . . . 2
- 1.3 The Fermilab Photoinjector R&D Effort . . . 6
  - 1.3.1 Single-Bunch Prototype Test [Phase I, through end FY96] . . 6
  - 1.3.2 High Duty Factor, Multi-Bunch Test [Phase II, through end CY97] . . . 7
  - 1.3.3 Installation of the Injector at DESY [Phase III, early 1998] . . 8
  - 1.3.4 Possible Future Applications and Experiments at Fermilab, [Phase IV, 1998 and beyond] . . . 8
- 1.4 Organization of the Dissertation . . . 9

2 Background **13**
- 2.1 Survey of Electron Injector Technology . . . 13
  - 2.1.1 Electron Sources . . . 13
    - Thermionic Emission Sources . . . 13
    - Field Emission Sources . . . 15
    - Ferroelectric Sources . . . 17
    - Photo-electric Emission Sources . . . 18
    - New Sources . . . 21
    - Hybrid Techniques . . . 21
  - 2.1.2 Acceleration Methods . . . 22
    - Pulsed-DC Acceleration . . . 22
    - Radiofrequency Acceleration . . . 23
- 2.2 Beam Manipulation Techniques . . . 25
  - 2.2.1 Transverse Space Charge Emittance Compensation . . . 26
  - 2.2.2 Guard Charge . . . 26
  - 2.2.3 Pulse Compression . . . 27
- 2.3 Technology Selection for the TTFL . . . 29
  - 2.3.1 Performance Requirements . . . 29

2.3.2 Consideration of the Alternatives 30

3 RF Photoinjector Theory **33**
3.1 Definition of Beam Quantities 34
3.2 K-V Envelope Theory 39
3.3 RF Photoinjector Theory: RF Effects 43
3.3.1 Longitudinal Dynamics 45
Pulse Compression 47
Emittance Growth 48
3.3.2 Transverse Dynamics 49
Ponderomotive Focussing 49
Emittance Growth 50
3.3.3 RF Structure Defects 52
3.4 RF Photoinjector Theory: Space Charge 54
3.4.1 Kim Theory 54
3.4.2 Carlsten-Sheffield Compensation Theory 57
3.4.3 Serafini-Rosenzweig Invariant Envelope Theory 63
3.5 Magnetic Pulse Compression 65
3.6 Scaling Laws for Photoinjector Design 70
3.7 Beamline Optics 72
3.7.1 Collimator 73
3.7.2 Solenoidal Focussing 73
3.7.3 Dipole Focussing 76
3.7.4 Quadrupole Focussing 78
3.8 Wakefield Effects 79

4 Numerical Modeling **81**
4.1 Survey of Considered Codes 82
4.2 Description of PARMELA 85
4.3 Modification of PARMELA 86
4.4 Additional PARMELA Improvements 88

5 Design Rationale **91**
5.1 General Design Considerations 91
5.2 Physical Considerations 93
5.3 RF Design of the Photoinjector 100
5.4 Engineering Considerations 111
5.4.1 Electrical Dimension Specifications and Tolerances 111

6 Design of the RF Photoinjector **113**
6.1 Simulation Results . . . 113
6.1.1 RF Structure Design . . . 113
Gun . . . 113
Linac . . . 114
6.2 Magnet Performance . . . 115
6.2.1 Solenoids . . . 115
6.2.2 Beam Dynamics . . . 116
6.2.3 Dark Current Propagation . . . 117
6.3 Summary of Expected Performance . . . 119

7 Diagnostics **129**
7.1 Introduction . . . 129
7.2 General Diagnostics . . . 135
7.2.1 RF Diagnostics . . . 135
7.2.2 Laser Diagnostics . . . 137
7.3 Electron Beam Diagnostics . . . 138
7.3.1 Bunch Charge . . . 138
ICT . . . 138
Faraday Cup . . . 140
Calibrated BPM Response . . . 142
7.3.2 Beam Position . . . 142
Capacitative "Button" BPM . . . 142
Phosphor Screen . . . 144
7.3.3 Transverse Bunch Size . . . 146
Phosphor Screen . . . 146
7.3.4 Transverse Emittance . . . 146
Slit Mask Method . . . 147
Pepper Pot Mask Method . . . 153
Quadrupole Scan Method . . . 157
7.3.5 Longitudinal Measurements . . . 159
Streak Camera . . . 159
Spectrometer . . . 164
Longitudinal "Compressor Scan" Emittance Measurement . . . 167
7.3.6 Other Diagnostics . . . 168
Beamline Alignment . . . 168
Magnet Multipole and Hysteresis Measurements . . . 170
Water Cooling Assessment . . . 171

8 Design of the Prototype Test Experiment **173**
8.1 Proposed Experimental Program 173
8.2 Actual Experimental Program 175

9 Analysis of Experimental Results **181**
9.1 Data Reduction Methods 181
9.2 Characterization of the Drive Laser Pulse 183
9.3 Examination of Emission Uniformity 192
9.4 Characterization of the Gun RF Properties 194
9.5 Characterization of the Linac RF Properties 202
9.6 Characterization of Magnet Properties 205
9.7 Other Calibrations 210
9.8 Beam Measurements 211
9.8.1 Gun Test Phase 212
Beam Charge Transmission 212
Solenoid Steering 212
Solenoid Focussing 213
Gun Emittance 214
Energy Spectra 216
9.8.2 Injector Test Phase 216
Gun/Linac Phasing Studies 216
Bunch Length and Pulse Compression 217
Emittance 219
Energy Spectra 222

10 Comparison with Simulation **225**
10.1 Simulation Using Measured Parameters 225
10.1.1 Laser Spot Profile 225
10.1.2 Non-uniform Longitudinal Profile 226
10.1.3 Laser Misalignment 227
10.1.4 RF Field Imbalance 228
10.1.5 Wakefield Effects 228
10.2 Comparison with Experiment 229
10.2.1 Emittance Dilution Summary 232

11 Discussion **235**
11.1 Implications for the Next Generation Injector 236
11.2 Conclusions 238

A Design of an *A*symmetric Emittance Photoinjector **239**

B Derivations, Explanations **245**
B.1 Explanation of "Measurement Emittance" 245
B.2 Newton-Raphson Based Fit Polisher 249

C Design of RF Tuning Paddles **253**

D Photocathode Excitation Laser Requirements **257**
D.1 Laser Stability Requirements 260
D.1.1 Integrated Intensity Fluctuation 262
D.1.2 Spot Radius Fluctuation 264
D.1.3 Pulse Length and Phase Fluctuation 265
D.1.4 Spot Centroid Fluctuation 267
D.1.5 Finite Risetime and Temporal Intensity Fluctuation 268
D.1.6 Summary 270

E New/Modified Features of PARMELA **271**

References **297**

List of Figures

2.1 Electric field $E_r(r)$ for an infinite Gaussian line charge, and transverse emittance versus collimated fraction. 27

3.1 Phase and energy evolution in a 1.5 cell gun for 35 MV/m and 50 MV/m accelerating gradients. 46
3.2 Transverse emittance kick at gun exit, from Kim theory 57
3.3 Longitudinal emittance kick at gun exit, from Kim theory 58
3.4 Radial electric field for longitudinally Gaussian and uniform charge distributions. Bunch charge is the same for both cases. 59
3.5 Simple emittance compensation model output 61
3.6 Emittance compensation model prediction of emittance evolution under a wide variety of operating conditions. 62
3.7 Phase spread for the compensation case shown in figure 3.5 above. . . 64
3.8 The dipole chicane pulse compressor, straight-through and most compressive orbits are shown. 66
3.9 Particle tracings (left) in pulse compressor, and bunch length (right). 66

5.1 Sketch showing location of focussing and bucking solenoids 95
5.2 Focussing fields in TTF Photoinjector II 95
5.3 Contour and density plot of $|\vec{B}|$ with all four solenoids powered . . . 97
5.4 9-cell copper linac during the retrofit. 99
5.5 Injector II geometry with reentrant full cell 103
5.6 Lumped circuit model of two cell electrically coupled π-mode structure 105
5.7 RF Fill of Half and Full Cell 107
5.8 Coupling β and cavity frequency shift (in MHz) versus aperture length (in cm). 108

6.1 Accelerating electric field profile in the gun and capture cavity. 114
6.2 Primary and secondary solenoid field profiles $B_z(z)$. 116
6.3 Injector II Beamline, shown configured for 8 nC operation. Drawing courtesy of DESY. 120

6.4 Envelope evolution for 8 nC operation 121
6.5 Emittance evolution for 8 nC operation 122
6.6 Phase space and configuration space plots at $z = 1245$ cm (the exit of the first cavity in the first cryomodule) for 8 nC operation. Of 15000 simulation particles, 2000 were randomly chosen for these plots. . . . 123
6.7 Envelope evolution for 1 nC operation 124
6.8 Emittance evolution for 1 nC operation, these calculated emittances do *not* include the thermal emittance contribution. 125
6.9 Phase space and configuration space plots at $z = 1245$ cm for 1 nC operation. Of 15000 simulation particles, 2000 were randomly chosen for these plots. 126
6.10 Dark current loss for 35 MV/m gun fields and nominal magnet settings. 127

7.1 Layout of beamline components for testing the photoinjector at A.N.L. 130
7.2 Schematic of time resolving emittance measurement apparatus 134
7.3 Faraday cup calibration curves for peak voltage response (left) and integrated current response (right) 141
7.4 BPM Sensitivity vs. Bunch charge 142
7.5 S_{11} response of BPM button mounted in beamtube feethrough 143
7.6 BPM Position sensitivity measurement and sensitivity versus bunch charge 144
7.7 Emittance slit geometry and physical quantities 148
7.8 Signal and background on emittance slit phosphor screen, from Monte Carlo (left) and envelope (right) calculations. 149
7.9 Screen intensity distribution and calculated emittance for 3.88 MeV, 20 π mm-mr normalized emittance beam incident on 10μ and 35μ slits, with 30.6 cm drift. 150
7.10 Screen intensity distributions for 16.0 MeV, 20 π mm-mr normalized emittance beam incident on 10 and 35 μ slits, with 108.0 cm drift. . . 151
7.11 Transmission/reflection photomicrograph of a single emittance slit. . . 152
7.12 Coherent and incoherent synchrotron radiation intensities of 1 mm bunch in dipole 161
7.13 Cerenkov light output from 8 nC, 16.5 MeV electron bunch in 3 mm thick aerojel radiator. 164
7.14 Čerenkov radiator geometry. 165
7.15 Spectrometer particle orbits and resultant calibration of the phosphor screen 166
7.16 Spectrometer window transmission versus energy. 167

8.1 The gun test beamline 177

8.2 Envelopes for a 10 nC beam in the test beamline. 178
8.3 Emittance evolution for a 10 nC beam in the test beamline. 179

9.1 Laser spot imaged at the cathode location (left) and at the entrance window (right). 186
9.2 Laser spot imaged at the exit of the beam expander (left) and the entrance of the KrF amplifier (right). 186
9.3 Laser pulse energy statistics. 187
9.4 Sample laser streak image (left) and ROI analysis (right). 188
9.5 TPF autocorrelator traces for varying dye oscillator pulse length setting. 189
9.6 Streaks of KrF UV pulse for three different dye oscillator pulse lengths. 189
9.7 Final UV pulse lengths as a function of oscillator pulse length. 190
9.8 Streaks of KrF UV pulse for three different Nd:YAG pump powers. . 191
9.9 Scatter-plot of measured UV pulse lengths vs. Nd:YAG pump laser power. 192
9.10 Cathode QE before (left) and after (right) polishing. Note the change in color coding range. 193
9.11 Image of cathode showing arc-damaged areas, which appear as lighter grey patches, especially to the upper right of center. 194
9.12 Gun TM_{010} passband structure 196
9.13 Dipole mode coupling to pickup loops: upper trace is half cell loop, lower is full cell 197
9.14 Longitudinal bead pull of symmetric gun structure 199
9.15 Transverse bead pull of the full cell 199
9.16 Bead rotation data and analysis 200
9.17 RF power traces from the gun during conditioning 201
9.18 Phosphor screen focussed image of dark current from gun 203
9.19 Linac cavity passband structure (complete) 203
9.20 Field balance of 9-cell copper linac structure after final tuning 204
9.21 Calibration curves for linac capacitive probes 205
9.22 Thermal tuning curve for linac structure 206
9.23 Fourier decomposition of primary solenoid field $B_x(\theta)$ 207
9.24 Primary solenoid magnetic alignment curves. 208
9.25 Measurement of B vs. I curves for the compressor dipoles 209
9.26 B vs. I curves for a representative quadrupole and the spectrometer magnet. 209
9.27 Cable loss factor in typical strand of feedthrough bundle. 211
9.28 Beam charge transmission out of the gun versus launch phase 212
9.29 Residual solenoid steering after magnetic alignment. 213
9.30 Spot after magnetic alignment 214

9.31 Gun emittance vs. solenoid field setting. 215
9.32 Gun energy spectrum measurement for 8 nC bunch. 216
9.33 Relative phase of gun and linac over a period of 35 minutes. 218
9.34 Sample beam Čerenkov light streak image (left) and ROI analysis (right). 218
9.35 Bunch compression measurements versus R_{56} (left) gun and linac phase (right). 219
9.36 Sample beam slit image (left) and computer analysis (right), showing vertical projection, Gaussian peak fitting, and reconstructed phase space. 220
9.37 Slit emittance measurements at 16.5 MeV versus solenoid strength (left) and launch phase (right). 221
9.38 Pepper pot images of nominally-focussed (left) and over-focussed (right) 8 nC beam. Calibration: 232 pixels/cm 222
9.39 Uncompressed 8nC bunch energy spectrum at end of injector (z=6579 mm). 223

10.1 Comparison of simulated [left] and measured [right] emittance versus solenoid strength variation 231
10.2 Comparison of simulated [left] and measured [right] emittance versus launch phase variation 231
10.3 Comparison of 8 nC simulated [left] and 8 nC measured [right] energy spectra. 232
10.4 Summary of emittance diluting effects. 233

A.1 Transverse space charge fields for a horizontal sheet beam as a function of the horizontal coordinate. 240
A.2 Gun structure based on coupled waveguides 242
A.3 Horizontal and vertical plane profiles for the accelerating mode. . . . 243

B.1 Noisy Gaussian with RMS (solid), FWHM (dotted) and Polished (dot-dash) fits. 246
B.2 Convergence of Newton-Raphson fit polisher with number of iterations. 251

C.1 Schematic Drawing of the Tuning Paddle 254
C.2 Frequency Tuning Performance of Paddle-Type Tuner 256

D.1 Preliminary design concept of MBI laser, from I. Will, TTF/Hasylab Meeting Proceedings, DESY, May 6, 1994. 259
D.2 A Schematic of the 1 Hz x 1 MHz UOR Laser. 261
D.3 Effects of integrated intensity fluctuation on transverse and longitudinal emittances 263

D.4 Effects of spot radius fluctuation on transverse and longitudinal emittances 265
D.5 Effects of pulse length fluctuation on transverse and longitudinal emittances 266
D.6 Effects of phase jitter on transverse and longitudinal emittances . . . 267
D.7 Effects of centroid fluctuation on transverse and longitudinal emittances 268
D.8 Initial longitudinal distributions with 20% amplitude modulation . . . 269
D.9 Effects of intensity fluctuations on transverse and longitudinal emittances 269

List of Tables

1.1 Summary of TESLA-500, TTFL and TTF-FEL parameters 5

3.1 Chicane parameter summary 70
3.2 Summary of parameter scale factors for charge and wavelength scaling photoinjector designs. 72

5.1 Summary of TESLA Injector II Parameters 92
5.2 Electrical characteristics of the focussing and bucking solenoids 96
5.3 Key electrical dimension specifications for the RF gun. 112

6.1 Electrical Properties of the RF gun 114
6.2 Electrical Properties of the 9-cell copper structure. 115
6.3 Predicted performance of the Photoinjector, values calculated at the end of the first cavity in the first cryomodule, $z = 1245$ cm. Emittances include 0.7π mm-mr thermal contribution from cathode. 119

7.1 Diagnostic station location and equipment, gun to linac. 131
7.2 Diagnostic station location and equipment, linac to compressor. . . . 132
7.3 Diagnostic station location and equipment, compressor to beamline end. 133
7.4 First and Second Moments for pepper pot beamlets with linear space charge forces. 156

8.1 Experimental goals vs. actual accomplishments 176

9.1 Table of predicted and measured RF properties for the gun. 196

D.1 Laser requirements for the TTF/TESLA500 Photoinjectors 258
D.2 Constraints on Laser Parameter Jitter 270

List of Symbols

Planck's Constant	h
Boltzmann's Constant	k_B
Vacuum permittivity	ϵ_0
Vacuum permeability	μ_0
Classical Electron radius	r_e
Alfven Current	I_A
Number Density	N
6-D Phase space probability density	$\Pi(\vec{x}, \vec{p})$
Centroid	μ
Standard Deviation	σ
Skewness	$\mathcal{S}$
Kurtosis	$\mathcal{K}$
Temperature	T
Fermi Energy	E_F
Work function	ϕ
Surface enhancement factor	β_{FN}
Mechanical momenta	$p, \vec{p}$
Canonical momenta	$\pi, \vec{\pi}$
Normalized relativistic energy	γ
Normalized velocity	$\vec{\beta}$
Lab frame coordinates, momenta	x, p_x, y, p_y, z, p_z
Beam frame coordinates, momenta	$x^*, p_x^*, y^*, p_y^*, z^*, p_z^*$
Total charge, charge densities	Q, λ, Σ, ρ
Line, surface, volume current densities	$I, K, \vec{K}, J, \vec{J}$
Electric Field	$E_q, \vec{E}$
Magnetic Field	$B_q, \vec{B}$
RF frequency, wavelength, wavenumber	$\omega_{RF}, \lambda_{RF}, k_{RF}$
RF normalized vector potential	α
Electromagnetic skin depth	δ
Conductivity, resistivity	σ,ρ_o

Resonator Energy Storage Quality factor	Q
Resonator Geometric Quality factor	R/Q
Resonator Accelerating Mode Shunt impedance	$Z_{\parallel}$
Resonator coupling constant	γ
Resonator fill time	τ
Peak current	I_p
Perveance	K
Larmor Frequency	Ω_L
Momentum spread	δ
Beam sigma matrix	Σ_q
Emittance, normalized	$\varepsilon_{q,N}$
Emittance, geometrical	$\varepsilon_{q,g}$
Slice emittance (normalized)	$\varepsilon_{q,N}^{sl}$
Courant-Snyder parameters	$\alpha_q, \beta_q, \gamma_q$
Betatron phase advance	$\mu(s)$
Lattice focussing strength	$\kappa(s)$
Dispersion function	η_q
Temporal dispersion function	η_t,R_{56}
Magnetic bunch compression ratio	r_c
RF bunch compression ratio	R_c
Brightness	B
Helmholtz-Lagrange invariant	R
Bending radius	ρ
Magnet bend angle	θ_b
Magnet edge angle	θ_e
Magnet gap height	g
Quadrupole gradient	k_q
Quantum efficiency	QE

ACKNOWLEDGMENTS

As with any experimental effort, a great many individuals have contributed to the success of this project. This prototype photoinjector experiment has succeeded primarily through the relentless support of my thesis advisors, James Rosenzweig and Gerry Jackson.

I thank Vinod Bharadwaj and Steve Holmes for their support and interest which launched the asymmetric photoinjector project; John Peoples for his unwaivering support of electron photoinjector development despite tight financial times and a hostile political environment, and Dave Finley, whose continued interest has made completion of the project possible.

I thank François Ostiguy for his insightful guidance in computation methods and RF acceleration theory; Ralph Pasquinelli, Bill Miller, Mark Champion, and Rene Padilla for helpful discussions on the practical aspects of RF systems; Danny Snee, Jim Schmidt, Jerry Peterson, Doug Weisman, Jan Wildenradt, Ron LeBeau, Mark Reichanadter, and Tim Hammerla for countless discussions on machining and brazing techniques, and who together helped me to engineer the working prototype, Helen Edwards for her help in preparing the 9-cell copper cold-test structure that became the prototype linac, and for help in procuring needed equipment, and Pat Colestock and Linda Spentzouris for help in procuring and testing diagnostics. Additionally, I owe thanks to many of the members of the Fermilab Beams and Technical Support Divisions for support ranging from detailed thermo-mechanical analysis (Tom Nicol, Ziejing Tang, Mark Reichanadter) and fabrication of the gun structure to vacuum system design to help in procuring the many parts that composed the working injector.

I thank Manoel Conde, who sacrificed half a year's worth of evenings and weekends to operate the RF and laser systems at the Argonne Wakefield Accelerator facility so

the prototype experiments could be conducted; Wei Gai, whose patience in maintaining the AWA laser system and scheduling indulgences have permitted the experiments to proceed; Jim Simpson for permitting the use of his facilities to test the injector, a substantial sacrifice which has permitted testing to proceed nearly two years sooner than if the currently commissioning Fermilab facilities were used; and the technical support staff of building 366 for plumbing, wiring, rigging, painting, mopping and good humor in helping to assemble the injector.

I thank my fellow graduate students Dennis Palmer (Stanford) and John Power (IIT) for sharing their respective insights on making RF photocathode guns. Nick Barov (UCLA), for equipment loans, assistance, software and wide ranging discussions on topics scientific and non, I thank.

I thank Rich Sheffield, Bruce Carlsten of Los Alamos National Laboratory and Pat O'Shea of Duke University for informative discussions of the AFEL injector and the physics of space charge emittance compensation; Chris Travier and Jie Gao of LAL-Orsay for frank and insightful discussions of the CANDELA photoinjector; Ira Lehrman of Northrup-Grumman for discussions on engineering the high duty-factor Princeton/Grumman gun; Roger Miller of Stanford Linear Accelerator Center for the key idea in searching for a suitable flat-beam acceleration cavity, and Jim Weaver of SLAC for informative discussions of RF structure engineering.

Finally, I again thank Jamie and Gerry for their steadfast support and guidance of this research despite the unusual circumstances surrounding linear electron accelerator R&D conducted at a hadron collider facility.

ERIC RALPH COLBY

University of California, Los Angeles, June, 1997

VITA

September 23, 1968	Born, Lawrence, Massachusetts
1986	Bausch & Lomb Honorary Science Award
1989	B.S., Physics, Minor in Mathematics University of California, Davis
1989	Associated Western Universities Fellowship Crocker Nuclear Laboratory
1990	Graduate Research Assistant Lawrence Berkeley National Laboratory Accelerator & Fusion Research Division
1989-1991	Teaching Assistant University of California, Davis
1991	M.S., Physics University of California, Davis
1991	Graduate Research Assistant U.C. Davis, SDC Group
1991	Certificate in College Teaching University of California, Davis

1992	Graduate Research Assistant
	Los Alamos National Laboratory
	Meson Physics Group
1991-1993	Teaching Assistant
	University of California, Los Angeles
1993	Outstanding Teaching Assistant Award
	University of California, Los Angeles
1993-Present	Accelerator Physics Division Graduate Fellowship
	Fermi National Accelerator Laboratory

PUBLICATIONS AND PRESENTATIONS

E. Colby, G. Karady, A. Thiessen,"Design of a 20 GeV Synchrotron for a KAON Factory at LAMPF", LAMPF Internal Document, (1992).

——,"Asymmetric Emittance Photoinjector Simulation Work", in Proc. of the Fifth Int. Wkshp on Next-Generation Linear Colliders, SLAC Report 436, (1993).

——, J.-F. Ostiguy, J. Rosenzweig,"High Brightness Symmetric Emittance RF Photoinjector Preliminary Design Report", FERMILAB-TM-1900, (1994).

——,"Design of High Brightness Symmetric and Asymmetric Emittance Photoin-

jectors for TESLA", presented to the American Physical Society, Washington D.C., April 18-22, (1994).

——,"High Brightness RF Photoinjector Design for TTF and TESLA500", TTF Collaboration Meeting, DESY, Hamburg, Germany, May 6, (1994).

——,"High Brightness Photoinjector Research and Development at Fermilab", in Proc. of the Schwerin Sources Conference, Schwerin, Germany, Sept. 30, (1994).

——,"TTF Injector II Calculations", TTF Collaboration Meeting, DESY, Hamburg, Germany, October 3, (1994).

——,"High Brightness RF Photoinjector R&D at Fermilab", TTF Collaboration Meeting, DESY, Hamburg, Germany, February 23, (1995).

——,"TTF Gun II at 1.5 nC", TTF Collaboration Meeting, DESY, Hamburg, Germany, February 23, (1995).

——, V. Bharadwaj, J-F. Ostiguy, T. Nicol, M. Conde, J. Rosenzweig,"Design and Construction of High Brightness RF Photoinjectors for TESLA", in Proc. of the IEEE Part. Accel. Conf., Dallas, TX, p. 967-9, (1995).

——, J.-F. Ostiguy, J. Rosenzweig,"Design of High Brightness Symmetric and Asymmetric Emittance RF Photoinjectors for TESLA", in Proc. of the Sixth Adv.

Accel. Concepts Workshop, Lake Geneva, WI, AIP Conf. Proc. no 335, p.708-23 (1995).

——, H. Edwards, "Status of Symmetric Emittance Photoinjector Experiments at Argonne", TTF Collaboration Meeting, DESY, Hamburg, Germany, February 26-9, (1996).

——, "The AØ High Brightness Photoinjector", presented to the Future Accelerators at Fermilab Committee, Fermilab, Batavia, IL, May 1, (1996).

——, M. Conde, J. Rosenzweig, "Experimental Characterization of the TTF Prototype Photoinjector", presented to the American Physical Society, Indianapolis, IN, May 5, (1996).

——, "A High Brightness 20 MeV Electron Source for Advanced Accelerator R&D", engineering seminar presented at Fermilab, June 10, (1996).

——, "Status of Prototype Injector II Experiments", TTF Collaboration Meeting, INFN, Milan, Italy, June 17-21, (1996).

——, "Simulation of High-Brightness Photoinjectors", in Proc. of the Computational Accelerator Physics Conference, Williamsburg, VA, Sept. 24, (1996).

——, et al, "Advanced Accelerator R&D at Fermilab", presented at the Advanced

Accelerator Concepts Workshop, Lake Tahoe, CA, October 14, (1996).

——, et al, "Experimental Testing of the TTF RF Photoinjector", in Proc. of the IEEE Part. Accel. Conf., Vancouver, B.C., (to be published), (1997).

S. Eylon, E. Colby, T. Fessenden, T. Garvey, K. Hahn, E. Henestroza,"Emittance Variations of Very Cold Off-Axis Ion Beams during Transport through MBE-4", Particle Accelerators, vol. 37-8, p.235-40, (1992).

J. Rosenzweig, N. Barov, E. Colby,"Pulse Compression in Radio Frequency Photoinjectors–Applications to Advanced Accelerators", IEEE Trans. on Plasma Science, V. 24 No. 2 p.409-420, (1996).

——, E. Colby, G. Jackson, T. Nicol,"Design of a High Duty Cycle, Asymmetric Emittance RF Photocathode Injector for Linear Collider Applications", in Proc. of the IEEE Part. Accel. Conf., Port Jefferson, NY, p.3021-3, (1993).

——, E. Colby,"Charge and Wavelength Scaling of RF Photoinjector Designs", in Proc. of the Sixth Adv. Accel. Concepts Workshop, Lake Geneva, WI, AIP Conf. Proc. no. 335, p.724-37 (1995).

——, E. Colby,"Charge and Wavelength Scaling of RF Photoinjector Designs", TESLA 95-04, April, (1995).

——, E. Colby,"Charge and Wavelength Scaling of RF Photoinjectors: a Design Tool", in Proc. of the IEEE Part. Accel. Conf., Dallas, TX, p.957-60, (1995).

ABSTRACT OF THE DISSERTATION

Design, Construction, and Testing of

a Radiofrequency Electron Photoinjector

for the Next Generation Linear Collider

by

Eric Ralph Colby

Doctor of Philosophy in Physics

University of California, Los Angeles, 1997

Professor James B. Rosenzweig, Chair

The design of a high bunch charge (8 nC), low emittance ($\leq$ 20 mm-mr) radiofrequency electron photoinjector matched to the requirements of the TESLA Test Facility is presented. A 1.625-cell iris-coupled π-mode structure with high average accelerating gradient is chosen for its high shunt impedance, simplicity, and ability to accommodate an externally mounted solenoid for simultaneous beam divergence control and emittance compensation. A novel split-solenoid focussing assembly is employed, allowing emittance compensated beam extraction over a wide range of gun gradients. Beam optics are optimized for an overall injector consisting of the electron gun followed by one linac capture section (providing acceleration to 18 MeV), and a

dipole chicane for magnetic bunch compression to achieve a bunch length $\sigma_z = 1$ mm. Analytic and simulation work yielding a space charge emittance compensated gun design in a new high charge regime is detailed. Experimental measurements made on a prototype gun and injector at the Argonne Wakefield Accelerator Facility are detailed. Experimental results indicate a beam of 8 nC charge with bunch length ≈ 1.1 mm has been produced at emittances of less than 60×60 π mm-mr at an energy of 16 MeV with an energy spread of 240 keV. Experimental results, although in significant disagreement (by a factor of two) with initial simulations (which assume idealized laser properties), are in fair agreement with simulations carried out using the measured performance of the laser.

Chapter 1

Introduction

1.1 Applications of High Brightness Electron Beams

High energy particle sources find application in many diverse areas of science and industry. The ionizing properties of high energy particles are used to treat materials and to sterilize food and medical products. The ability of moderate energy particles to transmute elements has permitted the production of short-lived radio-isotopes useful both for studying living systems, and in treating cancer, and may provide the basis of a new power source. The penetrating nature of high energy particles allows for minimally invasive imaging of the internal structure of machine parts and the human body. The extremely small De Broglie wavelength associated with very high energy particles permits probing the structure of matter at very fine scales, making possible sensitive tests of the Standard Model.

It is the pursuit of ever smaller scales in experimental particle physics that has primarily driven source development. Modern experimental particle physics is proceeding along four complementary lines: via particle discovery and form factor measurement of new particles using pp, $p\overline{p}$, or ep colliders (SPPS, Tevatron, HERA, LHC?), via quark-gluon plasma generation using nucleonic colliders (RHIC, LHC?), via de-

tailed characterization of particle properties using "factories" composed exclusively of e^+e^- colliders (SLC, LEP, CESR, BEPC, VEPP-2M,-4M, DAΦNE, PEP-II, KEKB), and via ultra sensitive observation of natural particle sources (e.g. SuperKamiokande, COBE). Experimental data suggest that the much sought-after Higgs boson lies outside the range of present colliders, motivating another generation of machines capable of detecting and studying the Higgs. A machine of the required mass reach and luminosity will require significant improvements both in luminosity and in acceleration technique, if the machine is to be affordable.

In addition to e^+e^- colliders, several other applications require electron sources capable of producing very dense, short electron bunches. The Free Electron Laser (FEL) has been the primary driver of electron injector development since the early 1970s, with demands on phase space density and average beam power analogous to those imposed by colliders. All new high gradient acceleration techniques share in common the need for greatly decreased beam emittances to obtain the small spot dimensions required as new acceleration techniques call for ever smaller structures in the pursuit of higher accelerating gradients and power efficiencies.

1.2 The TESLA Project

A number of next-generation e^+e^- colliders operating initially at 0.5 TeV center of mass energies have been proposed. In general, high frequency RF structures have higher structure breakdown limits, enabling higher gradients, but due to smaller dimensions on beam apertures have increased wakes and tighter alignment tolerances. Superconducting cavities can be employed to improve RF efficiency and increase beam power, but with the added complications imposed by difficult surface chemistry,

cryogenic cooling, and somewhat lower gradients. Seven normal-conducting colliders spanning the range from 2856 MHz (JLC-1(S)) to 30 GHz (CLIC) have been proposed, each trading power efficiency against gradient, and encompassing such innovations as the two-beam (distributed relativistic klystron) proposal of CLIC.

The TeV Superconducting Linear Accelerator (TESLA) is the only superconducting linear collider proposed. As the lowest frequency (1.3 GHz) RF linac proposed, it has the largest apertures (70 mm Ø!), resulting in the loosest alignment tolerances, the highest rational bunch charge (8 nC) and beam power (16.5 MW), and has the highest quoted wall-plug efficiency (23%) [1] of any of the proposals. High bunch charge and high average current translate into high duty cycle (1%) for all RF structures involved, and places limitations on normal conducting structures such as the injector and the klystrons. Interaction point beam parameters are somewhat relaxed due to the high average beam power, with $1 \times 20\pi$ mm-mr normalized emittances planned.

These interaction point emittance values come within reach of the brightest radiofrequency photoinjectors presently operating, allowing for the attractive option of eliminating one (for TESLA, very expensive) damping ring. This option motivates efforts to produce an asymmetric emittance photoinjector capable of providing the required beam quality without a damping ring. Even if the requisite emittances cannot be obtained directly, and a damping ring is required, the number of damping times required to reach the final emittance will be reduced, and the magnet apertures in the damping ring can be reduced in view of the higher initial beam quality.

To test the technical and economic feasibility of TESLA, a 0.5 GeV test linac (the TESLA Test Facility Linac (TTFL)) is under construction at the present time.

Objectives of the TTFL (reproduced from reference [1]) include the testing of:

1. Acceleration gradient achievable (15 MV/m sought)
2. SRF cavity construction and processing techniques
3. Input and HOM coupler designs
4. RF control of multi-cavity systems
5. Lorentz detuning effects and control
6. *In situ* high peak power processing (HPP)
7. Vacuum failure recovery potential
8. Cryostat design
9. Cryogenic operation and heat load (except possibly HOM)
10. Dark current emission and trapping
11. Energy and position beam feedback and control
12. Alignment and its stability (during thermal cycle also)
13. BPM system
14. First iteration on projected systems costs

Of the above stated objectives, none depend in a significant way on asymmetries in the transverse emittances, making a more conventional symmetric emittance electron source appropriate.

The major parameters of the TESLA-500 and TTFL (with Injector II) accelerators are summarized in table 1.1 (reproduced from reference [1]) below.

Parameter	TESLA-500	TTFL	TTF-FEL
Linac Energy	2×250 GeV	500 MeV	500 MeV
RF Frequency	1.3 GHz	1.3 GHz	1.3 GHz
Accel Gradient	25 MV/m	15 MV/m	15 MV/m
Q_0	5×10^9	3×10^9	3×10^9
# Cryomodules	≈ 2500	4	4
Energy spread, single bunch RMS	1.5×10^{-3}	$\approx 10^{-3}$	$\leq 10^{-4}$
Energy variation, bunch to bunch	10^{-3}	$\approx 2 \times 10^{-3}$	$\approx 2 \times 10^{-3}$
Bunch length RMS	1 mm	1 mm	150 μm
Bunch charge	8 nC	8 nC	1 nC
Microbunch frequency	1 MHz	1 MHz	8 MHz
Beam macropulse length	800 μs	800 μs	800 μs
Beam current	8 mA	8 mA	8 mA
Lattice β typical	$\langle$ 66 m $\rangle$	12 m max	12 m max
Injection energy	10 GeV	20 MeV	20 MeV
Emittance (x/y), $\gamma\sigma^2/\beta$	$20/1\mu$m	$< 20/20\mu$m	$1/1\mu$m

Table 1.1: Summary of TESLA-500, TTFL and TTF-FEL parameters

Upon completion of the SRF test phase of the TTFL, testing of an undulator for what is planned to be an VUV FEL user facility will commence. The physics goals for the FEL user facility are ambitious and numerous and the reader is referred to the extensive literature for their discussion[2, 3]. At that time, injector operation will shift from high peak current to high bunch density for optimal FEL gain, requiring a change of bunch charge to 1 nC and much reduced emittances, $1 \times 1\pi$ mm-mr normalized RMS, with commensurately small energy spread, $\delta E/E_o \leq 10^{-4}$. Another photoinjector, under development at DESY, is planned for the FEL operation, and incorporates a novel input power coupler intended to eliminate the emittance dilution associated with the dipole asymmetry induced by conventional aperture power

coupling. As will be seen below, the high current injector, with a suitable change of field strengths, has a performance not entirely unsuitable for the FEL.

1.3 The Fermilab Photoinjector R&D Effort

As one part of Fermilab's involvement in the TESLA and TTFL collaborations, an extensive photoinjector research and development program was conceived and has been evolving since 1993. Initially examining the possibility of producing very high quality asymmetric emittance beams, the program turned in 1995 to the production of symmetric emittance beams of the proper spectral content and amplitude to perform HOM power deposition and diagnostic testing at DESY.

The Fermilab effort is divided into four distinct phases, beginning with Phase I, a single-bunch prototype photoinjector, tests completed Nov 14, 1996 at Argonne National Laboratory, followed by testing of a full duty cycle photoinjector at Fermilab as Phase II, with a copy thereof to be installed in Halle 3 as Injector II for the TESLA Test Facility Linac in Phase III, and in Phase IV, modification of the Fermilab test photoinjector for use in an ongoing advanced accelerator research and development program.

1.3.1 Single-Bunch Prototype Test [Phase I, through end FY96]

The Prototype Test Phase was devoted to understanding the single-bunch beam dynamical issues, carried out with a very low duty cycle (10^{-4}) RF gun, test linac, pulse compressor and optics. Installation of the injector was completed at the Argonne Wakefield Accelerator (AWA) Facility, which at the inception of Phase I (fall 1995)

had RF, laser, shielding, and other utilities not present at Fermilab until the spring of 1997. The goals of the prototype test phase were to:

- Measure prototype injector performance (1 bunch x 10 Hz):
  - Study single bunch beam dynamics
  - Verify stability against laser property fluctuations
  - Directly observe the physical basis of emittance compensation
  - Check pulse compression
- Benchmark modifications to simulation code PARMELA
- Produce a Ph.D.

1.3.2 High Duty Factor, Multi-Bunch Test [Phase II, through end CY97]

The multi-bunch test phase will establish the effects of the long TTF pulse train, and the effects of the long RF pulse on the gun cavity. Fermilab's facility at the A$\emptyset$ building will be needed for this, as 800 μs length RF pulses and 1 MHz UV pulse trains are required from the RF and laser, respectively. In addition, the structure designed for low duty cycle testing in phase I will need to be significantly redesigned to handle more than two orders of magnitude higher dissipated power. At present, the engineering and re-design of the phase II cavity is nearly complete, with production having been underway for some seven months. The goals of the second test phase are:

- Design, construct high-power, high duty cycle (1%) gun

- Commission multi-bunch injector (800 bunches x 1 Hz)
  - Check RF properties of gun under long pulse, high duty cycle
  - Measure long pulse train beam dynamics
  - Develop RF control and feedback systems
  - Develop diagnostics for the long pulse trains

1.3.3 Installation of the Injector at DESY [Phase III, early 1998]

Installation of the high-power RF photoinjector at Halle 3 at DESY was originally scheduled to occur in the early winter of 1997. Schedules at both DESY and Fermilab have slipped such that installation of the first components at DESY (the pulse compressor assembly) will likely occur in early fall of 1997. Installation of the RF structure will not occur until the de-commissioning and removal of the currently operating thermionic injector, believed to occur in early 1998.

1.3.4 Possible Future Applications and Experiments at Fermilab, [Phase IV, 1998 and beyond]

A somewhat modified version of the photoinjector commissioned at DESY will be commissioned at Fermilab for use in an advanced accelerator R&D program. R&D projects which have real resources currently committed are:

- Thomson backscatter picosecond x-ray source with application to solid-state and biological systems (Led by Adrian Melissinos, University of Rochester [4])
- Plasma wakefield acceleration experiments in the under-dense regime (Led by James Rosenzweig, University of California, Los Angeles [5])

- High-efficiency photocathode material preparation and lifetime testing in RF cavity environment (Led by Carlo Pagani, Istituto Nazionale Di Fisica Nucleare, Milano [6])
- Wakefield testing of proposed Muon collider SCRF cavity geometries (Helen Edwards, FNAL)

In addition, many more applications have been discussed:

- Asymmetric Emittance photoinjector for next generation linear collider source, (James Rosenzweig, Sven Reiche, UCLA)
- Polarized photocathode source development for RF injectors, (Gerry Jackson, Dennis Palmer, FNAL)
- Testing of next generation photoinjector structures (Carlo Pagani/Lucas Serafini, INFN, Milano)
- Optical cavity based FEL (Adrian Melissinos, UOR)
- Bunched beam stochastic cooling (FNAL)
- Impedance probing of stochastic cooling pickup/kicker antennæ(Ralph Pasquinelli, FNAL)
- Beam-beam tune shift neutralization in the Tevatron (FNAL)

1.4 Organization of the Dissertation

A few words are in order about the organization of the dissertation. The subject of this doctoral research, as originally conceived, was the design, construction and testing

of an *a*symmetric emittance, or flat beam, photoinjector with the goal of reaching the extremely challenging design parameters of TESLA-500. Nearly two years' work was carried out, comprising code and theoretical development, a first pass conceptual design, and simulations of a suitable RF accelerating structure were completed with the purpose of building such an injector which would also be able to satisfy the somewhat less demanding parameters of the TTFL with suitable (straightforward) modifications.

Concerns about the timeliness of such an R&D venture motivated a shift of focus to produce a symmetric emittance injector matched to the immediate needs of the TTFL, and virtually all effort was redirected to this task. The design considerations, experimental concerns and methodology have substantial overlap, but where they differ, work uniquely associated with the asymmetric injector has been summarized in Appendix A.

Experimental work conducted on the prototype injector was carried out under circumstances appreciably different from those expected in the design simulations. Consequently, a second round of simulations employing the measured properties of the drive laser pulse, the gun and linac RF properties, etc., has been presented *after* the experimental analysis section, a chronological ordering chosen to highlight what was learnt from the experimental phase.

Chapter 2 provides a brief overview of the current state-of-the-art in electron source technology, with the requirements of the TTFL in mind. With the selection of a RF photoinjector as the source, chapter 3 introduces the basic theory governing RF photoinjector performance. Chapter 4 addresses the selection of numerical modeling codes developed and used in designing the hardware, with chapters 5 and 6

detailing the specific constraints and specific design properties of the injector, respectively. Chapter 7 details the construction and interpretation of the diagnostics used in the prototype experiment, with chapter 8 discussing the experimental program as originally planned, and as ultimately executed. Chapter 9 presents the experimental results of the prototype phase, and in chapter 10 reconciliation of the data with the original calculations is attempted. Issues which remain to be addressed for successful construction of the next generation electron injector are outlined in chapter 11. Appendix A has a brief discussion of the design issues particular to the *a*symmetric emittance injector, together with a brief history of the development efforts in this direction. Appendix B holds divers topics, including a discussion of "measurement emittance" and on robust fitting techniques. Appendix C houses a discussion of RF tuning paddle design, and Appendix D has a discussion of the allowable fluctuations of the laser drive system. Appendix E delivers minutiæ about the many modifications made to PARMELA.

Chapter 2

Background

2.1 Survey of Electron Injector Technology

The demands on the symmetric emittance photoinjector for the TTFL are such that the capabilities of existing and short-term realizable technologies had to be carefully considered. The existing technologies for electron extraction, acceleration and manipulation are very briefly surveyed in the sections which follow, with the requirements of the TESLA Test Facility Injector in mind.

2.1.1 Electron Sources

Thermionic Emission Sources

Although triboelectric sources (relying on friction-induced charge separation) are historically the oldest man-made sources of electric charge, low average current limitations (a few microamps for the best of the modern machines) and relatively low peak voltages (tens of MeV at most, and in practice somewhat less) make them unsuitable as injectors for high average power applications such as high output FELs or linear colliders.

Thermionic sources were the first non-mechanical sources of electrons, and are

currently in the widest use. Thermionic emission is simply the escape of the very hottest electrons from an emitting surface. Integration of the Fermi-Dirac distribution over particles with a velocity component perpendicular to the emitting surface yields an expression for the thermionic emission current[7]:

$$J_{th}[\mathrm{A/cm^2}] = 120T^2 \exp(-\phi/k_B T), \tag{2.1}$$

referred to as the Richardson-Dushman relation, in which T is given in [K]. For typical refractory metals ($\phi \approx 4-5$ eV, $T_{melt} \approx 3000$ K) the thermionic emission current is limited to $\approx 500\mu\mathrm{A/cm^2}$, requiring a large cathode surface area to achieve the required net average current, severe bunching (from $\sigma_t = 0.3\mu$s to $\sigma_t = 3$ ps, a factor of 10^5!), and the attendant problems of having a very large ($> 16\mathrm{cm^2}$), high temperature emission surface, radiative heat losses from which are easily in the kilowatt range.

A marked improvement in the emitted current density is possible with a lowering of the work function, motivating oxide-coated thermionic sources made of barium, strontium, calcium and nickel ($\phi \approx 1$eV) capable of current densities on the order of 10 $\mathrm{A/cm^2}$ at 1000 K[8]. Dispenser cathodes are a regenerable improvement of the oxide cathodes, and are typically of similar composition (eg. $(\mathrm{BaSr})\mathrm{CO_3}$[9] or 5 BaO-3 CaO, 2 $\mathrm{Al_2O_3}$[10]), but in a porous tungsten matrix. Surface analysis[11, 12] has shown that barium migrates to the surface ("dispenses") from the pores under heating, and forms a Ba-O layer on cooling, regenerating the emissive surface. Although the oxide cathodes are sensitive to contaminants, in well-prepared UHV systems, lifetimes in excess of 40,000 hours are possible[8]. A drawback of dispenser cathodes is that barium tends to condense on other surfaces during operation, leading to reduced transmission in gridded guns due to buildup. Flaking and enhanced multipactoring can also result.

In more hostile vacuum environments, higher temperature borated cathodes, such as LaB_6[13], eutectic LaB_6-based alloys with ZrB_2, HfB_2 and TiB_2[14] and iridiated cathodes such as IrCe and IrLa[15] are much less sensitive to contaminants, and give current densities as high as 100 A/cm^2, but require operating temperatures in the incandescent range, and plate materials on the walls of the electron gun.

Field Emission Sources

Field emission is a result of partial image barrier depression due to a large applied electric field. The work function measures the depth of the potential well the surface electrons must escape to enter the vacuum. With the application of a strong electric field, the potential well distorts, becoming both finite in thickness and more shallow. With the reduction in the barrier thickness and height, outright escape and tunneling both become more favorable, allowing for increased emission currents. This decrease in the effective work function is the "Schottky effect"[16] and is a slow function of the applied electric field:

$$\Delta\phi = \sqrt{\frac{eE_z}{4\pi\epsilon_0}}. \tag{2.2}$$

Very large applied electric fields are needed before the Schottky effect appreciably enhances the extracted current. As an example, a smooth copper cathode requires an applied field ≈ 1.1 GV/m to cold emit 1μA/cm^2. Such a gradient is a factor of 4 higher than the highest gradient attained to date (1997) in a copper structure[17].

Rough surfaces will exhibit local field line concentrations ("surface enhancement") 2-3 orders of magnitude or more above the ambient field, and can emit large currents at appreciably lower applied fields. The field emission current for a material with work function ϕ is a very rapid function of the applied field, given by the Fowler-Nordheim

relation [18]:

$$I_{FN} = S\frac{e}{2\pi h}\frac{E_F^{\frac{1}{2}}}{\phi^{\frac{1}{2}}(\phi+E_F)}\beta^2E^2\exp(-4\kappa\phi^{\frac{3}{2}}/\beta E) \quad (2.3)$$

$$= 6.2\times10^6\frac{E_F^{\frac{1}{2}}}{\phi^{\frac{1}{2}}(\phi+E_F)}\beta^2E^2\exp(-6.8\times10^7\phi^{\frac{3}{2}}/\beta E) \quad (2.4)$$

where S is the effective area of the emitting surface, E_F is the electron Fermi energy, E is the applied field strength, $\kappa \equiv \frac{8\pi^2 m_e}{h^2}$, and β is the "surface enhancement factor", meant to take account of the field line concentration near sharp points. The physical interpretation of β is roughly that it is the mean height-to-radius aspect ratio for surface protrusions. The numeric form (2.4) yields the current density in [A/cm^2] when the field, E, is given in [V/cm] and is from Gomer [7].

Comparisons of measured emission currents with Fowler-Nordheim theory routinely give surface enhancement factors β in the few times 10^2 range[19]. Cathodes with arrays of sharp features have been used to to produce enhanced cold emission currents. "Felt" cathodes, composed of fibers of conducting material, can be produced by introducing foreign conducting particles onto an otherwise flat cathode and exposing the surface to high fields. The particles align with the electric field lines and become resistance welded to the face of the cathode[20].

There is substantial evidence[21, 22, 23] that semi-conducting inclusions trapped between the grain boundaries give rise to the anomalous field emission observed at low extraction fields. Special metal-insulator-metal (MIM) structures have been deliberately formed to produce electron sources[24], and have been suggested [25] to form accidentally on cathodes, particularly if polished with insulating abrasives. Such MIM structures act as capacitors until the applied electric field across the insulator causes the insulator to "switch on" at which time electrons accelerate across the insulating

gap and some fraction penetrates the conductor and emits into the vacuum.

Ferroelectric Sources

Although first observed in 1960[26], emission of electrons from ferroelectric materials has only within the last decade received substantial attention. Ferroelectric (FE) materials, in direct analogy with ferromagnetic materials, can exhibit permanent electric polarization, and produce spontaneous emission current densities in excess of 100 A/cm^2 in the absence of any externally applied extraction field[27]. Emission results from spontaneous bulk polarization switching, which generates high surface electric fields, expelling the compensating electron layer (and on the opposite face, draws in electrons) which forms to "screen" the polarization field. Polarization switching can be induced by sub-microsecond HV pulses applied to an electrode grid, by laser irradiation, by acoustic waves, and by thermal heating[28].

Optical polarization switching holds the greatest promise for short (picosecond) electron pulse production, and gives electron yields typically an order of magnitude better than metals[29], on the order of 10 nC/mJ. As the emission is not photoelectric in origin, UV laser pulses are not needed to trigger the cathode, with excellent response available from IR pulses. Emission efficiency depends strongly (faster than the third power) on peak power and on the photon energy, so higher efficiencies are possible.

FE cathodes under investigation have been generally lead-lanthanum zirconium-titanate ceramics (PLZTs) which demonstrate great resistance to poisoning (cathodes have shown no degradation in performance at pressures to 10^{-5} mbar [29]) and to surface discharge damage. FE cathodes have been pulsed at repetition rates up to

2 MHz[30] and have sustained power densities of 1.7 TW/cm^2 without damage[29].

Given that the emission mechanism is a combination of a bulk spontaneous polarization reversal and subsequent surface charge expulsion, the time structure of the emitted electron pulse is not directly controlled by the laser pulse time structure, as is the case in photoemission. Pulses of the desired temporal flatness and brevity may be quite difficult to achieve from large area (> 1 cm^2) cathodes. Also, the large stored energies available to the emitted electrons at the time of a bulk polarization switch may well produce very large "thermal" or intrinsic emittance values which cannot be corrected by any means. Finally, the generation of significantly polarized electron bunches by this mechanism is likely impossible.

Photo-electric Emission Sources

Fundamentally a quantum mechanical effect, photo-emission is escape of electrons upon absorption of a photon with energy greater than the work function. Several steps are involved in photoemission, each of which introduces several influences on the quantum efficiency of the materials used. Light reflected from the emitting surface obviously does not contribute to liberating electrons. Light absorbed by the material penetrates to a few skin depths, generally a few nanometers for metals at ultraviolet wavelengths. Absorption will promote a fraction of the electrons α_{PE} above the vacuum level, with the remainder not contributing to photoemission. Electrons liberated at this depth must traverse a depth of material with a probability of transmission P_T dependence on the escape length L to reach the surface and will escape with a probability P_E only if their kinetic energy exceeds the work function. Combining these factors, an heuristic estimate of the photoemission current due to incident light

intensity I_0 is[31]:

$$\begin{aligned} I_{photo} &\approx \int_0^\infty I_0(1-\mathcal{R})\left[(\alpha_{PE}\exp(-x/\delta)(\exp(-x/L))(P_E)\right] \\ &= I_0(1-\mathcal{R})\left[(\alpha_{PE}P_E)\frac{\delta}{1+\frac{\delta}{L}}\right] \end{aligned} \tag{2.5}$$

where the quantity in square brackets is commonly referred to as the quantum efficiency (QE).

Clearly, materials for the which the skin depth to escape length ratio is small ($\delta/L \ll 1$) will have better QE values, and hence require less light intensity for a given extracted charge. While the skin depth is only a slow function of the incident photon wavelength, the escape length exhibits dramatic variation dependent on the dominant collision mechanism (electron/electron, as in metals, or electron/phonon, as in some semiconductors and insulators). While a single electron/electron collision can lower the kinetic energy of the liberated electron below the work function, many electron/phonon collisions are required before the electron loses enough energy to prevent escape, allowing electrons liberated at substantial depths ($\geq 10^4$ atomic layers for some negative electron affinity (NEA) cathodes) to contribute to the photocurrent.

Emitted current densities are limited by available light intensity, extraction field, and material damage thresholds, with one of the first two usually prevailing. Metals have been measured to supply current densities in excess of 100 kA/cm^2 without damage[32], three orders of magnitude greater than the best dispenser cathodes.

Response time is another important attribute of photoemitters, and is related to the escape length[31]:

$$\tau = \frac{L}{\langle v \rangle} \tag{2.6}$$

For most metals ($L \sim 10-50$Åwithin an eV of threshold) response times are very fast,

typically femtoseconds, but can be well into the nanosecond range for the high-QE NEA cathodes ($L \sim 10^4$Å). In general, the response time correlates to the QE, with higher QE implying greater escape lengths and thus longer response times.

Many conducting materials have been tested ranging from elemental metals (Cu, Au, Y, Mg) to metal oxides (MgO)[32] and other traditional thermionic cathode materials, such as LaB_6 and CeB_6[33, 34]. Semiconducting and insulating materials giving high QE values include the alkali antimonides (e.g. CsK_2Sb, [Cs]Na_2LSb, and Cs_3Sb[31]), and CsI, and the negative electron affinity cathodes such as GaAs, GaP, InGaAsP, and GaAsP[31]. As mentioned before, many of the highest QE photocathodes have long response times, which has the dual disadvantage of producing long pulses requiring substantial pulse compression and a temporal structure not simply related to that of the laser pulse.

Vacuum robustness varies widely from some of the metal cathodes (e.g. copper) which can survive operation at pressures as high as 10^{-6} mbar, to the majority of the more exotic high-QE cathodes which suffer significant degradation either from alteration of the vacuum surface level from contaminant accumulation (as with most cesiated cathodes), or by gross stoichiometry changes (as with Cs_2Te [35]). Many cathodes can be rejuvenated either by redepositing cesium, or by heating or UV irradiation or both. The working vacuum requirement for many of the interesting high-QE cathodes is generally gas species-specific, and typically well below 10^{-9} mbar for QE lifetimes to approach one day in length.

Polarized photoemission sources composed of strained-lattice GaAs have shown QEs in the 10^{-2} to 10^{-1} range, polarizations ($P \equiv (P_+ - P_-)/(P_+ + P_-)$) approaching 85%, and have emitted significant charges (12×10^{10} e^-/bunch for 120 bunches spaced

60 nS apart) [36]. Requirements on the drive laser are generally much easier than for metal or semiconductor cathodes given the higher cathode QE and relatively long wavelengths (e.g. Circularly polarized Ti:sapphire at 845 nm) required. As with the other exotic high-QE cathodes, however, vacuum requirements are very stringent.

New Sources

A promising new technique for generating and accelerating electrons has recently been demonstrated in a proof-of-principle experiment by Umstadter, et al[37]. Dubbed "LILAC" for Laser-Injected Laser ACcelerator, direct electron trapping out of a laser-produced plasma into a laser-induced wakefield has been demonstrated to produce 50 pC bunches at 1.6 MeV and with excellent brightness.

Given that the bunch dimensions are set by the plasma wave dimensions, which are ~ 100 μm or less, (dependent on plasma density), the emerging bunches will undergo substantial space charge-driven expansion on entry to a microwave accelerator, likely resulting in unacceptable longitudinal emittance growth. However, used as an injector to a laser-driven accelerator possessing similar lattice characteristics it may excel.

Hybrid Techniques

As already seen in the case of photoemission from thermionic cathodes, it is common that elements of two or more emission methods are present. Photocathodes built into RF guns often experience such high applied fields that the Schottky effect contributes factors of two or more to observed QE values[38]. Thermionically assisted photocathodes have been examined[39].

One fundamental distinction of prompt ($\tau \leq 1$ ps) photoemission sources from all others is that the longitudinal pulse shape is directly determined by the laser

pulse shape. This allows very interesting flexibilities with regard to current profiles and allows for direct production of short ($\sigma_t \sim 3$ ps) bunches of almost arbitrary distribution[40, 41], a capability not shared by RF buncher-based systems and derived from the vastly superior bandwidth of laser amplifiers over RF amplifiers.

Of course, preservation of short, shaped bunches requires suitably rapid acceleration to prevent space charge erosion of the distribution.

2.1.2 Acceleration Methods

Particle acceleration techniques fall simply into two categories: fundamentally DC acceleration, in which the beam always moves downhill in a constant potential gradient, and RF acceleration, in which the beam extracts energy from a slower than light ("subluminal") velocity electromagnetic wave.

Pulsed-DC Acceleration

Voltaic stacks, Cockroft-Walton voltage multipliers and Van-de-Graaff generators were the first DC voltage sources, all of which could be operated continuously. As higher voltages evolved gas insulator breakdown limited further increase in the voltages. The Paschen voltage breakdown limit[42] estimates the maximum DC voltage sustainable across a gap d immersed in a gas with secondary emission coefficient γ and pressure p:

$$V_{max} = \frac{B(pd)}{\ln(\frac{A(pd)}{\ln(1/\gamma)})} \tag{2.7}$$

where the constants A and B are determined from collision theory for the gas species of interest. For SF_6, a commonly used insulating gas, at 1 atmosphere the breakdown electric field value is approximately 9 MV/m for gaps on the order of 10 cm [43].

Where insulating gases may not be used, hold-off field levels fall to around 2 MV/m for steady-state operation, with the insulators and not poor vacuum being the weak point[44].

Advantages of DC acceleration derive from the simplicity both of the voltage generating mechanism and from the readily shaped, purely electrostatic fields that result. Disadvantages are low accelerating gradient and the attendant difficulty of working with high DC voltages. Additionally, minimum pulse lengths for pulsed HVDC circuits are generally in the 0.5-1 ns range, which will imply substantial bunch compression ($\geq$ 167:1) if used in conjunction with thermionic or field emission sources.

A new type of DC gun is under development[45]-[50] that has demonstrated better than 1 GV/m accelerating gradients in small gaps ($\sim$ 3 mm) for short times ($\sim$ 500 ps) with beam quality that rivals the best RF photoinjector sources. The "pseudospark" electron source is typically a pulsed power system (e.g. a Marx generator) matched through a tapering coaxial transmission line terminated in a diode. The diode is generally a flat cathode facing an annular anode a few millimeters away. The sub-nanosecond pulse lengths used allow for extreme gradients to develop without breakdown. Although many technical issues remain to be addressed (how to achieve high repetition rates, long term reliability), progress in this area will be exciting.

Radiofrequency Acceleration

Throughout much of accelerator development, RF acceleration has been restricted to acceleration of bunched beams in slow-wave resonant structures excited by external RF oscillators, but has broadened within the last two decades to include a remarkable array of coupling schemes. At present, RF acceleration schemes may be

loosely categorized by the energy source for acceleration: optically-driven, external RF oscillator-driven, and beam-driven.

Optically-driven accelerators are analogous in principle to the longer-wavelength microwave accelerators, with some provision for coupling the optical wave to the beam, but with some very different physical realizations. Many coupling schemes have been proposed, including through a mode-converting dielectric mask (the Dielectric-Loaded Resonant Laser Accelerator [51]), a plasma (inverse Čerenkov accelerator [52], Laser Wakefield Accelerator [53], Plasma Beat Wave Accelerator [54]), an undulator (inverse FEL [55]), an arrangement of mirrors, and with a conducting structures (Inverse Smith-Purcell Radiation [56], Photonic Band-Gap Structures [57]). At present, laser-based accelerators have reached the proof-of-principle experimental stage.

Beam-driven and RF-driven techniques are quite similar in spirit, with the major distinction being that in the former case the RF extraction and acceleration structures are one in the same. Many ways have been conceived to produce slow-wave (i.e. EM waves with $v_p < c$) structures by loading a vacuum waveguide with obstacles that raise the permittivity (e.g. disks, dielectrics, plasma, etc.). For the "solid state" structures, gradients have reached 130 MV/m at functioning facilities [38], and have reached over 330 MV/m in isolated, specially prepared copper cavities [17]. With such high gradients electron beams may be accelerated so rapidly as to experience almost no space charge emittance growth, despite record electron densities ($\geq 10^{12}$ cm^3). Plasma-based acceleration techniques hold the potential for GV/m scale gradients [58], but are still under development. Additionally, the introduction of gas at pressures necessary ($\geq 10^{-4}$ mbar) for high gradient plasma acceleration would preclude the use of all but the most robust cathodes.

A dielectric loaded waveguide, in contrast to a disk loaded structure, has no longitudinal structure to scatter the accelerating mode, and hence has only the lowest space harmonic present to accelerate the particles. This eliminates entirely the nonlinear RF emittance growth. Dielectric-loaded structures suffer at present from several problems: relatively high power losses in the dielectrics coupled with low thermal conductivities make them unsuitable for high duty cycle; the presence of a large quantity of such a porous media may make ultra-high vacuum very difficult to achieve and maintain.

Disk-loaded waveguide structures have the longest running experience of any of the RF alternatives. Many geometries have been tried, and much is known about engineering reliable structures. However, the introduction of longitudinal structure in a waveguide induces higher space harmonics in the accelerating field which can present a significant source of emittance growth.

With most of the schemes described above (all except wakefield) there is the possibility to introduce a reflecting boundary condition at both ends of the structure, causing a backward traveling wave to form in addition to the forward wave which accelerates the particles. The chief advantage of such "standing wave" structures is an improvement in the energy efficiency of the structure by a factor of two over the equivalent "traveling wave" structure, but with the added complication of introducing potentially strong ponderomotive focussing and exacerbating RF emittance growth.

2.2 Beam Manipulation Techniques

Detailed in the following sections are methods for accomplishing nontrivial (i.e. emittance or bunch length altering) changes to the beam, as such methods impact the

suitability of some technologies for the current purpose. A more general discussion of standard beam optics will be delayed until the end of the next chapter.

2.2.1 Transverse Space Charge Emittance Compensation

Beam degradation has two basic components: (1) genuine entropy increase, as with intra-beam scattering, and (2) correlation development, which if left uncorrected can also increase entropy. Transverse space charge fields, at a maximum near the charge centroid, must vanish at the ends of a bunched beam. This longitudinal variation of $E_r(z)$ gives rise to unequal phase advance along the length of the beam which, when projected into the (r, r') phase plane appears as an increase in the phase area occupied by the beam, even though the phase volume in (r, r', z) space is unchanged. The twisting of the beam in (r, r', z) space can, by suitable beam manipulation, be reversed, giving in simulation and in measurement projected transverse emittance reduction by factors of 4-5 for highly optimized designs. This mechanism has a number of opponents, who argue that it represents a violation of Liouville's theorem when, in fact, Liouville's theorem does not apply to the two-dimensional sub-plane in the presence of forces (space charge, RF and wakefield, to name three) that couple particle motion to other coordinates (principally the longitudinal). Additionally, direct experimental evidence for the emittance compensation picture has recently come to light in measurements at the Brookhaven ATF[59].

2.2.2 Guard Charge

Proposed by Lehrman for the Princeton/Grumman/BNL photoinjector[60], the addition of a small amount of sacrificial charge at the edges of the beam will allow for a collimation when the beam has reached high energy. Examination of figure 2.1 shows

that most particles in a Gaussian beam experience nearly linear space charge fields, with only a small population near the edges seeing the most nonlinear fields. As a consequence, much of the nonlinear space charge emittance growth may be collimated away by judicious scraping. Improvements in transverse emittance have been shown in simulation[61] to scale quadratically with the amount of beam scraped for transverse uniform distributions, while the gain is much faster than quadratic for Gaussian bunch distributions.

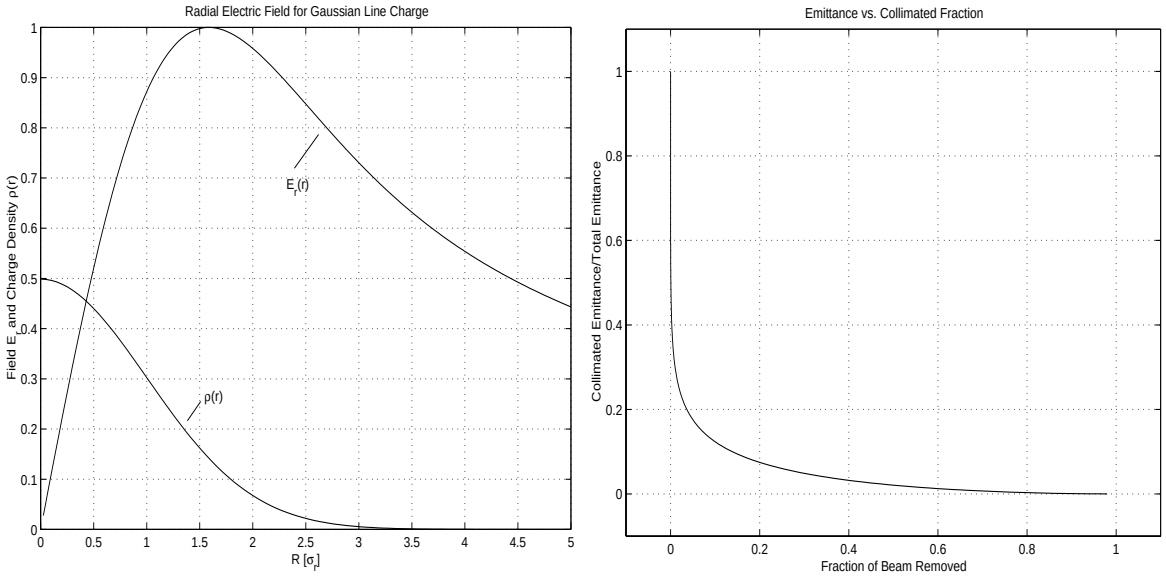

Figure 2.1: Electric field $E_r(r)$ for an infinite Gaussian line charge, and transverse emittance versus collimated fraction.

2.2.3 Pulse Compression

Bunch length compression can be accomplished by a variety of means. At low energies ($E \sim 500$ keV) velocity bunching is effective, and results from introducing a positive phase-energy correlation, typically with a RF cavity. Klystrons generally have a buncher cavity operating at the desired output frequency, with several "idler" cavi-

ties which exploit long-range wakes to improve bunching. DC injectors often have an intermediate-frequency RF cavity operating at a sub-harmonic of the main accelerating frequency to match the beam into the longitudinal acceptance of the subsequent linac. Common to both schemes is the need to drift the beam long enough for the velocity sheer to bunch the beam, a process which for L-band systems requires drifts on the order of 1 meter. At high charge, such long drifts at very low energy leads to substantial emittance growth. RF electron guns can be and usually are phased to achieve pulse compression. Phase slippage conditions favorable for good transverse beam quality naturally give rise to substantial phase focussing.

At relativistic and ultra-relativistic energies, velocity bunching is ineffective, RF bunching becomes too costly, and dispersive schemes must be used. Pulse compression can be achieved by arranging two conditions to be met: (1) the beam must have a nontrivial phase-energy correlation, (2) particles at the head of the bunch must take longer paths than those at the tail. Three magnet configurations are commonly in use to achieve this: (1) a 180^o arc, as at Bruyeres-la-Chatele and Boeing, (2) a "three-bump" or chicane, as at APEX, Boeing, and UCLA, and (3) a modified dipole called an "α-magnet", as at Vanderbilt. Pulse compression ratios in the 2-5 range are common. Extreme pulse compression using non-linear dispersion chicanes tailored to non-linearly sheer the longitudinal phase space to compensate for space charge nonlinearities have been measured to give compression ratios approaching 40 [62].

2.3 Technology Selection for the TTFL

2.3.1 Performance Requirements

While the detailed beam parameters required of the injector for the TTFL have been discussed in the introduction, additional constraints must be discussed which bear on the technology selection for the TTFL injector in particular. These derive from the objectives of the TTFL test program, as outlined in the introduction, from considerations of "existing planned" infrastructure, and from economic considerations.

The focus of the TTFL program is on understanding the engineering and economics of making a superconducting linac of appreciable size, not on electron injector technology. As such, a compact, technologically conservative injector is called for, with the more distant FEL program calling for a similarly compact injector with a performance that will be state-of-the-art.

Siting of the TTFL is in Halle 3 at DESY. The length of the hall is such that the injector must fit within a small region of the shielding enclosure, on the order of 12 meters in length by 5 meters width. Space for supporting apparatus is also comparably constrained. RF systems producing 4-5 MW per klystron with the required pulse length (1200μs) have been designed and several are already built. There is now the possibility of a more efficient klystron tube being used with the present modulators, pending successful development and production by the Thomson Electron Tube Division. With these power limitations, shunt impedance will be important, making a standing wave π-mode structure attractive. Concerns about the extraction field level (viz. the electric field available on the cathode) will limit the gun to just a few cells with the available power.

From the declared start of the R&D effort on the symmetric emittance photoinjector (May, 1994) for the TTFL to its planned installation at DESY (winter, 1997) was two and a half years, limiting the scope of the R&D effort.

2.3.2 Consideration of the Alternatives

Given the beam qualities desired and the additional constraints now delineated, a selection of technology becomes clear.

Compactness precludes a damping ring, requiring emittances that *ab initio* are excellent. Simulations of a DC electron source utilizing two sub-harmonic buncher cavities to obtain the required pulse charge and time structure have suggested that emittances of more than 50π mm-mr would result[63]. The significantly higher accelerating gradients (typically one to two orders of magnitude) present in an RF gun result in significantly less beam expansion and emittance degradation. Pseudospark sources possess still higher gradients (by still another order of magnitude) and have demonstrated remarkably good beam quality, but at the inception of this program, as now, are in their technological infancy. Thus the selection of an RF gun.

The required bunch density $n = Q/8e\pi\beta_x\beta_y\varepsilon_{x,ph}\varepsilon_{y,ph}\sigma_z \sim 10^{12}$ cm^{-3} will place difficult demands on thermionic or field emission sources. A good dispenser cathode capable of 100 A/cm^2 mounted in a RF gun at a moderate gradient for L-band (e.g. 1 Kilpatrick $\sim$ 32 MV/m) would not have appreciable Schottky enhancement, and would emit for almost the full half cycle during which the RF field has the correct polarity. A fraction of the charge would trap and accelerate in what is a rather voluminous RF bucket giving large longitudinal emittances. Longitudinal collimation either with a chopper or in the dispersive region of a magnetic pulse compressor could

be employed to reduce the longitudinal phase area, but would require punitive charge losses.

Since prompt photoemitters produce electron currents that mirror the light intensity down to sub-picosecond time-scales, short pulses can be launched from the cathode at the ideal phase for good beam quality. In addition, transverse charge profiles may be easily controlled by altering the illuminating light distribution, allowing for the production of tailored charged distributions. If the cathode is designed to be dismountable (as it almost always is) substitution of (laser triggered) ferroelectric cathode materials may be explored as an alternative to more conventional photoemitters. Additionally, polarized electron sources, such as are essential to linear collider operation, are traditionally photoemitters. For the extracted current densities ($> 100\text{A/cm}^2$) and pulse lengths ($\sim$ 10 ps) of interest optical intensities on the order of MW/cm^2 are required, typically at UV wavelengths, restricting the choice of light source to a laser.

Lastly and most significantly, RF photoinjectors of comparable operating parameters were built and operating at Los Alamos, Brookhaven, Boeing, Stanford, Orsay, CERN, Beijing, Taiwan and UCLA, aspects of the operation of which addressed both the beam quality concerns and the engineering concerns. Thus, a laser-driven dismountable-photocathode RF gun was chosen. As will be seen in the subsequent chapter on the design of the injector, a magnetic pulse compressor is required to obtain the desired bunch length, but first some theoretical ground work is needed.

Chapter 3

RF Photoinjector Theory

An excellent treatment of the history of linear accelerators in general is given by Lapostolle and Septier in *Linear Accelerators* [64]. Although originally developed in the context of proton and ion beam acceleration, theoretical work on RF acceleration, transport and space charge effects has been driven forward most recently by the tripartite demands of high bunch charge (making space charge important), very high bunch density (requiring much more detailed models), and high repetition rate (requiring accurate determination of halo evolution and subsequent beam loss) have led to significantly improved models of beam propagation. The theory of RF particle acceleration is well established, with space charge and wakefield effects having received substantial attention somewhat later.

Although the justification for particular design parameters will not be discussed for several chapters yet, two particular cases will be discussed throughout this chapter to illustrate the concepts. A 1.5 cell, 1.3 GHz gun operating at moderate (35 MV/m) and high (50 MV/m) electric field on the cathode with a 6 mm radius, 10 ps flat-top laser pulse producing 8 nC bunches will be considered.

3.1 Definition of Beam Quantities

Before proceeding with a treatment of the theory of photoinjector dynamics, it would be profitable to briefly define the relevant figures of merit used in characterizing beams. The subject of which parameters constitute a compact description of the beam distribution function is far from fully resolved, in part because the presumption of a Gaussian distribution often does not hold for cold electron beams, and in part because the relevant figure of merit depends on the end use for the particle beam. For designing transport optics, the standard 2-dimensional projected phase space area ("emittance") is generally adequate. For the free electron laser, the gain length scales as the bunch configuration space density to the one-third power, but only electrons within a "cooperation length" (generally much less than the bunch length) contribute appreciably to the radiation field, motivating usage of the "slice emittance". For the high energy linear collider, the luminosity scales with the inverse product of the spot sizes, and for a particular crossing geometry the correlations in the distribution will significantly influence the luminosity. For matching to the extremely low-β focusing channel of a plasma accelerator, correlations in the (x, p_x, z) and (y, p_y, z) phase volumes are important.

Fundamental to all beam quantities is the six-dimensional particle distribution function of the coordinates $\vec{x}$ and momenta $\vec{p} = \gamma\vec{\beta}mc$:

$$\Pi(\vec{x}, \vec{p}) \equiv \Pi(x, y, z, p_x, p_y, p_z) \tag{3.1}$$

which physically is simply the probability of finding a particle at the point $(\vec{x}, \vec{p})$. The distribution normalization is given by:

$$Q \equiv \int_\Gamma 1 \cdot \Pi(\vec{x}, \vec{p}) d\Gamma \tag{3.2}$$

where Γ is the full six-dimensional phase space, and, as expected yields the total charge in the distribution. The continuity equation:

$$\frac{\partial \Pi}{\partial t} + \frac{\partial (\Pi \dot{x_i})}{\partial x_i} + \frac{\partial (\Pi \dot{P_i})}{\partial P_i} = 0 \tag{3.3}$$

reduces for conservative (i.e. Hamiltonian) systems to:

$$\frac{d\Pi}{dt} = 0 \tag{3.4}$$

which is the statement that the probability density (following the particle trajectories) is a constant for conservative systems. This is Liouville's theorem, and applies, formally speaking, only in the full six-dimensional particle phase space. If particle motion is fully decoupled for any one coordinate q_c:

$$\frac{\partial^2 \Pi}{\partial q_c \partial q_i} \equiv 0 \qquad \forall q_i \neq q_c \tag{3.5}$$

then Liouville's theorem applies to the projected phase space distribution $\Pi_{n-1} = \int \Pi_n dq_c$ as well.

The full probability distribution is rather unwieldy theoretically, and is (at present) inaccessible experimentally, motivating a wide variety of abstracted parameters. Least ambiguous of the parameters commonly employed are the first five moments of the charge distribution. The zeroth moment has been given already as the normalization condition (3.2). The next two moments are defined:

$$\mu_q \equiv \langle q \rangle \equiv \frac{1}{Q} \int_\Gamma q \cdot \Pi(\vec{x}, \vec{p}) d\Gamma \tag{3.6}$$

$$\sigma_q \equiv \sqrt{\langle q^2 \rangle - \langle q \rangle^2} \equiv \frac{1}{Q} \int_\Gamma (q - \mu_q)^2 \cdot \Pi(\vec{x}, \vec{p}) d\Gamma \tag{3.7}$$

respectively the centroid ("beam position") and standard deviation ("spot size"), integration is over all phase space Γ, and $q \in \{x, p_x, y, p_y, z, p_z\}$. The skewness and

kurtosis are occasionally used to characterize the influence of aberrations in a transport system:

$$\mathcal{S} \equiv \frac{1}{Q}\int_{\Gamma}\left(\frac{q-\mu_q}{\sigma_q}\right)^3 \cdot \Pi(\vec{x},\vec{p})d\Gamma \tag{3.8}$$

$$\mathcal{K} \equiv \frac{1}{Q}\int_{\Gamma}\left(\frac{q-\mu_q}{\sigma_q}\right)^4 \cdot \Pi(\vec{x},\vec{p})d\Gamma - 3 \tag{3.9}$$

These moments are combined to yield two additional longitudinal parameters, the peak current:

$$I_p \equiv \frac{Q\beta c}{\sqrt{2\pi}\sigma_z} \tag{3.10}$$

and the (one-sigma) momentum spread:

$$\delta \equiv \frac{\sigma_{p_z}}{\mu_{p_z}} \tag{3.11}$$

the former of which presumes that the longitudinal distribution is Gaussian in the respective coordinate.

As correlations between the coordinates and momenta are not captured by the above quantities, often a beam sigma matrix is used for the purpose (the horizontal 2-dimensional sigma matrix is given as an example):

$$\Sigma_x \equiv \begin{bmatrix} \langle xx\rangle & \langle xx'\rangle \\ \langle xx'\rangle & \langle x'x'\rangle \end{bmatrix} = \varepsilon_{q,g}\begin{bmatrix} \beta & -\alpha \\ -\alpha & \gamma \end{bmatrix} \tag{3.12}$$

where the quantities in the second matrix are the associated Courant-Snyder ellipse parameters of the beam distribution:

$$\varepsilon_{q,g} \equiv \sqrt{|\Sigma_q|} = \sqrt{\langle q^2\rangle\langle q'^2\rangle - \langle qq'\rangle^2} \tag{3.13}$$

$$\varepsilon_{q,N} \equiv \gamma\beta_z\varepsilon_{q,g} \tag{3.14}$$

$$\alpha_q \equiv -\frac{\langle qp_q\rangle}{\varepsilon_{q,g}} \tag{3.15}$$

$$\beta_q \equiv \frac{\langle q^2 \rangle}{\varepsilon_{q,g}} \tag{3.16}$$

$$\gamma_q \equiv \frac{\langle p_q^2 \rangle}{\varepsilon_{q,g}} \tag{3.17}$$

and evidently $\beta_q \gamma_q - \alpha_q^2 = 1$ as with the lattice-based Courant-Snyder parameters, although the relation is purely geometric in origin, rather than arising from a symplectic condition. The normalized emittance $\varepsilon_{q,N}$ is the preferred measure of beam quality, as it is not subject to adiabatic damping under acceleration, while the geometrical emittance $\varepsilon_{q,g}$ is the quantity revealed by experimental measurements. The above definition for the normalized emittance encompasses one sigma of the distribution, and does **not** include the factor of π, which is written explicitly with the units.

The slice emittance is simply the transverse emittance of the beam particles in a thin longitudinal slice of the beam in $[z, z + dz]$ and is defined similarly to (3.14), but with the integrals over z replaced by multiplication by δz.

Alternate measures of beam quality have received substantial attention with notions from thermodynamics (entropy), plasma physics (electron temperature) and information theory all finding discussion in the literature. A summary of discussions up until 1980 with an encyclopædic bibliography may be found in the work of Lejeune and Aubert [65].

While figures of merit for the two-dimensional projections of the particle distribution are well established, figures of merit for the higher-dimensional projections of the distribution are not.

The four-dimensional emittances become interesting for systems where transverse motions couple to the longitudinal but not to each other (or vice-versa), and are simply the determinants of the three 4×4 cofactors of the six-dimensional beam

sigma matrix:

$$\Sigma_{xyz} = [\sigma_{ij}] = [\langle q_i q_j \rangle] \tag{3.18}$$

in which the meaning of the abbreviated matrix notation $[a_{ij}]$ is self-evident. As an example, take the 4-dimensional horizontal/longitudinal emittance, of interest in horizontally dispersive systems:

$$\varepsilon_{xz,g} = |\Sigma_{xz}| = \begin{vmatrix} \sigma_{xx} & \sigma_{xx'} & \sigma_{xz} & \sigma_{xz'} \\ \sigma_{x'x} & \sigma_{x'x'} & \sigma_{x'z} & \sigma_{x'z'} \\ \sigma_{zx} & \sigma_{zx'} & \sigma_{zz} & \sigma_{zz'} \\ \sigma_{z'x} & \sigma_{z'x'} & \sigma_{z'z} & \sigma_{z'z'} \end{vmatrix} \tag{3.19}$$

The six-dimensional emittance is again simply $\varepsilon_{xyz,g} \equiv \sqrt{|\Sigma_{xyz}|}$. It is worth pointing out that in the literature, the six-dimensional emittance is often shown as equal to the product of the three two-dimensional emittances:

$$\varepsilon_{xyz} = \varepsilon_x \varepsilon_y \varepsilon_z \tag{3.20}$$

which is true only for fully decoupled systems. For high bunch charge photoinjectors this condition is strongly violated.

For continuous beam applications in non-dispersive systems, the Helmholtz-Lagrange invariant (sometimes called by the German word for brightness, "*Richtstrahlwert*") is used:

$$R \equiv \frac{dJ}{d\Omega} \tag{3.21}$$

where $d\Omega$ is the differential solid angle occupied by the differential current density dJ.

For Gaussian, bunched beams, the beam "brightness" [66] is often used as a figure of merit:

$$B \equiv \frac{2Q}{\sqrt{2\pi}\sigma_t \varepsilon_{x,N} \varepsilon_{y,N}} \tag{3.22}$$

but suffers from a true but misleading divergence at zero charge (since $\varepsilon \propto aQ^{2/3} + bQ^{4/3}$). This measure also fails to include information about the beam energy spread, an important parameter for the majority of beam applications. An alternative proposition:

$$B_{3\times 2} \equiv \frac{Q}{\varepsilon_x \varepsilon_y \varepsilon_y} \tag{3.23}$$

remedies the situation, but still lacks information about correlations between the phase planes. For future applications it may well become necessary to use the true six-dimensional charge density:

$$B_6 \equiv \frac{Q}{\varepsilon_{xyz}}. \tag{3.24}$$

3.2 K-V Envelope Theory

K-V Envelope theory [67], named for its discoverers, Kapchinskij and Vladimirskij, encompasses the equations of motion for the second moments of the distribution under influences of focussing and space charge. As such, only the large scale coherent motion is considered. This simplification makes envelope theory an excellent tool for designing transport lattices, even if subtle influences induce relative motions of the particles within the beam (up to a point; the usual paraxial condition ($p_z \gg \sqrt{p_x^2 + p_y^2}$) must hold). With suitable enhancement, envelope theory can give powerful insight into even rather subtle beam dynamics, as will be seen with the Serafini-Rosenzweig theory of emittance compensation.

A number of derivations exist for the envelope equations for an accelerating beam of perveance K in a focussing channel $\kappa(s)$. I will begin with the relativistically

correct Lagrangian for particle motion in a 4-potential $(\phi, \vec{A})$:

$$\mathcal{L} = -mc^2\sqrt{1-\beta^2} - q\phi + \frac{q}{c}\vec{A}\cdot\vec{v} \tag{3.25}$$

which for electrons in cylindrical coordinates may be expressed as:

$$\mathcal{L} = -m_e c^2\sqrt{1-\frac{\dot{r}^2 + r^2\dot{\theta}^2 + \dot{z}^2}{c^2}} + e\phi - \frac{e}{c}(\dot{r}A_r + r\dot{\theta}A_\theta + \dot{z}A_z) \tag{3.26}$$

The canonical momenta follow directly:

$$\pi_r = \frac{\partial\mathcal{L}}{\partial\dot{r}} = \gamma m_e\dot{r} - \frac{e}{c}A_r \tag{3.27}$$

$$\pi_\theta = \frac{\partial\mathcal{L}}{\partial\dot{\theta}} = \gamma m_e r^2\dot{\theta} - \frac{e}{c}rA_\theta \tag{3.28}$$

$$\pi_z = \frac{\partial\mathcal{L}}{\partial\dot{z}} = \gamma m_e\dot{z} - \frac{e}{c}A_z \tag{3.29}$$

as do the generalized forces:

$$F_r = \frac{\partial\mathcal{L}}{\partial r} = \gamma m_e r\dot{\theta}^2 + e\frac{\partial\phi}{\partial r} - \frac{e}{c}\dot{\theta}A_\theta + \frac{e}{c}\left(\dot{r}\frac{\partial A_r}{\partial r} + r\dot{\theta}\frac{\partial A_\theta}{\partial r} + \dot{z}\frac{\partial A_z}{\partial r}\right) \tag{3.30}$$

$$F_\theta = \frac{\partial\mathcal{L}}{\partial\theta} = e\frac{\partial\phi}{\partial\theta} - \frac{e}{c}\left(\dot{r}\frac{\partial A_r}{\partial\theta} + r\dot{\theta}\frac{\partial A_\theta}{\partial\theta} + \dot{z}\frac{\partial A_z}{\partial\theta}\right) \tag{3.31}$$

$$F_z = \frac{\partial\mathcal{L}}{\partial z} = e\frac{\partial\phi}{\partial z} - \frac{e}{c}\left(\dot{r}\frac{\partial A_r}{\partial z} + r\dot{\theta}\frac{\partial A_\theta}{\partial z} + \dot{z}\frac{\partial A_z}{\partial z}\right) \tag{3.32}$$

and an application of the calculus of variations yields immediately the equations of motion. Using $\vec{E} = -\nabla\phi$ and $\vec{B} = \nabla\times\vec{A}$ and convective derivatives to express the result:

$$\dot{\gamma}m_e\dot{r} + \gamma m_e\ddot{r} - \gamma m_e r\dot{\theta}^2 = -e(E_r + \frac{1}{c}(r\dot{\theta}B_z - \dot{z}B_\theta)) \tag{3.33}$$

$$\dot{\gamma}m_e r\dot{\theta} + \gamma m_e r\ddot{\theta} + 2\gamma m_e\dot{r}\dot{\theta} = -e(E_\theta + \frac{1}{c}(\dot{r}B_z - \dot{z}B_r)) \tag{3.34}$$

$$\dot{\gamma}m_e\dot{z} + \gamma m_e\ddot{z} = -e(E_z + \frac{1}{c}(r\dot{\theta}B_r - \dot{r}B_\theta) \tag{3.35}$$

For rotationally symmetric RF photoinjectors, $E_\theta = 0$, and A_θ has no θ dependence and the azimuthal equation of motion becomes a statement of conservation of angular momentum since $F_\theta = \partial\mathcal{L}/\partial\theta \equiv 0$:

$$\dot{\theta} = \frac{1}{\gamma m_e r}(\pi_{\theta,0} + \frac{e}{c}A_\theta) = \frac{p_\theta}{\gamma m_e r} \tag{3.36}$$

which is essentially Busch's theorem [68]. For RF guns with solenoidal focussing, $B_\theta = 0$ as well. Substituting (3.36) for $\dot{\theta}$, and changing from time to z using:

$$\dot{r} = \beta c r' \tag{3.37}$$

$$\ddot{r} \approx \beta\beta' c r' + \beta^2 c^2 r'' \tag{3.38}$$

(primes denoting differentiation with respect to z), yields:

$$r'' + \frac{(\beta\gamma)'}{(\beta\gamma)}r' - \left(\frac{L_\theta}{\gamma\beta m_e c}\right)^2 \frac{\gamma}{r^3} = -\frac{e}{\gamma m_e \beta^2 c^2}\left(E_r + \frac{p_\theta B_z}{\gamma m_e c}\right) \tag{3.39}$$

$$z'' + \frac{(\gamma\beta)'}{(\gamma\beta)}z' = -\frac{e}{\gamma m_e \beta^2 c^2}\left(E_z + \frac{p_\theta B_r}{\gamma m_e c}\right) \tag{3.40}$$

where the angular momentum term ($\propto L_\theta^2$) is the usual emittance pressure term (ε^2/r^3), but in a form that makes obvious the physical mechanism limiting focal spot size. For an axisymmetric beam with $\sigma_r \ll \sigma_z$ in the lab frame, the radial electric field is just:

$$E_r = \frac{I}{2\pi\epsilon_o\gamma^2 r\beta c} \tag{3.41}$$

where I is the beam current. The radial electric field term becomes:

$$K_{SC} r = \frac{2I}{I_A(\beta\gamma)^3 r^2} \tag{3.42}$$

where the beam perveance K_{SC} and Alfvén current $I_A = 4\pi\epsilon_o m_e c^3/e$ have been defined. Defining the focussing strength $\kappa(z) = (eB_z(z)/\gamma\beta m_e c)^2$, and substituting

(3.42) yields the transverse envelope equation:

$$r'' + \frac{(\gamma\beta)'}{(\gamma\beta)}r' - \left(\frac{L_\theta}{\gamma\beta m_e c}\right)^2 \frac{\gamma}{r^3} = (K_{SC}(z) + \kappa(z))r \tag{3.43}$$

In Cartesian coordinates, the transverse envelope equations take an analogous form:

$$x'' + \frac{(\gamma\beta)'}{\gamma\beta}x' - \frac{\varepsilon_{x,g}^2}{x^3} = (K_{x,SC}(z) + \kappa(z))x \tag{3.44}$$

$$y'' + \frac{(\gamma\beta)'}{\gamma\beta}y' - \frac{\varepsilon_{y,g}^2}{y^3} = (K_{y,SC}(z) + \kappa(z))y \tag{3.45}$$

where the perveance term is modified to account for potentially non-axisymmetric beams:

$$K_{x,SC} = \frac{2I}{I_A\gamma^3\beta^2(x+y)x} \tag{3.46}$$

$$K_{y,SC} = \frac{2I}{I_A\gamma^3\beta^2(x+y)y} \tag{3.47}$$

The physical interpretation of these equations is simple: the beam RMS envelopes follow the single particle trajectories of three particles each sitting one sigma away from the origin along the respective coordinate axes. The particles are subject to external focussing forces and internal space charge forces and a "pressure" term arising from the beam's emittance.

Although the envelope equations provide an excellent picture of the large scale coherent motion of the beam, and hence of the beam size, it does not provide a complete enough description (in the form of equation (3.45)) to adequately address the "bow-tie" emittance growth that results from the z dependence of the RF, wake and space charge fields. As will be seen shortly, envelope descriptions of beam motion

provide a usefully complete picture of bunch evolution once the beam reaches relatively high energies ($\gamma > 30 - 50$). In the injector, however, more physical detail is required to adequately describe the bunch evolution.

3.3 RF Photoinjector Theory: RF Effects

The spatially rapid field strength variations in RF accelerating and space charge fields in the injector impart a twisting of the bunch phase space both transversely and longitudinally. To quantify the emittance degradation that results, additional detail about the functional form of the RF and space charge fields must be incorporated into the theory. For cylindrically symmetric, periodic structures, Floquet's theorem applies and the RF fields have a simple Fourier representation, here displayed for the nonzero components of the $\mathrm{TM}_{010,\pi}$ accelerating mode for a standing wave structure:

$$\begin{aligned}
E_z(r,z,t) &= E_o \sin(\omega t + \phi_o) \sum_{m=-\infty}^{\infty} \sum_{n=-\infty}^{\infty} a_{mn} J_m(k_{rn} r) e^{im\phi} cos(k_{zn} z) \\
E_r(r,z,t) &= E_o \sin(\omega t + \phi_o) \sum_{m=-\infty}^{\infty} \sum_{n=-\infty}^{\infty} a_{mn} \frac{k_{zn}}{k_{rn}} J_{m+1}(k_{rn} r) e^{im\phi} sin(k_{zn} z) \quad (3.48) \\
B_\theta(r,z,t) &= E_o \sqrt{\frac{\epsilon_o}{\mu_o}} \cos(\omega t + \phi_o) \sum_{m=-\infty}^{\infty} \sum_{n=-\infty}^{\infty} a_{mn} \frac{|\vec{k}|}{k_{rn}} J_{m+1}(k_{rn} r) e^{im\phi} cos(k_{zn} z) \\
k_{zn} &= k_o + \frac{2\pi n}{d} \quad (3.49) \\
k_{rn} &= \kappa_{mn}/R \quad (3.50)
\end{aligned}$$

where κ_{mn} is the n^{th} zero of the Bessel function of order m, R is the cavity radius, and d is the structure periodicity length. The eigenvalue equation produces the usual dispersion relation:

$$k_{rn}^2 = \left(\frac{\omega}{c}\right)^2 - k_{zn}^2 \quad (3.51)$$

which yields imaginary transverse wave numbers (hence $I_o(k_{rn}r)$ form) and much lower (and negative) velocities for all harmonics other than the fundamental since:

$$v_{ph} = \frac{\omega}{k_{zn}} = \frac{\omega}{k_o + \frac{2\pi n}{d}}, n = -\infty, ..., 0, ..., \infty \tag{3.52}$$

Consequently, a speed of light bunch will slip forward relative to the subluminal space harmonics, and receive no net energy gain from them. In an electron gun, however, the bunch accelerates from rest, and can therefore weakly couple to even the subluminal space harmonics.

The equations of motion for the centroid of an electron bunch accelerated from rest in a cylindrically symmetric standing wave structure composed of $(n + \frac{1}{2})$ half-wavelength cavities are:

$$\frac{d\gamma}{d\zeta} = \alpha[\sin(\phi) + \sin(\phi + 2\zeta)] \tag{3.53}$$

$$\frac{d\phi}{d\zeta} = (\frac{\gamma}{\sqrt{\gamma^2 - 1}} - 1) \tag{3.54}$$

$$\frac{dp_r}{d\zeta} = 0 \tag{3.55}$$

$$\frac{dp_\theta}{d\zeta} = 0 \tag{3.56}$$

where the normalized accelerating vector potential $\alpha = \frac{e(E_o/2)}{ck_o}\frac{1}{m_e c}$, normalized longitudinal coordinate $\zeta = k_o z$, and normalized energy $\gamma = \frac{E}{m_e c^2} + 1$ are introduced.

The particles have transverse relative motions within the bunch governed by:

$$\frac{dp_r}{d\zeta} = \frac{e}{\beta\omega}(E_r - \beta c B_\theta) \tag{3.57}$$

$$\frac{dp_\theta}{d\zeta} = 0 \tag{3.58}$$

which do not contribute to the motion of the centroid, but which have real implications for the beam quality.

3.3.1 Longitudinal Dynamics

The longitudinal equations of motion may be approximately integrated, following Kim [69] (with typographic corrections) to yield:

$$\gamma \approx 1 + \alpha\left[k_o z\sin(\phi) + \frac{1}{2}(\cos(\phi) - \cos(\phi + 2k_o z))\right] \tag{3.59}$$

$$\approx 1 + 2\alpha k_o z\sin(\phi_o) \tag{3.60}$$

$$\phi \approx \frac{1}{2\alpha\sin(\phi_o)}\left[\sqrt{(\gamma^2-1)} - (\gamma - 1)\right] + \phi_o \tag{3.61}$$

where (3.61) neglects the backward wave modulations of the energy gain. Insertion of (3.61) into the equation of motion for ϕ (3.55) yields (3.61). The backward wave contribution integrates to zero only for long structures traversed at the speed of light, which is not the case for the electron gun. A better approximation of the energy gain may be found by substituting the expression for $\phi(z)$ (3.61) into the equation of motion for γ (3.54) and integrating (neglecting the variation of ϕ with z) yielding (3.60).

Evidently, particles will gain energy at a rate approximately equal to the normalized potential ($\gamma' \approx \alpha$) with modulation at half the RF wavelength induced by the backward wave. Phase slippage occurs as the particles accelerate from rest and trap in the RF wave, requiring launch phases well in advance of the crest to achieve optimum beam energy (and, as will be seen shortly, lowest transverse emittance), and hence phase focussing will occur, slowing the space-charge induced bunch lengthening that normally occurs in the gun. To exit the gun on-crest requires:

$$\phi(z_f) = \frac{\pi}{2} \tag{3.62}$$

$$\text{when} \qquad \gamma(z_f) \gg 1 \qquad \text{at the gun exit} \tag{3.63}$$

$$\Rightarrow \phi(z_f) \quad \rightarrow \quad \frac{1}{2\alpha \sin(\phi_o)} + \phi_o = \frac{\pi}{2} \tag{3.64}$$

Solving the transcendental equation for ϕ_o yields the optimal launch phase for highest energy, and also yields the minimum extraction gradient for trapping to occur, below which no solution exists. If $\alpha < 0.8911$, the RF bucket has zero area and no trapping can occur; at 1.3 GHz this gives a minimum gradient of roughly 24.8 MV/m and corresponds to a launch phase of 40.7^o. For $E_o = 35$ MV/m ($\alpha = 1.257$) the prescribed launch phase is $\approx 64.8^o$ while at $E_o = 50$ MV/m, $\alpha = 1.796$, and the launch phase advances to 73.3^o. In fact two solutions to equation (3.64) exist, one of which gives maximal energy and an exit phase $\phi_\infty \rightarrow 90^o$, while the second solution (earlier in phase than the first) also approaches the optimal exit phase, but much more slowly, and gives appreciable pulse compression. Figure (3.1) below shows phase and energy evolution in the 1.5 cell example case.

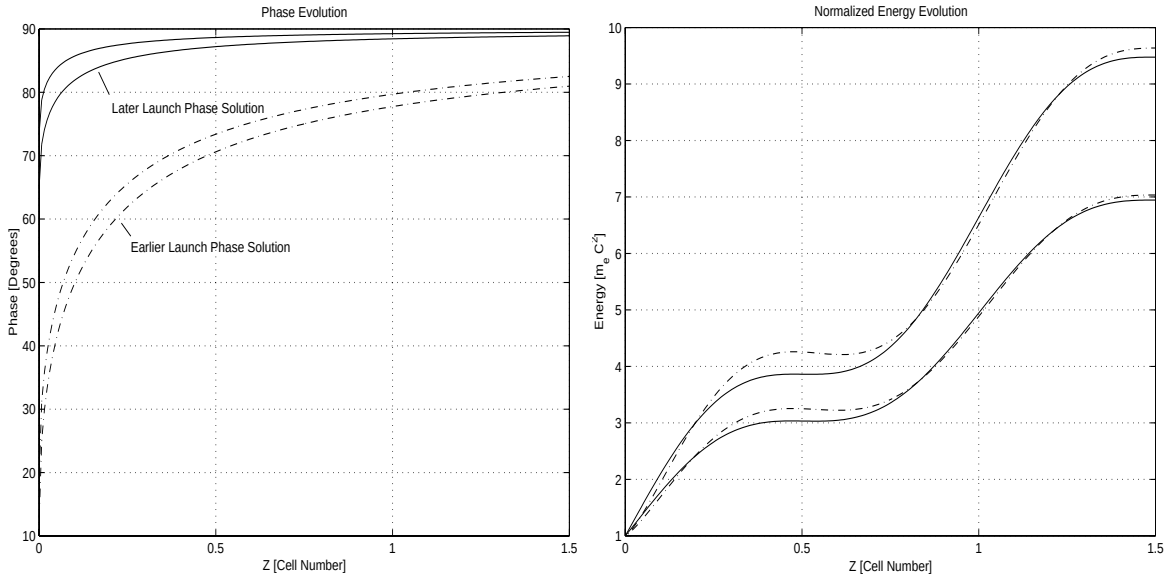

Figure 3.1: Phase and energy evolution in a 1.5 cell gun for 35 MV/m and 50 MV/m accelerating gradients.

Both launch phase solutions are shown, with the earlier launch phase solution indicated with a dashed line.

In high charge injectors for which longitudinal wakefield forces are comparable to the RF forces, the optimum launch phase value is advanced to compensate. In guns with a lengthened half cell, the launch phase is retarded to compensate for the additional time-of-flight.

Pulse Compression

Given that optimal launch phases are usually well ahead of the voltage crest, differential acceleration takes place, giving pulse compression. The RF pulse compression ratio follows immediately from equation (3.64) above:

$$R_c \equiv \frac{\Delta\phi_\infty}{\Delta\phi_o} = 1 - \frac{\cos(\phi_o)}{2\alpha \sin(\phi_o)^2} \tag{3.65}$$

where *only* RF effects are considered. For $\alpha = 1.257$, $\phi_o = 64.8^o$, and $R_c = 0.79$, while for $\alpha = 1.796$, $\phi_o = 73.3^o$, $R_c = 0.91$ and RF pulse compression is lessened. For bunches typical of TTF, ($Q_b = 8$ nC, $\Delta z = \frac{1}{2}a(\Delta t)^2 = 0.19$ mm (at launch!), σ_r =6 mm), the available pulse compression voltage is:

$$V_c = \left.\frac{\partial V}{\partial \phi}\right|_{\phi_o} \Delta\phi = E_o \cos\phi_o \Delta\phi \tag{3.66}$$

which is approximately 140 kV for the 35 MV/m case. This is to be compared with the space charge decompressing voltage, which is on the order of $E_{z,max}\Delta z \approx \frac{2Q_b}{\epsilon_o 4\pi(\Delta z/2)} \approx 1.6$ MV and the longitudinal wakefield voltage at the moment the bunch is fully emitted (again decompressing) of $\frac{Q_b}{\pi\sigma_R^2\epsilon_o}\Delta z \approx 1.5$ kV. Clearly, space charge will cause rapid expansion of the bunch initially and impact the final compression ratio significantly.

Emittance Growth

The phase-dependent acceleration received by the bunch electrons will impart a slope (correlation) and a curvature to the longitudinal phase space that grows quickly with bunch length, resulting in longitudinal emittance growth. Kim obtains:

$$\varepsilon_{z,N}^{rf} = \frac{1}{k_o}(\gamma_f - 1)\sqrt{\langle(\Delta\phi)^4\rangle\langle(\Delta\phi)^2\rangle} \tag{3.67}$$

which for Gaussian beams evaluates to:

$$\varepsilon_{z,N}^{rf} = \sqrt{3}(\gamma_f - 1)k_o^2\sigma_z^3 \tag{3.68}$$

and for uniform beams evaluates to [71]:

$$\varepsilon_{z,N}^{rf} = \sigma_z^4\frac{\alpha}{2\cdot 5!\sqrt{21}}\sqrt{1+\pi^2(N+\frac{1}{2})^2} + \sigma_z^3\frac{\alpha}{4\sqrt{2\cdot 5!}}\sqrt{\pi(N+\frac{1}{2})\sin(\phi)+\cos(\phi)} \tag{3.69}$$

with the rather punitive σ_z^3 scaling for Gaussian beams arising from the curvature ($\propto \sigma_z^2$) and extent ($\propto \sigma_z$) of the phase space. This strong curvature contribution to the emittance can be reduced by exiting the gun close to bunching phase (i.e. $\phi(z_f) = 0^o$), which in practice is never done as it increases the transverse emittance and lowers the exit energy. The exit phase for minimum longitudinal emittance occurs when the second term of (3.69) vanishes:

$$\cot(\phi(z_f)) = -\pi(N+\frac{1}{2}) \tag{3.70}$$

where N is the number of full cells in the gun, and gives an exit phase around -12^o (for 1.5 cells), very far from the condition needed for optimal transverse emittance ($\phi(z_f) = \frac{\pi}{2}$), as will be shown below. When substituted into the launch phase condition (eq. (3.64)) no real solutions for either 35 MV/m or 50 MV/m are found.

Another method of reducing the RF-induced longitudinal emittance growth involves adding another independently phased RF cavity after the gun to cancel the curvature induced by the gun, as the CANDELA injector effectively does with its independently phased half and full cell cavities[72].

3.3.2 Transverse Dynamics

The transverse RF dynamics are dominated by the effects of the backward wave, which in the beam's frame is Doppler up-shifted by $\sqrt{\frac{1+\beta}{1-\beta}}$ such that within the distance of a lab-frame RF wavelength, 2 RF wavelengths pass. As a result, within each accelerating cell of the gun, an entire cycle of the backward wave passes, resulting in RF focussing and defocussing at the entrance and exit of each cell, respectively. For a $\beta = 1$ beam, all effects cancel to first order, and RF structures act (transversely) like drifts. For $\beta \neq 1$, the second-order focussing effects can be quite strong.

Ponderomotive Focussing

Hartman and Rosenzweig [73] calculate the effective focussing strength imposed by a standing wave structure by two methods, the first by direct averaging of the Lorentz force over an RF period, the second by direct calculation of the electromagnetic pressure gradient, with both approaches leading to identical results. Although the first method is mathematically rigorous, the second is intuitively appealing, and is followed here.

For a single space harmonic RF field of the form

$$E_z(z,t) = E_o \cos(k_0 z) \sin(\omega t + \phi_o) \tag{3.71}$$

the average electromagnetic energy density in a single RF cell is

$$\overline{U} = \frac{\epsilon_o}{2}(\overline{\vec{E}^2} + c^2\overline{\vec{B}^2}) \tag{3.72}$$

$$= \frac{\epsilon_o E_o^2}{2}\left(1 + \frac{(kr)^2}{4}\right) \tag{3.73}$$

For the purposes of computing a total energy displaced in the RF photon/electron interaction, an interaction volume, which is the product of the photon cross section $2\pi/k_o^2$ and the lab-frame electron "length" r_e/γ, is used:

$$V_{eff} = \frac{2\pi}{k_o^2}\frac{r_e}{\gamma} \tag{3.74}$$

and the resultant time-averaged force on the electron is just:

$$\overline{F_r} = -\frac{\partial(\overline{U} \cdot V_{eff})}{\partial r} = -r\frac{e^2 E_o^2}{8\gamma m_e c^2} \tag{3.75}$$

For the $E_o = 35$ MV/m case this focussing strength is approximately $300/\gamma$ [kV/mm] at the cathode (equivalent to 1 T/m for a $\beta = 1$ particle), making this a nontrivial concern in designing the transverse optics.

Emittance Growth

RF induced emittance growth occurs through two mechanisms: the first derives from the nonlinear focussing forces developed from the higher space harmonics (which are transversely of $I_0(k_{rn}r)$ form), and can be effectively reduced by careful selection of the cavity geometry; the second derives from the non-zero curvature of the RF fields across the bunch, and can only be appreciably affected by the choice of RF frequency and the bunch dimensions.

For the treatment that follows, the accelerating field E_z will be divided into a Fourier term and an overall scale function $E(z)$ that is equal to the peak electric field

throughout the structure, and vanishes at the exit:

$$E_z(z,t) = E(z)\sin(\omega t + \phi_o)\cos(k_o z) \tag{3.76}$$

where ϕ_o is the launch phase of the electron bunch, and the structure length $z_f = (n + 1/2)\frac{\lambda}{2}$. Maxwell's equations for the transverse fields reduce for rotationally symmetric systems to:

$$E_r(z,t) = -\frac{r}{2}\frac{\partial E_z(z,t)}{\partial z} \tag{3.77}$$

$$B_\theta(z,t) = \frac{r}{2c}\frac{\partial E_z(z,t)}{\partial t} \tag{3.78}$$

The radial Lorentz force component F_r may be written, with the aid of convective derivatives, as:

$$F_r = e(E_r - \beta c B_\theta) \tag{3.79}$$

$$\begin{aligned} = & -\frac{er}{2}(-\frac{1}{c}\frac{d}{dt}(E(z)\sin(k_o z)\cos(\omega t + \phi_o)) - \frac{1}{2}(\frac{d}{dz}E(z))\cos(k_o z)\sin(\omega t + \phi_o) \\ & + \frac{\beta}{2}(\frac{d}{dz}E(z))\sin(k_o z)\cos(\omega t + \phi_o)) \end{aligned} \tag{3.80}$$

The function $E(z)$ is used to terminate the RF fields at the physical exit of the gun, which to zeroth order may be represented by a Heaviside step function:

$$E(z) = E_o(1 - \Theta(z - z_f)) \tag{3.81}$$

The momentum p_r is then given by integrating (3.80), a task made trivial by the delta functions introduced by E_z':

$$p_r = \alpha k_o r[-\cos(k_o z_f)\sin(\omega t + \phi_o) + \beta\sin(k_o z_f)\cos(\omega t + \phi_o)] \tag{3.82}$$

or, since $\beta \approx 1$ at the gun exit,

$$p_r = \alpha k_o r \sin(\phi(z_f)) \tag{3.83}$$

which implies $p_x = \alpha k_o x \sin(\phi)$. Note that this represents a defocussing kick when $0 < \phi < \pi$. Performing the requisite moment integrals, the normalized one-sigma transverse emittance gain at the exit of the RF gun for a Gaussian distribution will be:

$$\varepsilon_{N,x} = \frac{\alpha k_o^3 \sigma_x^2 \sigma_z^2}{\sqrt{2}} \tag{3.84}$$

when the optimum launch phase is chosen, and varies as

$$\varepsilon_{N,x} \sim \alpha k_o^3 \sigma_x^2 \sigma_z^2 |\cos(\phi)| \sim \left| \frac{\pi}{2} - \phi \right| \tag{3.85}$$

in the neighborhood of the minimum. It is apparent from (3.83) that the optimal exit phase for the transverse emittance gives the largest defocussing kick, which requires external focussing (a solenoid or quad doublet, for instance) to follow the gun.

Equation (3.85) allows a computation of the incremental emittance growth given a knowledge of the beam dimensions at the *exit* of the gun, not at the cathode. Inferences may still be drawn as to what bunch dimensions are desired to minimize the effect, but are strongly influenced by space charge and external focussing forces along the way. The quadratic dimensional scalings clearly point to the smallest bunch size possible, an optimization that must be balanced against countermanding space charge considerations.

3.3.3 RF Structure Defects

Power coupling into normal-conducting microwave structures is generally accomplished by magnetically coupling one or two of the resonant cavities to a waveguide through an aperture. The opening of a coupling aperture breaks the rotational symmetry of the structure and scatters energy into the higher order multipoles of the

RF field, of which the dipole component is the lowest order and most destructive to the transverse beam quality. Given that many photoinjectors have a solenoid near the cathode for focussing, the induced quadrupole component can contribute appreciably as well, as the beam will rotate through the RF quadrupole field, resulting in a time-dependent skew quadrupole kick to the beam that is virtually impossible to compensate.

Estimates of the emittance dilution resulting from the coupler-produced multipole moments have been made by Chojnacki [74] (dipole in half cell only) and Palmer [75], and scale as follows:

$$\Delta\varepsilon_{N,x} \approx \frac{e}{m_e c^2}\frac{\sigma_z}{2\pi}\sigma_x\lambda_{rf}E_o\sum_{n=1}^{\infty}a_n\frac{r^{n-1}}{r^n}\int_0^L E_z(z)dz \tag{3.86}$$

An additional phase front distortion must be present across the coupled cavity for power to flow. This Poynting-vector derived distortion is very small, as the large cavity Q indicates, since the energy entering the cavity per cycle is small compared to the energy stored in the cavity, thus the phase distortion due to the power flow is also very small.

Field imbalance, or unequal field amplitude from one cavity of an RF structure to the next, can also give rise to emittance growth for precisely the same reason as at the exit, namely the discontinuity in $E_z(z)$ at the cavity boundary has an associated time-dependent kick that will not cancel in first order as it usually does. This emittance growth is given by a slightly modified version of equation (3.84):

$$\Delta\varepsilon_{N,x} = \frac{e(E_n - E_{n+1})k_o^2\sigma_x^2\sigma_z^2}{2m_e c^2\sqrt{2}} \tag{3.87}$$

Additionally, a defocussing or focussing kick will accompany the emittance growth, depending on the sign of the difference $E_n - E_{n+1}$.

3.4 RF Photoinjector Theory: Space Charge

Space charge emittance growth in bunched beams has received numerous treatments. Three recent treatments directly aimed at emittance growth in RF photoinjectors will be discussed here. The first is Kim's theory which gives an estimate of the dilution based on scaling laws and field moments. Carlsten's treatment of the reversal of a space charge induced (x, x', z)-space correlation under certain conditions is given, followed by a brief treatment of the physically detailed explanation of the "emittance compensation" as a special case of Brillouin flow [76] presented by Serafini and Rosenzweig.

3.4.1 Kim Theory

Kim's treatment [69] is founded on the observation that the space charge forces on an accelerating bunch may be cast in a form which divorces a manifestly geometric form factor, responsible for the shape of the phase space distortion, from a magnitude responsible for the size of the distortion:

$$eE_q(x, y, z) = \frac{1}{\gamma^2} f(\gamma, x, y, z) \tag{3.88}$$

with the function $f(\gamma, x, y, z)$, containing the geometric field information. In this form, a straightforward estimation of the momentum kick integral:

$$\Delta\vec{p} = \frac{1}{m_e c} \int_0^{z_f} \frac{1}{\gamma^2 \beta} f(\gamma) dz \tag{3.89}$$

(where p is in units of $m_e c$) by changing to an integration in γ by means of (3.54) and evaluating:

$$\Delta\vec{p} = \int_1^{\gamma_f} \frac{d\gamma}{\gamma^2 \beta} f(\gamma) \tag{3.90}$$

At higher energies, the bunch rest frame aspect ratio A is smaller than unity (the bunch is rod-like), and is a slowly varying function of γ. If the brief period after launch of the electron beam, in which $A >> 1$ and the bunch is disk-like, is neglected, then the approximation $f(\gamma) \approx f(1)$ can be made and f may be subsequently extracted from the integral:

$$\Delta\vec{p} = \frac{1}{eE_o \sin(\phi_o)} f(1) \int_1^{\gamma_f} \frac{d\gamma}{\gamma^2 \beta} = \frac{1}{eE_o \sin(\phi_o)} e\vec{E}^{SC} \left[\frac{\pi}{2} - \sin^{-1}\left(\frac{1}{\gamma_f}\right) \right] \tag{3.91}$$

Since $\gamma_f \gg 1$ for typical RF guns, the term in brackets is well approximated as simply $\frac{\pi}{2}$. Thus the integrated transverse kick due to space charge fields is:

$$\Delta\vec{p} = \frac{1}{E_o \sin(\phi_o)} \frac{\pi}{2} \vec{E}^{SC} \tag{3.92}$$

The emittance growth can be evaluated by calculating the requisite moments, and takes the form:

$$\varepsilon_{N,q}^{SC} = \frac{\pi}{4} \frac{1}{\alpha k_o} \frac{1}{\sin(\phi_o)} \frac{I}{I_A} \mu_q(A) \tag{3.93}$$

where $I_A = 4\pi\epsilon_o m_e c^3/e$ is the Alfvén current, $A = \sigma_x/\sigma_z$ is the lab-frame bunch aspect ratio, and

$$\mu_q(A) = \sqrt{\langle q^2 \rangle \langle \mathcal{E}_q^2 \rangle - \langle q\mathcal{E}_q \rangle^2} \tag{3.94}$$

and the normalized space charge field $\mathcal{E}_q$ is defined by $E_q^{SC} \equiv \frac{Q_b}{e4\pi\epsilon_o} \mathcal{E}_q$.

Kim evaluates the integrals (3.94) numerically and obtains simple, empirical representations for Gaussian beam distributions:

$$\mu_x(A) = \frac{1}{3A + 5} \tag{3.95}$$

$$\mu_z(A) = \frac{1}{1 + 4.5A + 2.9A^2} \tag{3.96}$$

Taking the space charge and RF emittance growth effects together, one can estimate the expected emittance from an RF photoinjector as a function of the beam parameters, which has been done for the optimal transverse emittance case ($\phi_\infty = \pi/2$) and a range of bunch radii and lengths, and is shown in figure 3.2 for the transverse emittance and in figure 3.3 for the longitudinal case. Plotted are the natural logarithms of the respective emittances to more clearly separate the contours. Global minima for long, small radius bunches in the transverse case, and short, large radius bunches in the longitudinal case are plainly visible. Plotted across the emittance contours are contours of constant aspect ratio A (radiating from the origin) and contours of constant bunch density (avoiding the origin).

Several conclusions may be drawn from equation (3.93). Launching close to crest ($\phi_o \rightarrow 90^o$) lessens the space charge emittance growth, as do raising the gradient (the Brookhaven ATF approach) and lowering the peak current (the Los Alamos APEX approach) by starting with longer bunches. Raising the RF frequency (the MIT approach) also lowers the space charge contribution, but like the prior three variations, results in *increased* RF emittance growth.

This theory obviously depends on the rest frame bunch lengthening as being the primary geometric distortion taking place. Radial charge distribution deformation and the evolution of correlations within the distribution due to z-variation of the transverse space charge fields are absent from the estimate here. As will be seen, these unaccounted effects can significantly influence the beam quality.

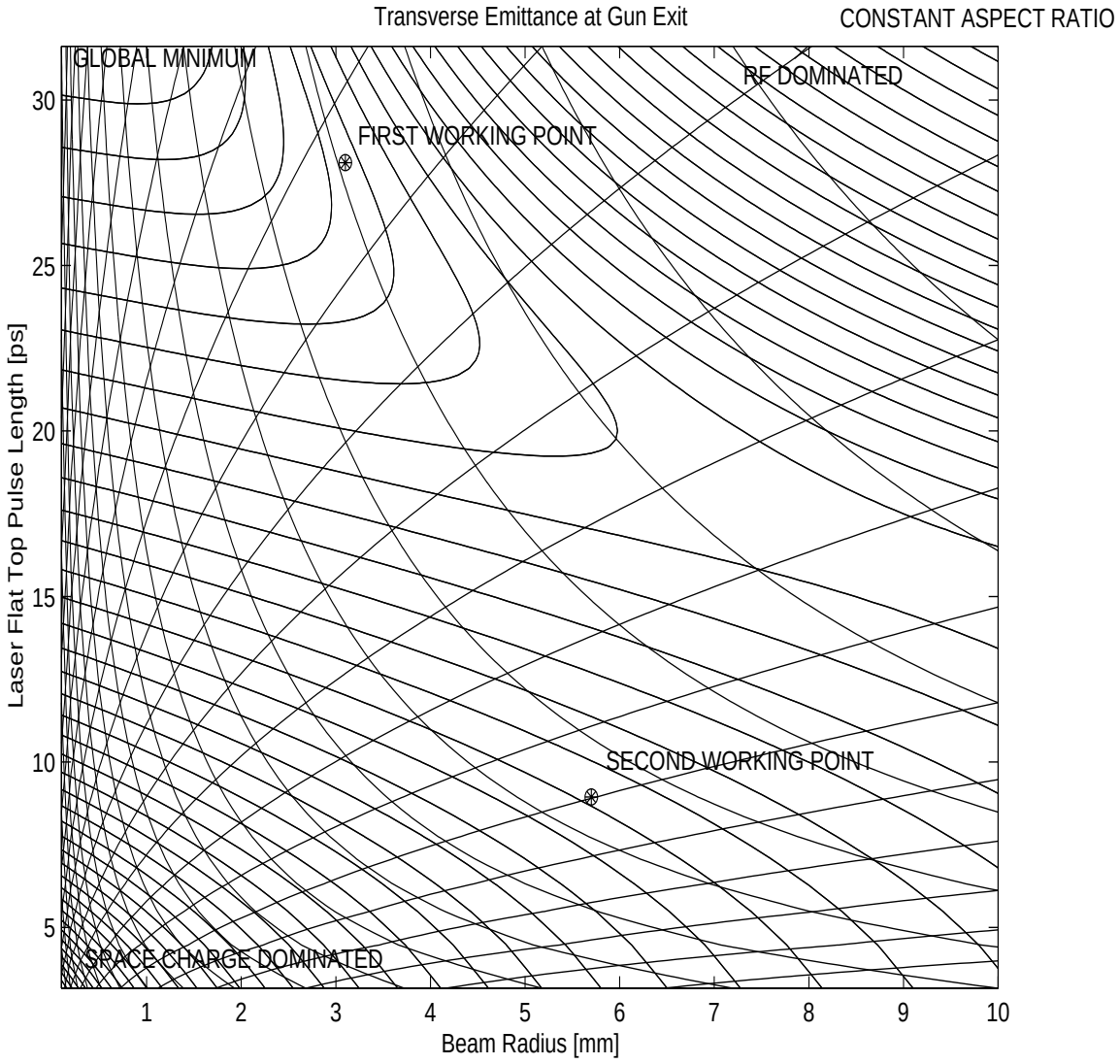

Figure 3.2: Transverse emittance kick at gun exit, from Kim theory

3.4.2 Carlsten-Sheffield Compensation Theory

Careful consideration of the form of the transverse space charge fields, as shown in figure 3.4 below for both longitudinally Gaussian and uniform bunches, shows that the radial defocussing force experienced by electrons at various z-locations within the

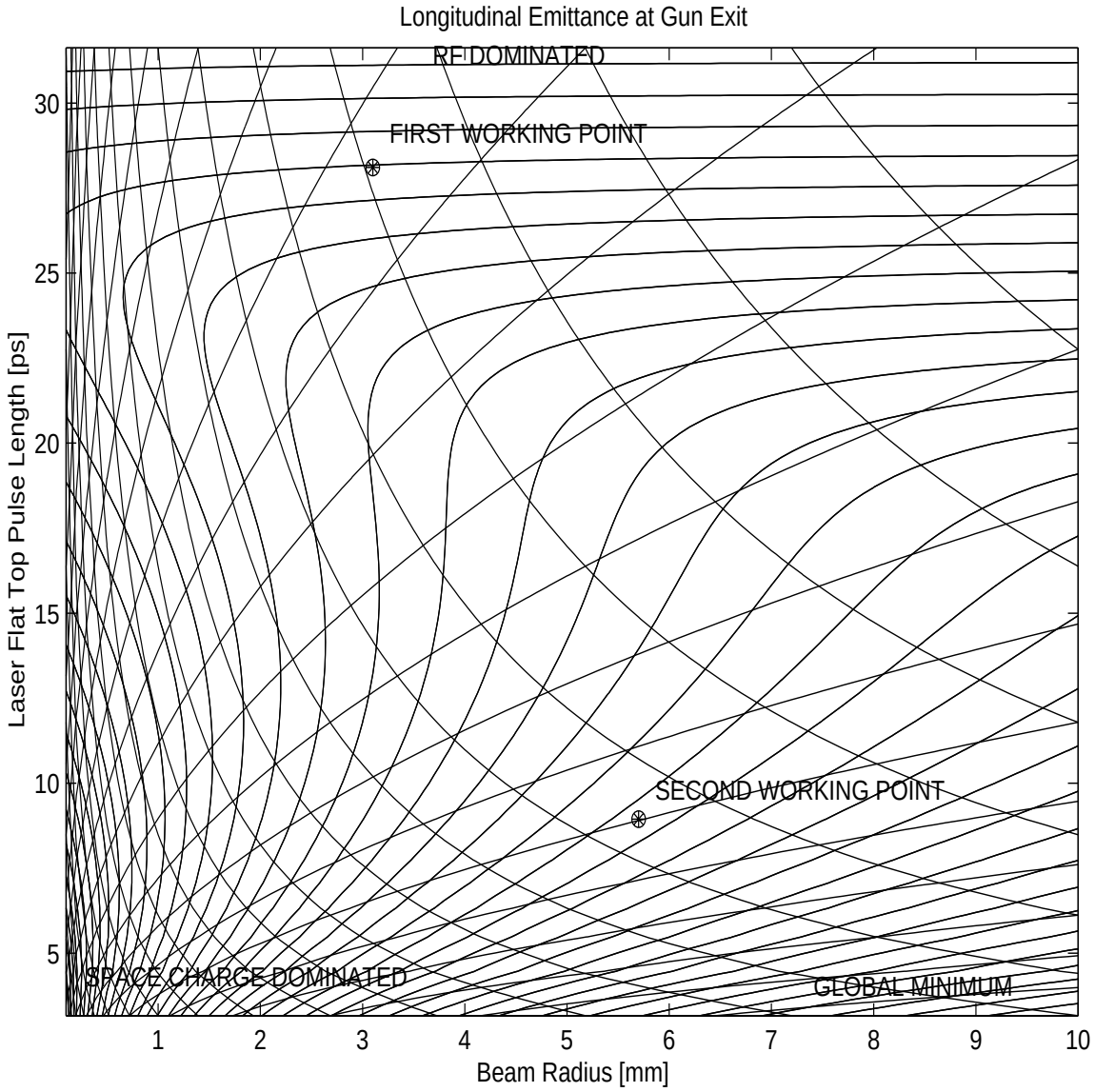

Figure 3.3: Longitudinal emittance kick at gun exit, from Kim theory

bunch will be very different, resulting in a twisting of the (x, x') phase space along the bunch.

As a result of the varying radial space charge field, the betatron phase advance $\mu(s) = \int_0^s \beta(s)^{-1} ds$ is not the same for all particles, being larger for particles close

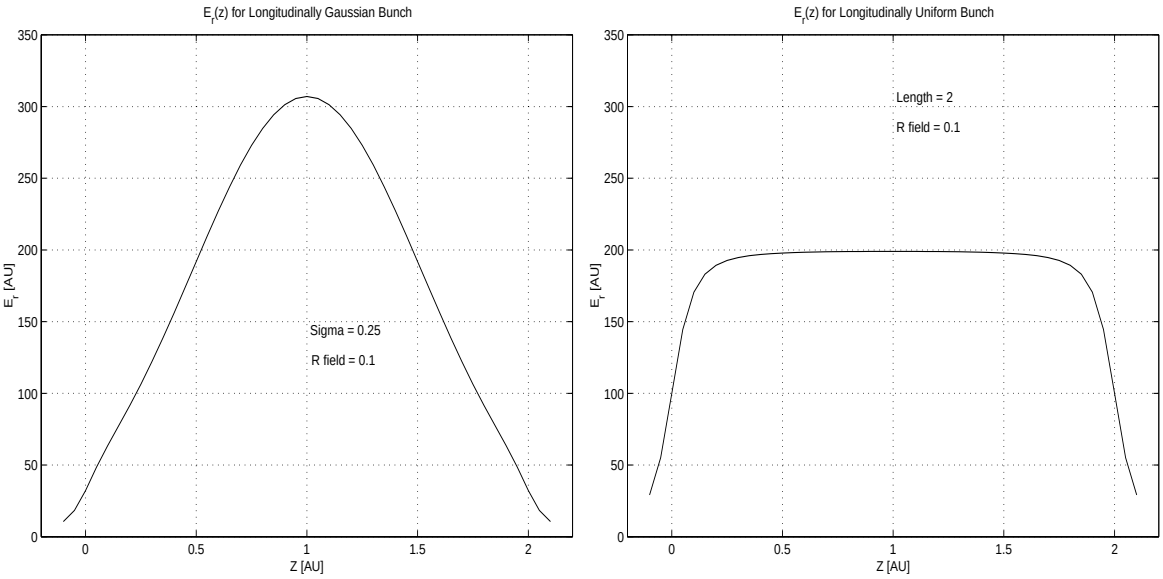

Figure 3.4: Radial electric field for longitudinally Gaussian and uniform charge distributions. Bunch charge is the same for both cases.

to the center of the bunch, where space charge forces are strongest, and smaller for particles close to the ends. The spread of phase advances gives rise to a correlation in (r, r', z) space that when projected into (r, r') phase space appears as an emittance increase. Under the nearly laminar flow conditions present in most RF photoinjectors, this correlation persists for many meters of transport. As acceleration rapidly reduces the space charge forces, the beam will eventually make a transition from space charge dominated laminar flow to emittance dominated non-laminar flow, and the correlation will wash out, causing irreversible emittance increase.

From kinematics considerations of the focussing of different particles within a drifting bunched beam, Carlsten writes [95]:

$$r(\zeta) = r_0 + \lambda(r_0, \zeta) z_1^2/2 \tag{3.97}$$

$$r'(\zeta) = \lambda(r_0, \zeta) z_1 \tag{3.98}$$

where $\lambda \equiv F_{SC}/mc^2$ is the normalized space charge force, the local beam radius $\rho = r_0$ at launch, and the internal z coordinate $\zeta = z - \beta ct$ has been defined. The cathode is positioned at $z = -z_1$. When subject to the focussing of a linear lens of strength $k \equiv 1/f$ is applied the following condition on the phase space angles of all the beam slices arises:

$$\frac{r'(\rho,\zeta)}{r(\rho,\zeta)} = \frac{2(z_1+z)}{z(z+2z_1)} \tag{3.99}$$

Minimum emittance for a drifting, compensating beam is obtained when the focal strength satisfies:

$$k = \frac{\int_{-z_1}^{z} \lambda(z')dz'}{z\int_0^z \lambda(z')dz' \int_0^z \int_{-z_1}^{z''} \lambda(z')dz'dz''} \tag{3.100}$$

Given that the electron beam is accelerating while focussing, the condition (3.100) is only approximately correct. Modification of the kinematic considerations to include acceleration is straightforward if the result is not (see eq. (4) in reference [95]). Numerical integration of the condition is required for most cases of interest.

Simple models of beam propagation under space charge, constant acceleration and solenoidal focussing were constructed in MathCAD by Rosenzweig and in Matlab by myself. These models differed in physical detail, but both performed numerical integration of simplified equations of motion in the radial plane for a few representative particles. For this toy model, unequal space charge force $K_{SC,i}$ is applied to each particle, which is integrated along the theoretically Spartan equation of motion:

$$\frac{d^2y}{dz^2} + \frac{\alpha}{\gamma}\frac{dy}{dz} \approx \frac{K_{SC,i} - K_{FOCUS}(z)}{\gamma^2} y \tag{3.101}$$

$$\gamma = 1 + \alpha z \tag{3.102}$$

$$K_{FOCUS}(z) = A\exp(-(z-z_c)^2/(2\sigma_m^2)) \tag{3.103}$$

with the resultant particle motion and emittance evolution shown in figure 3.5 below.

Although the model is incomplete in many respects (lacking geometric form factors for the RF and space charge fields, and wakefield effects), it is nonetheless instructive, as the basic emittance compensation mechanism is preserved, and execution time is a few seconds rather than hours.

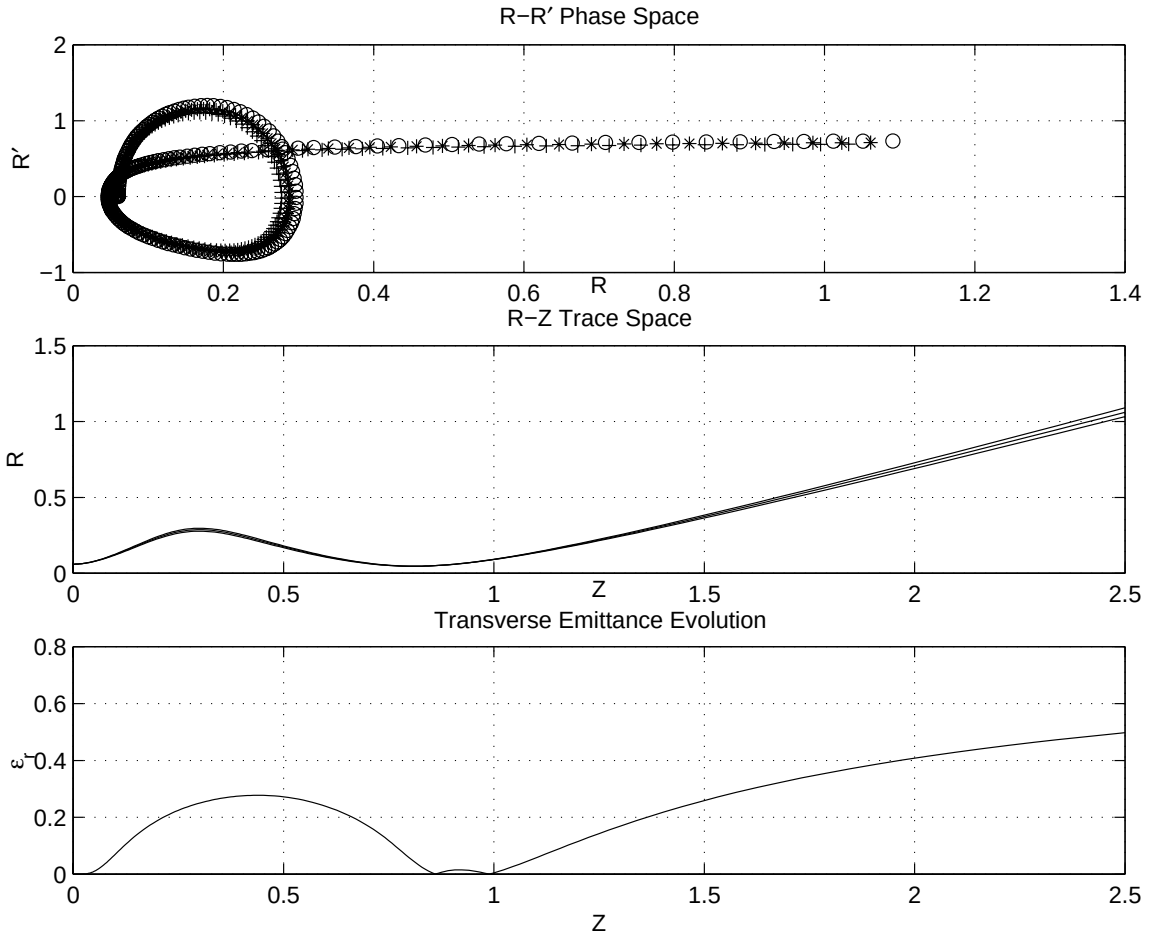

Figure 3.5: Simple emittance compensation model output

With such a model, it becomes possible to probe large regions of the basic parameter space. Shown in figure 3.6 below is the emittance of a set of 11 test particles with currents ranging linearly from 0.95 to 1.05.

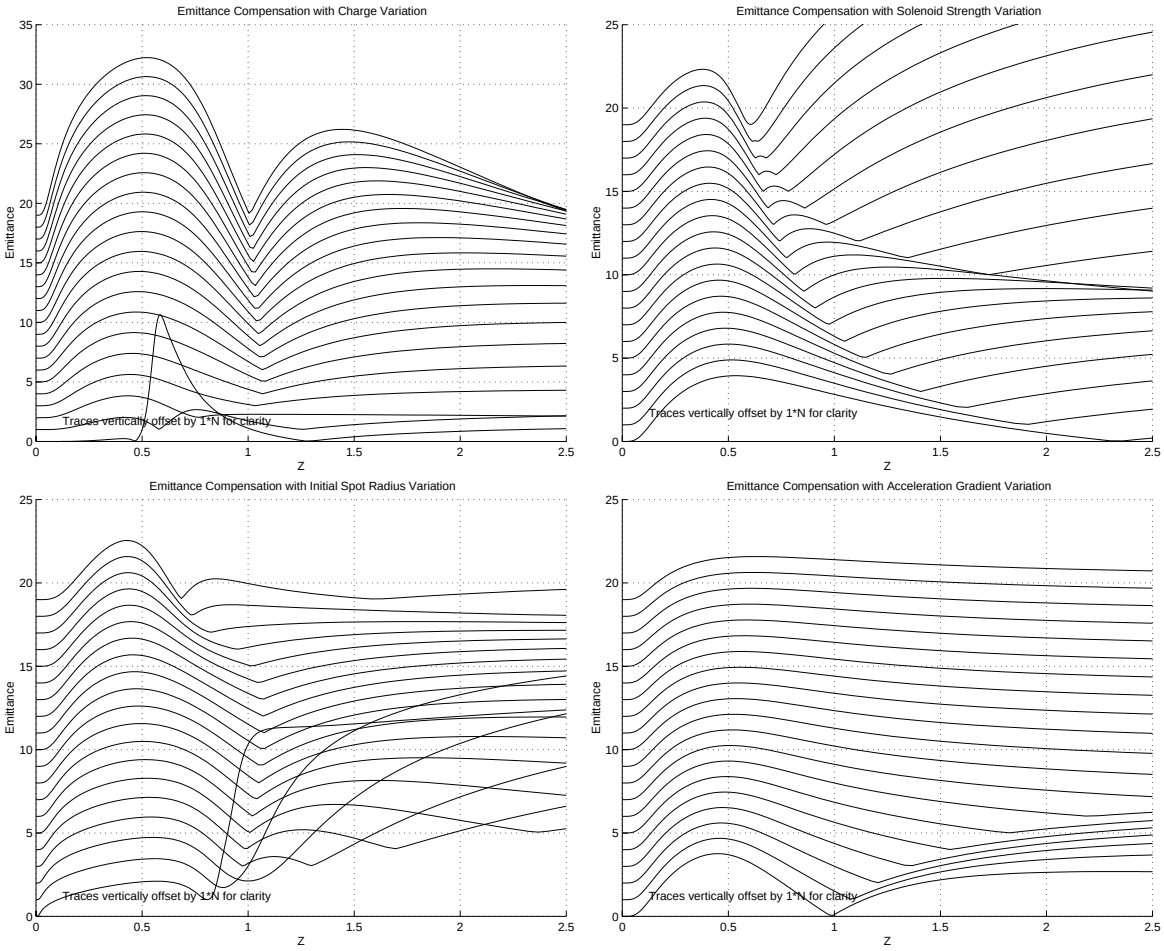

Figure 3.6: Emittance compensation model prediction of emittance evolution under a wide variety of operating conditions.

The upper left plot shows the effect of increased charge per bunch, with the lower bunch charge cases showing slower post-compensation emittance growth than the high charge cases. The relative charge insensitivity of the location of the emittance minimum is a hallmark of the compensation process, as alignment of the phase ellipses occurs at this point for a wide range of transverse space charge $F_r(z)$ strengths. The upper right plot shows the effect of increased solenoid strength, with lower strength causing later compensation at two locations, one before the focal waist, one after. At

higher solenoid fields, the two minima coalesce at the waist itself. Clear from this plot is the possibility to establish an emittance minima over a wide variety of beam divergence conditions, making possible a successful match to the entrance conditions required for matched transport in a standing wave linac.

The plot at lower left shows the effect of increased spot size, with small spots undergoing sufficiently violent space-charge driven expansion at the start that the resultant envelope oscillations can never be made to realign. For larger spot sizes, there is less significant space-charge driven expansion, and compensation is relatively insensitive to the launched spot radius. The last plot at lower right shows the effect of accelerating gradient increase, and as is readily anticipated from the simplified equation of motion, the only effect is to delay the emittance compensation minimum.

Although phenomenologically descriptive, the above theory does not explain the basic physical condition being satisfied in the emittance compensation process.

3.4.3 Serafini-Rosenzweig Invariant Envelope Theory

The most descriptive theory of "emittance compensation" arises from the envelope theory formalism, and has recently been documented [70] by Serafini and Rosenzweig as a form of Brillouin flow. The necessary condition that the phase space orientation of the slice emittance ellipses be independent of z requires that the accelerating channel focus particles within a range of the design current with exactly the same space charge shifted phase advance. This theory has evolved since the design of the TTF photoinjector, and will here be treated briefly and heuristically only.

The motion of the particles under the combined space charge, RF and focussing forces resembles that of an ensemble of biased pendula. In an RF photocathode gun,

the particles are launched with very little transverse momentum, with the corresponding condition for the ensemble being that all pendula are in phase at the launch of the bunch (more specifically, all phases are zero at launch). The angular velocities of the pendula are set by the local details of the charge distribution, and to a lesser degree, the local RF fields (which vary slowly along the bunch by comparison). The pendula velocity spread will give rise to a spread of particle phases, which is to say, emittance. Figure 3.7 below shows the phase spread $\equiv \phi_i - \langle \phi_i \rangle$ for the compensation case in figure 3.5 above. The phase spread becomes substantial (but correlated!) at several locations, and nearly vanishing at two locations, where the emittance is also a minimum.

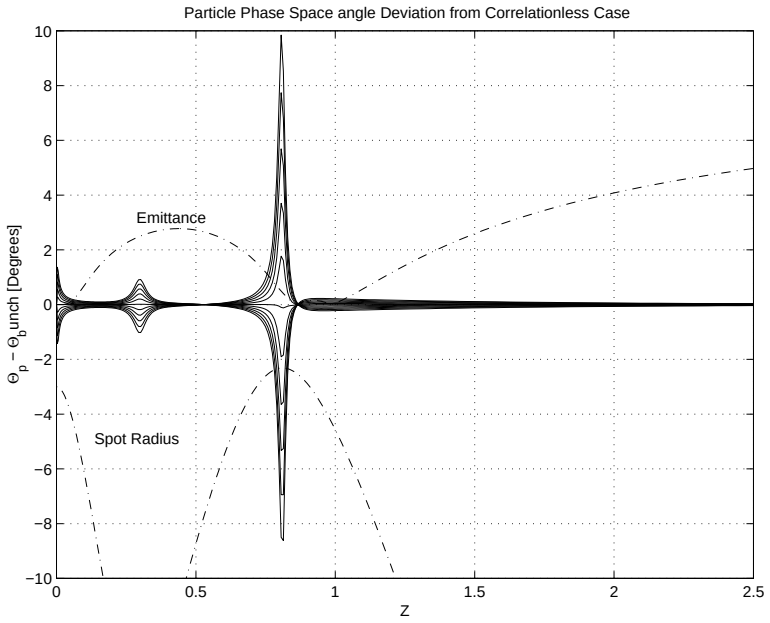

Figure 3.7: Phase spread for the compensation case shown in figure 3.5 above.

Linear space charge emittance compensation, viewed in this context, reduces to a

stationary betatron phase advance condition:

$$\frac{\partial \mu(s)}{\partial I} = 0 \tag{3.104}$$

where $\mu(s) \equiv \int_0^s \beta(s)^{-1} ds$.

It has been suggested [77] that the emittance compensation process is simply a beam "echo", with the magnetostatic focussing kicks causing the initial beam condition (correlationless $\rightleftharpoons$ pendula all at same phase) to reappear as a beam echo.

3.5 Magnetic Pulse Compression

Magnetic pulse compression, as described in the background section, can take principally three forms, the alpha-magnet, a non-zero momentum compaction arc, or a chicane. The alpha magnet is a modified dipole which bends the beam through approximately 270^o, and is generally limited to low energies (< 5 MeV), making it unattractive for the high bunch charge TTF injector, as pulse compression at such an early stage would greatly exacerbate the space charge emittance growth. The latter two cases are similar, with the chicane and arc capable of operating with either positive or negative temporal dispersion, R_{56}. A compressive arc would require non-trivial modification of the layout of the TTF injector section, and is not considered here. The chicane enjoys relative compactness and easy tunability.

A dipole chicane is shown, with relevant dimensions, in figure 3.8 below. By inspection, the chicane is dispersionless to first order in $\delta p/p_o$ in the absence of perturbing forces, such as space charge.

Simple numerical integration of the particle trajectories under the influence of the bend fields only, produced figure 3.9. On the upper left are two traces, the upper trace

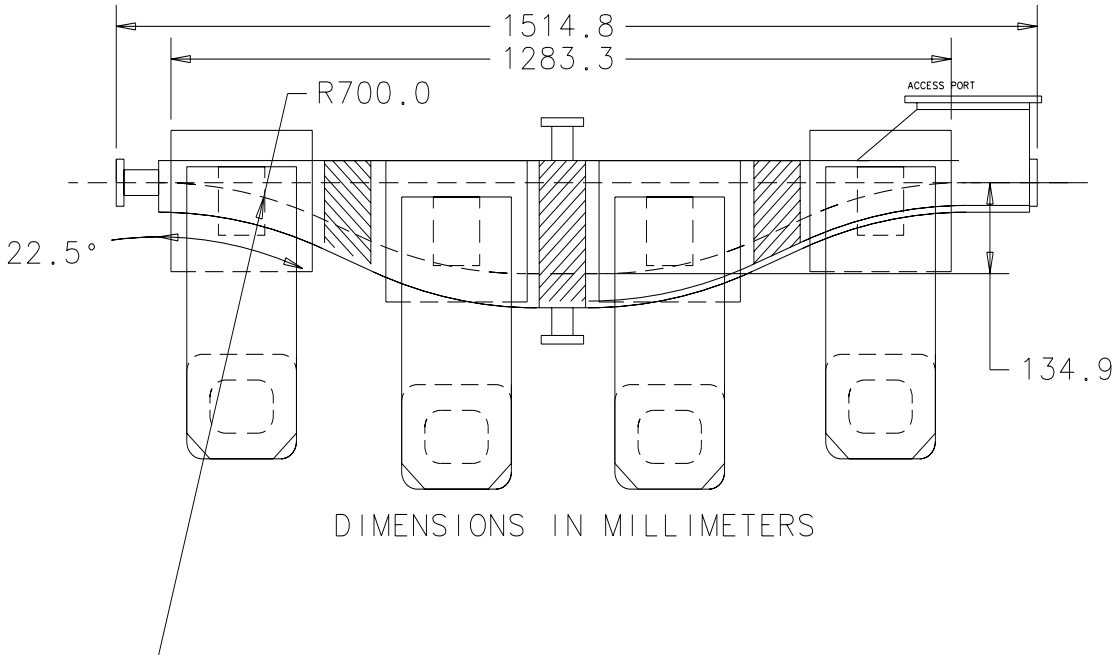

Figure 3.8: The dipole chicane pulse compressor, straight-through and most compressive orbits are shown.

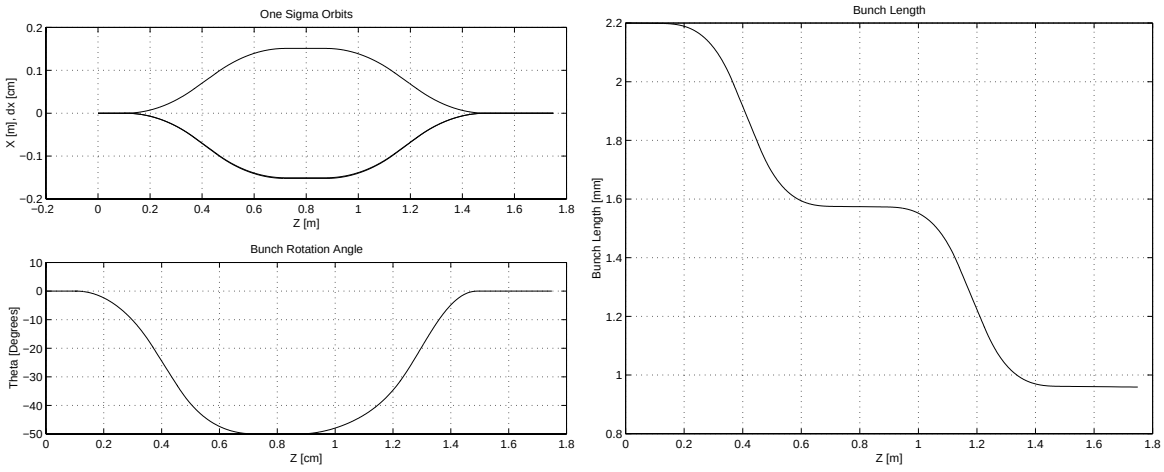

Figure 3.9: Particle tracings (left) in pulse compressor, and bunch length (right).

representing the lab-frame displacement of a set of representative particles spanning the bunch length, the lower trace representing the displacement of the head relative to the tail (essentially a plot of the dispersion function). The lower plot shows the rotation of the bunch on passing through the chicane, and gives an indication of how a collimator would perform at the highest dispersion point of the chicane. The plot on the right shows the pulse length compression. For all three plots, the fractional energy spread is $\sigma_E/\mu_E = 1.3\%$, the bend radius and angle of the magnets are $\rho = 70$ cm and 22.5^o, and the inter-magnet spacing $L_{12} = 8.5$cm.

Bunch lengthening or compression result from the differing path lengths traversed by different energy particles. If the bunch is given an negative energy-phase correlation, with the head having lower energy than the tail, the more energetic particles bend less in the dipoles, take the inside path, and catch up to the lower energy particles, which took the longer outside path. Obviously, if the energy-phase correlation is reversed, the bunch will lengthen. The bunch length after traversing the chicane for a transversely cold beam ($x' = y' = 0$) is given by:

$$\Delta\phi_f = \Delta\phi_o + \eta_\phi \delta \tag{3.105}$$

where $\Delta\phi \equiv \sigma_\phi$, $\delta \equiv \delta p/p_o$ is the usual fractional momentum difference from the reference orbit, and η_ϕ is the temporal dispersion of the chicane. Equation (3.105) neglects the effects of all higher order distortions of the longitudinal phase space beyond the first-order correlation. In particular, RF fields induce second-order curvature (the leading and dominant term, there are higher-order terms as well), space-charge fields induce first- and third-order terms as can wakefields. The first-order effects of RF, space charge and wakefields must be balanced to give the needed phase-energy correlation to achieve compression. The higher order distortions prevent full compression

of the beam, and must be minimized or directly addressed with nonlinearly dispersive chicanes, as suggested [78], and subsequently tested [79] by Carlsten.

The pulse compression ratio is defined:

$$r_c \equiv \frac{\Delta\phi_o}{\Delta\phi_f} \tag{3.106}$$

which for a purely linear phase-energy correlation becomes:

$$r_c \approx \frac{\Delta\phi_o}{\Delta\phi_o + \eta_\phi \delta} \tag{3.107}$$

The temporal dispersion or the momentum correlation must be negative for the compression ratio to be greater than unity (i.e. compressing). As the compression arises from a path length difference between different energy particles, it is purely geometry-dependent.

The some straightforward if ungraceful geometry will show that the displacement of the bunch at the mid-plane of the chicane (between dipoles 2 and 3) is:

$$\Delta x = 2\rho(1 - \cos(\alpha)) + L_{12}\frac{\sin(\alpha)}{\cos(\alpha)} \tag{3.108}$$

where $\rho(\gamma) = p/qB$ is the bend radius within the magnet, L_m is the magnetic length of the dipole, L_{12} is the length of the drift between dipoles 1 and 2 (and $L_{34} = L_{12}$). From the definition of the dispersion function:

$$\eta_x(s) \equiv \frac{\partial(\Delta x(s))}{\partial(\frac{\delta p}{p_o})} \approx \frac{\partial(\Delta x)}{\partial\left(\frac{\delta E}{E_o}\right)} \tag{3.109}$$

where the approximate form $\delta p/p_o = \delta E/E_o + \delta\beta/\beta \approx \delta E/E_o$ is exact in the limit $\beta \to 1$. The derivative may be evaluated yielding the dispersion at the mid-plane of the chicane:

$$\hat{\eta}_x(s) = 2\rho(1 - \cos(\alpha) - \frac{\sin^2\alpha}{\cos\alpha}) - L_{12}\frac{\sin(\alpha)}{\cos^3(\alpha)} \tag{3.110}$$

The "temporal dispersion" of the chicane is the key parameter in determining the amount of compression possible for a bunch with a given correlation parameter α_ϕ. The temporal dispersion, η_ϕ is defined by the relation:

$$\eta_\phi(s) \equiv \frac{\partial(\Delta\phi)}{\partial(\frac{\delta p}{p_o})} \approx -\frac{2\pi}{\lambda_{RF}} \frac{\partial(\Delta s)}{\partial\left(\frac{\delta E}{E_o}\right)} \tag{3.111}$$

where again the ultra-relativistic approximation $\beta = 1$ is applied, and the $\delta\beta/\beta$ velocity bunching term has been neglected. In Transport notation [80] this corresponds to the $(\phi|\delta p/p_o)$ element of the first-order transport matrix, R_{56}. The temporal dispersion of the chicane controls the degree of phase space rotation and sheer in the (ϕ, E) plane, and sets the maximum compression ratio.

$$\begin{aligned}
\eta_\phi &= \int \left[\frac{1}{\gamma^2} - \frac{\eta_x(s)}{\rho}\right] ds & (3.112)\\
&\approx \frac{2\pi}{\lambda_{RF}} \left[4\rho\alpha - 4\rho\tan(\alpha) - 2L_{12}\sec(\alpha)\tan^2(\alpha)\right] & (3.113)\\
&\approx \frac{2\pi}{\lambda} \left[2L_{12}\alpha + (2L_{12} + \frac{2}{3}L_{12} + \frac{4}{3}\rho)\alpha^3 + \cdots + \mathcal{O}(\alpha^5)\right] & (3.114)
\end{aligned}$$

It is worth noting that in the absence of space charge effects, the length of the drift between dipoles 2 and 3 is irrelevant to the compression process, allowing considerations of the transverse focussing of the chicane, and convenience in positioning diagnostics and (well-motivated, but likely damaging) longitudinal collimation slits to control its length.

Table 3.1 below lists the parameters for the chicane shown in figure 3.8.

The last parameter, "nominal bunch inclination" angle, is the orientation of the bunch's former "z" axis with respect to the local z-axis at the high dispersion point of the chicane. For clean collimation of the longitudinal head and tail of the bunch, which carry most of the transverse emittance, the inclination should be 90^o. That it

Parameter	Symbol	Value	Units
Magnet physical length	L_m	23.24	cm
Gap height	g	3.56	cm
Drift length	L_{12}	8.5	cm
Maximum bend angle	θ_b	22.5	Degrees
Minimum bend radius	ρ	70	cm
Maximum excursion	Δx_{max}	14.54	cm
Maximum dispersion	$\hat{\eta}_x$	-15.66	cm
Temporal dispersion	R_{56}	2.501	rad
Nominal compression ratio[a]	$\hat{r}_c$	2.18	
Nominal bunch inclination	$\langle \frac{dx}{dz} \rangle$	60	Degrees

[a] For $\delta = \sigma_E/E = 1.3$ %

Table 3.1: Chicane parameter summary

is only 60^o indicates that effective collimation of the head and tail of the bunch will also remove an appreciable fraction of the core of the bunch.

Additionally, and more importantly, energy jitter of the beam will result in transverse position jitter at the collimation slits, and consequently charge jitter. Thus phase and laser amplitude jitters will be converted into charge jitter by the collimation process. Wakefields associated with the slits add one more reason to avoid this theoretical expediency.

3.6 Scaling Laws for Photoinjector Design

Motivated by the difficulties involved in optimizing photoinjector designs, a set of scaling laws was sought to allow first-order estimation of how to alter photoinjector design parameters to suit different bunch charges and different RF accelerating frequencies [81, 82]. With such a set of scaling laws also comes the ability to make across-the-board comparisons of the world's photoinjector designs on an equal foot-

ing, despite bunch charges spanning almost four orders of magnitude (from the UCLA ultrashort pulse injector (33 pC) to the AWA drive injector (100 nC)), and RF frequencies spanning more than two order of magnitude (from Bruyeres-la-Chatele at 133 MHz to MIT at 17.136 GHz).

An inspection of the form of the equations of motion for the longitudinal plane (3.61) shows that they are already dimensionless, implying that the longitudinal evolution of the RF accelerated beam is universal in the variable $\zeta = k_{RF}z$. Thus scaling the frequency implies scaling all longitudinal dimensions by k_{RF}^{-1}. One other dimensionless quantity enters into (3.61), which is the normalized accelerating vector potential, α. For the longitudinal equations of motion to be unchanged, the accelerating gradient must also be scaled, but $\propto k_{RF}^{1}$.

Following Rosenzweig [82], the horizontal envelope equation (3.45) may be rewritten:

$$\sigma_x'' + \sigma_x' \left(\frac{(\beta\gamma)'}{\beta\gamma} \right) + \kappa\sigma_x = \frac{2I}{I_o(\beta\gamma)^3\sigma_x} f(\frac{\sigma_x}{\beta\gamma\sigma_z}) \tag{3.115}$$

in which the perveance term may be further subdivided:

$$K_{SC} = \frac{2I}{I_A(\beta\gamma)^3x^2} f\left(\frac{x}{\beta\gamma z}\right) = \left(\frac{2c}{I_A\beta^2\gamma^3}\right)\left(\frac{Q}{gzx^2}\right) f\left(\frac{x}{\beta\gamma z}\right) \tag{3.116}$$

where g is a distribution dependent form factor (e.g. $\sqrt{2\pi}$ for a Gaussian distribution). The first bracketed factor is composed of constants not dependent on the bunch charge or shape, the second bracketed factor is the peak beam density, and the last factor is dependent on the bunch aspect ratio.

A photoinjector design may be scaled for different bunch charges by preserving the perveance constant. This implies holding the peak density constant and the aspect ratio constant. Therefore, the bunch dimensions must all scale $\propto Q^{1/3}$, and, less

importantly, the distribution shape (Gaussian, uniform, etc.) must be held constant.

Table 3.2 below summarizes the relevant dependencies for charge and wavelength scalings.

Operational Parameters			
Quantity	Symbol	Charge Scaling	Wavelength Scaling
Accelerating Field	E_o	1	$k_{RF} \equiv k$
Solenoid Field	B_z	1	k
Solenoid Current Density	J_s	1	k^2
Bunch Charge	Q	Q	k^{-1}
Initial Spot Radius	r_o	$Q^{1/3}$	k^{-1}
Initial Bunch Length	σ_z	$Q^{1/3}$	k^{-1}
System dimensions	L_q	1	k^{-1}
Performance Parameters			
Quantity	Symbol	Charge Scaling	Wavelength Scaling
Spot sizes	σ_q	$Q^{1/3}$	k^{-1}
Normalized emittances	$\varepsilon_{q,N}$	$\sqrt{aQ^{2/3} + bQ^{4/3}}$	k^{-1}

Table 3.2: Summary of parameter scale factors for charge and wavelength scaling photoinjector designs.

3.7 Beamline Optics

A very brief survey of beamline optical components is made here, for more detailed treatment, see Humphreys [44] for a hardware description and basic optics, Carey [83] for detailed matrix element evaluation. The brief survey below is intended to provide formulæ for quick estimation of field strengths and alignment tolerances in the absence of space charge effects.

3.7.1 Collimator

The simplest in principle of all beamline optics, the collimator is simply a high-density geometric obstruction placed at a location of low beam divergence, where particles of highest transverse momenta inhabit the largest radii positions and may be intercepted easily. Such simplicity is unfortunately complicated when the bunch charge is substantial, as the placement of a conducting object so close to the beam (by definition it is in the beam) causes severe wakefield effects, most notably a quadratic distortion to the longitudinal phase space, and potentially a quadratic distortion to the transverse phase spaces as well, if the beam traverses the collimator along other than the geometric centerline.

3.7.2 Solenoidal Focussing

Solenoidal focussing is somewhat unusual in that beam motion passes through three distinct phases while traversing a solenoid: on passing through the upstream fringe field, angular momentum $p_\theta = \frac{e}{c}A_m\theta$ evolves from the radial component of the fringe field: $F_\theta = ec\beta_z \times B_r$. As the beam "spins up", the focussing develops from the angular velocity: $F_r = ec\beta_\theta \times B_z$. On passing through the exit fringe field, B_r has opposite sign, and the beam "spins down" again. Two side effects of this process are, (1) the focussing strength is second order in beam momentum, and (2) solenoids *always* focus.

The focal strength of a solenoid is (assuming $\partial B_z/\partial r \approx 0$):

$$K_{SOL} = \frac{1}{f} = \frac{q^2 \int_{-\infty}^{\infty} B_z(z)^2 dz}{4\gamma^2 m_e^2 c^2} \tag{3.117}$$

For 4 MeV electrons in a 0.1 T peak field distributed uniformly over 20 cm, K_{SOL} is approximately 2.22 m^{-1}. If the beam accelerates through the solenoid, as it would

were the solenoid to enclose some portion of the gun, the equations of motion are somewhat complicated by the introduction of a mass-change term $\dot{\gamma}mv_r$:

$$\dot{\gamma}mv_r + \gamma m\dot{v_r} = -qv_\theta B_z + \gamma m v_\theta^2/r \tag{3.118}$$

which gives rise to the easily solved first-order linear differential equation:

$$\frac{dv_r(z)}{dz} + \frac{\gamma(z)'}{\gamma(z)}v_r(z) = \frac{-q^2 B_z(z)^2}{4\gamma(z)^2 m^2 c}r \tag{3.119}$$

which can be solved with the integrating factor $\rho(z) = \exp(\int \gamma'(z)/\gamma(z)dz) = \gamma(z)$ yielding:

$$K_{SOL} = \frac{q^2 \int_{-\infty}^{\infty} B_z^2(z)/\gamma(z)dz}{4\overline{\gamma}^2 m_e^2 c^2} \tag{3.120}$$

where the acceleration term has contributed a $\gamma(z)^{-1}$ weighting in the integral (3.117), which derives from the progressive Lorentz contraction of the solenoid as the beam accelerates, hence $dz \rightarrow dz/\gamma(z)$.

Given the angular momentum developed within the solenoid, it is not surprising that the solenoid rotates the beam during its passage through the field. This rotation angle is given by:

$$\Delta\theta(z) = \frac{q}{2m_e c}\int_{-\infty}^{z} \frac{B_z(\tilde{z})}{\gamma(\tilde{z})}d\tilde{z} \tag{3.121}$$

which for the 4 MeV accelerating beam (2 MeV average) passing through a 0.1 T field that is uniform and 20 cm long, yields an overall rotation angle of approximately 84^o. This rotation of the beam has several effects. Obviously, whatever charge distribution is launched from the cathode is rotated by this amount, requiring some thought in tracing phosphor screen images back to cathode effects. Less obviously, if the solenoid surrounds an RF gun, the beam will be rotated through the RF cavities as it accelerates, causing dipole and quadrupole field errors in the cavities to sheer and skew focus the beam in a manner that is essentially impossible to reverse.

The solenoidal field must vanish at the cathode, or else the beam will be produced with nonzero canonical angular momentum, initially purely due to the vector potential ($p_\theta = qA_\theta = q(B_z/2)r$), but on exit from the solenoid will convert into mechanical angular momentum. If the residual field at the cathode is B_z^{res}, the emittance contribution will be:

$$\Delta\varepsilon_{x,N} \approx \sigma_x\sigma_{\gamma\beta_x} \approx \sigma_x\frac{p_\theta}{m_ec} \approx \sigma_x\frac{q|B_z^{res}|\sigma_x\sqrt{1/8-1/9}}{2m_ec} \approx \frac{1}{8}\frac{q|B_z^{res}|}{2m_ec}\sigma_x^2 \qquad (3.122)$$

where for a uniform distribution $\langle p_\theta\rangle = \frac{1}{3}qB_z^{res}r$, $\langle p_\theta^2\rangle = q^2(B_z^{res})^2r^2/8$. For a 6 mm radius spot, a residual longitudinal field component of magnitude 10 Gauss will result in a emittance contribution $\approx 1.3\pi$ mm-mr. For the high bunch charge operation at TTF, this is a small contribution, but for reduced charge FEL operation, this would more than double the desired emittance, 1π mm-mr. Setting of the proper bucking coil strength is therefore important for very high brightness beams, and is best done by observing the beam emittance as a function of bucking coil strength.

The solenoid must have its magnetic axis aligned to the beamline centerline (which itself is defined by the electrical centerline of the gun accelerating mode), or steering results. A solenoid with its magnetic axis parallel to, but displaced a distance δr from the beamline axis develops a field of the form:

$$B_r(r) \approx B_o r(1 - \frac{\delta r}{r}\cos(\theta)) \qquad (3.123)$$

where θ measures the angle between the observation point and the vector defining the offset. Clearly the error appears as a feed-up dipole field [84] which although potentially small, integrates over the length of the solenoid to produce a non-negligible kick. Thus the offset of the solenoid from the beamline axis may be deduced from the

dipole component developed, and forms the most accurate means (next to beam-based alignment) of aligning a solenoid to the beamline.

3.7.3 Dipole Focussing

Pure dipole magnet ($n \equiv dB_y/dx \equiv 0$) focussing divides into two mechanisms: path-length focussing and fringe field focussing. The first arises in sector magnets, with particle orbits displaced away from the bend center but parallel to the reference orbit spending more time in the magnetic field, thus receiving stronger kicks toward the reference orbit, and orbits displaced toward the bend center and parallel to the reference orbit spending less time in the bend field, receiving weaker kicks resulting in an outward divergence toward the reference orbit. The focal strength of a horizontal sector magnet is simply:

$$K_x = \tan(\theta_b)/\rho \tag{3.124}$$

where $\rho = p/qB_y$ is the bending radius of the reference particle, and θ_b is the bend angle of the reference trajectory. As an example, the focal strength of a horizontal sector magnet with bend radius 70 cm and a 22.5^o bend angle is 0.60 m^{-1}.

The second arises if the beam passes through the fringe field at an angle, in which case a component of the fringe field will be perpendicular to the forward velocity, and a focussing (or defocussing) kick results. This type of focussing is typical of bending magnets with parallel entrance and exit faces, one or both of which the beam must traverse at an angle to the surface normal. The focal strength for this case is:

$$K_y = \tan(\theta_e)/\rho \tag{3.125}$$

where $\rho = p/qB_y$ is the bending radius of the horizontal bending magnet, and θ_e is the angle between the particle trajectory and the surface normal on the boundary

being crossed. If $\theta_e = 0$ the particle enters the magnet normal to the edge, and there is no fringe focussing. This is the case for the sector magnet, which focuses only in the bend plane. If $\theta_e = \theta_b$, as is the case for a rectangular (from a viewpoint normal to the bend plane) magnet, there is no path length focussing. The analogous forms of (3.124) and (3.125) suggest that the focussing in the two transverse planes is complementary, which is indeed the case, and which has the important consequence that dipoles will always focus (or defocus) in at least one of the transverse coordinate planes.

The flexibility of focal strength in the two planes can be exploited to meet various demands. For the spectrometer, achieving maximum momentum resolution requires that a betatron waist be obtained on the momentum imaging plane since:

$$\sigma_x = \sqrt{\beta_x \varepsilon_{g,x}} + \eta_x \frac{\delta p_z}{p_z} \tag{3.126}$$

and the spectrometer resolution will be limited to approximately

$$\mathcal{R} \equiv \frac{\delta p_z}{p_z} \approx \frac{\sqrt{\beta_x \varepsilon_{g,x}}}{\eta_x} \tag{3.127}$$

in the absence of an independent means of determining the emittance contribution to the dispersed spot size. Clearly, the smaller β_x is, the better the resolution, and is the primary reason for choosing a sector magnet.

For a pulse compressor, balancing the focussing in both planes is appealing as it reduces the probability of unreasonable small focal spots occurring (which can cause severe beam degradation under some conditions) and in general reduces the excursions of the beta functions, allowing smaller magnet apertures. Thus, some combination of fringe and path length focussing is appropriate for the dipole chicane.

With respect to alignment errors, the dipole field:

$$B_x + iB_y = B_o \exp(i\theta) \tag{3.128}$$

clearly is unaffected by translations, but will develop a dipole field in the otherwise unaffected plane if rotated about the axis parallel to $\vec{v_z} \times \vec{B}$. In addition, the fringe field and path length focussing will become weakly mixed in the two coordinate planes.

Systems of dipoles, such as the chicane, clearly are affect by translations of the components. An examination of relation (3.114) for the temporal compression ratio shows that the compression will vary roughly linearly with the relative offsets (i.e. $Z_2 - Z_1 = L$ and $Z_4 - Z_3 = L$) of the various dipoles. The other effect will be a net offset between the entrance and exit transverse coordinates that depends on the bend angle: $\delta x \propto \delta z \tan\alpha$.

3.7.4 Quadrupole Focussing

Quadrupole focussing results from a field of the form:

$$B_x + iB_y = B_o r \exp(i2\theta) \tag{3.129}$$

and is defocussing in one transverse plane, focussing in the other. The focal strength of a thin quadrupole is (applying the usual fringe field length correction):

$$K_x = -K_y \approx \frac{q\kappa(L+D)}{\gamma m_e \beta c} \tag{3.130}$$

where $\kappa = dB_x/dy|_{x=0}$ is the quadrupole field gradient, L is the physical length of the quadrupole, D is the bore, and the magnetic length of the quadrupole is approximated as $\frac{D}{2} + L + \frac{D}{2}$. As an example, for 4 MeV electron beam traversing a 7.6 cm long,

35 mm bore quadrupole with field gradient 0.2 T/m, the effective focal strength is $\approx 1.16\ \mathrm{m}^{-1}$.

Quadrupoles parallel to the beam axis, but translated a distance δr generate a feed-down dipole field:

$$B_x + iB_y \approx B_o(r\exp(i2\theta) - \delta r\exp(i\theta)) \tag{3.131}$$

which produces "steering" of the beam in a manner dependent on the focal strength of the quadrupole. Rotations of the quadrupole, like the dipole, produce focussing kicks that couple the transverse phase planes.

3.8 Wakefield Effects

No serious calculation of wakefield effects was done for the dissertation research. For estimates of wakefield effects in the TTF symmetric emittance photoinjector and suggested remedies, see reference [85].

Chapter 4

Numerical Modeling

Although the theoretical understanding of photoinjector dynamics is rather complete, the equations of motion are not integrable except for a few instructive cases, but which are not necessarily of direct interest. Consequently, the development of a range of numerical models of varying sophistication was desired to illuminate the basic processes and speed design.

Very simple numerical models were constructed by Rosenzweig (MathCAD-based), Ostiguy (Octave-based), and myself (Matlab and Mathematica based) to illustrate everything from pulse compression in the chicane to the emittance compensation process. Additional sophistication, in the form of complete first-order beam transport and a more sophisticated space charge model, was employed (in the Los Alamos code Trace3D) to establish zeroth-order lattice parameters and perform rapid optimization of designs. The highest level of physical sophistication was obtained with a much-modified version of the Los Alamos code PARMELA [86] (Phase and Radial Motion in Electron Linear Accelerators), with provisions added to model all physical effects in a fully 6-D manner.

In addition, many supporting codes were used to design the RF cavities and

couplers (SUPERFISH [87], HFSS [88]), model the time domain response of the gun under beam loading (custom Matlab code), model wakefield effects (ABCI [89]), model solenoid magnet fields (Poisson [87]), model interactions of the beam with diagnostic materials (custom Monte Carlo written for the purpose [90]), model optical transport of diagnostic light (custom Matlab code), and more than 30 other Matlab simulation codes ranging from synchrotron light output calculations in the compressor bends to spectrometer calibration curves.

4.1 Survey of Considered Codes

Initially, the dynamics of an *a*symmetric emittance beam were studied, requiring codes capable of modelling 3-D problems with space charge. Of the envelope codes considered (Transport, MAD, DIMAD, Trace3D), the uniform ellipsoid model of space charge employed by Trace3D [91] was the only space charge treatment available, and the source code was available. Of the PIC/CIC/tracking codes considered (Mafia v.2, Argus, Quicksilver, PARMELA), Argus simulations were attempted but hampered by my inexperienced use of scant computing time at NERSC, and PARMELA (modified) was preferred over Quicksilver and Mafia based on the worldwide experience building RF guns with the former, and the availability of its source code. Subsequent comparisons of PARMELA against ITACA (a 2-D CIC EM simulation code) and ATRAP (a relativistically correct 3-D particle tracking code) show excellent agreement, despite being very different calculation methods. As mentioned earlier, supplemental simulations with MathCAD and Matlab envelope codes augmented the design process.

RF cavity design was also a manifestly 3-D problem. Argus was used until computing resources ran out, followed by Hewlett Packard's High Frequency Structure

Simulator (HFSS). Design work on the symmetric emittance cavity was completed largely with the 2-D finite element code SUPERFISH, with coupler design calculations again being treated with HFSS. Time domain response of the gun structure was simulated with custom Matlab code based on coupled L-C oscillators. Wakefield effects were analyzed with Xwake v.2 and ABCI, with wake-kicks introduced in a non-self-consistent fashion into PARMELA, as described below.

Detailed thermal and mechanical calculations for the gun were completed using Swanson's Ansys [92] system in two passes, the first to establish equilibrium and pulse-condition temperature distributions, the second to evaluate the structural stresses and establish whether appreciable RF detuning would result or spalling of the surface might occur. 3-D solid modelling of the gun and 2-D production drafting were done in IDEAS [93]. Design of the solenoid assembly for the gun was a 2-D problem, and treated with Poisson. Water cooling calculations were done in Microsoft Excel using the Dittus-Boelter and thermal diffusion equations.

Static deflection of the compressor vacuum chamber wall was analyzed using ANSYS to establish safe wall thickness and appropriate gussetting.

Beam dumps, Faraday cups, and emittance slits were evaluated using a custom low energy electron/matter interaction Monte Carlo code written by N. Barov [90] modified by the author for the purpose. Bremßtrahlung and ionization were the only energy loss mechanisms included, as pair production even at 20 MeV is negligible by comparison.

Matlab macros were written to evaluate many additional aspects of the experiment, including:

- Coherent synchrotron light output in the compressor bends

- Energy calibration curves for the spectrometer
- Spectral output and CCD-registered photon counts for Čerenkov radiators
- Optimal pepper pot hole placement patterns
- Emittance mask transmit/scatter signal-to-noise ratios
- RF time domain response of the gun
- Waveguide-to-gun power coupling
- Higher order modes of gun and $\lambda/4$ transformer
- Gaussian optics modelling for Čerenkov light transport from diagnostic to streak camera
- Detailed testing of Gaussian fitting algorithms in the presence of noise
- Particle motion in RF fields
- Particle motion in a chicane compressor
- Particle motion under space charge

Several of these simple Matlab models reached a sufficiently developed state to be included either into PARMELA (e.g. slit-based emittance calculation) or into the control system (e.g. Gaussian fitting algorithms).

4.2 Description of PARMELA

The basic 1994 PARMELA was a 6D particle tracking code with provisions for modelling RF cavity and space charge fields on an (r, z) grid with modules for handling quads, solenoids, dipoles, etc. Space charge was calculated using a Green's function approach that reduced the beam to a set of annular segments and performed a weighted discrete integral over a selected region of the bunch, then interpolated field values at the location of each macroparticle. Another algorithm existed for calculating space charge fields that directly employed Coulomb's Law called the "point-by-point" method for its direct computation of the mutual repulsion between each pair of particles. Particle motion was and still is integrated using a non-symplectic first-order finite-difference method that pushed particles in z in the lab frame, rather than time, simplifying somewhat the user's choice of step size in the brief sub-relativistic range of motion. Solenoid fields were modeled using Busch's theorem and a map of $B_z(z, r = 0)$ built up from a set of user-defined Ampèrian loops. RF Fields could be modeled in 2-D through a Fourier-Bessel series representation using either pre-loaded coefficients (from various Los Alamos structures) or from user-specified coefficients. Diagnostics were limited to various plots of 2-D emittances, envelopes, and macroparticle phase spaces, with provisions for driving a teletype display. PARMELA's main virtues were an excellent space charge calculation method that placed the mesh resolution where it was needed, and its long track record in the design of electron sources from Los Alamos to Beijing to CERN. It had the additional benefit of having the source code freely distributed.

4.3 Modification of PARMELA

Modifications proceeded on a version of PARMELA obtained from Kirk MacDonald, and subsequently modified by people at UCLA. PARMELA has been modified to permit modelling of space-charge correlation corrected electron guns (with diagnostics specifically for this purpose) with or without axisymmetry (through 3-D field maps for RF cavity fields and several fully 3-D space charge calculating algorithms) with provision for approximating wakefield effects in structures (by applying kicks in a non-self-consistent fashion derived from another code, such as ABCI/Xwake/W3WAK, etc.) Solenoidal focussing fields may be modeled either using one-dimensional maps (and employing Busch's Theorem) derived from a collection of Amperian loops, from a map of $B_z(z)$, from an axisymmetric map of $[B_r(r,z), B_z(r,z)]$, or from a comprehensive map of $[B_x(x,y,z), B_y(x,y,z), B_z(x,y,z)]$.

In additional, two bug fixes from the canonical version of PARMELA were made: (1) space charge fields on the cathode are not subject to the curious weighting function present in the original, which caused underestimation of the longitudinal decelerating field on the cathode, and hence lead to overestimates of the quantity of charge extractable, and underestimates of the energy spread; and (2) numerical (completely non-physical) bunching of the particles in the longitudinal coordinate has been eliminated by introducing mixing (by dithering the time step value) to avoid coherent excitation of any longitudinal bunch harmonics.

Longitudinal and transverse wakefield modelling has been added by applying a kick to each particle at the exit of specified elements derived from wake potential tables developed by, for example, ABCI, Xwake or TBCI. The approach is clearly not self-consistent and meant only for applications where wakefield effects are small

compared to space charge and RF effects.

Graphics output from this version of PARMELA is nil. All output is in the form of ASCII data files. A large number of macros (> 200) have been written for analyzing and displaying the data from all of the various diagnostics using the program Matlab. A small number (~ 20) macros also exist for Mathematica, but are neither maintained nor complete.

Given the long running times for detailed simulations ($\sim$1-3 hours for (r, z) mesh method, 8-12 hours for point-by-point) of the injector, a parallelization of PARMELA was implemented using the Parallel Virtual Machine (PVM) subroutines developed at Oakridge National Lab[94]. Simply a single-instance, multiple-data (SIMD) implementation, code was written to act as a job scheduler over a heterogeneous group of over 70 computers spanning 7 domains. Load monitoring, leveling, and queue servicing were added, together with data archiving on a central node, and data summarization. The volumes of data produced were semi-automatically analyzed using custom programs and human patience.

Operation of the PVM proved instrumental in rapid optimization of the injector. With the guidance of theory, ranges of parameters could be rapidly explored, permitting not only a definition of the working point, but a rather comprehensive characterization of the neighborhood of the working point, and the engineering implications resultant. Appendix D covering the beam-quality imposed fluctuation limits on the laser derives from these studies.

4.4 Additional PARMELA Improvements

Much work remains in improving PARMELA to better model modern photoinjectors. Relativistically correct modelling of cathode wake and space charge effects, particularly through bends, remains a challenge to future modifications. Also, lower noise fully 3-D methods for evaluating space charge fields are needed to accurately model flat beam injector dynamics. New code diagnostics, together with provisions for thoroughly simulating all aspects of modern beam diagnostics would also make an excellent addition.

Elimination of the "pseudo-electrostatic approximation" used in all space charge algorithms for PARMELA would allow more accurate treatment of the beam's emission from the cathode, where velocity sheer within the bunch exceeds 10-20% the speed of light, and magnetic fields of early emitted particle act on later emitted particles. Coherent synchrotron radiation effects in bends have received recent attention as a potentially serious source of emittance degradation, but is an essential piece of physics not included in the present pseudo-electrostatic methods.

Upgrading from the first-order, non-symplectic integration algorithm currently used to a symplectic, possibly higher order method would improve the quality of simulation time spent. Simple exercises, such as monitoring the beam's total energy (kinetic+potential) under free expansion in a drift or monitoring the beam's energy on traversing a quadrupole show energy changes on the order of a percent, even with thousands of time steps per plasma period.

A numerical instability that gives rise to false micro-bunching with a spatial period coincidentally close to $c \cdot \delta t$ speaks to a deeper problem I have not fully appreciated. The symptom has been treated (as noted above), but the cause remains undiagnosed.

Much less important are some rudimentary checks that have been added to catch some of the more common input and parameter range errors, but the code would profit from greatly enhanced warning messages to alert the user of potential problems that would severely impact the simulation accuracy.

Lastly, comprehensive 3-D wakefield modelling, of real interest to the next generation of high brightness injectors and very high frequency accelerators, is needed. However, the introduction of the needed description of the structure boundaries and the propagation and subsequent beam interaction of the radiation fields imply particle-in-cell methods, a difficult evolutionary step for PARMELA.

Chapter 5

Design Rationale

5.1 General Design Considerations

With the basic physics and modelling of RF photoinjectors outlined, it is now possible to approach a design. TTF beam requirements, summarized in table 5.1 below, together with constraints on the amount of RF power available, the physical beamline space available, the existence of a 9-cell capture cavity already installed in the beamline at DESY, and engineering considerations well circumscribe the design.

In addition to beam quality requirements there are a number of practical considerations which will impact the design. These are:

1. The available klystron and modulator systems are capable of 4.5 MW for the duration of the 1200μs pulse. With margin for feedback, transmission and coupling losses, deliverable power to a structure is conservatively more like 3.5 MW.

2. State-of-the-art lasers produce $\sim$ 1 W average power, no matter the pulse structure. Coupled with the high average beam current (8 mA) this will require a high quantum efficiency (QE) photocathode, with the minimum allowable

Parameter	*Symbol*	*Value*
Bunches per macropulse	N_m	1000 (800)
Macropulse spacing	τ_m	100 ms
Bunch spacing	τ_b	$1\mu s$
Overall Duty Cycle		1 %
Bunch Charge	Q_b	8.0 nC
Bunch length	σ_b	1 mm
Peak Current	I_p	958 A
RF Frequency	f_{RF}	1.3 GHz
RF Power per klystron	P_{RF}	4.5 MW
TESLA Test Facility		**Symmetric**
Horizontal Emittance	ϵ_x	$< 20\pi$ mm-mr
Vertical Emittance	ϵ_y	$< 20\pi$ mm-mr
Brightness	B	$4.8 \times 10^{12} A/m^2$

Table 5.1: Summary of TESLA Injector II Parameters

QE set by the average laser power available: $QE \geq P_{laser}/(E_\gamma[eV]I_{ave}[A]) = 1[W]/(5[eV].008[A]) = 0.04$.

3. DESY Halle 3 infrastructure properties, e.g. , the available cooling water pressure drop (60 psi).

For the prototype test phase (conducted at Argonne National Laboratory's Wakefield Accelerator Facility), a number of additional considerations arise:

1. The AWA facility laser can produce sufficient laser pulse energy to produce $>$ 10 nC bunches from even low quantum efficiency cathodes with outputs of 4-6 mJ per pulse in the ultraviolet.

2. Maximum RF power out of the klystron is 16 MW for 6 μs at 30 Hz repetition rate, for an average power of 2.9 kW, making cooling straightforward.

3. As the gun is operated in single-bunch mode, diagnostics need not be capable of resolving individual pulses of a train, allowing integration over the whole RF pulse to suffice for most applications.

4. AWA infrastructure properties, such as space.

5.2 Physical Considerations

The need for substantial bunch charge with good beam quality requires that the RF accelerating gradient in the photoinjector be relatively high to reduce space charge induced emittance growth, and that emittance compensation [95] be implemented to reduce the correlated space charge emittance growth. RF contributions to the emittance must be carefully controlled, requiring that nonlinear variations of the accelerating field in both the radial and longitudinal direction be minimized, and that the beam dimensions and accelerating gradient be carefully optimized.

The space charge emittance compensation scheme requires that the bunch be given a focussing kick early on to start the gradual reclosure of the phase space "fan" that results from the longitudinal variation of the transverse space charge fields. The variation of the space charge fields results in a correlated emittance growth that can be partially reversed with a focussing kick from a linear lens. Ideally, the kick should take place ahead of the beam's exit from the RF photoinjector, as the time-dependent defocussing that takes place within the RF structure, which can interfere with emittance compensation, depends on the square of the transverse beam size [69] and will be significantly smaller if the beam is focussed as close to the cathode as possible.

As the emittance compensation scheme is sensitive both to the strength and to

the longitudinal position of the focussing kick, and placement of the primary solenoid is highly restricted by the RF input waveguide and cathode location, the primary solenoid was split into two solenoids, a large primary mounted against its mirror image to obtain zero longitudinal field on the cathode, but rapidly rising thereafter, and a smaller secondary solenoid just after the gun. This combination permits exploration of emittance compensation as a function of lens strength and position, with the ratio of the currents in the upstream and downstream solenoids determining the effective magnetic center of the lens, and the sum of the currents determining the overall focal length. Figure 5.1 is a sketch of the gun and solenoids. The truncated yoke on the downstream side of the first focussing solenoid broadens the on-axis field profile with the bucking coil manifesting the same truncation for symmetry. A trim coil is wound within the inner bore of the bucking coil to provide for cancellation of the fields due to the second focussing solenoid at the exit of the photoinjector and any longitudinal misalignment of the solenoid assembly.

The first focussing solenoid and bucking coil have identical geometric and electrical attributes, but opposing fields, with a geometry determined by the space available between the gun exterior, input coupler, and the cathode plane, and the need to have the maximum of the magnetic field as close to the cathode as possible. The third solenoid follows immediately after the full cell of the gun and has much more relaxed space constraints. The solenoids were designed to provide sufficient on-axis focussing strength to allow emittance compensation of beams with normalized energies up to $\gamma = 9.0$ on exit from the gun. The peak field is specified with the bucking solenoid set to cancel the magnetic field at the cathode. Conductor cross section and winding topology were chosen to allow operation of the gun at gradients exceeding 50

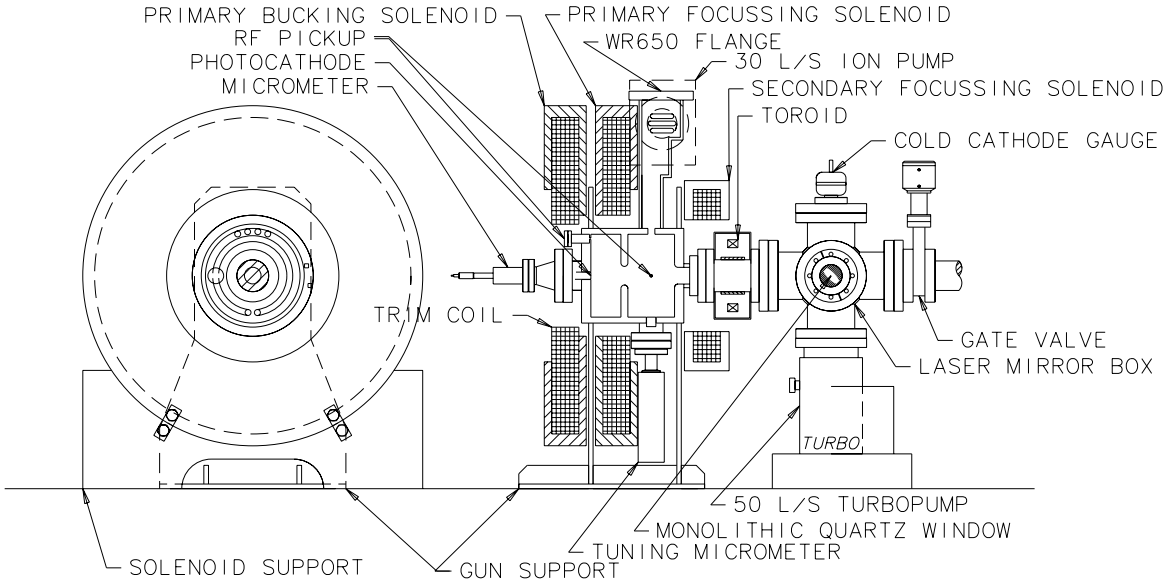

Figure 5.1: Sketch showing location of focussing and bucking solenoids

MV/m, of interest both for compressionless high charge operation, and very high brightness low charge operation. Table 5.2 below details the electrical and physical characteristics of the focussing solenoids.

A plot of the longitudinal magnetic field strength at $r = 0.0$ cm is shown in figure 5.2 below.

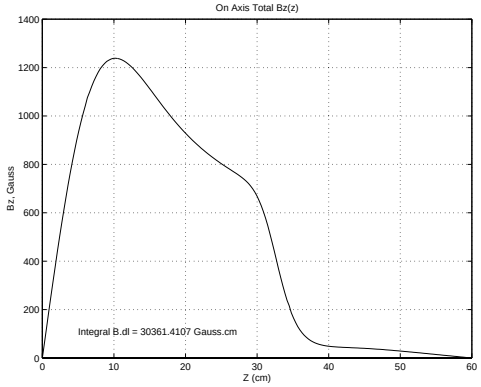

Figure 5.2: Focussing fields in TTF Photoinjector II

Solenoid			Pri.	Sec.	Trim
Parameter	*Symbol*	*Units*	*Value*	*Value*	*Value*
Maximum magnetic field	B_z^{max}	Gauss	1415	552	-
Maximum current density	J_{max}	A/cm^2	0.7	0.6	0.6
Number of windings	N		23×6	7×6	2×6
Total coil resistance	R_c	mΩ	64.6	13.73	3.81
Coil Inductance (at 1 kHz)	L_c	μH	430	555	42
Max. voltage drop	V_s	Volts	23	3.7	0.5
Max. Power dissipation	P_{diss}	kW	8.9	1.1	0.2
Physical Dimensions					
Bore	r_i	cm	13.0	12.0	11.3
Outer radius	r_o	cm	36.5	25.3	13.0
Length	L	cm	9.0	5.2	9.0
Hydrostatic resistance		MPa s/L	6.60	2.97	0.4

Table 5.2: Electrical characteristics of the focussing and bucking solenoids

The total field strength induced in the area immediately surrounding the primary and secondary solenoids is mapped out in figure 5.3 below, indicating the possibility of interaction with nearby ferrous objects.

A short section is introduced after the photoinjector to allow the positioning of a six way cross for diagnostics, the laser mirrors, a vacuum gate valve, and a short drift, to allow the emittance compensation the required time to act before accelerating the beam further, thus "freezing out" the space charge forces.

Numerical optimization of the RF gradient showed that fields of 45-50 MV/m on the cathode provided for optimum emittance and bunch length. Realistic power constraints imposed by klystron capabilities (both at AWA and at TTF) indicate that a maximum field of 35 MV/m is attainable with sufficient overhead to allow for feedforward. As the photoinjector is optimized to deliver the required transverse beam quality with reasonable RF power, the lower accelerating gradient will require a longer

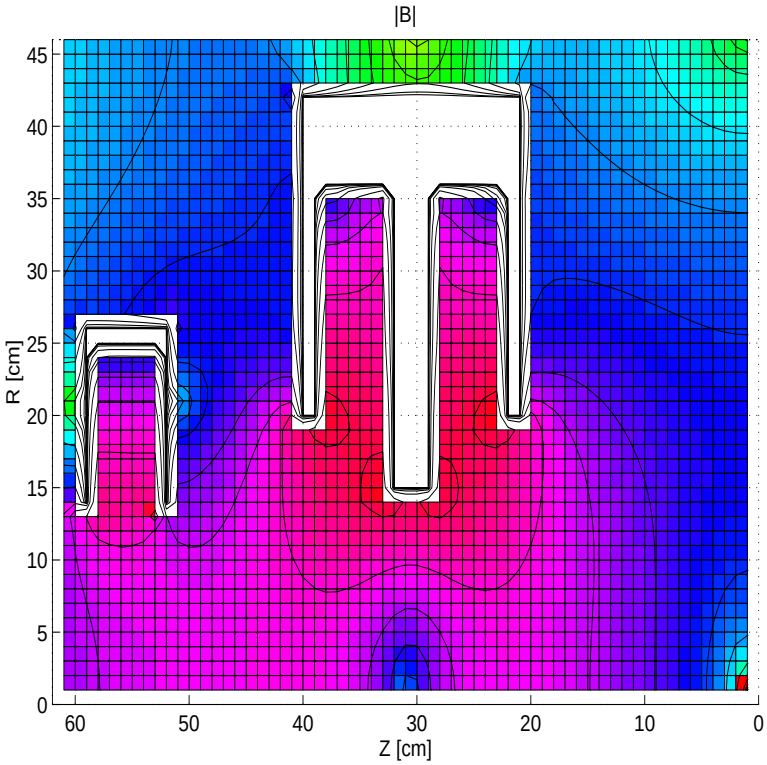

Figure 5.3: Contour and density plot of $|\vec{B}|$ with all four solenoids powered

bunch length to reduce the space charge emittance growth during the relatively longer acceleration time. As a result, compression of the beam must be undertaken once the beam reaches moderate energy. Magnetic compression requires that the beam pass through a dispersive optical element, making use of a linear energy-phase correlation to reduce the bunch length. Space charges forces will degrade all three emittances during compression, resulting in poor beam quality if compression proceeds for too long or at too low a beam energy. It is therefore optimal to compress at the highest energy possible (thereby reducing the space charge forces) that beamline space allows. The TTF experimental area has rather limited space, motivating the choice to place a magnetic compression chicane at a lower energy (20 MeV).

The linac, or capture cavity, follows shortly after the gun to accelerate the beam sufficiently to slow the space charge emittance growth, and permit transport for several meters through the pulse compressor and injector diagnostics to the first cryomodule.

Several alternative linac structures were considered for the prototype test experiment, including a plane wave transformer [96] and reentrant structures such as could be borrowed from the decommissioned APEX experiment at Los Alamos. A relatively large aperture structure was desired for both wakefield and beam propagation reasons. As the injector was to be used with the TESLA 9-cell capture cavity [1], a similar structure would be ideal for modelling the injector performance to be expected from Injector II. Several copper cold test models of the 9-cell cavity existed, one in Fermilab's possession. It was decided to make the structure vacuum-worthy by plugging the 12×9 probe holes, add a custom RF input coupler capable of handling 5 MW of power, add a water cooling system, and mount a means for tuning the structure. Coupling was magnetic, through an iris in the wall of the 5th cell, rather than electric through the end beam tube, as is done for the superconducting cavity.

Cooling was straightforward as the duty cycle was low. Average power dissipation of no more than 10 MW $\times$ 6 μs $\times$ 30 Hz = 1.8 kW was expected, and was easily removed by copper tubes joined by thermally conductive epoxy to the outside of each cell. Tuning was accomplished by means of a set of moving clamps, shown in figure 5.4 below.

Compression was initially estimated using the longitudinal emittance of the beam and assuming an ideal linear transformation on the phase space to produce the compressed bunch. Emittance growth resulting from compression is here estimated from

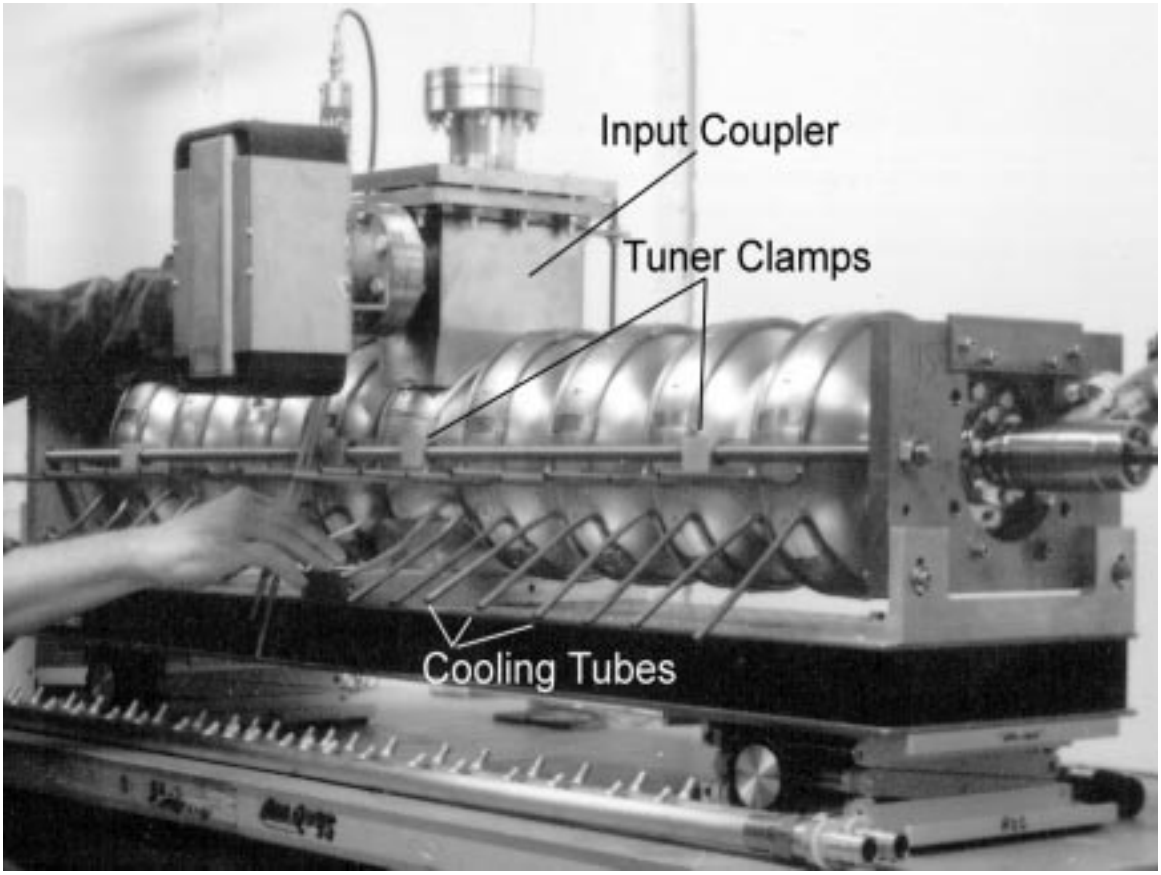

Figure 5.4: 9-cell copper linac during the retrofit.

Carlsten's analysis [97], assuming a short bunch with a radially uniform charge distribution:

$$\epsilon_N = \frac{ISG}{4I_A\beta^2\gamma^2} \tag{5.1}$$

where I is the peak compressed current, S is the path length over which the compressor dipole fields act on the beam, G is a geometric factor between 0.2 and 0.5, and the Alfven current $I_A = 4\pi\epsilon_o m_e c^3/e$. Preliminary numerical simulation of the compressor performance has also been completed, and is reflected in the values quoted below. Simulations accounted only for normal space charge and aberration effects, not for

near-field coherent synchrotron radiation or non-inertial space charge effects, both believed to be significant.

Table 6.3 below details the predicted performance of the photoinjector. Emittance values quoted are one sigma FWHM normalized values (see section B.1 for an explanation of "FWHM emittance") enclosing 100% of the stated bunch charge. Two different operating scenarios were examined: high bunch charge (8 nC/bunch) operation for testing of HOM energy deposition in superconducting RF linac structures, and low bunch charge (1 nC/bunch) operation for use as a source for a free electron laser (FEL). Significant effort was devoted to optimizing the 8 nC scenario, both for highest beam quality, and for lowest possible RF power consumption. The low charge (1 nC) case was derived by scaling the bunch radius and length to preserve the bunch core charge density, thereby allowing the emittance compensating lens configuration and strength to remain essentially unchanged [99].

5.3 RF Design of the Photoinjector

Simplicity, high shunt impedance, and the ability to accommodate an externally mounted focussing solenoid close to the cathode region motivated the choice of a 1.625 cell $TM_{010,\pi}$ mode structure. The need to induce a strong on-axis magnetic field made the use of a superconducting cavity problematic, and the need for a high accelerating gradient eliminated the choice of a superconducting gun altogether. The Brookhaven/Grumman [Gun I] S-band photoinjector [105] was taken as a starting point for the design of the TTF injector; the resonant frequency, waveguide coupling, intercavity coupling, and longitudinal exit aperture profile were modified to yield an L-band structure with good shunt impedance and field balance characteristics.

Placement of the focussing solenoid around the first half cell of the gun completely occludes all reasonable locations for an RF coupling slot, requiring power for the half cell to be coupled in either magnetically through a series of coupling slots placed at the maximum of the azimuthal magnetic field, or electrically by widening the iris. Slot coupling excites higher order azimuthal spatial harmonics in the RF field causing unwanted nonlinear RF transverse emittance growth. Widening the iris for improved group velocity lowers the shunt impedance and affects the radial spatial harmonics (flattening the near-axis radial variation of E_z as a benefit) and reduces the strength of the higher order longitudinal spatial harmonics. This somewhat unusual coupling scheme has already been employed successfully in a photoinjector for a free electron laser [100, 101], and is the coupling scheme of choice for the new high-brightness LCLS photoinjector [102].

Although RF power efficiency was of prime concern in designing the photoinjector, the standard shunt-impedance increasing procedure of decreasing the gap length with the addition of "reentrant noses" on the entrance and exit irises was not undertaken. Although such a geometric modification can appreciably improve the power efficiency of an RF structure, it does so at the expense of significantly enhancing the nonlinear components of the accelerating field. As the rms bunch radius for the high-charge case is significant (6.3 mm at the maximum, 10 cm from the photocathode), nonlinear RF emittance growth in such a cavity would be unacceptably large, as subsequently demonstrated by numerical simulation. Also, the large accelerating gradient (at the Kilpatrick threshold) makes an RF structure with a low peak-field to accelerating-field ratio especially desirable, making the addition of any geometric disturbances in the high electric field region of the cavity undesirable.

Modifications to geometry of the full cell only [103] were examined as a possible means of improving the shunt impedance of the structure further. Reentrant noses of varying gap length and geometry were added, with the bore of the connecting beam tube (between half and full cells) adjusted to preserve the cell-to-cell coupling constant. The outer cavity wall was deformed from right-cylindrical to toroidal to further increase the shunt impedance. The increase in effective tube length (between the half and full cell) in all cases led to a significant decrease in coupling that required a corresponding increase in bore, the net result of which was a decrease in the overall shunt impedance of the gun.

Under the constraint that the intercavity coupling constant be held constant, perturbative "bumps" to concentrate the electric field closer to the beam axis where tried in two sizes, and a third geometry, taking into account an optimization study carried out on 1350 MHz TM_{010} cavity citemanc, with full nose cones and a curved outer cavity wall, were simulated with the 2D finite element code, SUPERFISH. Figure 5.5 shows the third geometry studied.

The effective shunt impedance per unit length calculated for this structure is 26.4 MΩ/m, as compared to 27.9 MΩ/m for the original structure. Simulations results from the other two structures confirmed the downward trend in the shunt impedance with decreasing gap length. As an additional consideration, reentrant nose cone structures are more difficult to machine and to cool. The deposited RF power for Injector II is 22 kW (at 35 MV/m, 45 kW at 50 MV/m), with adequate cooling of the aperture posing an engineering challenge.

The desire to hold the intercavity coupling constant to a specified value precludes significant improvement in the overall shunt impedance of the gun. In addition,

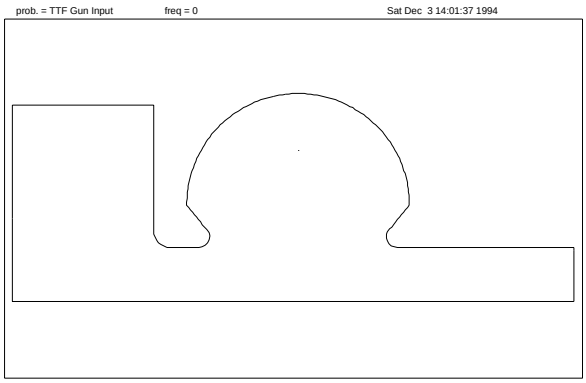

Figure 5.5: Injector II geometry with reentrant full cell

the added machining and heat removal difficulties make adding reentrant nose cone structures to the full cell unattractive.

An elongated half cell was chosen to provide improved beam divergence control (A small amount of RF focussing occurs in the region right off the cathode as a result of the lengthening) and additional time to start the solenoidal focussing kick to initiate the emittance compensation before the time-dependent kick of the first iris becomes appreciable. After some optimization, a half cell length equal to $\frac{5}{4}\frac{\lambda_{RF}}{4}$ was chosen. To limit further higher spatial harmonic pollution of the accelerating mode, the full cell has a length that is exactly $\frac{\lambda_{RF}}{2}$.

The iris diameter between the full cell, where RF power is coupled in, and the half cell was chosen to yield strong enough coupling that the longitudinal position of the photocathode could be used as a frequency tuning mechanism without causing a substantial shift in the field balance between the two cells. Various field balance

options were considered, motivated by the possibility of using RF focussing at the first iris on the one hand, and by the possibility of improved longitudinal phase space linearity (and thus compressibility) on the other. A field imbalance between the half and full cell could be made to enhance the time dependent focussing kick centered at the first iris, but was found to significantly interfere with emittance compensation, degrading final beam quality, and was not pursued further. Thus a balanced ($E_{z,max}^{halfcell} = E_{z,max}^{fullcell}$) field profile was chosen. To ensure the field balance, the mode separation was chosen to be approximately 2.5 MHz (40 times the -3dB cavity bandwidth), implying a coupling constant of $\gamma = 0.19\%$. Assuming the half cell field to be $E_1 = 45$ MV/m, the full cell field $E_2 = 35$ MV/m, the stored energy $U = 10.5$J, the iris thickness to be $d = 1.5$cm, and the free space wavelength $\lambda = 23.061$cm, the electrical coupling iris radius needs to be [106]:

$$r_o = \left[\frac{3\gamma U}{2\epsilon_o E_1 E_2 e^{-\alpha d}}\right]^{\frac{1}{3}} \approx 2.0cm \tag{5.2}$$

where $\alpha = k_o\sqrt{(\lambda/\lambda_c)^2 - 1}$ is the attenuation length for the TE_{11} mode present in the beamtube between the cells. Simulation of the cavities using the Superfish code yields $\gamma = 0.189$ for an iris radius of 2.0 cm, in good agreement with prediction. As the hole is not uniform in radius, (rather the edges are rounded to prevent field line concentration) the coupling constant for the simulated and actual photoinjector will be somewhat higher than equation (5.2) predicts.

The effects of beam loading also bear directly on the choice of coupling strength, as loading in each cell of the photoinjector is different, leaving the fields slightly imbalanced (i.e. the zero mode is weakly excited) after the bunch has passed. The coupling strength will influence the recovery time of the photoinjector, which must be significantly less than the time between bunches. In view of the short time between

successive bunches, and the large number of bunches per pulse, a simple examination of the RF transient response of the photoinjector was made. A lumped circuit model, shown in figure 5.6, was used to analyze the fill rates of the two cavities, and verify that the coupling was adequate. The coupled differential equations governing the

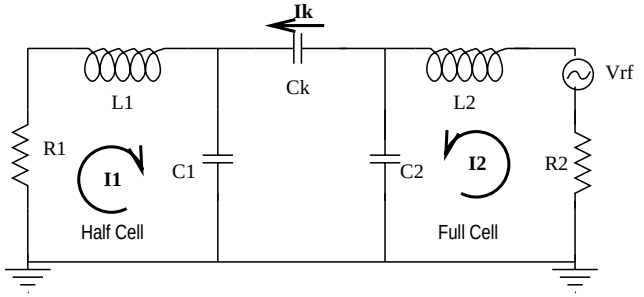

Figure 5.6: Lumped circuit model of two cell electrically coupled π-mode structure

currents $\dot{Q}_1(t)$, $\dot{Q}_2(t)$ and $\dot{Q}_k(t)$:

$$\ddot{Q}_1 L_1 + \dot{Q}_1 R_1 + \frac{Q_1 + Q_k}{C_1} = 0 \tag{5.3}$$

$$\ddot{Q}_2 L_2 + \dot{Q}_2 R_2 + \frac{Q_2 - Q_k}{C_2} = V_{RF}\sin(\omega_{RF} t) \tag{5.4}$$

$$\frac{Q_1 + Q_k}{C_1} + \frac{Q_k}{C_k} - \frac{Q_2 - Q_k}{C_2} = 0 \tag{5.5}$$

may be solved in the weak coupling approximation ($C_k \ll C_1$ and $C_k \ll C_2$) to yield the fill times for the two cavities:

$$\tau_1 \approx \tau_2 \approx \frac{2L}{R} = \frac{2Q}{\omega} \approx 2.91\mu s \tag{5.6}$$

where the lumped circuit component values were estimated using the loaded Q, structure impedance Z, (not ZT^2), and the resonant frequency of the individual cavities as calculated by SUPERFISH.

Direct numerical integration of the exact equations using a 4th order Runge-Kutta algorithm generated figure 5.7. The mode amplitudes are shown on the left as

a function of time for the first $25\mu s$, and in a Lissajous plot on the right, showing the relative phase of the two cavities as the π-mode builds up. The beating of the zero and pi modes is plainly visible during the fill in both mode plots, but as the zero mode is undriven and damps exponentially, there is little modulation of the mode amplitudes once the cavities are filled. More significant, however, is that the fill times for the two cavities are indeed comparable, despite the small coupling constant. This can be explained by noting that the Q of the cavities (which sets the time scale for filling the cavity) is much larger than the inverse of the coupling constant (which sets the time scale for energy propagation through the structure).

Beam loading in the half cell is expected to be:

$$P_{beam} = \int E_z dz \cdot \frac{N_b Q_b}{\tau_{RF}} \approx 18.5kW \tag{5.7}$$

which is to be compared with the power dissipation on the walls of the half cell:

$$P_{diss,HC} = \frac{R_s}{2} \int H_\phi^2 d\mathcal{S} \approx \frac{R_s}{2} \frac{\epsilon_o}{\mu_o} \frac{k^2}{k_r^2} E_o^2 J_1^2(k_{01}) 2\pi R \frac{L_z}{2} \approx 0.94MW \tag{5.8}$$

for $E_o = 35$ MV/m, or less than 2%. Since the entire cavity fills in $\sim 3\tau_{RF} = 8.7\mu$s, recovery from beam loading will be well within the 1 μs requirement. The aforementioned π-mode iris-coupled structure [100] has much more severe beam loading (2.3 MW, versus a wall loss of only 0.7 MW) and a lower intercavity coupling constant.

The input coupler for the photoinjector was simulated using Hewlett Packard's High Frequency Structure Simulator (HFSS), which is a fully three-dimensional finite element frequency domain electro-magnetic code. As a guide for choosing the dimensions of the coupling slot, Gao's expression [107] for the coupling constant, β, derived using Bethe's formalism for computing the perturbation of cavity fields due

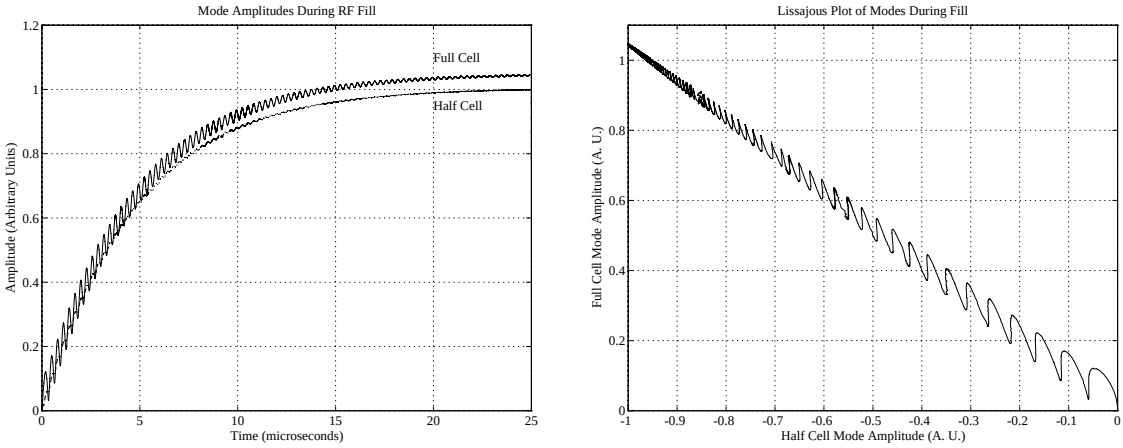

Figure 5.7: RF Fill of Half and Full Cell

to apertures [108], was employed, with the dissipated power P_o taken to be the total power dissipated in both cavities:

$$\beta = \frac{\pi Z_o k_o}{9} \frac{\Gamma_{10}}{W_{wg} H_{wg}} \frac{e_o^4 e^{-2\alpha\delta} l_1^6}{(\mathcal{K}(e_o) - \mathcal{E}(e_o))^2} \frac{H_\phi^2}{P_o} \tag{5.9}$$

With the impedance of free space $Z_o = 120\pi$, the free space RF wavenumber $k_o = \frac{2\pi}{\lambda_o}$, the waveguide propagation constant $\Gamma_{10} = k_o\sqrt{1-(\lambda/2a)^2}$, the aperture mode attenuation constant $\alpha = k_o\sqrt{((\frac{\lambda}{\lambda_c})^2 - 1)}$ with cutoff wavelength $\lambda_c = 3.41\sqrt{l_1 l_2}$, δ being the aperture depth, W_{wg} and H_{wg} the width and height of the waveguide, respectively, H_ϕ the tangential magnetic field strength at the aperture location, and the aperture eccentricity $e_o = \sqrt{(1-(\frac{l_2}{l_1})^2)}$. Figure 5.8 below shows the characteristically rapid variation of β with aperture length. The length of the aperture in the z-direction

is held fixed at 2.0 cm for both plots. In view of the very light beam loading (18.5

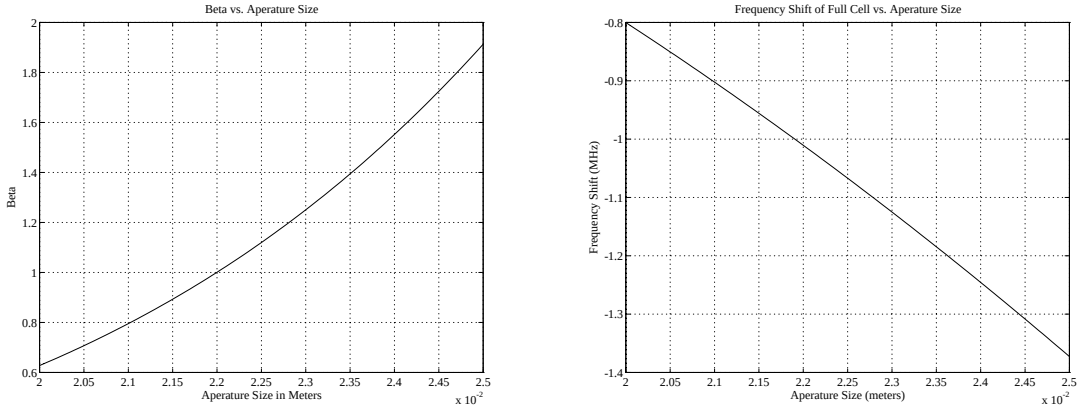

Figure 5.8: Coupling β and cavity frequency shift (in MHz) versus aperture length (in cm).

kW at E_o=35 MV/m), the unloaded cavity coupling coefficient need not be adjusted much to assure critical coupling with the beam present. The adjusted unloaded cavity coupling coefficient should be $\beta_o = 1 + \frac{P_{beam}}{P_{cav}}$ or approximately 1.02 for this case. This deviation in β is small enough to ignore the reflected power (< 2 %) and apply feed-forward to stabilize the RF amplitude and phase.

The two cavity system can be viewed as two pillbox resonators connected by a short circular waveguide operating significantly below cutoff. Lengthening this circular waveguide by the addition of nose cones exponentially decreases the coupling between the cavities, requiring an increase in the radius of the coupling hole to compensate. Increasing the coupling hole diameter decreases the shunt impedance by moving more of the stored field energy away from the beam axis. If the latter effect dominates, then the shunt impedance will decrease with the addition of reentrant noses.

The opening of the coupling slot on the outer wall lowers the cavity frequency

because of the effective increase in the cavity volume in a magnetic field dominated region. We examined the possibility of compensating for the frequency depression by a simple technique. The waveguide end may be pushed into the volume of the cavity, producing a flat region that not only decreases the volume of the cavity, thereby raising the frequency, but makes the thickness of the waveguide coupling slot more uniform. The two frequency perturbations can be made to cancel by an astute choice of the waveguide's penetration distance into the cavity, once the required dimensions of the coupling slot are known. The intrusion depth for this RF structure was calculated and found to be too small to warrant the added machining complication. Instead, the radius of the full cell has been adjusted to provide the required equal and opposite frequency shift.

Lastly, the waveguide taper, required to allow space for the first focussing solenoid (see figure 5.1) and to match the WR650 waveguide to the cavity, was chosen to be a standard $\lambda/4$ stepped transformer. Simulations with HFSS indicate that suppressing reflections by 20 dB or more is straightforward.

As with any asymmetric iris-coupled structure, the electrical center of the fields is shifted towards the driving iris. A least squares fit of the near-axis data from HFSS reveals that the displacement of the field maximum is $\leq 0.39mm$ from the geometric center of the cavity. Such a small shift (which is present only in the full cell, owing to the RF coupling scheme used) is not enough to warrant a cavity geometry alteration to compensate.

Run time tuning of the photoinjector was accomplished with the aid of four largely separate controls. Gross frequency tuning of the photoinjector as a whole was accomplished by regulating the cooling water temperature. Thermal analysis of a similar

L-band structure dissipating much higher average power (150 kW, versus 25 kW for the present case) found no serious difficulties in providing adequate cooling[104]. Indeed, an S-band structure sustaining the same duty cycle (1%) but higher accelerating gradient (by a factor of 2), and thus substantially higher dissipated power density (by a factor of 20), has been designed and successfully operated at Brookhaven National Lab [60]. Initial thermo-mechanical analysis using Ansys shows that frequency detuning within the RF pulse remains within 6 kHz [109], and is unaffected by the placement of the water cooling channels.

For an L-band copper structure, the frequency change per degree Kelvin is approximately:

$$\frac{\partial f}{\partial T} = -\frac{k_{01} c \kappa_T}{2\pi R} \approx 21.8 kHz/K, \tag{5.10}$$

with the thermal coefficient of expansion $\kappa_T = 16.92 \times 10^{-6}/K$ for copper. Initial tuning of the photoinjector is accomplished with the usual procedure of dimpling the cavity wall to raise the corresponding cell's frequency. Working temperature of the gun is chosen to be 310 K, at which temperature the detuning due to temperature change and evacuation of the air (351 kHz) match, allowing for tuning of the gun to the correct working frequency at room temperature in air. *In situ* tuning of the photoinjector was accomplished by means of precise cooling water temperature regulation. If drift of the phase of the gun due to thermal effects is constrained to $\pm 1^o$, this implies the constraint:

$$\Delta\phi < 1^o \Leftrightarrow \Delta f < \frac{f \tan(\Delta\phi)}{2Q_L} = 1.33 kHz \Leftrightarrow \Delta T < 0.06K \tag{5.11}$$

A commercially manufactured water temperature controller good to 0.1 K was used, with the remaining regulation taken up in the low-level RF system.

Field balance of the photoinjector is controlled with a 2.0cm plunger tuner in the full cell. Field phase and amplitude was monitored in both RF cells by means of inductive loops recessed in narrow chambers that couple magnetically to the RF cavity fields. (See figure 5.1.)

5.4 Engineering Considerations

5.4.1 Electrical Dimension Specifications and Tolerances

Electrical dimensions and tolerances derived from physical constraints on the resonant frequency, coupling constant, and normalized structure impedance are listed in table 5.3 below.

Constraints on the cavity resonant frequency, f_o, set by the available tuning range of the paddle tuners, cathode plunger, and thermal control system, are necessary to have the resonant frequency of the structure fall at the desired frequency, and to avoid field imbalance (viz. the ratio $E_{z,max}^{halfcell}/E_{z,max}^{fullcell}$) problems due to a mismatch in the individual cavity resonant frequencies. As the outer walls of the cavity experience substantial magnetic field, the frequency of the cavity varies rapidly with radius, placing tight tolerances on the radii. Tolerances listed below derive from the frequency constraint $\Delta f \leq 1MHz$.

The coupling constant γ prescribes the frequency separation of the zero and π modes of the structure, and controls to what extent movement of the photocathode perturbs the field balance. So long as gamma is large enough to provide for well separated zero and π mode frequencies, (i.e. the separation is greater than a half Q-width: $\omega_\pi - \omega_o \geq \frac{\omega_0}{2Q}$, where ω_0 is the resonant frequency of the uncoupled cavity) small changes in γ will not appreciably alter the field balance. Correspondingly, the

tolerance on the coupling constant is generous at $\Delta\gamma \leq .05\%$.

The normalized structure impedance, β, determines the behavior of the photoinjector when coupled to an RF source. Optimal power transfer from RF source to accelerating structure occurs when $\beta \equiv \frac{P_{cavities}+P_{beam}}{P_{\text{transmission system}}} = 1$. Tolerance on the physical dimensions of the coupling hole are tight, owing to the rapid ($\propto$ (slot area)^6) variation of β. Stipulating that the reflected power from the cavity not exceed 1% requires $0.818 < \beta < 1.222$.

Dimension	*Nominal Value*	*Tolerance*	*Quantity Affected*
radius of half cell	8.904	±0.0068=2.7 mil	f_o^{HC}
radius of full cell	8.884	±0.0068=2.7 mil	f_o^{FC}
radius of iris	2.0	±0.0833=33. mil	γ
thickness of iris	1.5	±0.0142=5.6 mil	γ
length of coupling slot	6.0	±0.0500=19. mil	β
width of coupling slot	2.0	±0.0167=6.6 mil	β
depth of coupling slot	0.5	±0.0548=22. mil	β
All dimensions in centimeters unless specified			

Table 5.3: Key electrical dimension specifications for the RF gun.

Chapter 6

Design of the RF Photoinjector

In the sections that follow is a summary of the calculated performance characteristics of the photoinjector described in the previous chapter. Information has been gathered here in a terse format for future reference.

6.1 Simulation Results

6.1.1 RF Structure Design

Gun

The electrical properties of the gun accelerating structure are summarized in table 6.1 below.

A plot of the longitudinal electric field profile through both the gun and linac, as seen by the beam, is given in figure 6.1 below. The decelerative fields at the exit of the gun and entrance of the linac arise from the fringe fields of the respective cavities. No deceleration is seen at the exit of the linac because the cavity is phased 15^o ahead of crest, and thus the fields reverse polarity after the beam is well into the fringe field region. The effects of launching well ahead of crest in the gun are also plainly visible.

Parameter	*Symbol*	*Value*
Operating mode		$TM_{010,\pi}$
Frequency	f	$1300MHz$
Transit time factor	T	0.73127
Structure quality factor	Q_o	23601
Structure fill time	τ_{RF}	1.45 μ s
Effective Shunt Impedance	ZT^2	$24.418M\Omega/m$
Peak-to-accel field ratio	E_{pk}/E_{acc}	1.870
Average Operating Gradient	E_{pk}	35 MeV/m
Power diss at $E_{pk} = 35MV/m$	P_{diss}	$2.2MW$
Average Power diss at $E_{pk} = 35MV/m$	P_{ave}	$22.0kW$
Power diss at $E_{pk} = 50MV/m$	P_{diss}	$4.5MW$
Average Power diss at $E_{acc} = 50MV/m$	P_{ave}	$45.0kW$

Table 6.1: Electrical Properties of the RF gun

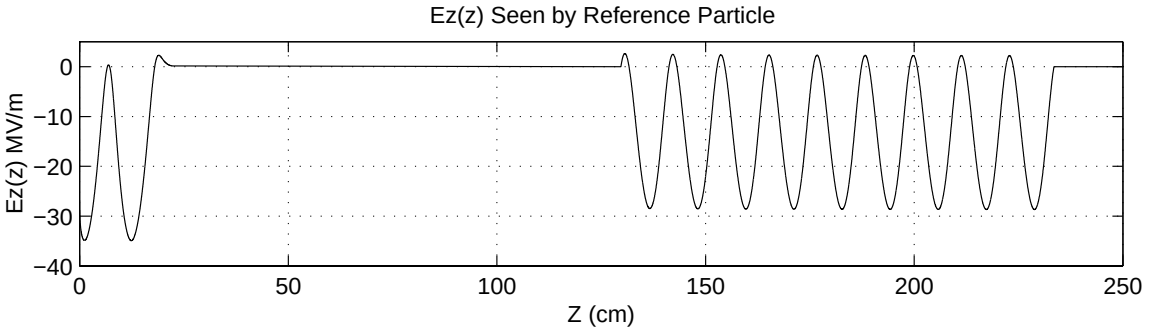

Figure 6.1: Accelerating electric field profile in the gun and capture cavity.

Linac

Electrical properties of the 9-cell copper linac structure are summarized in table 6.2 below. The maximum duty factor (0.00015) is not that of the TTF (0.01), since the prototype test injector was operated in single-bunch mode. This reduction in average power handling made the thermal control straightforward.

Parameter	*Symbol*	*Value*
Operating mode		$TM_{010,\pi}$
Frequency	f	$1300MHz$
Transit time factor	T	0.77046
Structure quality factor	Q_o	28928
Structure fill time	τ_{RF}	1.77 μ s
Effective Shunt Impedance	ZT^2	$48.387M\Omega/m$
Peak-to-accel field ratio	E_{pk}/E_{acc}	1.685
Average Operating Gradient	E_{accel}	15 MeV/m
Power diss. at $E_{pk} = 35MV/m$	P_{diss}	$4.83MW$
Maximum duty factor	η	0.00012
Average Power diss. at $E_{accel} = 15MV/m$	P_{ave}	$1.8kW$

Table 6.2: Electrical Properties of the 9-cell copper structure.

6.2 Magnet Performance

6.2.1 Solenoids

The primary and secondary solenoid field patterns are shown in figure 6.2 below. Field profiles are from two-dimensional (r, z) calculations from POISSON [87], and use a table of permeability values (as a function of applied field strength) typical of low-carbon steel (e.g. similar to ANSI-SAE grade 1008, with a carbon content under 0.10%). The actual yokes were made from slightly higher carbon steel, grade 1018 (which has a carbon content between 0.15% and 0.20%), giving rise to slightly different field strengths than those presented below.

Additionally, this calculation does not take account of the three-dimensional perturbations to the solenoid yoke, namely: the winding penetration gaps (each approximately 40 mr of the back leg of the yoke, symmetrically placed), the low-carbon steel bolts used to assemble the yoke pieces, or errors in the yoke and coil geometry.

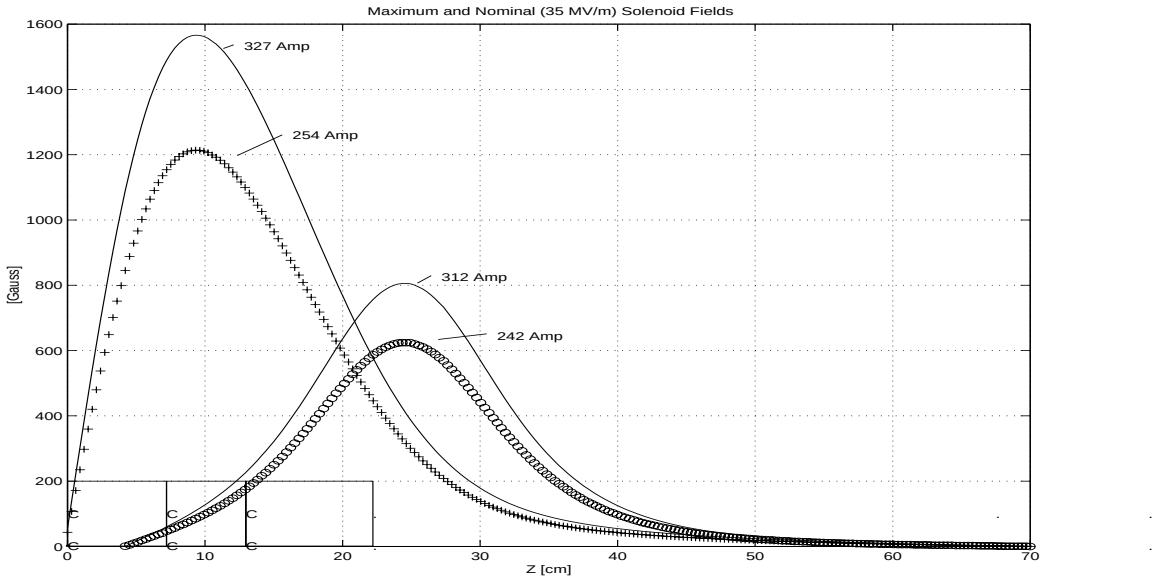

Figure 6.2: Primary and secondary solenoid field profiles $B_z(z)$.

Measurements of the spectrometer, focussing quadrupole, chicane dipole and kicker dipole magnets are presented in the Analysis chapter.

6.2.2 Beam Dynamics

On the subsequent pages, are shown PARMELA simulations of the envelope evolution (figure 6.4), emittance evolution (figure 6.5), and final phase space plots (figure 6.6) from the photocathode to the entrance of the first accelerating cavity of the first cryomodule. Six emittance traces are shown, representing the traditional one-sigma normalized 100% RMS emittance (darkest line), and FWHM one-sigma normalized emittances of 100%, 95%, 90%, 80%, and 70% of the bunch particles (see Appendix B for an explanation). The onset of emittance compensation is clearly visible in the decrease of all emittances after the solenoid focussing kick. Transverse and longitudinal phase space plots at the end of the injector beamline (at the exit of the compres-

sion) are shown as well. Strong ponderomotive focussing in the linac section (average gradient is 15 MeV/m) can be clearly seen.

Momentary increases in the transverse emittances in the linac and compressor result from two causes, first, the mechanical (not canonical) momenta are used in the calculation of the emittances, second, the emittance is computed at a single point in time ("snapshot" emittance), rather than at a single z-location ("phosphor" emittance), as it is usually measured.

Emittance and envelope evolution, as well as final phase space plots are shown in figures 6.7, 6.8, and 6.9 on the following pages for operation of the TTF Injector at low charge (1.0 nC) for possible use with the FEL. Emittances shown do *not* include the thermal emittance contribution. An accelerating gradient of 45 MV/m (peak, on the cathode) has been used. The increased gradient requires more RF power (i.e. 3.8 MW versus 2.3 MW) as operation at 35 MV/m, and thus is achievable only with a higher power klystron, such as the higher efficiency multiple-beam klystron currently under development at Thomson's Electron Tube Division.

6.2.3 Dark Current Propagation

Simulations of dark current trapping and transport have been carried out for the specific case believed to be the most troublesome. As the momentum acceptance of the injector beamline is very limited, electrons which are field emitted at any point except near the cathode will have energy and transport characteristics very different from the photoemitted electrons, and will be strongly over-focussed or bent out of the beamline as a result. Therefore simulations of cathode-produced dark current were carried out to understand the probable rejection ratio and approximate impact

locations for the dark current.

In modelling the dark current source term, field emission is the only emission mode treated, as thermionic emission at room temperature is negligible, and multipactoring results from geometry and field specific resonance conditions that can be spoiled (e.g. by slight changes in magnetic or accelerating fields) relatively easily. Thus the temporal emission characteristics are controlled by the electric field strength only through the Fowler-Nordheim relation (equation 2.4) which has an extremely strong dependence on the field strength, and thus dark current emission is significant only close to the crest of the RF. For modelling purposes, the temporal distribution is taken to be Gaussian, with an emission time centered on the RF crest, with a distribution sigma of $\pm 7^o$ of RF, and with space charge and wakefield effects neglected.

Figure 6.10 below shows the location of dark current losses with nominal photocurrent magnet settings. The majority of the dark current is lost in the gun or into the beamtube before the 9-cell cavity, with $\sim 15\%$ reaching the inside of the cavity, and most of the remainder hitting the beamtube shortly after the chicane.

From the transmission loss, it is possible to estimate the deposited power at cryogenic temperatures, and place an upper bound on the acceptable amount of dark current. Heat production of 1 J/s begins to be comparable to the cryogenic heat load of the powered structure itself, which limits the dark current (cathode-derived, 3.9 MeV) to ~ 250 nA impinging in the cavities, and to no more than 1.7μA at the source. Clearly collimation before the cryomodule is the best option for rejecting the dark current.

6.3 Summary of Expected Performance

A summary of the foregoing PARMELA simulations of the injector performance is displayed in table 6.3 below. Unlike the simulation results above, the quoted emittance figures include an estimated 0.7π mm-mr thermal contribution to the transverse emittances from the residual kinetic energy of the photoemitted electrons.

Parameter	*Symbol*	*Value*	*Value*
		HOM Analysis	FEL
Before Compression			
Bunch Charge	Q_b	8 nC $= 5 \times 10^{10} e^-$	1 nC $= 6 \times 10^9 e^-$
Laser pulse length FWHM	Γ_t	10 ps	8 ps
Launch Phase (w.r.t. $E_z = 0$)	ϕ_o	50^o	60^o
Beam radius at cathode	r_o	6.0 mm	1.0 mm
Post-Gun Gamma	γ_1	8.6	11.1
Post-Linac Gamma	γ_f	37.5	40.0
Horizontal Emittance	ϵ_x	25π mm-mr	2.1π mm-mr
Vertical Emittance	ϵ_y	25π mm-mr	1.1π mm-mr
Longitudinal Emittance	ϵ_z	300 deg-keV	10 deg-keV
Energy Spread	σ_E	200 keV	57 keV
Momentum Spread	σ_p/p_o	1.07 %	0.16 %
Bunch Length	σ_b	1.0 mm	0.24 mm
Peak Current	I_p	957 Amperes	498 Amperes

Table 6.3: Predicted performance of the Photoinjector, values calculated at the end of the first cavity in the first cryomodule, $z = 1245$ cm. Emittances include 0.7π mm-mr thermal contribution from cathode.

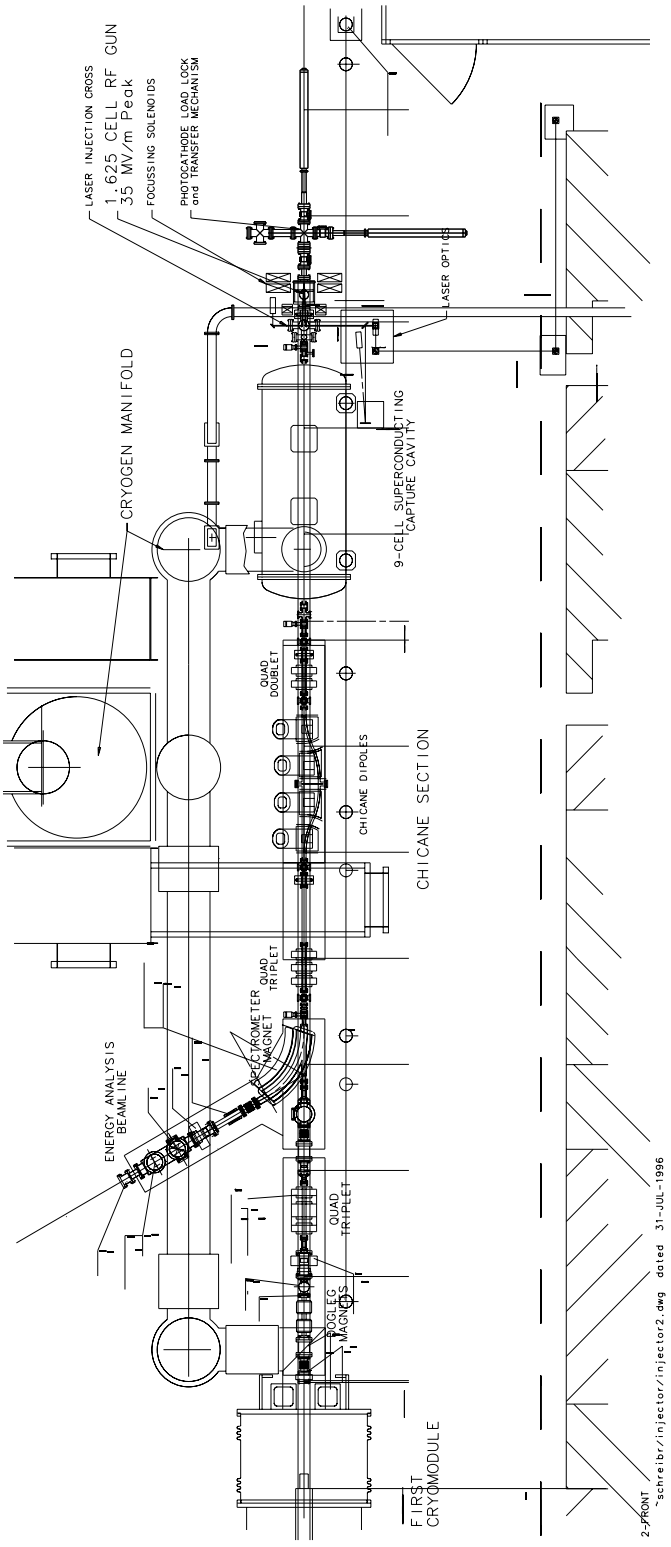

Figure 6.3: Injector II Beamline, shown configured for 8 nC operation. Drawing courtesy of DESY.

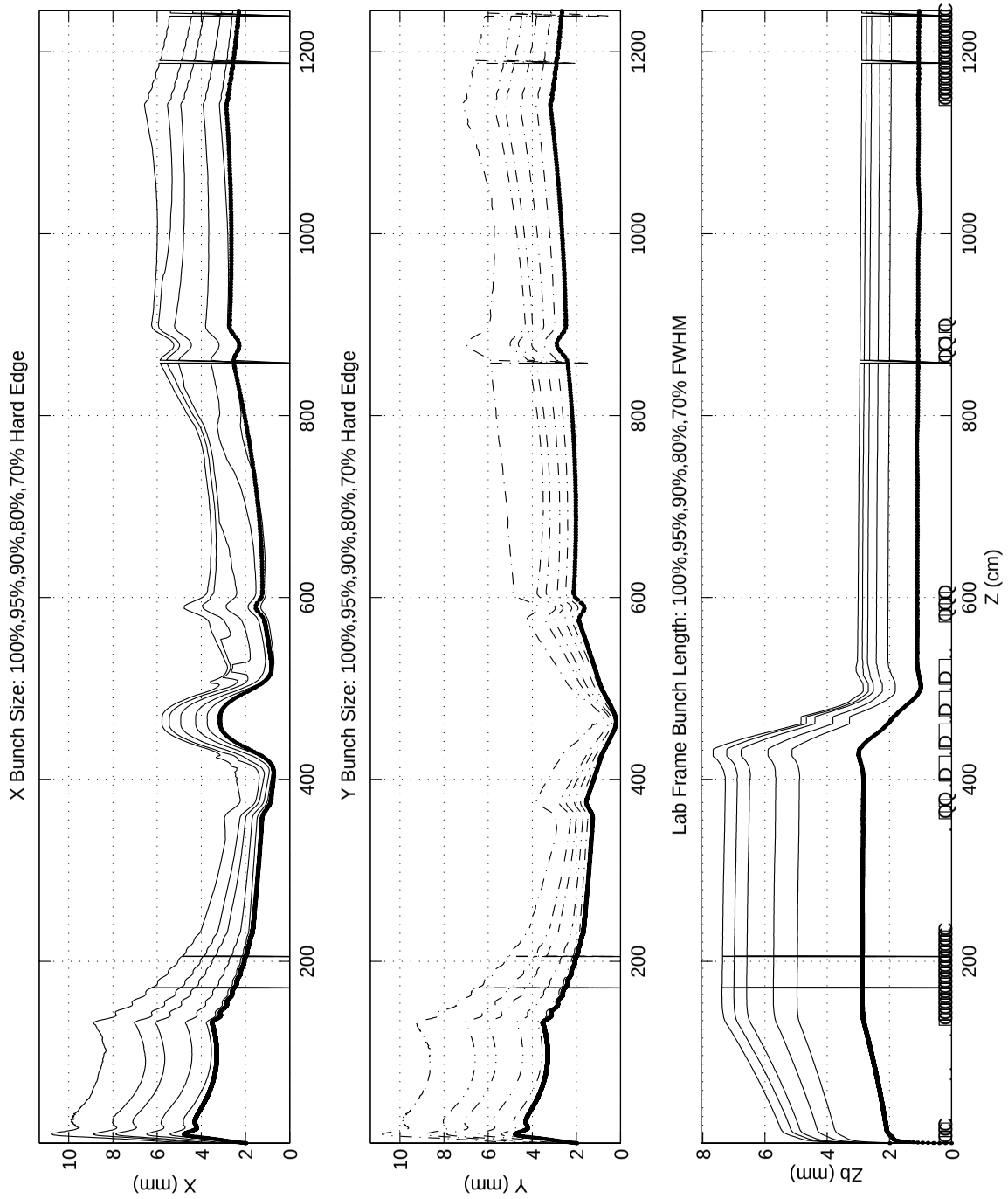

Figure 6.4: Envelope evolution for 8 nC operation

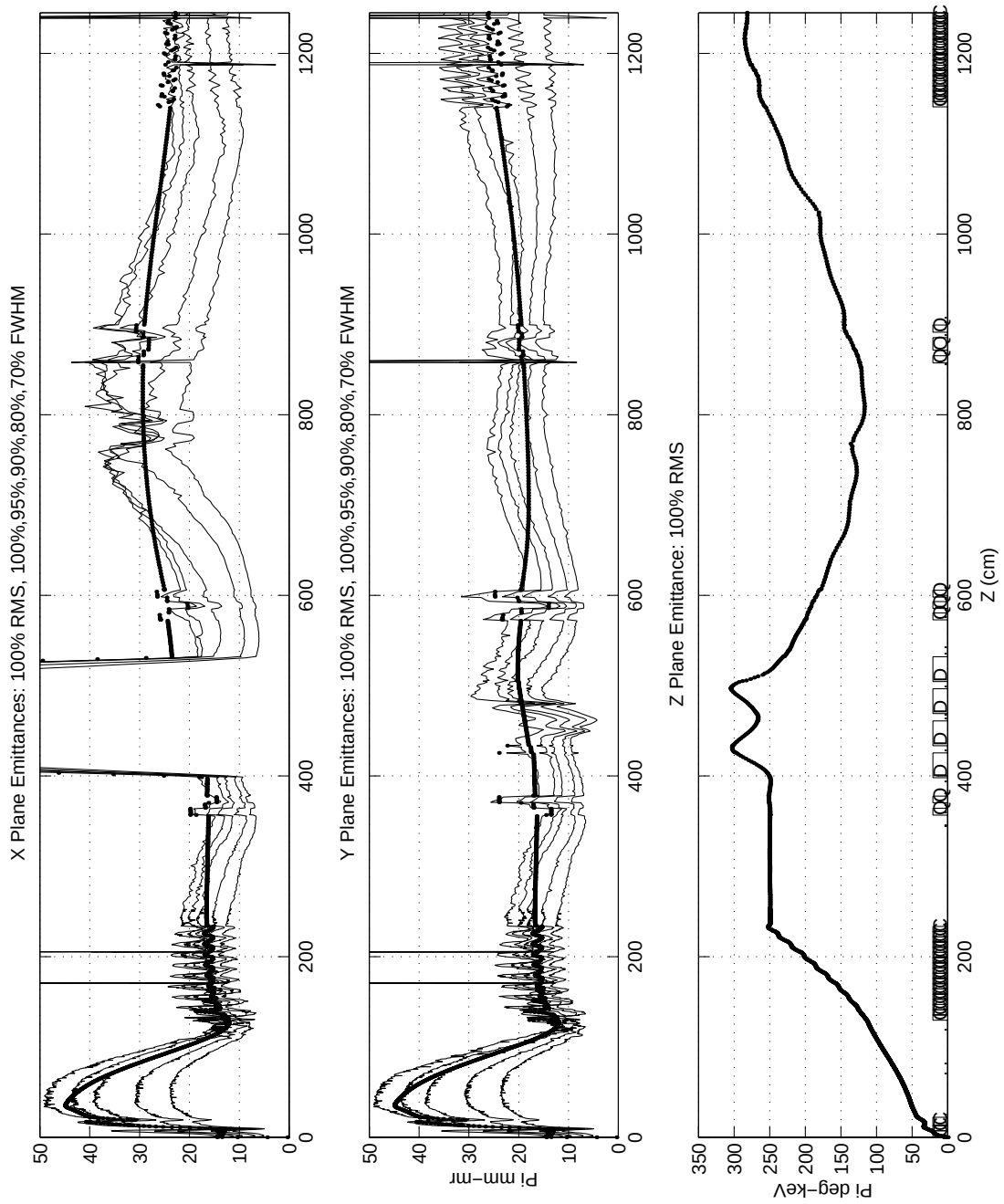

Figure 6.5: Emittance evolution for 8 nC operation

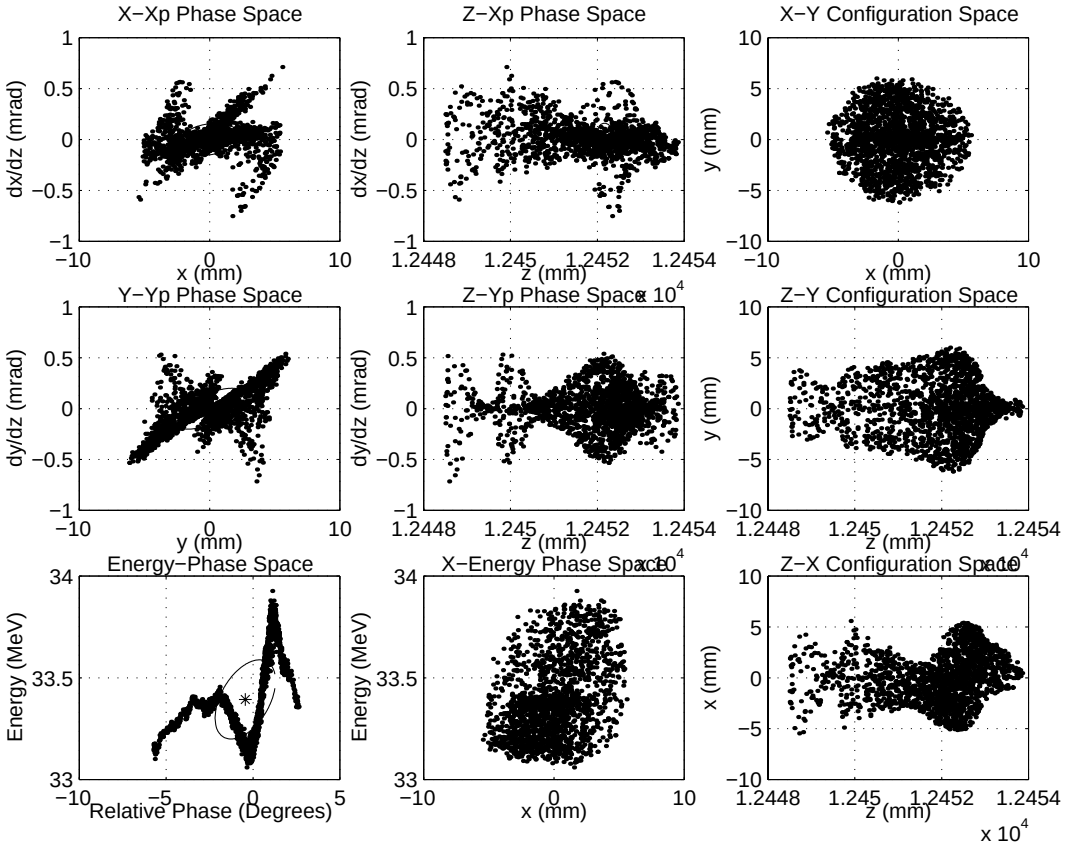

Figure 6.6: Phase space and configuration space plots at $z = 1245$ cm (the exit of the first cavity in the first cryomodule) for 8 nC operation. Of 15000 simulation particles, 2000 were randomly chosen for these plots.

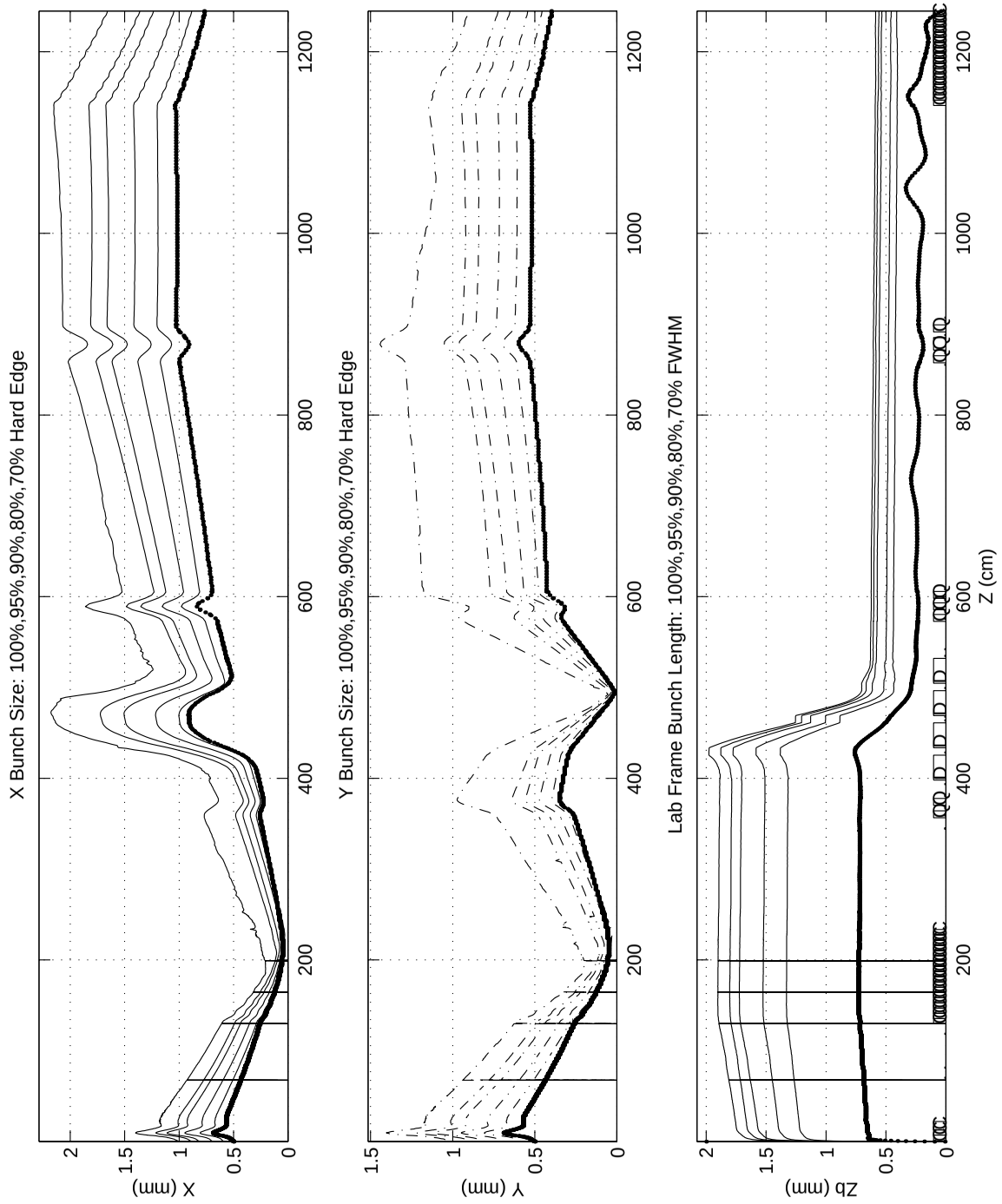

Figure 6.7: Envelope evolution for 1 nC operation

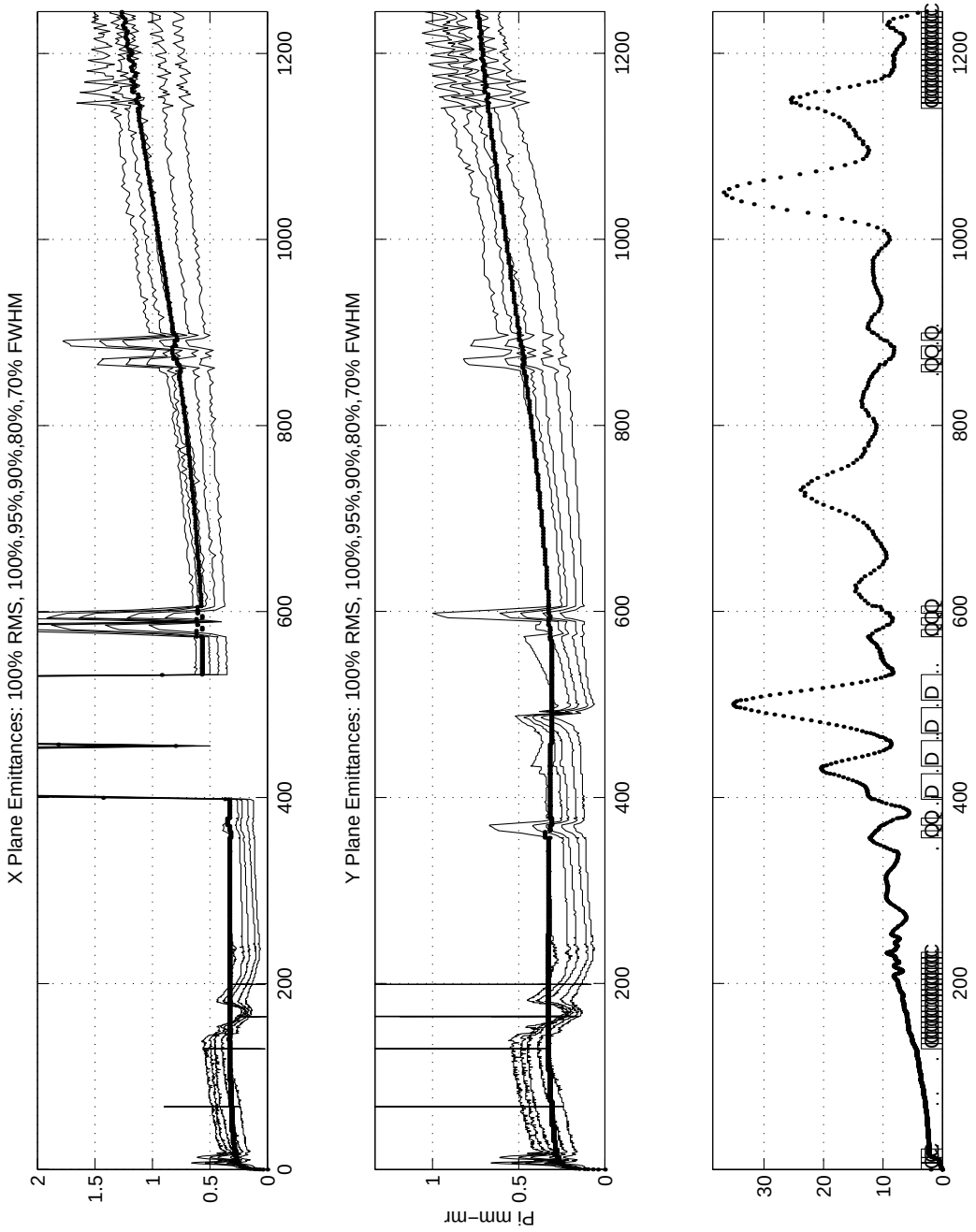

Figure 6.8: Emittance evolution for 1 nC operation, these calculated emittances do *not* include the thermal emittance contribution.

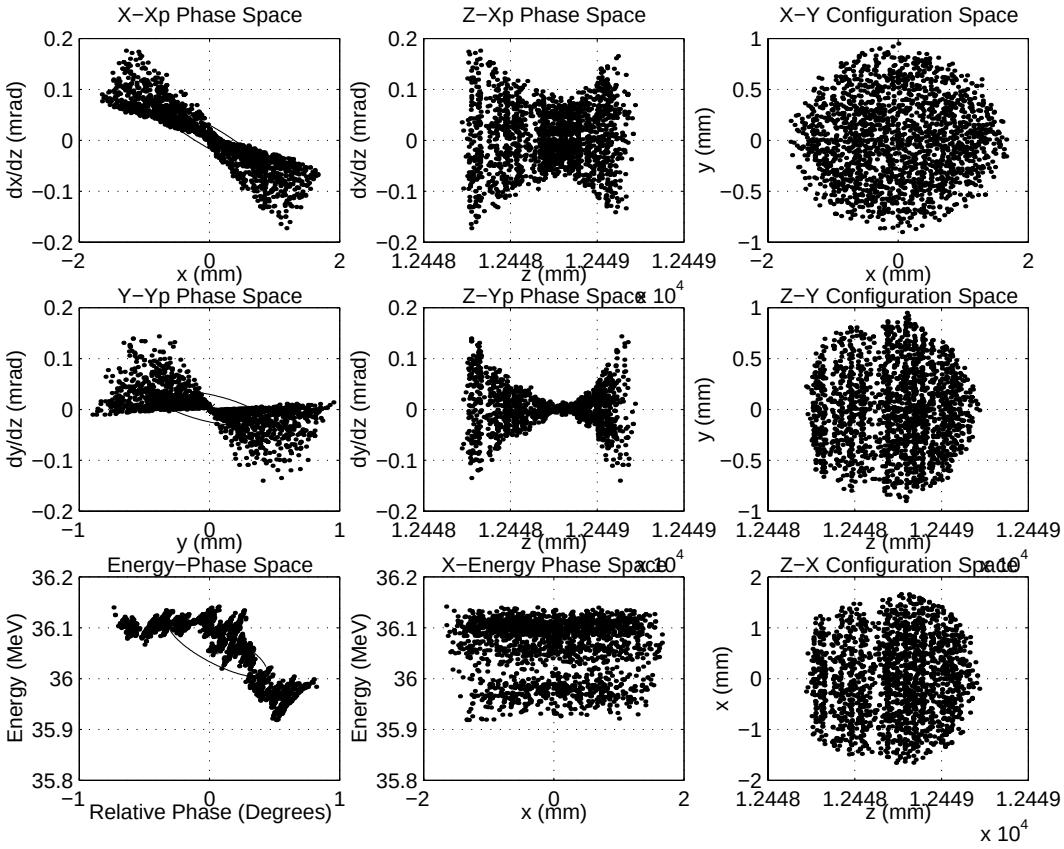

Figure 6.9: Phase space and configuration space plots at $z = 1245$ cm for 1 nC operation. Of 15000 simulation particles, 2000 were randomly chosen for these plots.

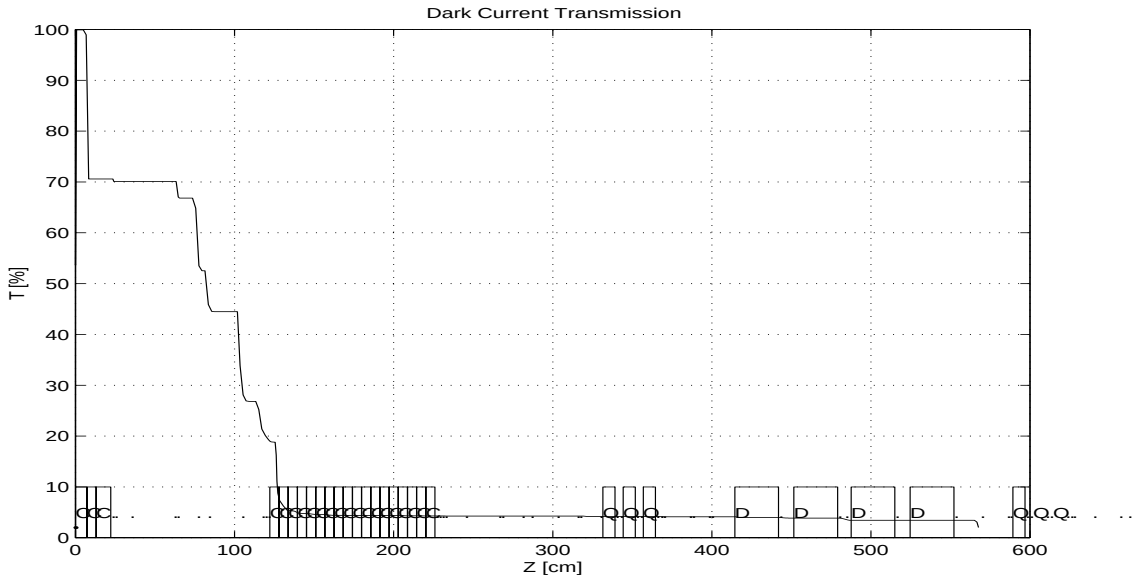

Figure 6.10: Dark current loss for 35 MV/m gun fields and nominal magnet settings.

Chapter 7

Diagnostics

Central to an experiment are the diagnostics. Diagnostics have been grouped here into four categories: RF, Laser, Electron Beam, and all other.

7.1 Introduction

The layout of the prototype photoinjector beamline at Argonne National Laboratory is shown in Figure 7.1 on the next page. Instrumentation of the beamline has been chosen to permit exploration both of the injector performance in general, and to allow direct observation of emittance compensation, as well as more general aspects of the beam phase space.

A summary of the placement of the beam diagnostics is given in tables 7.1 through 7.3 below.

A new approach to emittance measurement has been proposed to explore the physical basis for emittance compensation [110]. A time-resolved variation of a slit emittance measurement technique (similar in principle to the pepper pot) employed at UCLA[111] will be used, providing emittance measurement in one transverse plane as a function of longitudinal position within the beam. While prior time-

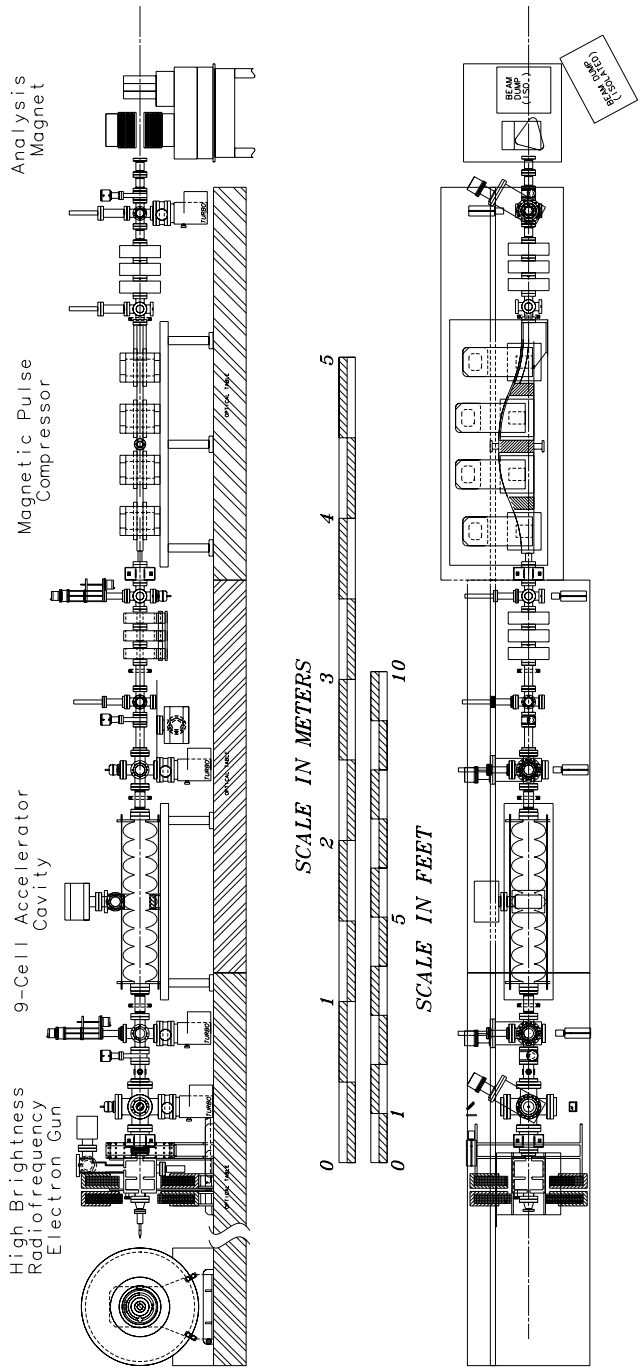

Figure 7.1: Layout of beamline components for testing the photoinjector at A.N.L.

Station	*Device*
Diagnostics between Gun and Linac	
z=304	122mm ID Fast Current Transformer
1 z=516	top: Laser Mirror Suspension, Penning Gauge
	bottom: 150 L/s Turbopump
	front: Quartz Window (Laser in)
	rear: Quartz Window (CCD Camera)
2 z=971	Phosphor Screen
	Faraday Cup
	Borosilicate Glass window (CCD Camera)
	30 L/s Ion pump

Table 7.1: Diagnostic station location and equipment, gun to linac.

resolved measurements of electron beam emittance on the nanosecond time scale at Los Alamos [112], and of three-dimensional spatial distribution at LEP [113] have been successfully undertaken, measurements with sufficient resolution (picosecond or better) to observe the emittance compensation process have not. Figure 7.2 provides a schematic of the proposed measurement. A detailed analysis of the apparatus will appear in the near future, but a brief description is included here for completeness.

The space charge dominated beam is brought to a non-ballistic waist (i.e. particles do not cross the axis) and collimated into several emittance dominated beamlets by a slit emittance mask. The beamlets retain the transverse temperature of the original beam, but at such reduced charge that space charge forces within the individual beamlets contribute negligibly to their momentum spread. The beamlets then drift several meters to allow the correlated transverse momentum enough time to impart a measurable transverse distance offset, and are passed through a Čerenkov radiator to produce an optical signal that can be extracted from the beamline. The light is focussed (optics not shown) onto the photocathode of a streak camera, and the

Station	*Device*
Diagnostics between Linac and Chicane	
3	Emittance Slit
z=2607	Penning Gauge
	Glass window
	30 L/s Ion pump
4	OTR Foil (Al on mylar)
z=3028	Blank
	Glass window (CCD Camera)
	Blank
5	Phosphor Screen
z=3687	Blank
	Glass window
	30 L/s Ion pump
z=3825	122mm ID Fast Current Transformer

Table 7.2: Diagnostic station location and equipment, linac to compressor.

streak image recorded with a high resolution CCD camera. The spread of the light from each beamlet may be analyzed to unfold the contribution due to the transverse temperature of the beam from the natural spread angle of the Čerenkov radiation. The centroid of the beamlets at the radiator provides the centroid of the transverse momentum spread, while the transverse position centroid is known immediately from the separation of the collimator slits. From these data the transverse phase space of the beam may be reconstructed as a function of longitudinal position within the beam. The slit separations are chosen to ensure that the light from adjacent beamlets does not overlap at the CCD camera.

With this diagnostic, investigation of the effectiveness of emittance compensation will be explored as a function of compensating lens position and strength by adjusting the current sum and the current ratio, respectively, of the two focussing solenoids

Station	*Device*
Diagnostics between Chicane and Spectrometer	
6	Phosphor Screen
z=5470	Pepper Pot
	Glass window
	30 L/s Ion pump
7	Aerojel Čerenkov Radiator
z=6065	Glass window
	Phosphor screen
	Glass window
8	Spectrometer
z=6579	Faraday dump station

Table 7.3: Diagnostic station location and equipment, compressor to beamline end.

depicted in figure 5.1 above. Owing to limitations of machine performance and time, this measurement was not completed during the prototype test phase at Argonne, but will be attempted in the future. With information about the actual slice emittances (viz. the emittance of a subset of the beam electrons between z and $z + \Delta z$) and the orientation of the slice emittance ellipses before and after compensation, detailed study of emittance compensation will be possible for the first time.

The RF and laser systems at Argonne National Laboratory Wakefield Accelerator Facility were computer controlled through a combination of LabView and custom Tcl/Tk based software. The TTF prototype photoinjector made use of the existing RF and laser systems, adding a separate LabView-based control system on a separate computer to run the diagnostics and magnets. Many LabView "virtual instruments" (VIs) were developed to handle everything from proper de-Gaussing and magnet set point cycling to image data reduction to the monitoring of vacuum and power supply status.

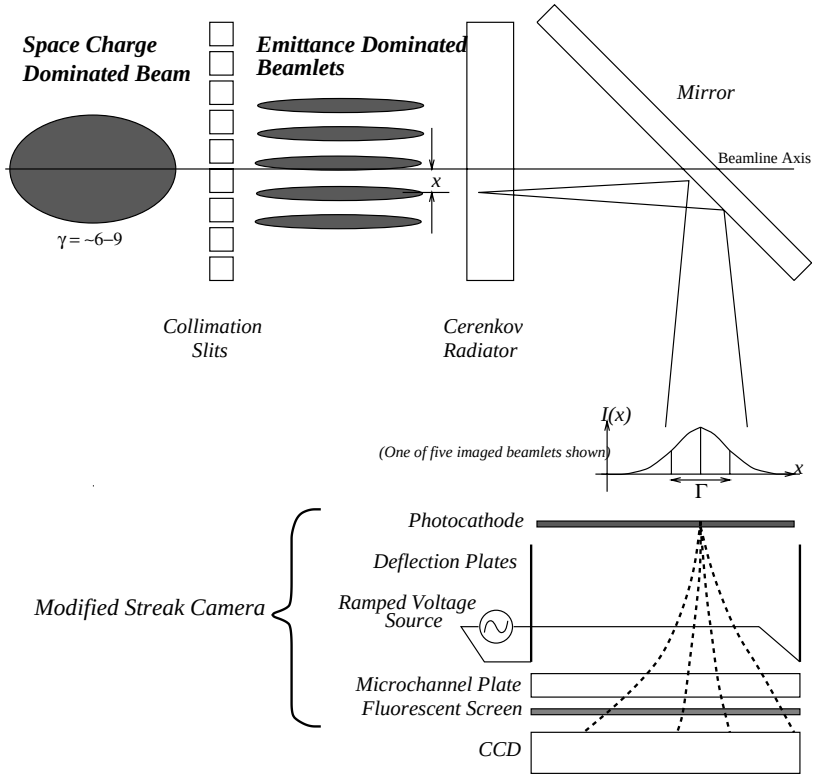

Figure 7.2: Schematic of time resolving emittance measurement apparatus

The primary interfaces to the hardware were through Fermilab Internet Rack Monitors (IRM) [114]. The IRM is a 68xxx based control and acquisition interface that supports up to 64 analog input channels (ADC), 32 analog output channels (DAC), and 4 word-wide bi-directional digital I/O channels, and is communicated with directly via the User Datagram Protocol (UDP) over Ethernet. Power supply and vacuum monitoring, as well as stepper motor position read back where read by the IRMs, with the analog output channels used to program power supply currents and the digital output channels used to control stepping motors.

Interface to the AWA RF system was done via a TCP/IP communication program [115] specifically written to interface with the AWA Tcl/Tk based control sys-

tem [116] to allow control of the RF phases from the diagnostic control computer. Control of the laser and streak camera was manual.

7.2 General Diagnostics

7.2.1 RF Diagnostics

Field amplitudes in each gun cavity and in the two end cavities of the linac were measured directly either via recessed inductive loops, as in the gun, or with beam-tube mounted capacitive pickups. All loops and pickups were network analyzer calibrated by coupling power into the structure through an N-type to WR650 mode launcher and observing S_{21} at the drive frequency of the klystron, approximately 1.3 GHz $\pm$ 1 kHz. In general, the pickup signals were attenuated further, and detection diodes used to amplitude detect the RF response. Signals from the forward/reverse power couplers (inductive couplers in the high power waveguide itself) were treated similarly.

The AWA RF system [117] has neither phase nor amplitude feedback except within the preamplifier itself, making long-term drift in the phase of the RF with respect to the laser an important drifting variable. Long-term drifts in the klystron were hand-corrected based on (1) beam energy and energy spread, and (2) phase detection of the klystron output mixed with the output of the low-level preamplifier. Long term drifts of 10-15 degrees could easily accrue within a run if ignored. The klystron gun voltage was observed to routinely droop a few percent over the course of a run, and could easily account for most of the observed phase shift.(Relativistically correct estimate: $\frac{\partial \phi_{ko}}{\partial V_{gun}} = \frac{L * f_{RF} * 360}{\beta^3 \gamma^3 c} \sim 4.2^o/kV$).

Four-port reflectometers were liberally placed throughout the waveguide system to measure power flow at various points in the RF distribution system. Peak power

output of the klystron was observed to be limited to slightly less than 16 MW, not 25 MW, as in reference [117]. Reflectometers were calibrated by the manufacturer, and a test check of the calibration of one of the devices was acceptably close (within 0.5 dB) to the manufacturer's value. Reflectometer signals were further attenuated (typically another 30 dB) and amplitude detected locally with calibrated tunnel diodes. The video signal was sent through approximately 36 m of RG223 to the control room, where the signal was observed on an oscilloscope. Cable calibrations were produced by shorting the cable at the source end, and performing S_{11} measurements with a sweep oscillator in the control room, with the square of the needed frequency-dependent transfer function resulting.

Field amplitudes in the half and full cells of the gun were directly measured by means of recessed inductive field antennæ. Calibrations of the loops were obtained via S_{21} measurements from the waveguide input coupler to the pickup loops *with the gun balanced* (i.e. with $E_{HC} = E_{FC}$). Together with experimental measurements of the cavity Q-factors, the field amplitudes could then be directly computed. Capacitative antennæ observed the fields in the end-most cells of the 9-cell linac structure, were similarly calibrated, and yielded an estimate of the field tilt within the linac.

On a single run, thermal effects on the phase stability of the gun and linac structure were measured by mixing the half cell loop signal from the gun with the upstream pickup signal from the linac. Different thermal masses, cooling system properties, and dissipated power characteristics were expected to give rise to rather different thermal behavior, most noticeable when the repetition rate (and, hence, the average power) was changed. Consequently, adjustments in repetition rate came at the expense of a re-tuning of the RF phases once thermal equilibrium was restored. Unfortunately,

data acquisition (1 Hz) and machining tuning (generally done at 10 or 15 Hz) were not compatible for this reason.

7.2.2 Laser Diagnostics

The AWA laser has been described in some detail in the conference literature[118]. Average power from the frequency tripled Nd:YAG pump laser was measured at two points, the first in the IR using the detector built into the laser head, the second in the UV, using a Coherent power meter. The same power meter was also used to measure average power output from the dye oscillator. The pulses emerging from the dye oscillator were split, with a fraction of the energy entering an Inrad two-photon fluorescence (TPF) autocorrelator. This provided an on-line monitoring of the output pulse length and amplitude from the dye oscillator. Signals from the autocorrelator were analog voltage encodings of the TPF intensity. Signals generally were monitored on a analog scope in the laser room, but for laser studies were digitized and stored.

Per-pulse energy emerging in the UV from the final KrF amplifier was monitored using the split-off pulse (normally used for the AWA "witness" beam generation) at the output using a Molectron pyroelectric detector with a sensitivity of 1.3 V/mJ incident energy and a sub-microsecond rise time and a decay time in the milliseconds, making resolution of individual laser pulses possible. In addition, another pyroelectric detector could be placed in the main beam to cross-calibrate the online detector.

Temporal profiles of the amplified UV pulses from the KrF were deduced using a Hamamatsu streak camera (C1587 streak tube, 1 ps quoted resolution) viewing the UV directly (through a number of attenuators). Observed resolution for the slit widths generally used (20 μ) was found to be more like 2.6 ps, completely satisfac-

tory for the measurements made. Great care in measuring short pulses is required with any streak camera, that light intensity does not reach such an intensity that the space charge effects within the streak tube influence the measurement. For all measurements shown here, light striking the tube photocathode was attenuated to give a signal requiring highest gain from the micro-channel plate (MCP) while still giving reasonable statistics.

Spatial profiles of the laser pulse at various points in the system were captured using a standard CCD camera, accompanied by a fluorescent screen (the whiteners used in paper for business cards proved satisfactory) when imaging UV pulses. Care had to be exercised with the fluorescent screens that saturation and burning did not appreciably taint the result.

7.3 Electron Beam Diagnostics

Electron beam diagnostics fall into two categories: destructive (intercepting), and non-destructive. Non-destructive diagnostics used here are the integrating current transformer (ICT) for measuring bunch charge and the beam position monitor (BPM). All other measurement techniques depend on intercepting the beam with an electron/photon converter (phosphor, OTR screen, Čerenkov radiator), a sampling mask (pepper pot, slits), or an instrumented beam stop (Faraday cup).

7.3.1 Bunch Charge

ICT

Two integrating current transformers (ICTs) were used to continuously monitor the bunch charge at two locations: at the exit of the gun, and at the entrance of the pulse

compressor. The ICT inductively couples to the beam, requiring an image current bypass around the device so that the space charge fields of the beam pass through the pickup windings. The ICTs used (Bergoz ICT122-40:1) gave unipolar pulses approximately 20-30 ns wide, the integral of which was proportional to the bunch charge. Under the conditions of interest, the pulse height was also very linearly dependent on the bunch charge, and being a rapidly measurable quantity on a digital scope, was the preferred measure. After propagation through 36 m of RG223 cable, the charge sensitivity was degraded to approximately 37 mV/nC. Of course, given the filtering and extremely limited bandwidth of the device, no bunch length information could be obtained.

Image current returns around the ICT are needed, or else the fields of the beam will not couple to the pickup. Normal practice places the ICT in a copper cavity built around a ceramic break in the beamline at the location of the ICT. Image current return from the present usage was arranged using six inch-wide copper strips (for low inductance) joining the upstream and downstream beam tubes electrically.

ICTs were calibrated by passing a single loop of wire through the bore of the pickup. The loop was driven in series with a 50 Ω resistor by a pulse generator producing 20 ns wide pulses, and the ICT was readout remotely, as when used to measure beam. Comparison of the voltage integrals and peak voltage response of the ICT led to the calibrations used. Cable losses inferred from this calibration (0.77) agreed well with those directly determined earlier by S_{11} measurements and with the manufacturer's specification of 1dB/100 m at 100 MHz.

Faraday Cup

Two styles of Faraday cup were implemented. The first was an actuator-mounted stainless steel beam stop with a fairly open Albedo trap connected through an RC low pass filter to a 50 Ω line. No impedance matching of any of the components was undertaken. The actuator was electrically isolated from the remainder of the vacuum system via mylar washers and a viton gasket. Isolation of this Faraday cup remained poor (25 kΩ) despite efforts to remove potential charge drainage pathways. Contamination of the viton gasket by trace amounts of anti-seize lubricant (graphite suspended in molybdenum disulfide) is the suspected cause. (The following curious behavior was observed on each cleaning/re-installation of the Faraday cup: isolation was initially excellent, degraded to $\approx$ 10 MΩ on tightening the vacuum flange into place, and then degraded over several hours to the nominal value of 25 kΩ.) Such a leakage pathway required that the desired discharge pathway through the oscilloscope have even lower impedance to avoid substantial leakage current errors. Consequently, the discharge pathway was chosen to have 189 Ω resistance, with an integrating capacitance (cup+external capacitor) of approximately 10 nF, for a time constant of 1.9 μs.

Two additional Faraday "cups" were implemented, and were simply instrumented beam dumps composed of a $4 \times 6 \times 6$ inch carbon showerer enclosed in at least 4 inches of lead on all (but the upstream) sides. The "Faraday Dump" was isolated from the world by a copper clad G-10 circuit board, onto which was soldered the RC filter. Again, no effort to impedance match the components was made.

Calibration of both styles of Faraday cup was accomplished by driving the cup directly with a pulse generator through a 10:1 voltage divider to minimize charge back-

flow into the pulse generator on readout. Unlike the ICTs, the Faraday cup waveforms were always integrated to produce charge estimates, as impedance discontinuities in the circuits made the peak voltages subject to numerous reflections. Calibration curves for the three Faraday cups are shown in figure 7.3 below.

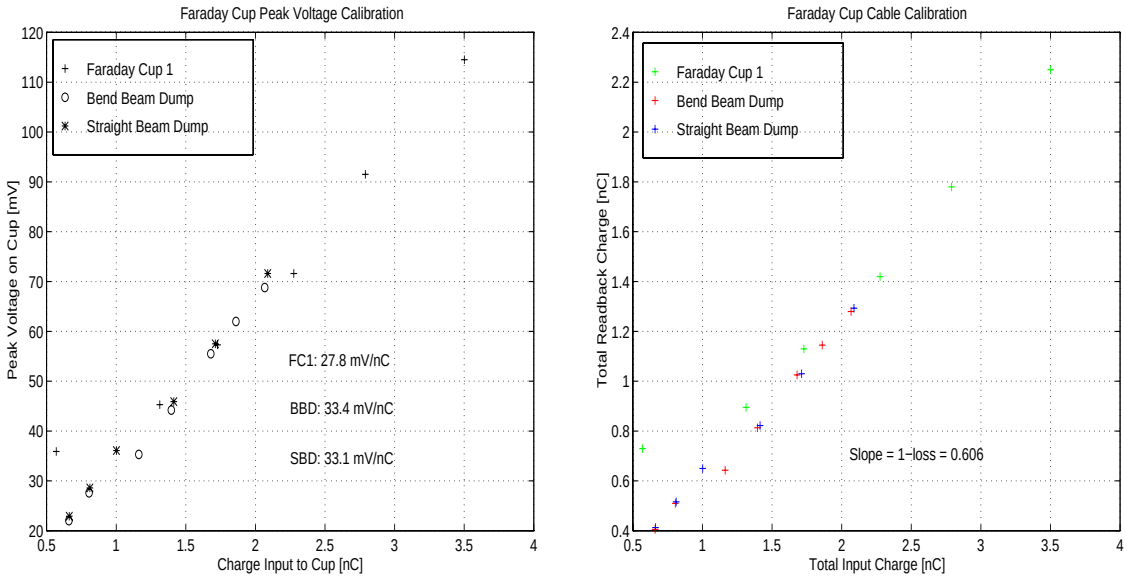

Figure 7.3: Faraday cup calibration curves for peak voltage response (left) and integrated current response (right)

Measurements of the bunch charge from the Faraday cup in cross 2 and ICT after the gun showed a consistent discrepancy of approximately a factor of 2/3, with the ICT always reading more charge than the Faraday cup. I speculate that the extremely short electron bunches at 4 MeV stop in a few millimeters in the Faraday cup (made of stainless steel), resulting in a momentarily large field capable of expelling secondary electrons (the "knock-on" electrons) from thee cup, causing a significant under reading of the bunch charge. For this reason (as well as for their non-intercepting nature), the ICTs were adopted as the standard for measuring bunch charge.

Calibrated BPM Response

Although not calibrated or used as a charge monitoring device, the BPM (beam position monitor) was determined to have better sensitivity to the bunch charge than did the ICTs, at ≈ 120 mV/nC. Figure 7.4 below shows the results of the sensitivity test.

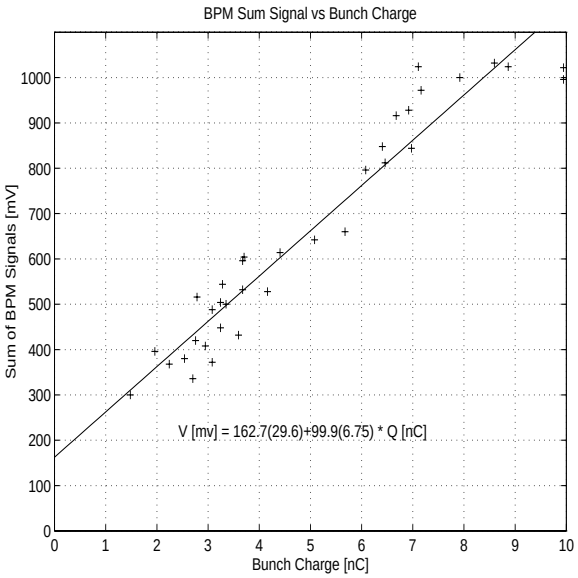

Figure 7.4: BPM Sensitivity vs. Bunch charge

7.3.2 Beam Position

Capacitative "Button" BPM

A button BPM, composed of four 1 cm diameter capacitative pickups mounted nearly flush with the vacuum chamber wall at 90^o intervals, was tested together with processing electronics from the Advanced Photon Source (APS) at Argonne National Laboratory. The individual buttons were examined with a network analyzer, and found to have fairly flat passband characteristics, with one resonance (see figure 7.5

below) at 13.23 GHz. Capacitances measured close to the manufacturer's listed 4.3 pF value.

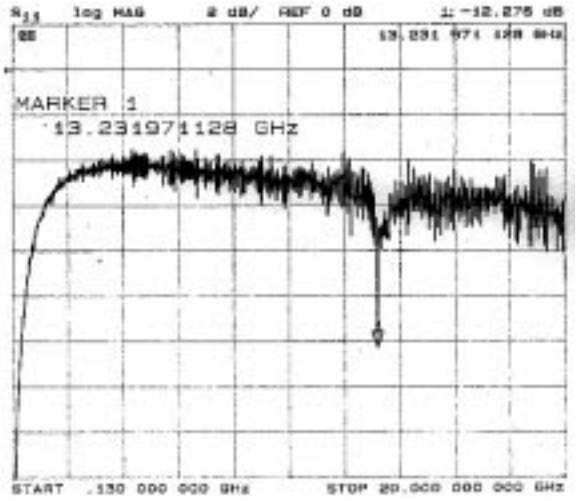

Figure 7.5: S_{11} response of BPM button mounted in beamtube feethrough

Impedance measurements on the buttons in the center of the power output spectrum (around 3 GHz) show that the buttons would not match to a 50 Ω line. Processing electronics, described in the literature [119, 120] and borrowed from the APS was employed to readout the BPM signals.

The processing electronics provided not sum and difference signals, but the logarithms of the upper and lower (or right and left) button signals. The usual difference-over-sum ratio taken as an approximate measure of the beam position (exact only on axis) is seen to be just:

$$x \approx \frac{\Delta}{\Sigma} \approx -\frac{1}{2}\log\left(\frac{1-\Delta/\Sigma}{1+\Delta/\Sigma}\right) = -\frac{1}{2}(\log(A) - \log(B)) \tag{7.1}$$

where $\Delta = A - B$ and $\Sigma = A + B$, and A, B are the raw voltage signals from one pair of buttons, and the Maclaurin series for $log((1-x)/(1+x))$ is used.

Position sensitivity was found to be consistent with APS documentation of 10 μm at 43 mV/mm for 8nC bunch charge. Curiously, both beam and bench tests of the electronics suggest that the range of bunch charges over which the processing electronics is useful is rather limited, with noise and saturation effects setting in below 1 nC and above 10 nC, respectively. Position sensitivity measurements are summarized in figure 7.6 below.

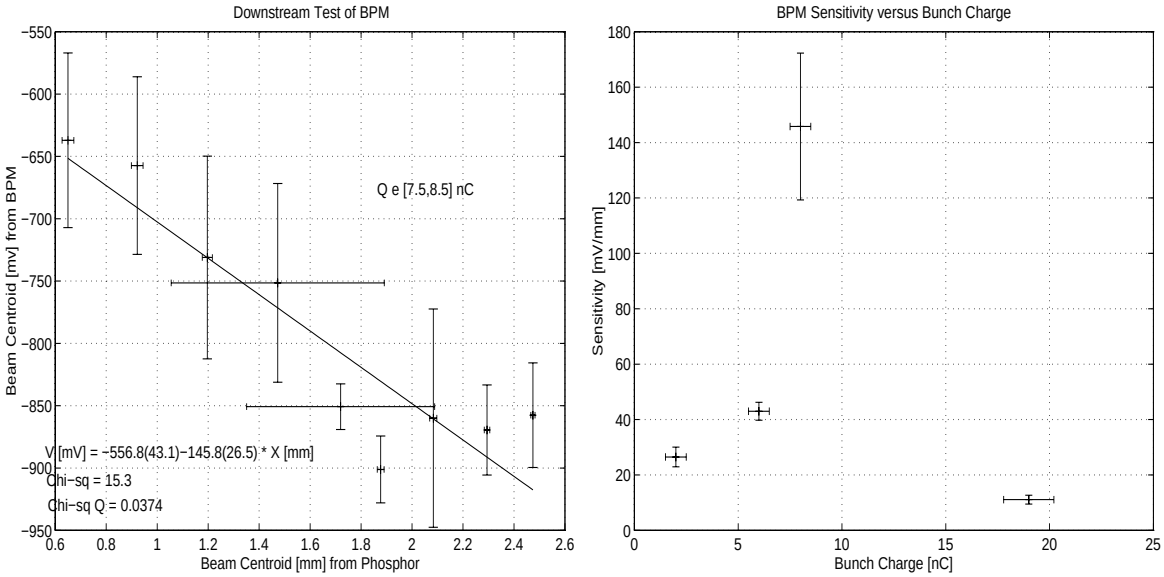

Figure 7.6: BPM Position sensitivity measurement and sensitivity versus bunch charge

Phosphor Screen

Sand-blasted aluminum plates with a few hundred micrograms of terbium activated gadolinium oxysulfate (Gd_2O_2S:Tb) [Osram Sylvania Phosphor type 2611 [121]] bound with barium silicate produced with procedures prescribed by SLAC [122] were manufactured and installed at several locations for beam position and transverse charge distribution measurement. This phosphor, a "very-short" fluorescence time (tenth-

value time 100μs) X-ray sensitive phosphor emitting primarily in the yellow-green, was imaged through a borosilicate vacuum window onto a CCD camera, usually with a 75mm lens with +2 closeup lens added, and an iris setting of f/11 or f/22. With the +2 closeup lens and Cohu 4914 CCD camera, resolutions of 190 Pixels/cm were routine. The five-parameter fits (Gaussian+linear background) require that spot images occupy five pixels minimum to obtain a reasonable fit, implying minimum resolution of $\sigma \approx 80\mu$m. Phosphor "bloom" (enlargement of luminescent area due to material opacity, re-emission, etc.) was not measured to establish its contribution to the measured spot sizes, but examination of the smallest features imaged on the phosphor suggest that blooming is a small effect in comparison to the minimal (geometric) resolution.

Fiducial marks were placed in a variety of ways. Phosphors made by the author had scratches placed 0.50 inch apart in a vertical and horizontal pair. Phosphors made by UCLA had fine wire stretched between precision machined grooved holders 1.00 cm apart in a vertical and horizontal pair, although in practice tensioning the wires sufficiently to make them straight was difficult, with serpentine fiducials typically resulting.

Phosphor linearity, known to be a potential source of measurement error, was never successfully measured. Several attempts to calibrate the entire phosphor-to-CCD camera transport system for linearity with respect to incident bunch charge were all swamped in noise. (In order to minimize charge loss between ICT and phosphor screen, small charges were used). Variations in phosphor concentration were made in an attempt to provoke saturation, with success.

7.3.3 Transverse Bunch Size

Phosphor Screen

Phosphor screens, as described before, were used to provide information about the transverse charge distribution as well as the bunch size. Resolution is estimated at 80μm from geometric considerations, with blooming effects presumed to be negligible by comparison.

7.3.4 Transverse Emittance

Emittance measurements fall, in general, into two categories: methods which sample the parent phase space distribution and allow a drifting of the beam to convert the relevant transverse RMS angular spreads into measurable transverse coordinate spreads, and methods which presume linear optics apply to the entire beam, take spot size information at either three locations or (equivalently) at a single location under three separate focussing conditions, and fit ellipse parameters to the trajectory.

The former method has the advantage that it can be made to work with heavily space charge dominated beams and is inherently a single-shot measurement, making it suitable for a wide variety of applications. The main drawbacks are that the beam is irrevocably damaged, with substantial X-ray production resulting. The technique is usually limited to two decades or so, given the conflicting design constraints that one wants to remove enough charge that the freely propagating beamlets do not suffer appreciable space charge damage over what may be a rather long drift and the desire to clearly resolve the "wings" or highest momentum portions of the distribution, which generally account for most of the emittance. In contrast to the linear optics based techniques, there are a great many circumstances under which the measurement can

significantly underestimate the true emittance, not all of which are readily avoided. Additionally, present-day accelerators produce beams of such high densities that very small slits and pepper pot holes (10 μm) must be produced in fairly thick, dense materials, posing a challenge to modern machining technology.

The quadrupole scan is suitable whenever space charge forces are negligible compared to external focussing or emittance pressure at all points in the transport enclosed by the focussing element(s) and the spot imaging device used for the measurement. Then simple matrix theory applies. The latter method is often subject to an additional constraint, depending on the imaging diagnostic used. If the diagnostic intercepts the beam destructively (as do phosphor screens), then the measurement must be conducted on three separate bunches, requiring the accelerator to have reasonably good shot-to-shot reproducibility for the measurement to be meaningful. If a minimally intercepting imaging diagnostic (an optical transition radiation (OTR) screen) is used, the beam is somewhat degraded, but depending on the emittance resolution desired, may permit simultaneous imaging of the same bunch at three separate locations.

Slit Mask Method

A mask composed of a set of narrow slits is used to sample the parent phase space distribution, resulting in a single-phase-plane measurement of emittance. A sketch of the relevant quantities and geometry is shown in figure 7.7 below.

From the figure, kinematics provides:

$$\sigma_{x,f} = \sigma_{x,i} + \sigma'_{x,i} L + \frac{e}{2mc^2} \int_0^L \int_0^{\xi'} E_x(\xi) d\xi d\xi' \tag{7.2}$$

where evidently the individual slit image widths $\sigma_{x,f}$ directly measure the uncorrelated

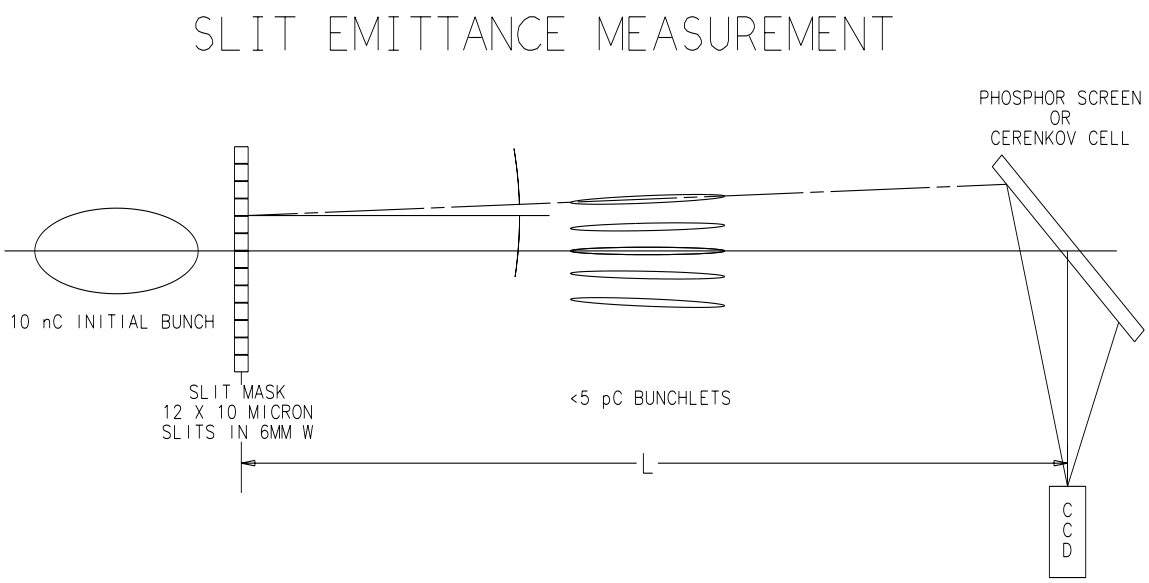

Figure 7.7: Emittance slit geometry and physical quantities

part of the beam emittance, and the spreading of the centroids of the slit images measures the correlated part of the emittance.

Slit scatter and beam pass-through will lower the signal-to-noise ratio at the imaging screen. Estimates of the image contrast ratio were made using a simple Monte Carlo code with ionization and bremßtrahlung the only energy loss mechanisms accounted for. Figure 7.8 below shows the signal and background levels, computed with a Monte Carlo beam/matter interaction code [90], without space charge effects. The case shown is similar to the higher energy ($\gamma = 36$) case from above, but with larger emittance, 43 π mm-mr, and smaller bunch size, $\sigma_x = 3$ mm.

Clearly the background level exceeds the end-most peak on either side, but as it is almost strictly uniform, may be easily subtracted, allowing the highest of the end peaks to be resolved. The separated traces in the Monte Carlo simulation (left) represent particles that scattered exactly zero times, and particles that scattered one

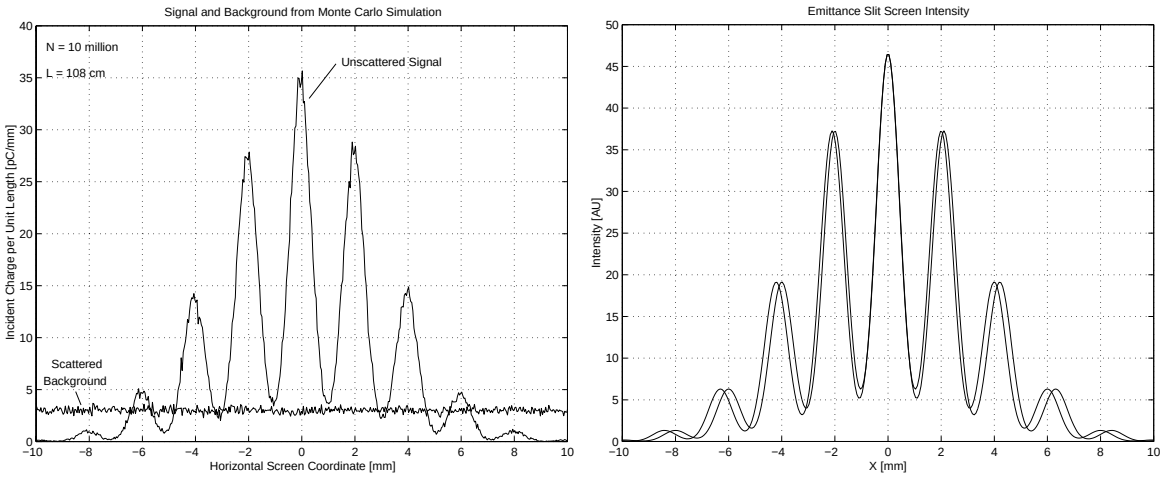

Figure 7.8: Signal and background on emittance slit phosphor screen, from Monte Carlo (left) and envelope (right) calculations.

or more times. The scattered particles do not contribute anything more than a nearly uniform background, and hence no slit scatter correction is needed. That the Monte Carlo and simple-minded envelope integration (right) are in good agreement validates the approximation in equation (7.2).

A pessimistic, simple estimate of the space charge contribution to the measured spot size results from assuming that the charge distribution is unmodified during the drift from the mask to the screen. The beamlets produced are generally extremely thin in the slit width direction, and large in the longitudinal direction by comparison, suggesting that the fields are reasonably approximated by those of an infinite sheet: $E_x \approx \Sigma_i / 2\epsilon_0$ where Σ_i is the surface charge density of the i^{th} beamlet. Plots of the calculated space-charge washout for 10 μm wide and 35 μm wide slits are shown in figure 7.9 below. Lapostolle's expressions [123] for the space charge fields of a uniformly charged ellipsoid have been used for these calculations. Clearly the wider (35μ) slits have significantly more space charge broadening (approaching 20%) than

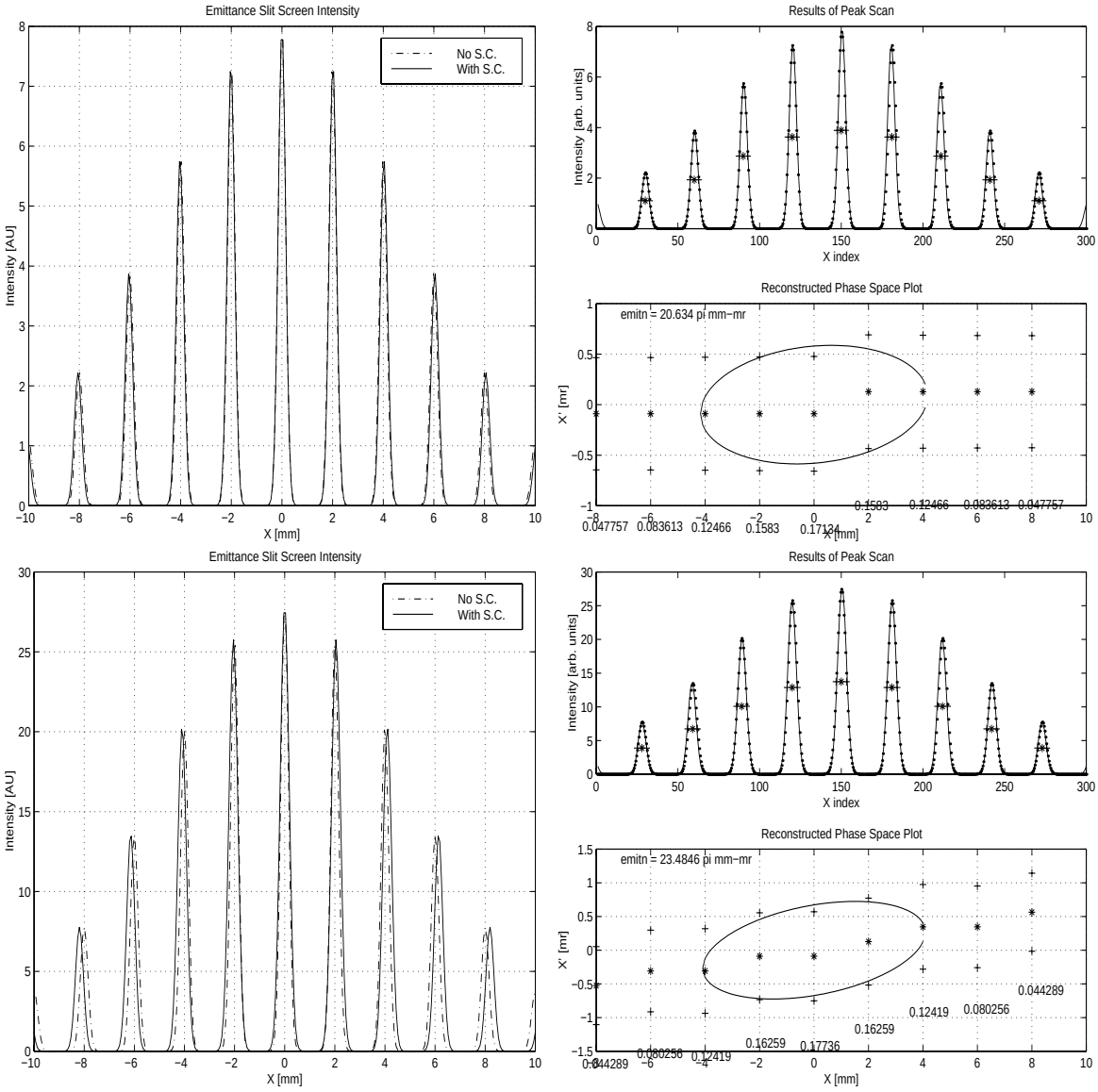

Figure 7.9: Screen intensity distribution and calculated emittance for 3.88 MeV, 20 π mm-mr normalized emittance beam incident on 10μ and 35μ slits, with 30.6 cm drift.

do the 10μ slits, at 3%. Image calculations repeated for the higher energy emittance measurements are shown in figure 7.10 below, with smaller spot size ($\sigma_x = 3$ mm).

The influence of space charge on the measurement has diminished from the 4-fold

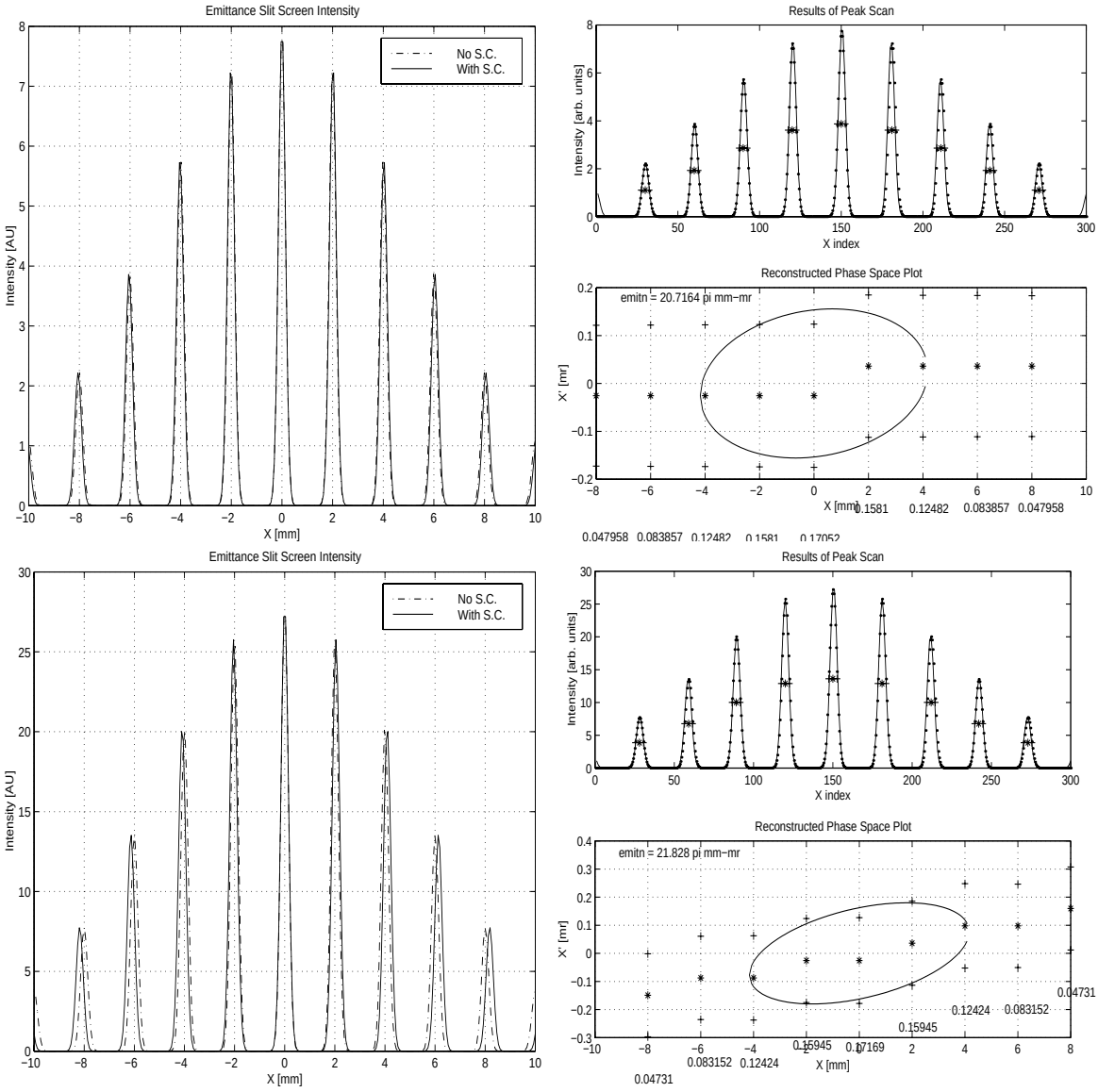

Figure 7.10: Screen intensity distributions for 16.0 MeV, 20 π mm-mr normalized emittance beam incident on 10 and 35 μ slits, with 108.0 cm drift.

increase in beam energy, despite the 3-fold increase in mask-to-screen drift distance.

Emittance calculation from the screen image is accomplished by straightforward

weighted averaging of the deduced quantities:

$$\varepsilon_{x,N} = \gamma\beta\sqrt{(\langle x^2\rangle\langle x'^2\rangle - \langle xx'\rangle)} \tag{7.3}$$

where I_i , σ_i and μ_i are the peak intensity, RMS width, and mean of the i^{th} Gaussian, respectively.

Construction of 10 μm wide slits is challenging, and was accomplished by EDM (electron discharge machining) burning 10 μ depressions into tungsten bars, and stacking the bars to form the slit grating. Microscopic examination of the slits was performed to check slit width and uniformity, and to check that the surface roughness did not lead to slit occlusion. Figure 7.11 below shows a combination transmission/reflection light photomicrograph of one slit. The dotted lines are separated by .0008" or approximately 20 μ for scale. Surface roughness was substantial in places, with craters and protrusions equal to the width of the slit occurring infrequently. The slits were, after substantial inspection, found to be largely unoccluded by machining features.

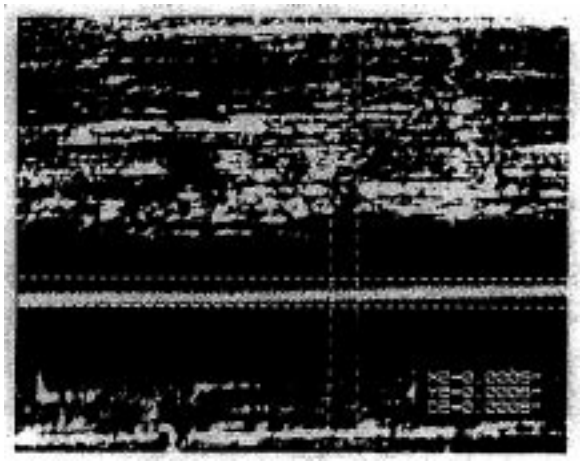

Figure 7.11: Transmission/reflection photomicrograph of a single emittance slit.

The 2 mm spacing of the slits, taken together with the drift distance to the

imaging screen, will set the largest emittance that can be resolved. A condition similar to Rayleigh's Criterion is adopted: the maxima on the imaging screen must be separated by at least three times the variance of the distribution. For a slit separation s and drift distance L, this implies a maximum resolvable emittance of:

$$\varepsilon_{N,x}^{max} = \sigma_x \sigma_x' = \sigma_x \frac{s}{3L} \beta\gamma \tag{7.4}$$

Pepper Pot Mask Method

Although analogous to the emittance slit in basic aspects, the pepper pot [124, 125] enjoys two distinct advantages. As the beam is reduced to tiny dimensions in both transverse coordinates, not just one, the problems of space charge washout are lessened. Since the mask is non-degenerate in both coordinates, information about both phase planes is available simultaneously. In fact, for intelligent choices of hole pattern, information about the entire four-dimensional transverse phase volume, correlations included, is available.

As often happens, the availability of much more information comes at the cost of increased calculational complexity. The calculation proceeds analogously, but with the added bookkeeping of an additional dimension.

For typical charge distributions, each pepper pot hole will produce an elliptic spot on the downstream screen with a bi-Gaussian intensity distribution. The intensity due to the hole in the i^{th} row and j^{th} column is:

$$I_{i,j}(x,y) = (I_o)_{i,j} exp(-\frac{(x-x_o)^2}{2\sigma_x^2}) exp(-\frac{(y-y_o)^2}{2\sigma_y^2}) exp(-\frac{(x-x_o)(y-y_o)}{2\sigma_{xy}^2}) \tag{7.5}$$

A suitable two-dimensional six parameter least-squares fit will produce the first three moments of the distribution, from which the emittance of the original beam

many be deduced. The relation between the screen intensity parameters and the original distribution is readily found by some straightforward if lengthy algebra.

The single particle equations of motion after the pepper pot may be written:

$$x_f = x_o + x'_o L + \frac{1}{2}\frac{e(E_x^i + E_x^a)}{m_e}\left(\frac{L}{c}\right)^2 \tag{7.6}$$

$$y_f = y_o + y'_o L + \frac{1}{2}\frac{e(E_y^i + E_y^a)}{m_e}\left(\frac{L}{c}\right)^2 \tag{7.7}$$

where L is the drift distance between pepper pot and screen, and the space charge forces have been separated into an internal component (E_q^i) (due to particles passing through the same hole in the pepper pot) and an aggregate component (E_q^a) (due to all particles passing through all holes in the pepper pot). The reason for this separation is that the internal component will enlarge the measured spot sizes on the phosphor screen, while the aggregate component will displace the hole image centroids, resulting in an increase in the phase space area and curvature, respectively. The space charge fields appearing in equations (7.7) and (7.7) should be the average applied fields during the beamlet's flight from pepper pot to screen. For a properly designed pepper pot, these fields are small and approximately constant in time, an approximation that will be used from here on.

Taking the required moments of (7.7) and (7.7) yields ($C \equiv \frac{1}{2}\frac{e}{m_e}\left(\frac{L}{c}\right)^2$):

$$\langle x\rangle_f = \langle x\rangle_o + \langle x'\rangle_o L + C\langle E_x^i\rangle + C\langle E_x^a\rangle \tag{7.8}$$

$$\langle y\rangle_f = \langle y\rangle_o + \langle y'\rangle_o L + C\langle E_y^i\rangle + C\langle E_x^a\rangle \tag{7.9}$$

$$\begin{aligned}\langle x^2\rangle_f &= \langle x^2\rangle_o + L^2\langle x'^2\rangle_o + 2L\langle xx'\rangle_o + +2C\langle xE_x^i\rangle + 2C\langle xE_x^a\rangle + 2C\langle x'E_x^i\rangle \\ &+ 2C\langle x'E_x^a\rangle + C^2\langle (E_x^i)^2\rangle + C^2\langle (E_x^a)^2\rangle + 2C^2\langle E_x^a E_x^i\rangle\end{aligned} \tag{7.10}$$

$$\begin{aligned}\langle y^2\rangle_f &= \langle y^2\rangle_o + L^2\langle y'^2\rangle_o + 2L\langle yy'\rangle_o + +2C\langle yE_y^i\rangle + 2C\langle yE_y^a\rangle + 2C\langle y'E_y^i\rangle \\ &+ 2C\langle y'E_y^a\rangle + C^2\langle (E_y^i)^2\rangle + C^2\langle (E_y^a)^2\rangle + 2C^2\langle E_y^a E_y^i\rangle \qquad (7.11)\\ \langle xy\rangle_f &= \langle xy\rangle_o + L\langle xy'\rangle + L\langle yx'\rangle + L^2\langle xy\rangle + +C\langle xE_y^i\rangle + C\langle xE_y^a\rangle \\ &+ C\langle x'E_y^i\rangle + C\langle x'E_y^a\rangle + C\langle yE_x^i\rangle + C\langle yE_x^a\rangle + C\langle y'E_x^i\rangle + C\langle y'E_x^a\rangle \\ &+ C^2\langle E_x^i E_y^i\rangle + C^2\langle E_x^i E_y^a\rangle + C^2\langle E_x^a E_y^i\rangle + C^2\langle E_x^a E_y^a\rangle \qquad (7.12)\end{aligned}$$

Approximation of the beam frame internal field as that of an infinite rod of charge are completely reasonable as $A \equiv \sigma_r/\sigma_z \ll 1$:

$$E_x^i(x) = \frac{q_n}{2\pi r_o^2 4\sigma_z\gamma\epsilon_o}(\langle x\rangle - x) = k_i(\langle x\rangle - x) \qquad (7.13)$$

$$E_y^i(y) = \frac{q_n}{2\pi r_o^2 4\sigma_z\gamma\epsilon_o}(\langle y\rangle - y) = k_i(\langle y\rangle - y) \qquad (7.14)$$

where q_n is the individual beamlet charge, r_o is the pepper pot hole radius, σ_z is the lab frame bunch length. Approximation of the aggregate field as that of an infinite rod of charge is reasonable for $\gamma \gg 1$:

$$E_x^a(x) = \frac{Q_p}{2\pi\sigma_r^2 4\sigma_z\gamma\epsilon_o}x = k_a x \qquad (7.15)$$

$$E_y^a(y) = \frac{Q_p}{2\pi\sigma_r^2 4\sigma_z\gamma\epsilon_o}y = k_a y \qquad (7.16)$$

where $Q_p = \sum_n q_n$ is the total charge in all the beamlets, and σ_r is the full beam RMS radius. The internal and aggregate space charge forces will give rise to beamlet expansion and divergence, respectively, which in turn will lower the applied field strengths, as well as the rate of expansion. For the calculations here, the beam expansion will be neglected, the electric fields will be assumed constant and equal to their initial value at the pepper pot mask, resulting in an overestimate of the effects due to space charge.

If the pepper pot holes are approximated as squares of dimension $x_o = 2\sqrt{\pi}r_o$ and the usual paraxial beam condition (beam is focussed onto the pepper pot) holds, then the moments in (7.12) are easily found. Table 7.4 below enumerates the moments.

	x	x'	E_x^i	E_x^a	y	y'	E_y^i	E_y^a
1	μ_x	$\mu_{x'}$	0	$k_a\mu_x$	μ_y	$\mu_{y'}$	0	$k_a\mu_y$
x	$\mu_x^2 + \frac{x_o^2}{3}$	0	$\frac{x_o^2}{3}$	$k_a(\mu_x^2 + \frac{x_o^2}{3})$	$\mu_x\mu_y$	0	0	$k_a\mu_x\mu_y$
x'		$\sigma_{x'}^2$	0	0	0	0	0	0
E_x^i			$k_i^2\frac{x_o^2}{3}$	$k_ik_a\frac{x_o^2}{3}$	0	0	0	0
E_x^a				$k_a^2(\mu_x^2 + \frac{x_o^2}{3})$	$k_a\mu_x\mu_y$	0	0	$k_a^2\mu_x\mu_y$
y					$\mu_y^2 + \frac{x_o^2}{3}$	0	$k_i\frac{x_o^2}{3}$	$k_ik_a\frac{x_o^2}{3}$
y'						$\sigma_{y'}^2$	0	0
E_y^i							$k_i^2\frac{x_o^2}{3}$	$k_ik_a\frac{x_o^2}{3}$
E_y^a								$k_a^2(\mu_y^2 + \frac{x_o^2}{3})$

Table 7.4: First and Second Moments for pepper pot beamlets with linear space charge forces.

Substitution into (7.9)-(7.12) yields the required relation between the initial and final moments, including the linear effects of residual space charge:

$$\langle x\rangle_f = \mu_x(1+Ck_a) + \mu_{x'}L \tag{7.17}$$

$$\langle y\rangle_f = \mu_y(1+Ck_a) + \mu_{x'}L \tag{7.18}$$

$$\begin{aligned}\langle x^2\rangle_f &= \mu_x^2 + \frac{x_o^2}{3} + \sigma_{x'}^2 L \\ &+ \mu_x^2(Ck_a(2+Ck_a)) + \frac{x_o^2}{3}(C(2(k_i+k_a) + C(k_i+k_a)^2))\end{aligned} \tag{7.19}$$

$$\begin{aligned}\langle y^2\rangle_f &= \mu_y^2 + \frac{x_o^2}{3} + \sigma_{y'}^2 L \\ &+ \mu_y^2(Ck_a(2+Ck_a)) + \frac{x_o^2}{3}(C(2(k_i+k_a) + C(k_i+k_a)^2))\end{aligned} \tag{7.20}$$

$$\langle xy\rangle_f = \sigma_{x'y'}^2 L + \mu_x\mu_y(1 + Ck_a(2+Ck_a)) \tag{7.21}$$

Setting the perveances $k_a = k_i = 0$ in the above expressions recovers the more

usual space charge free case. From these expressions it is apparent that the space charge contribution enters more rapidly into both the correlated and uncorrelated portions of the emittance $\propto Ck + C^2k^2 \propto L^2r_o^2 + L^4r_o^4$ than was the case for the slits, $\propto L^2x_o$. The reason is that the fields of the "infinite" sheets produced by the slits are constant in two coordinates, and correlated only in the third coordinate, and hence the second moments of the E_q^i are largely trivial. Here the fields are functions of the coordinates, and the correlative moments of the fields contribute additional powers of the beamlet charge and drift length. Like the slits, the drift distance and hole size are key parameters in the design of the pepper pot.

Quadrupole Scan Method

The quadrupole scan is one variant from a family of equivalent multi-point measurement methods. The three Courant-Snyder parameters, or, equivalently, the three linearly independent members of the 2×2 sigma matrix may be obtained experimentally by observing the beam spot size at three separate locations in a lattice with known optical properties. Typically, three screens are placed in amongst quadrupoles and drift spaces, and the spot observed on each screen for a constant setting of the quadrupole fields. As the pseudo-harmonic motion of the beam has a phase advance which depends both on the distance coordinate s and the focal strength $\kappa(s)$, one may effectively duplicate the three screen measurement with a single, fixed screen by choosing three different values of the focussing channel strength, and hence the phase advance $\Psi(s)$. This variant is referred to as a "quadrupole scan", and has the advantage of requiring only one screen, and has the additional advantage that the *only* property changed from one point of the three point method to the next is the

quadrupole field strength. The three screen method requires the beam to propagate through two additional sections of beamline which may bring different wakefield effects or different quadrupole field harmonic content that will complicate the measurement.

Linear matrix transport theory from the quad to the measuring screen yields the final beam sigma matrix:

$$\Sigma_f = R\Sigma_o R^T = \begin{bmatrix} 1 & 0 \\ -\frac{1}{f} & 1 \end{bmatrix} \times \begin{bmatrix} 1 & L \\ 0 & 1 \end{bmatrix} \times \begin{bmatrix} \sigma_{11,o} & \sigma_{12,o} \\ \sigma_{21,o} & \sigma_{22,o} \end{bmatrix} \times \begin{bmatrix} 1 & 0 \\ L & 1 \end{bmatrix} \times \begin{bmatrix} 1 & -\frac{1}{f} \\ 0 & 1 \end{bmatrix} \Bigg] \tag{7.22}$$

from which the equation relating the final measured spot sizes $\sigma_{11,f}$ to the quadrupole settings may be found:

$$r_f = \sqrt{\sigma_{11,f}(k)} = \sqrt{\sigma_{11,o} + (2\sigma_{11,o}L + 2\sigma_{12,o})k + (2\sigma_{12,o}L + \sigma_{11,o}L^2 + \sigma_{22,o})k^2} \tag{7.23}$$

where $k \equiv -\frac{1}{f}$. Equation [7.23] is the equation of a hyperbola. Generally, a series of measurements of the spot size $r_f = \sqrt{\sigma_{11,f}}$ as a function of the quadrupole focal length is taken, a fit to a function of the same form as equation 7.23 is performed, with identification of the coefficients yielding the Courant Snyder parameters, and hence the beam geometrical emittance.

The exclusion of space charge, wakefield, thick-lens, chromatic and geometric aberration effects from [7.23] requires that a careful assessment of each effect be made prior to using a quad scan or three-point method to evaluate the emittance of a beam. For the TTF Injector, space charge effects alone will be enough to disqualify this method for emittance determination.

7.3.5 Longitudinal Measurements

Streak Camera

The streak camera is a device useful for measuring the spatio-temporal profile of photon pulses with resolutions in the sub-picosecond regime. Photons pass through a (e.g. horizontal) slit, reducing the photon packet to a two-dimensional sheet. Photons reaching the underlying photocathode produce electrons which are accelerated to energies of a few hundred electron-Volts, and are then passed through an electric deflector. A series of avalanche transistors rapidly switch on, charging the plates of the deflector to $\pm 1kV$ or so while the bunch is in transit between the plates, giving a time-dependent transverse kick to the particles. The bunch, now rotating in the (y,t) plane, strikes a microchannel plate to amplify the signal by $\sim 10^4$, then strikes a phosphor which is subsequently readout by a CCD (charge coupled device) camera and digitized. Resolutions of modern streak cameras reach into the low hundreds of femtoseconds, corresponding to minimum bunch lengths on the order of 100 μm.

Photon sensitivities are generally excellent, with signals of 10^4 photons per pulse being reasonably resolvable. As a result, care must be taken to shield the camera from stray light during measurement and to protect the camera from exposure to much higher intensity light, such as ordinary fluorescent light. The photocathode material prescribes the range of frequencies the camera is sensitive to, with materials available from the near-infrared well into the x-ray region.

Streak cameras may be used with so-called "prompt radiators", which have characteristic light output response times shorter than the electron bunch itself, to give information about the longitudinal profile. Optical transition, Čerenkov , and synchrotron radiation are all [126] suitable for this purpose. Transition radiation is a

surface effect, and therefore produces less light than bulk effects. Edge-effect derived synchrotron radiation produced in the fringe fields of dipoles is generally preferred for its directivity and shorter wavelength spectra, but arises only in the fringe field, and again can suffer poor efficiency. Bulk synchrotron radiation (generated continuously in the bending field of dipoles, for example) generally has broad angular distribution, owing to the tangentially swept source generating it. Čerenkov radiation has the dual advantage of being a bulk effect with good directivity, with a proper choice of media.

Care must be taken in orienting and enclosing the radiator to avoid multi-path reflections which will severely impact the bunch length resolution. For Čerenkov radiators, the solution is to orient the exit face of the radiator so that the radiation exits the surface at Brewster's angle, defined by $\theta_B = \arctan(n_c/n_o)$ where n_c is the index of refraction of the Čerenkov radiator, $n_o = 1$ is that of vacuum.

In general, the streak camera is mounted some substantial distance (~ 10 m) away to prevent radiation damage to the streak tube, and to permit easy modification of final optics and camera gain settings while data is being taken. Consequently, care must also be taken in transporting the photons to avoid dispersive effects which would also broaden the photon pulse. Bandpass filters are the easiest solution when statistics permit. Achromatic optics are the preferred solution when they do not.

Three sources of prompt radiation were considered for bunch profile measurements. Coherent synchrotron radiation (CSR) produced in the final dipole of the pulse compressing chicane was initially thought significant [127], and provisions were made in the chicane vacuum chamber (see figure 3.8) to allow extraction of the CSR. Subsequent evaluation of the output intensity [126, 128] showed low output power for 8 nC bunches, as seen in figure 7.12 below.

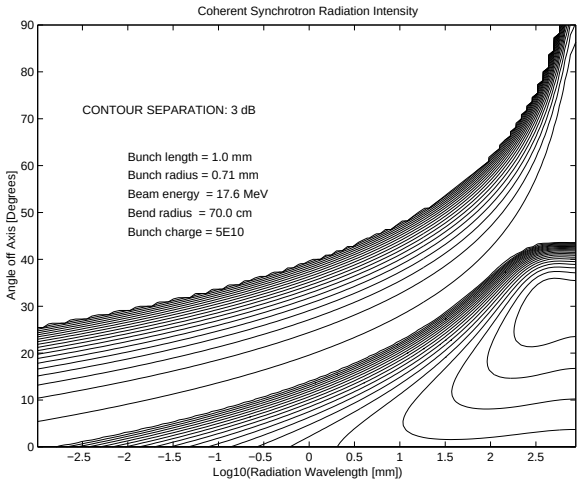

Figure 7.12: Coherent (bottom right) and incoherent (upper family of curves with high angular divergence) differential synchrotron radiation intensities from the final compressor dipole.

Two sets of contours are distinctly visible, with the angularly localized peak at center right being the coherent portion of the SR spectrum. Since CSR arises from the radial acceleration of the bunch space charge fields, it is not surprising that the spectrum peaks at the bunch length, with components only extending to longer wavelengths. Total emitted energies are approximately 3.3×10^7 eV (coherent) and 3.1×10^{-3} eV (incoherent). Given that emission is in the microwave region, CSR is unsuitable for profile measurements with a streak camera. A microwave spectrometer, however, would permit determination of the power spectra of the bunch, which, together with an assumed functional form for the bunch profile, could be "inverted" to produce the profile [128], with direct Fourier inversion being impossible without phase information.

Optical transition radiation (OTR) was also considered for bunch length measurements. An optical pellicle (aluminized mylar mounted in a frame) was mounted

at 45^o to the electron beam and radiation exit window in a 6-way cross (cross 4), and observed by a Cohu CCD camera. The beam energy at the pellicle location was 16.5 MeV, giving a transition radiation cone opening angle of $\theta_{OTR} \approx 1/\gamma \approx 1.7^o$, within which roughly 20 % of the photons were emitted. With such a narrow outgoing cone of photons, the geometric acceptance of the exit window and camera were excellent. On examination of the camera image, however, no signal was observed. This is due both to poor photon count and to an unintelligent choice of optics. I opted for spatial resolution over photon sensitivity, spreading the signal over as many pixels as possible. Owing to the short time allocated for examining OTR as a possible radiation source, no further trials (e.g. with wide angle lenses) were made.

Čerenkov radiation was expected to be the best source for profile measurements, and indeed was. Two candidate materials were considered, (1) the traditional choice for solid Čerenkov radiators, quartz, with $n = 1.45 - 1.53$ over the visible Čerenkov spectrum, and (2) a novel material suggested and implemented by Rosenzweig, aerojel (a tenuous form of SiO_2), with $n = 1.009$. With an index of refraction near unity (and tunable at the time of fabrication), the aerojel emits Čerenkov radiation in a narrow cone of only 7.7^o, versus over 50^o for quartz. With the much improved photon bunch emittance, it is possible to get many more photons through a limited acceptance transport system. The disadvantage of aerojel is mechanical, with the remarkable porosity and fragility of the material making it unsuitable for vacuum applications. Thus a vacuum enclosure had to be made to protect the aerojel. A thin aluminum window on the upstream side and a thin quartz window on the downstream side allowed for the passage of electrons, and electrons+photons, respectively. The Čerenkov radiation from the quartz window, being much more divergent than that of

the aerojel, was rapidly lost in the photon transport system.

The Čerenkov emission spectrum is fairly broad, being given by [129]:

$$\frac{d^2N}{dEdx} = \frac{\alpha}{\hbar c}\sin^2\theta_{\check{c}}\left(1-\frac{1}{\beta^2 n(E)^2}\right) \tag{7.24}$$

$$\approx 370\sin^2\theta_{\check{c}}(E)\mathrm{eV}^{-1}\ \mathrm{cm}^{-1} \tag{7.25}$$

for electrons. For electrons in 3 mm of aerojel, the photon production efficiency is nearly unity, giving excellent light output. As the index of refraction for both quartz and of aerojel is fairly constant up into the UV, so is the emission spectrum. In practice the vacuum window (in this case 7056 Borosilicate glass) will provide the cutoff on the higher frequency components. As the emissions are broadband, care must be taken to minimize dispersion in the transport optics to prevent temporal broadening of the pulse. Achromatic lenses and optical bandpass filtering are two techniques for controlling the dispersive contributions to the temporal resolution. Figure 7.13 below shows the anticipated photon output spectra, with the transfer function of the vacuum window and the response function of a CCD camera folded in.

Light output was found to be remarkably good, with Čerenkov light plainly visible to the eye through the $\sim$ 15 m system of a lens and 5 mirrors. For the profile measurements shown in the Analysis chapter, the transverse coordinate information at the streak camera was integrated to increase the statistics. Figure 7.14 below shows a schematic of the Čerenkov radiator with descriptive variables.

For the radiator chosen, the light output from a Gaussian charge distribution of negligible transverse dimensions will have the temporal behavior:

$$I(t) = I_o\sum_{k=0}^{\infty}(1-\mathcal{R})\mathcal{R}^{2k}(\exp-(t-t_o)^2/(2*(\sigma_z/c)^2)) \tag{7.26}$$

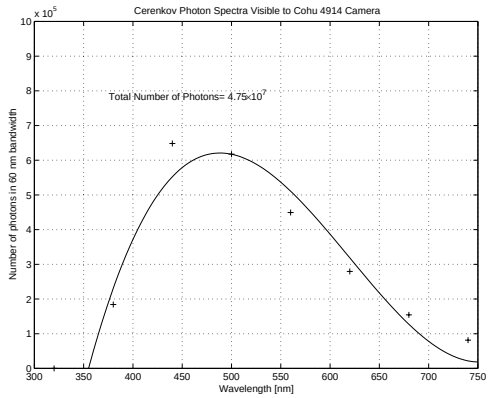

Figure 7.13: Cerenkov light output from 8 nC, 16.5 MeV electron bunch in 3 mm thick aerojel radiator.

where I_o is the peak Čerenkov light intensity, $\mathcal{R}$ is the reflection coefficient at the radiator/vacuum boundary, k is the order of the reflection, σ_z is the electron bunch length, and n is the index of refraction of the Čerenkov radiator. As the Čerenkov radiator is comparable in thickness to the electron bunch length, the successive Gaussian pulses represented by (7.26) will stack up, compromising the temporal resolution. It is therefore important to minimize $\mathcal{R}$ by choosing a radiator orientation and exit plane geometry that ensures that the radiation escapes at the Brewster angle, defined by $\tan(\theta_B) = n_{\check{c}}$.

Spectrometer

A $\theta_b = 62^o$ wedge dipole magnet was used to provide momentum dispersion for energy measurements. A vacuum chamber with a 1/16" thick aluminum exit window, followed immediately by a phosphor screen, was used to measure the beam energy. Bending radii of the order $\rho \sim 10$cm were possible with the vacuum chamber geometry show in figure 8.1. For a sector magnet with a phosphor screen parallel to the exit pole

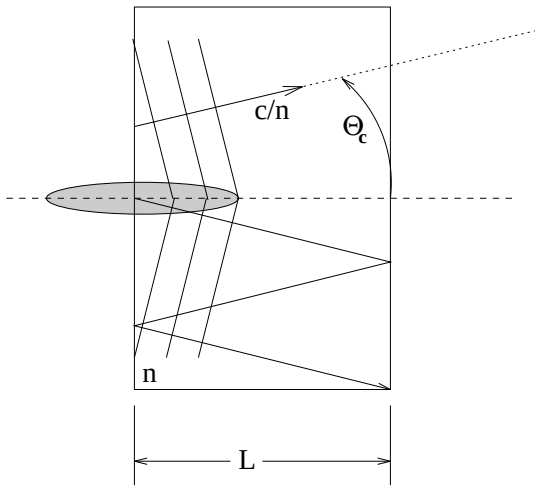

Figure 7.14: Čerenkov radiator geometry.

face a drift distance d_s away, relativistic orbits close to the design orbit ($\theta_{e,1} = \theta_{e,2} = 0$ Degrees) will shift an amount:

$$\eta_x/E \approx \frac{dx_f}{dE} = \frac{d\rho}{dE} \approx \frac{1}{ecB_y} \approx 7.5\text{mm MeV}^{-1} \text{ at } B_y = 4424 \text{ G} \tag{7.27}$$

The actual screen was not parallel to the exit pole face, rather it was placed approximately along the locus of horizontal foci for optimal resolution. The tilted phosphor screen and extremely wide energy viewing range (roughly ±40%) require much more careful treatment of the geometry to extract the position/energy calibration, and was done by computer program.

Calibration of the spectrometer was done using measured field and survey data by a simple ray-tracing program written for the purpose in Matlab. Physical data (position and orientation of magnet edges, location of phosphor screen) were taken from a photographic enlargement of the apparatus, scanned at high resolution (1200 dpi). Magnetic data were taken from an F. W. Bell hall probe, with a stated accuracy of ±3%. Figure 7.15 below shows representative particle orbits for zero-space-charge

beams in relation to the phosphor screen. A derived energy versus position curve is shown at right. Space charge effects will clearly affect the energy spread measurements, but not the mean energy measurements. Given a magnet/screen location accuracies of $\pm 2^o$,± 0.5 mm, and B-field measurement accuracy of $\pm 3\%$, and the imaging system used, the expected zero-space-charge energy resolution is 200 keV.

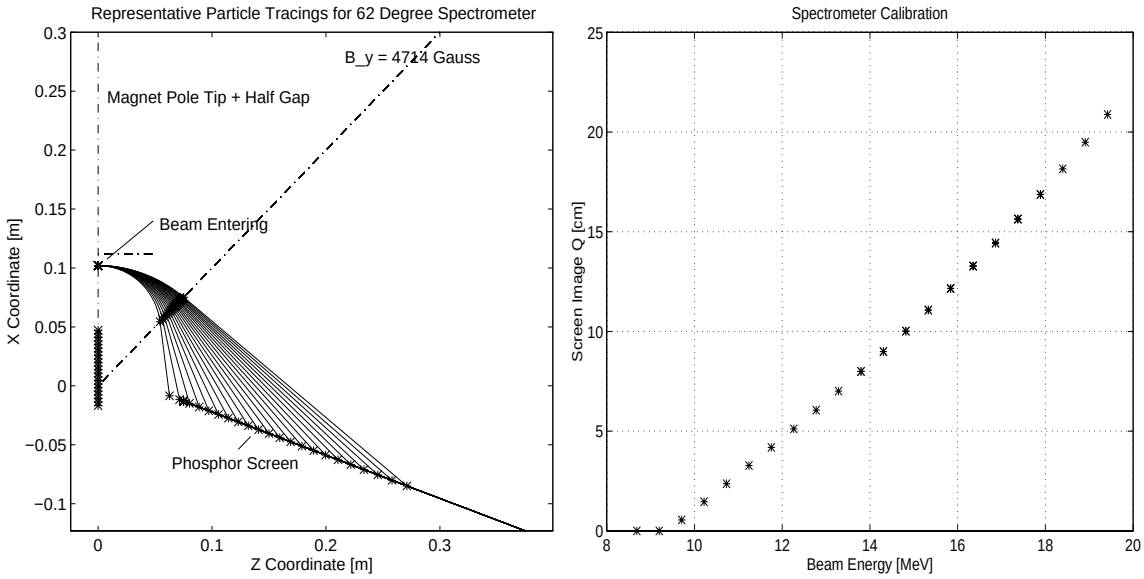

Figure 7.15: Spectrometer particle orbits and resultant calibration of the phosphor screen

The aluminum window contributes an energy loss dependent on the energy, with particles below about 1.5 MeV ranging out in the window itself, as shown in figure 7.16 below.

Thought was given to using the compressor dipoles for energy measurements, but the dispersion possible within the compressor vacuum chamber provides for only rather poor resolution, and would make impossible energy spread measurements on the compressed beam.

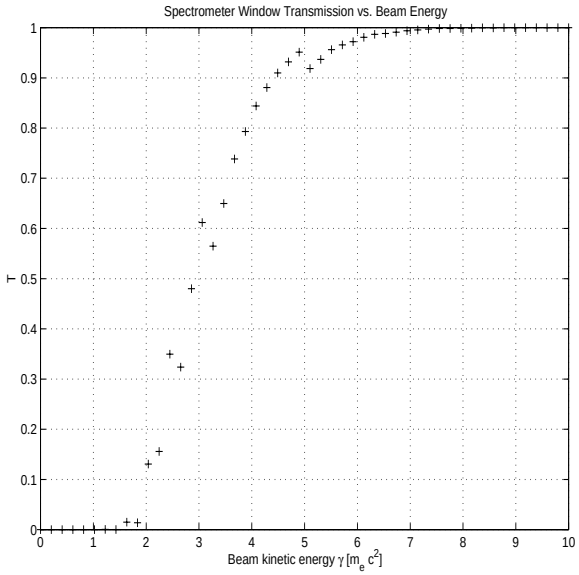

Figure 7.16: Spectrometer window transmission versus energy.

Longitudinal "Compressor Scan" Emittance Measurement

The longitudinal "compressor" scan is conceptually analogous to the transverse quadrupole scan. Three or more measurements of the bunch length are made for several settings of the chicane temporal compression ratio r_c, and a set of Courant-Snyder parameters are fit to the data, yielding the emittance as well as the correlation and beta functions.

Like the quadrupole scan, however, interpretation of the measurement relies on linear matrix transport without space charge or wakefield forces, and thus these effects must be small for the interpretation to be valid. As with the quadrupole scan, at 10 nC bunch charges the space charge effects are strong enough to disqualify this technique for measuring the longitudinal phase space.

7.3.6 Other Diagnostics

Characterization of the solenoid field quality, magnet hysteresis, alignment of the beamline components, and miscellaneous cooling issues are addressed in the sections which follow.

Beamline Alignment

Beamline geometric alignment was accomplished with the aid of a theodolite and a precision sight level. Fiducial marks defining a horizontal plane at the beamline height and a vertical plane offset from the beamline were attached to the shielding walls. Offsets were calculated from the beamline drawing from the vertical reference plane to external contact points (generally points of tangency on vacuum flanges), and measured by sighting a leveled ruler with the theodolite. Accuracy is estimated at better than 1/32" ($\approx$ 1 mm) for transverse offsets. Leveling of the structure was accomplished by computing offsets to contact points (again on flanges, generally), and measuring the vertical offsets with a precision optical level.

Greater alignment accuracy (than 1 mm) was required for the magnet centers, and was accomplished by one of two means. For the gun solenoids, decomposition of $B_r(\theta)$, with the radius r measured from the beam centerline was used to measure the dipole component of the solenoid field resulting from misalignment. For the quadrupoles, beam-based alignment was necessary, with the feed-down dipole strength again providing information about the displacement. For the chicane magnets, relative alignment of the dipoles (most importantly, the longitudinal separations) was accomplished with a pair of vernier calipers, measuring from the pole tip iron itself, to guarantee parallelism and accurate separation distances, with the separation

of the first and final pairs of dipoles being most important. Irregularities in the paint applied to the magnet pole tips guaranteed that the accuracy was at best a few mils. Remaining errors in the alignment were compensated for by small corrections in the magnet drive currents.

For gun solenoid alignment, a simple aluminum fixture was made that tightly grasped the edge of a standard ConFlat vacuum flange that could accommodate a hall probe. Although not the ideal fiducial, the vacuum flanges were easily within a few thousandths of the beam centerline owing to the natural concentricity of the RF cavity, beamtube, and subsequent flange enforced by lathe machining. The far greater concern in using the flanges as fiducials arises from their somewhat less accurate longitudinal positioning, which is subject to the vagaries of the welding and braze processes used to join the flange to the beamtube, and the beamtube to the gun body, respectively. As the gun solenoids are short, B_r has a strong dependence on the longitudinal coordinate as well. If the flange was tilted but otherwise centered within the solenoid, a false dipole component would result, owing to the longitudinal probe excursions produced by the tilted flange.

The spectrometer was eye-balled into position, with after-the-fact survey data and ray tracing producing the needed corrections.

In addition, four horizontal and vertical combination steerers were mounted on the beam line to allow additional adjustment of the beam to suit the idiosyncrasies of the installation.

Magnet Multipole and Hysteresis Measurements

Owing to their high field strength, large integral $\vec{B} \cdot \vec{dl}$, and position at a sensitive point in the beamline, the gun primary solenoids were examined for multipole content. Penetrations through the back leg of the iron yoke must be made to pass the conductor out of the core. An additional opening was cut in the yoke opposite the conductor penetration to increase the order of the lowest multipole component from dipole to quadrupole. As a result, a moderate quadrupole component was expected. Significant shimming errors (in particular, radial dislocation of the conductors within the iron yoke) could also be expected to produce a dipole field component, particularly as the yoke is driven into saturation.

For these measurements, three linear stepping stages in an XYZ configuration were bolted together, and a hall probe mounted on a fixture attached to the assembly. Given the degrees of freedom of the apparatus, the hall probe measured $B_x = B_r \cos(\theta)$. The probe was revolved twenty times at approximately half the inner radius of the solenoid (chosen as a compromise between resolution and avoidance of local field inhomogeneities close to the conductors and yoke), and the analog output of a Bell 615 Gaussmeter was fed into an HP54512B scope, which subsequently performed the necessary FFT, revealing the field multipole content at a glance. It was with this apparatus that the final shimming of the coil within the yoke was done.

Magnet hysteresis was also studied, with specific magnetization curves being recorded for the chicane dipoles. Despite being made by a single shop, the magnetization curves for the four dipoles were quite different and had to be compensated for by careful trimming of the magnet currents. Hysteresis studies were performed with a Bell 610 Gaussmeter using a LabView VI designed for the purpose. Hystere-

sis and residual magnetization were substantial effects for the quadrupoles, chicane dipoles, and spectrometer, and required careful de-Gaussing and magnet standardization procedures to be followed to ensure repeatable field strength setting. The small trim dipoles contained little iron, were low field, and were always set by direct beam observation rather than dead reckoning, and thus were never studied for hysteresis effects.

Water Cooling Assessment

Deflection of the central aperture cooling channel under pressurization was tested using a Giddings & Lewis coordinate measuring machine with a special laser-triangulation head[1] capable, in principle, of 0.2μm resolution. The channel was pressurized with nitrogen to 120 psig while the laser head observed the surface height. A deflection of $\leq 2\mu$m was expected from a back of the envelope estimate, and was measured in 7 observations to be $2.3 \pm 0.1\mu$m. This measurement confirmed the expectation that the static frequency detuning of the gun would be negligible.

More problematic was the dynamic detuning issue. The noise generated by water turbulence within the cooling channel can drive mechanical resonances of the annular "drumhead" formed by the cooling channel cover plate. Subsequent operation of the gun at approximately 60 gpm flow rates (approximately $6 - 7$ gpm through the aperture water channel) has shown no observable detuning during RF pulses as long as $400\mu s$.

Temperature stability of the gun and linac temperature control systems was tested by RF measurement of the resonant frequency, and found to be acceptable, provided that sufficient equilibration time (generally a half hour) was allotted after adjust-

[1]CORDAX 1808-MZ DCC MEA, LC0222 laser readout head, Keyence LC-2100 controller

ments. Owing to the fairly low flow rates supplied by the two commercial chillers used to temperature control the gun and linac, changes in repetition rate (hence duty factor) resulted in slight changes in temperature, requiring some fine temperature set-point adjustment to compensate.

The considerably more mundane issue of whether cooling for the spectrometer magnet was adequate (at fields of 5 kG required for 17 MeV measurements, the dissipated power was 1.5 kW) was addressed by a simple flow rate measurement.

Chapter 8

Design of the Prototype Test Experiment

As Phase I, the prototype test phase is charged with understanding the beam dynamics, and with verifying the calculated performance for the single bunch case. Testing of long-range wakefield and system stability issues inherent in the long bunch TESLA trains will not occur until Phase II.

8.1 Proposed Experimental Program

Given the goals of the prototype test phase set out in the introduction, the experimental program follows directly. The beam dynamics of the gun should be understood to the fullest extent possible, with the beam dynamics of the injector as a whole following. Correspondence between the design model (a PARMELA model) and the actual device should be checked.

Given that the injector performance depends critically on two nontrivial phase space manipulations (space charge compensation and pulse compression), both should be investigated. As the emittance compensation process is essentially complete by the linac entrance (see figure 6.5), measurements of the beam emittance to check the

compensation scheme should occur at approximately this location. This would require placing emittance slits ahead of the linac, then allowing the beamlets to drift nearly two meters to the phosphor screen, placed in the first available cross downstream of the linac. Such a long drift would severely reduce the largest emittance resolvable on the screen, and would greatly exacerbate the space charge pollution of the measurement. As a result, I decided to build a gun test beamline composed simply of the gun, a few diagnostic crosses and a spectrometer, as shown in figure 8.1 below.

Laser injection occurs at the first window on the left, with a vertically oriented emittance slit plate located at the next cross, 971 mm downstream from the cathode and close to the predicted emittance compensation point (see figure 6.5). Immediately following is a phosphor screen, 336 mm away. For the 2 mm separation slits described earlier, this gives an upper emittance limit (from eq 7.4) of $16 \cdot \sigma_x \pi$ mm-mr at $\gamma = 8$. With typical spot sizes of $\sigma_x = 5$ mm, this yields 80π mm-mr.

No additional diagnostics were contemplated, given the rapid space charge degradation of the beam. Figure 8.2 shows that space charge has severely degraded the longitudinal phase space even at the end of the 2 meter long beamline, with emittance growth in the transverse planes significant as well. The emittance "bounce" plainly visible at about 1 meter is an emittance compensation point, which occurs prematurely without the linac in place to alter the plasma frequency of the bunch.

Once the beam dynamics in the gun were understood, the spectrometer and test crosses were removed, and the entire injector built, encompassing the linac, dipole chicane and associated matching optics, and the spectrometer at the end. Testing would then proceed analogously, with the focus on beam quality versus gun and linac parameters, and a concerted study of pulse compression and its effects on the beam

quality. It was also hoped at this point to undertake a world-first observation of the physical basis of emittance compensation by making temporally resolved emittance measurements of the beam, as discussed in the diagnostics section.

Additionally, a proposal was made to study the effects of multibunch operation using a series of closely spaced (nanoseconds apart) bunches of reduced charge produced by splitting the laser pulse into 4 or 8 pulses, with appropriate extrapolation made to the 1 μs spacing of TESLA.

Studies of the gun at higher gradient (50 MV/m, instead of 35 MV/m) were also made to establish the effects of gun gradient on the beam quality, with an eye toward operation of the gun at 1 nC for the VUV-FEL at DESY.

8.2 Actual Experimental Program

The actual experimental program encompassed 35 experimental run days spread out over 40 weeks, divided into 16 run days with the gun test beamline, and 19 run days with the complete photoinjector beamline. Most of the days were taken up simply commissioning the injector, diagnostics and control system, with a few run days of devoted beam diagnosis. Significant time was expended trying four different emittance slit geometries, testing BPM pickups and electronics, and debugging control and data acquisition software.

The actual experimental program executed during the prototype test phase covered most of the proposed aspects, with some additions and two notable deletions. Table 8.1 below indicates the discrepancies.

Direct observation of emittance compensation by time resolved emittance measurement was not attempted because of poor beam quality and machine stability.

Phase I Goal	Measurements Made
Understand single bunch beam dynamics	Emittance, transport in gun Emittance, transport in injector
Measure stability against Laser Fluctuations	Stability measured w.r.t.: Pulse energy and launch phase Spot homogeneity, centroid jitter
Directly observe emittance Compensation	NOT ATTEMPTED beam quality too poor
Check pulse compression	Pulse compression measured
Attempt multi-pulse operation	NOT ATTEMPTED
General development of beam measurement techniques	Emittance slit development BPM and electronics testing New Čerenkov radiator used

Table 8.1: Experimental goals vs. actual accomplishments

Likewise, verification of the charge scaling law discussed in the theory section was not attempted.

Multi-pulse operation was not attempted for two reasons, (1) time (the significant modification to the laser pulse and subsequent careful timing of 4 to 8 pulses against the RF would have cost several weeks, if not months, as it did for a similar undertaking at CLIC) and (2) direct measurement of the phenomena would be undertaken within two years at Fermilab.

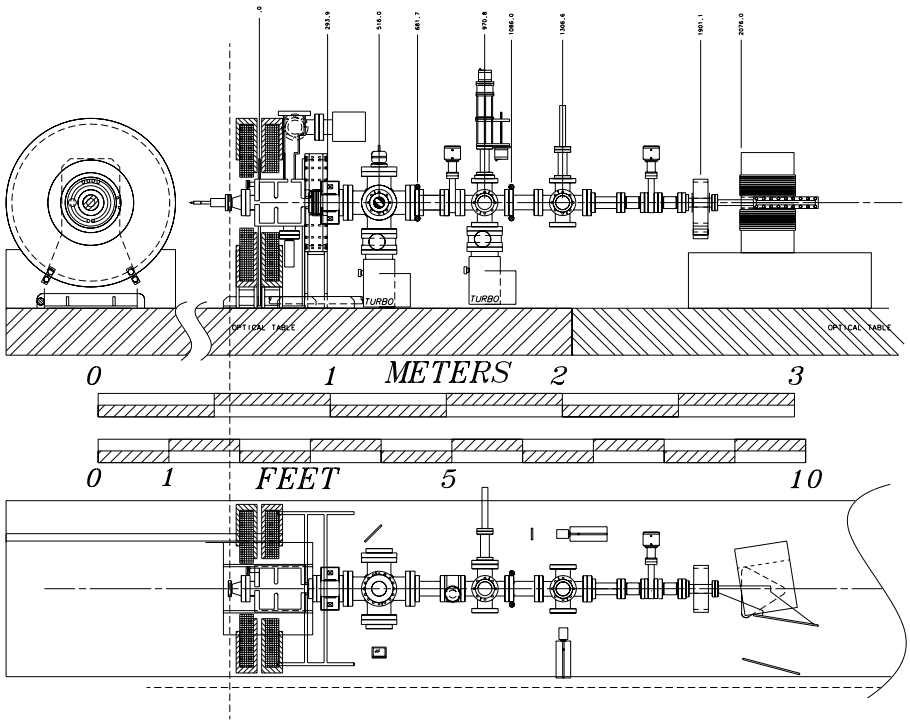

Figure 8.1: The gun test beamline

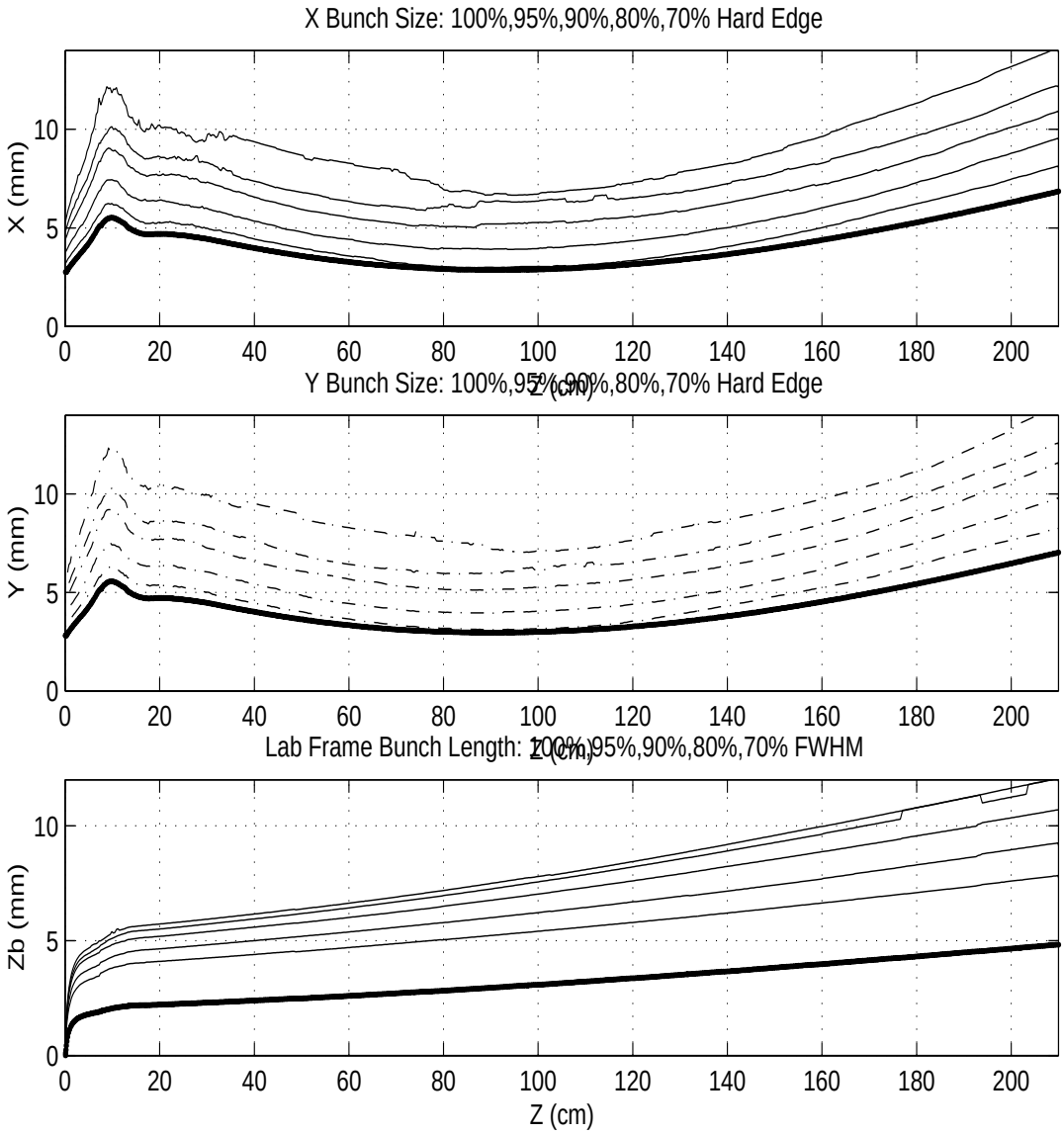

Figure 8.2: Envelopes for a 10 nC beam in the test beamline.

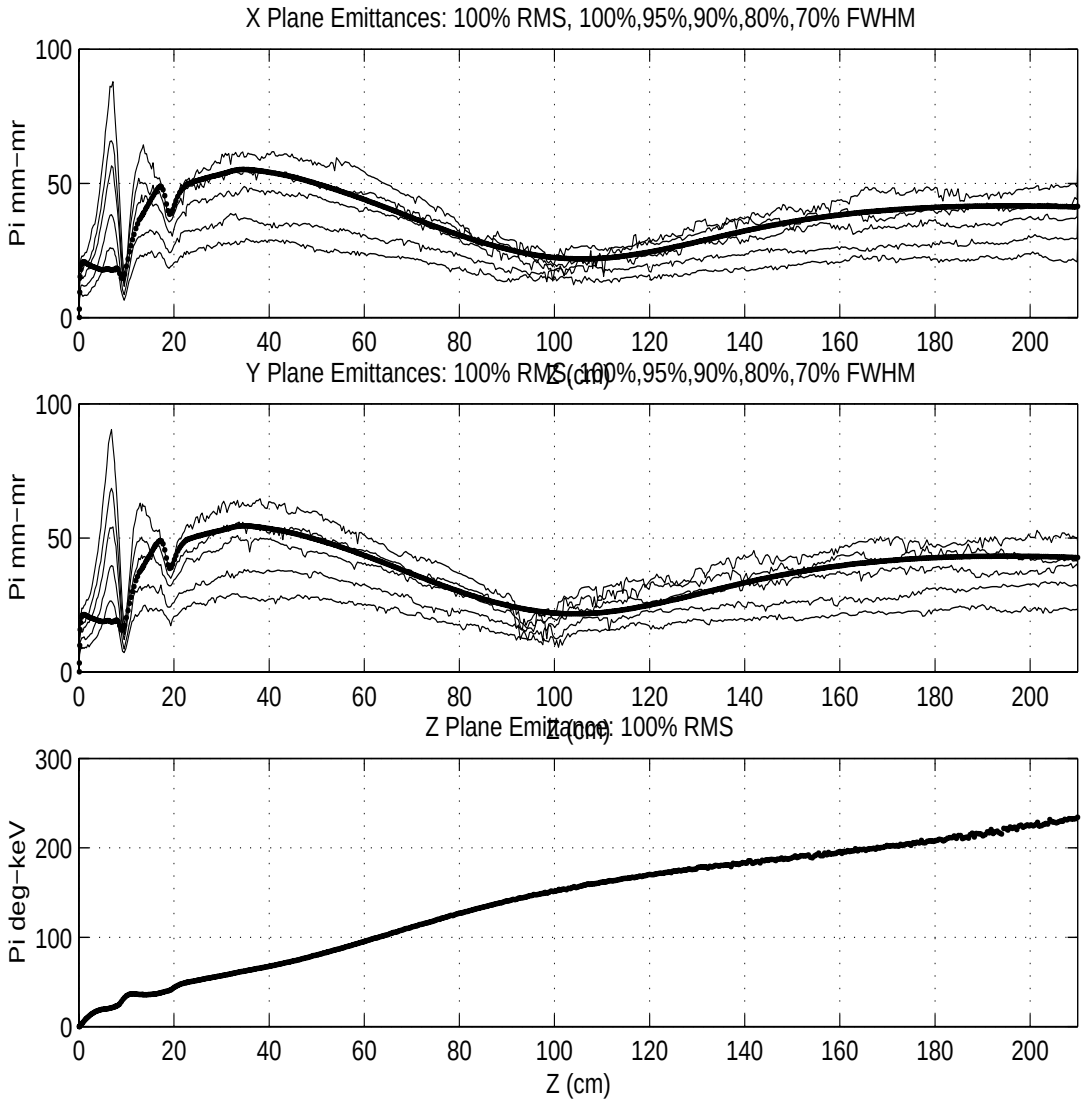

Figure 8.3: Emittance evolution for a 10 nC beam in the test beamline.

Chapter 9

Analysis of Experimental Results

9.1 Data Reduction Methods

Prototype diagnostics frequently present the dual challenge of supplying information in quantity (requiring astute reduction techniques to preserve salient features), and supplying noise in quantity (requiring careful filtering and substantial skepticism). Detailed below are techniques used to extract and reduce data from the various diagnostics described, all of which are proven statistical techniques, but some of which are seldom used.

Although maximum likelihood (in particular with the L^2 statistic) analysis is the most widely used technique of data reduction, it has several flaws which make it unsuitable for use by itself. The χ^2 (defined in eq. 9.1 below) statistic

$$\chi^2 \equiv \sum_{n=1}^{N} \left[\frac{y_i - f(x_i)}{\sigma_i} \right]^2 \tag{9.1}$$

is sensitive to outliers and is easily rendered useless by poor estimates of the measurement uncertainties, σ_i. Where data are noisy, rank statistics are employed instead. As an illustration, the full-width at half-maximum (FWHM) of normally distributed data may be computed either as $\sqrt{4\ln(4)}$ times the L^2 functional fit value for the

variance, or by ordering the data sequentially and searching for the two pairs of values that bracket the half-maximum values and computing the difference of the averages of each pair. In general, where data are consistent and outlier-free, the fit technique has the noise-suppressing advantage of using the entire data set, making it less sensitive to the individual measurement errors, unlike the latter approach, which will depend rather sensitively on the errors of the four data points used. In practice a hybrid technique is used, with pedestal subtraction done with the first and last members of the rank-ordered data set, then with subsets of data on the "slopes" of the Gaussian being fit to interpolate the half-maximum values, while excluding the outliers, followed by "polishing" of the Gaussian fit (within $\pm 2\sigma$ of the maximum only) with a multidimensional nonlinear least-squares fitter which fits the Gaussian and background simultaneously[1].This technique has proven to be remarkably robust even with signal-to-noise ratios approaching unity.

For the purpose of refining fits to noisy data, a fit "polisher" was implemented. The method is simply a multidimensional generalization of Newton's root finding method applied to the gradient of the χ^2 merit function. Although far more advanced techniques exist for multidimensional optimization, this technique was chosen initially for its pedagogical value, and found to be sufficiently rapidly converging. Details of the fit polisher may be found in the appendices.

Experimental uncertainties are quantified in one of three ways: (1) where theory is rigorous, direct propagation of estimated uncertainties of source parameters to the derived parameter (e.g. spectrometer measurements), (2) where direct propagation would require an approximate theory to be used and shot-to-shot reproducibility

[1]Method suggested by Alan Hahn

allows, the sample variance is taken as an estimate of the experimental uncertainty (e.g. BPM readings, slit emittance measurements), (3) where theory is approximate and shot-to-shot reproducibility is questionable, uncertainties are estimated by the Bootstrap Technique [130] (e.g. the quadrupole scan).

9.2 Characterization of the Drive Laser Pulse

The prompt and linear nature of photoemission implies a beam charge distribution that is simply related to the photon distribution of the drive pulse. As a result, the precise nature of the drive pulse bears on the quality of the beam produced, and must be quantified.

For various reasons, a characterization of the longitudinal properties of the drive laser pulse was not possible until near the end of the experiment. Detailed study of the transported laser spot was performed to understand the longitudinal and transverse spatial profiles as well as the pointing, amplitude, and timing stability.

Transverse spot profiles were mapped out at two times during the experiment. Once during the gun test phase, and again at the machine's de-commissioning. The UV laser was substantially attenuated with a UV-transmissive neutral density filter and allowed to strike a business card, the bleach and brighteners therein forming the fluorescent converter. A CCD camera viewed the business card, and the image was digitized. The cards had two significant drawbacks as screens: first, the response easily saturated (hence the need for substantial attenuation), and second, the cards had a tendency to burn, leading to nonuniform spatial response. The possibility of burning was guarded against by frequently replacing the card with an unexposed one.

During the gun test phase examination of the laser spot, it became apparent that

the air turbulence over the beam's approximately 10 meter transport was causing substantial time-dependent refraction of the spot profile. Much of the transport ($\approx 80\%$) was consequently enclosed, with transport within the laser room, and over the last 0.25 meter of transport to the vacuum window remaining unshielded. In addition, all but one of the tunnel ventilation fans were stopped when the beam was on. This had the desired effect of reducing the temporal variation of the laser profile.

However, substantial transverse profile inhomogeneity remained. The Galilean laser beam expander (used to match the diameter of the final amplifier media to the cathode diameter) was discovered to have a flawed lens which contributed to the spatial profile, and was subsequently replaced, although this far from solved the problem.

Pin hole filtering (which removes high spatial frequency components of the beam) is the obvious solution to such profile problems, however, with beam energies of 3-5 mJ per pulse, focussing with even 2 meter focal length lenses resulted in atmospheric breakdown. As a plasma is a wholly undesirable nonlinear optical element, this requires placing the focal region (and the pin hole) in an evacuated chamber with UV-transmissive windows. The expense ($\sim 5 - 10$ k\$) and time (4-8 weeks) involved in creating and commissioning a vacuum pin hole filter were thought not to be warranted, a decision regretted in hindsight. Pin hole filtering between the doubling crystal and the final amplifier would have helped matters somewhat (see figure 9.2), as would expanding the doubled beam through the final amplifier to make use of more of the stored energy.

Several naïve schemes were attempted to produce a more homogeneous transverse intensity distribution. Ground quartz plates with successively finer and finer surface

roughness were produced and found to scatter the beam far too much, even with surface finishes as fine as 100 nm. Attempts to relax the sharpest features of the roughened surface by heating to 1500K failed to produce an improvement in the outgoing beam divergence. Ultimately, the solution was to expand the laser spot slightly and select the most uniform subregion with a collimator.

At the conclusion of the experiment, the cathode was removed and the laser spot imaged as described earlier, revealing precisely the spatial profile that generated the electron beam. The laser was also imaged at the entrance window of the vacuum chamber, to establish the extent of window and mirror damage; immediately after the pulse expander; and immediately before the KrF final amplifier. In the latter two cases, a 20 foot drift and diverging lens were applied to the spot to expand the image. As before, cards were frequently replaced to ensure that observed spatial profiles were not contaminated by nonuniform card response. The lens was moved about to check that it contributed nothing to the observed intensity patterns. Figures 9.1 and 9.2 below show sample images from these four locations. In addition, the temporal length of the dye oscillator seed pulse was varied and the spatial profile recorded to look for any dependence of the transverse profile on the pulse length. (None was observed, suggesting that the final KrF amplifier was saturating either weakly or not at all).

Laser amplitude stability proved to be an important issue. Figure 9.3 shows both a shot energy history for approximately 45 minutes and a histogram of the events. A clustering of data near the desired pulse energy, and again at low energy (due to amplified spontaneous emission in the final KrF amplifier) are the principle features, with a downward drift of the pulse energy visible before a re-tuning was undertaken. The dotted line on the shot history plot marks a re-tuning of the dye oscillator to

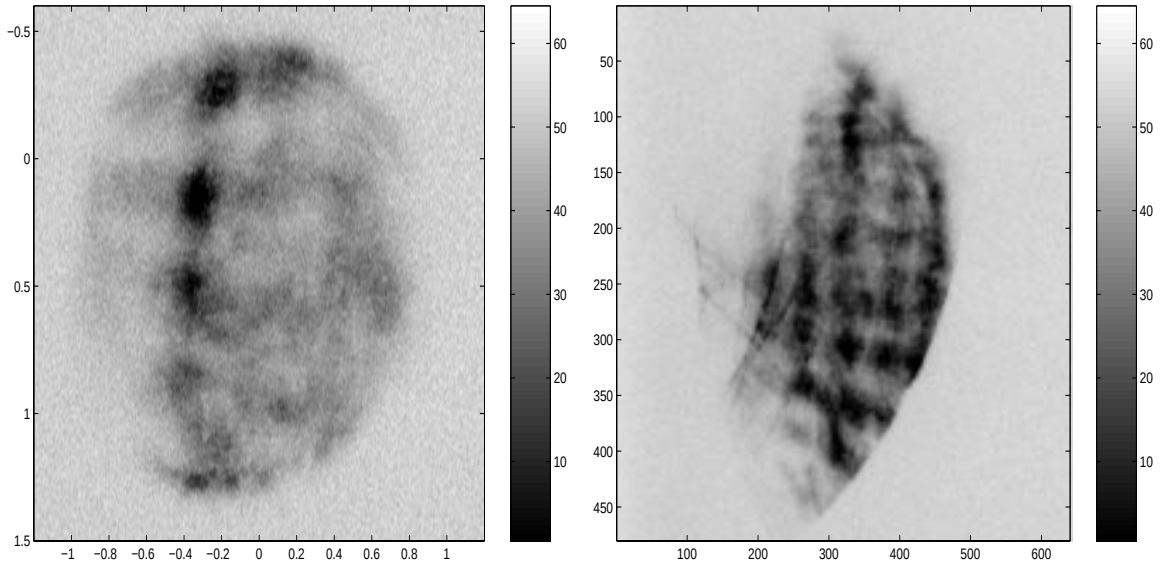

Figure 9.1: Laser spot imaged at the cathode location (left) and at the entrance window (right).

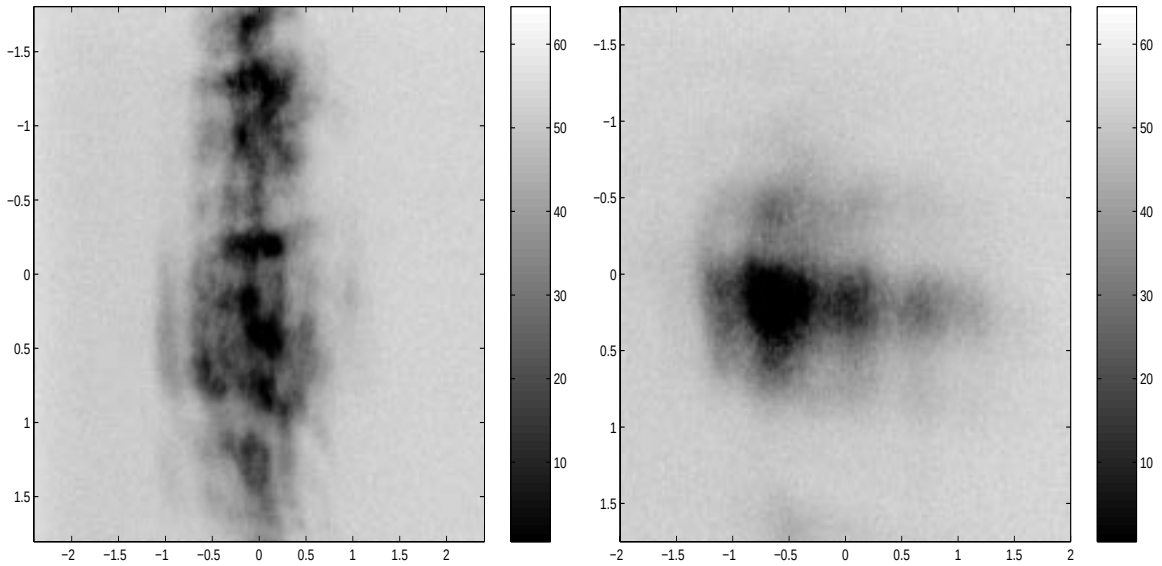

Figure 9.2: Laser spot imaged at the exit of the beam expander (left) and the entrance of the KrF amplifier (right).

improve performance. The plus signs on the histogram indicate a binning of only the events after the re-tuning, with a Γ_E/μ_E spread of 43% for this subsample. This spread in pulse energies led to significant spread in bunch charges, which in turn required judicious gating of data from the diagnostics.

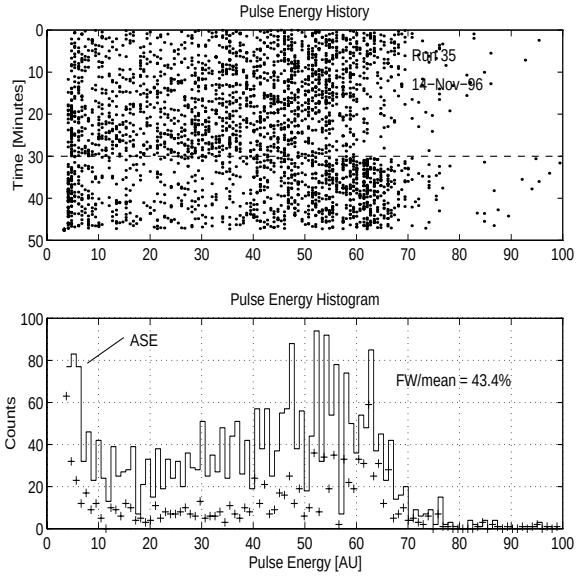

Figure 9.3: Laser pulse energy statistics.

Laser intensity profiles were measured with the Hamamatsu streak camera by directly observing the (much attenuated) UV pulses from the final amplifier. Attenuation was carefully arranged to avoid multiple reflections from attenuator plates and attenuating (non-UV) mirrors. A diverging lens and collimator were employed to provide variable intensity control just before the streak camera. Streak images consequently required sagittal correction to recover the pulse length from the diverging wavefront. A sample (sagittally corrected) image of the laser spot is shown in figure 9.4, together with curve fits of the image integrations. Dye oscillator pulse length and pulse energy were both varied to (1) look for correlation between the pulse length

of the dye oscillator pulse, as observed continuously with the TPF autocorrelator, and (2) look for evidence of saturation in the final amplifier.

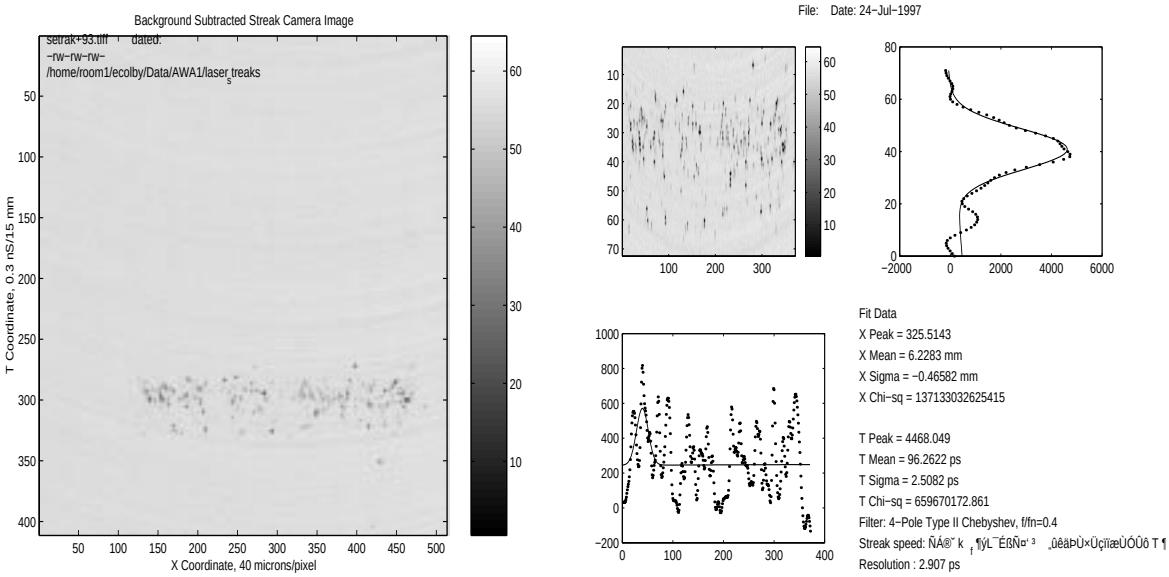

Figure 9.4: Sample laser streak image (left) and ROI analysis (right).

Also of serious concern was the interpretation of the rather disturbing autocorrelator traces observed for oscillator pulse lengths beyond 6 ps FWHM, shown in figure 9.5. Autocorrelation of a Gaussian pulse produces another Gaussian pulse with $\sqrt{2}$ times the width of the original. Autocorrelator traces showed substantial noise in the tails of the distribution, which is potentially an indication of partial loss of mode lock [131]. Further evidence from longitudinal profile data was sought to test this speculation, and the results are shown in figure 9.6. Evidence of degradation from a single, Gaussian pulse, as seen in the 3.6 ps streaks on the left, to a burst of noise as seen in the 6.7 ps streaks on the right, providing support for the mode lock loss hypothesis suggested by the autocorrelator data.

Whether or not the cause is correctly identified as partial loss of mode lock, the

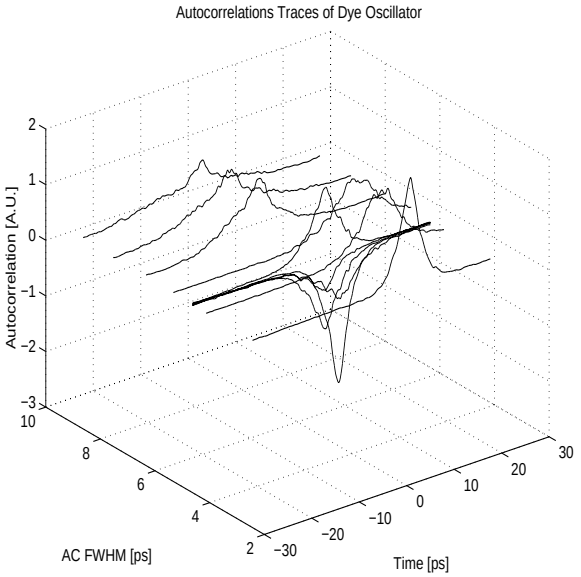

Figure 9.5: TPF autocorrelator traces for varying dye oscillator pulse length setting.

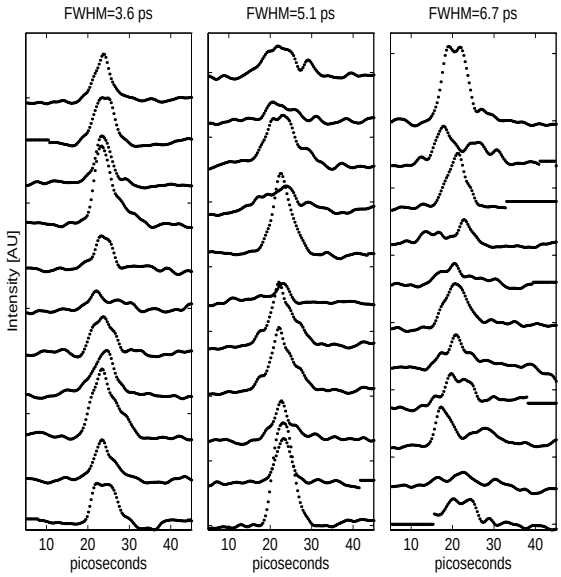

Figure 9.6: Streaks of KrF UV pulse for three different dye oscillator pulse lengths.

implication for beam operation is clear. Since the electron beam produced will mimic the structure of the laser pulse, the relatively clean Gaussian pulses derived from

the shorter oscillator pulses are the preferred case, despite being significantly shorter length pulses (3.6 ps vs. 10 ps) than those prescribed by simulation.

As to whether the autocorrelator provided a measure of the bunch length, figure 9.7 provides clear evidence that it does, although the data manifest a few odd features. A linear fit to the data points yields a slope of 1.05, when the expected slope (the doubling crystal gives an output proportional to the square of the intensity, shortening incoming pulses by a factor of $\sqrt{2}$) is $1/\sqrt{2} \approx 0.71$. Also, the residual pulse length (i.e. y-intercept) is non-zero, implying that the streak camera resolution is a bit worse than the estimate derived from illuminating the streak camera slit in focus mode, 2.6 ps. The black line across the bottom of the graph indicates the expected behavior, a zero-intercept line with a slope of $1/\sqrt{2}$.

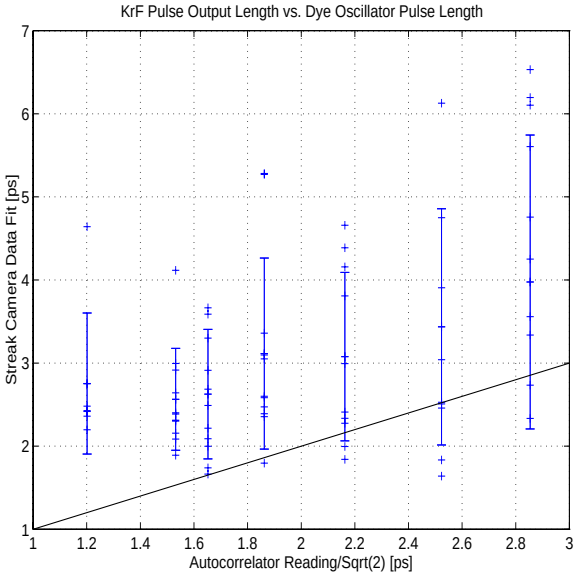

Figure 9.7: Final UV pulse lengths as a function of oscillator pulse length.

The minimum in the sample variance (hence error bar width) for dye oscillator pulse lengths on the order of 1.55 ps gives further evidence that the oscillator is well

mode-locked at this point, and is operating more stably than at other pulse lengths.

The power of the Nd:YAG pump laser (pumping the dye oscillator) varied widely during runs, beginning as high as 1.4 W in the UV and sagging to below lasing threshold for the dye oscillator, and required periodic adjustment. As a continuously varying, uncontrolled parameter, it is important to establish whether it has significant impact on the electron beam properties. The Nd:YAG pump laser power was varied to look for possible saturation effects in the final KrF amplifier, and hence UV pulse length variations, with the results shown in figure 9.8.

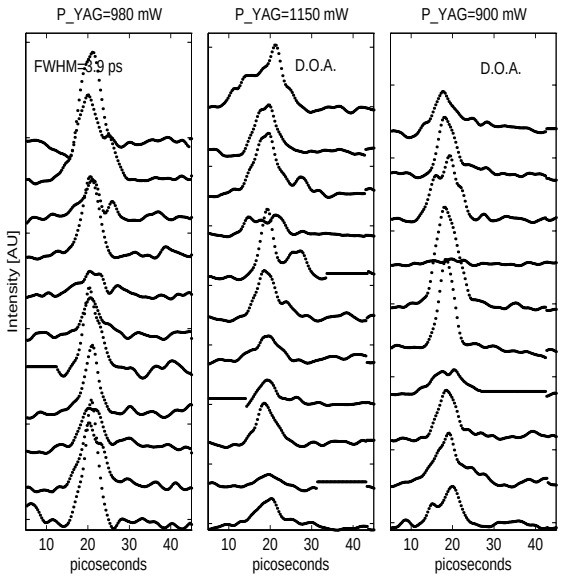

Figure 9.8: Streaks of KrF UV pulse for three different Nd:YAG pump powers.

No clear variation pattern is discernible either in the streak images, or in a scatter-plot of the pulse lengths, shown in figure 9.9. Thus the principle effect of variation of the oscillator pump laser is to cause variation in the overall beam intensity only, unaccompanied by significant change in the spatio-temporal profiles.

It is clear from the foregoing data that the drive laser possesses both substantial

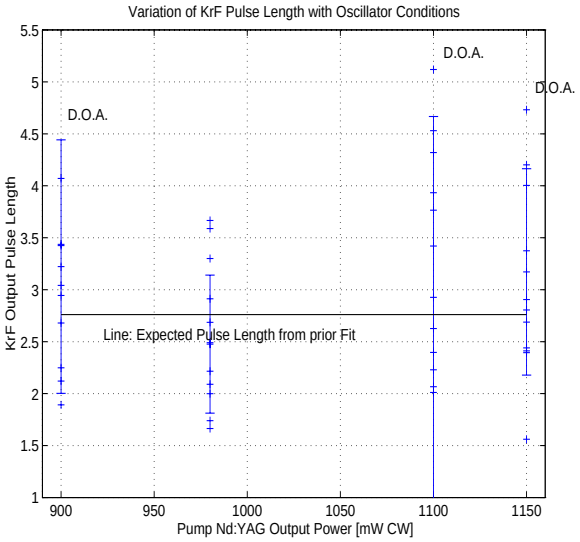

Figure 9.9: Scatter-plot of measured UV pulse lengths vs. Nd:YAG pump laser power.

shot-to-shot amplitude variation, and significant spatial structure; both are characteristics that will fundamentally impact the measurements that follow.

9.3 Examination of Emission Uniformity

As stated earlier, the beam charge distribution is directly related to the laser photon distribution, with the local quantum efficiency (QE) of cathode folding in as the "constant" of proportionality between the two. The local QE was measured using a highly collimated spot of approximately 1 mm radius, attenuated to give bunch charges that would have sufficient charge to give good signal-to-noise on the ICT, but small enough charge to minimize the probability of scraping.

Measurements of the peak voltage response of the ICT (known to be proportional to the bunch charge) and the peak voltage response of a fast Molectron pyroelectric detector (known to be proportional to the total laser pulse energy) were taken in ratio

as proportional to the real QE. The real QE, (the ratio of the number of electrons in the bunch to the number of photons striking the cathode) requires precise knowledge of all transport losses between the location of the pyroelectric detector and the cathode surface, and was not thought interesting enough to warrant the time and vacuum break required to measure the required transfer functions.

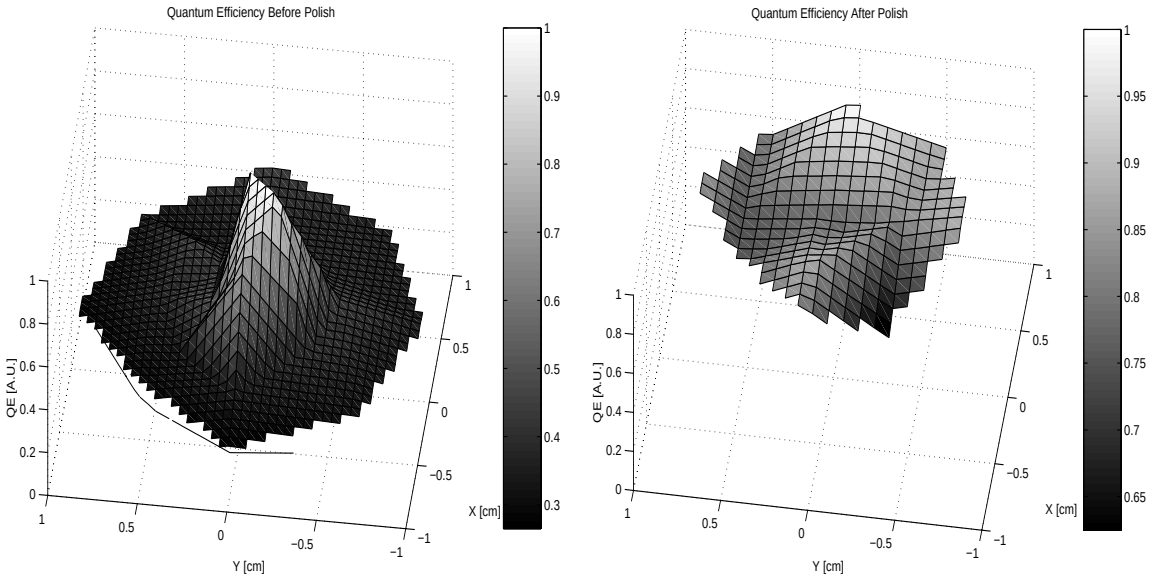

Figure 9.10: Cathode QE before (left) and after (right) polishing. Note the change in color coding range.

The QE was found to be sharply peaked toward the center of the cathode, and on close inspection of the cathode surface, pitting was found in the same region, likely caused by arcing during RF operation. The cathode was polished, removing both a circular tool pattern imposed by the lathe that originally machined the cathode face, and the arc pitting. Buehler Metadi oil base diamond suspensions of 6 μ and 1 μ grain size, followed by 0.3 μ alumina in acetone were used to ensure an extremely flat but optically rough surface (to prevent reflective losses and subsequent QE degradation).

The cathode was ultrasonically cleaned in acetone for 1 hour to remove the abrasive and suspension components. Following advice from Brookhaven, no alcohols were applied to the cathode face. The QE was again measured, with the results showing a significantly more uniform emitting surface, as seen in figure 9.10 (right).

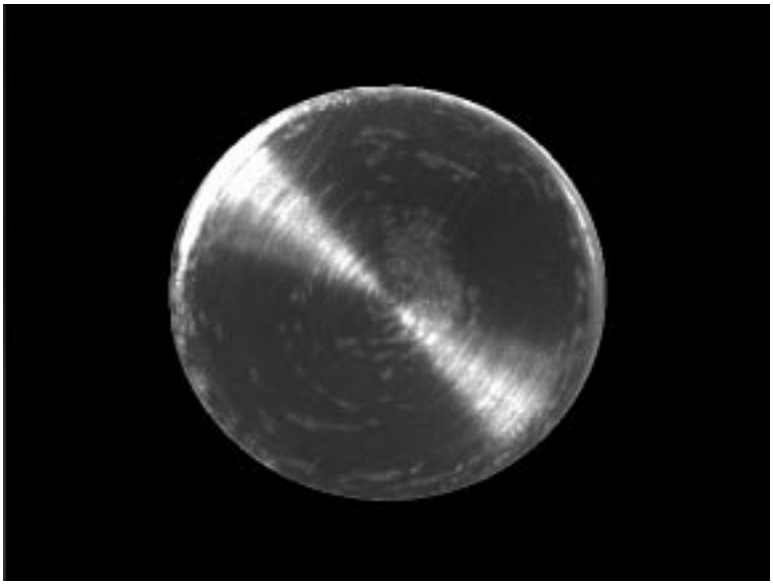

Figure 9.11: Image of cathode showing arc-damaged areas, which appear as lighter grey patches, especially to the upper right of center.

It is noted that these data establish correlation between polishing and flattening of the QE while causal connection between the arc damage pits, concentric machining grooves and the nonuniform QE remains speculative.

9.4 Characterization of the Gun RF Properties

The gun RF properties were tested in essentially two distinct phases. A "cold test" (low RF power, not low temperature) model of the cavity was created from a combination of copper and brass parts. The expected cathode and tuning paddle geometries

were also present, as well as the input coupler iris and $\lambda/4$ impedance matching transformer. Network analyzer (NWA) measurements were performed to confirm simulation predictions as to passband characteristics, field balance behavior, and coupling. Prime among the concerns was the sensitivity of the field balance to machining errors. Preliminary studies confirmed that the moderately strong coupling between the cells (0.2 %) had the desired effect of making the field balance fairly insensitive to small tuning (and thus machining) errors. Given the excellent agreement with simulation, the low duty cycle gun was fabricated.

Characterization of the prototype gun structure was done entirely by NWA measurement of either the reflection coefficient (S_{11}), used in determining resonant frequency, line width, coupling, and passband bandwidth, or the transmission coefficient (S_{21}) to the installed inductive loop pickups, or to specially made bore-mounted antennæ designed to preferentially couple to the four members of the dipole mode passband (2 polarizations $\times$ 2 eigenmodes).

Measurement of the gun TM_{010} passband is shown below in figure 9.12, with the predominantly electric coupling giving the π-mode frequency a higher frequency than the zero-mode. Superfish prediction of the passband width is 2.847 MHz, implying a coupling of 0.22%, as compared with the measured width of 2.596 MHz (0.20%).

A summary of the properties of the accelerating mode passband are listed in table 9.1 below. Measurements are made at 36^oC, with the π-mode balanced, and the cathode and tuning plunger flush with their respective surfaces.

The couplings and loss factors depend on a 3D knowledge of the fields not present in the Superfish simulations, and not sufficiently accurately modeled in HFSS. The shunt impedance listed is calculated by the simulation code for a $\beta = 1$ particle, an

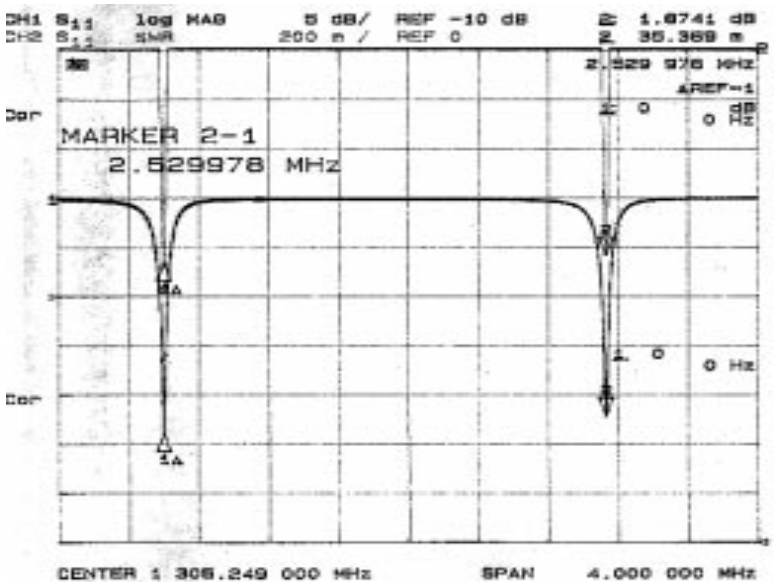

Figure 9.12: Gun TM_{010} passband structure

Parameter	Symbol	Simulation	Measurement	Units
Ø-mode frequency	$f_{\emptyset}$	1297.154	1297.40388	MHz
π-mode frequency	f_{π}	1300.000	1300.000	MHz
Coupling $\Delta\omega/\omega$	k	0.22	0.20	%
Return loss, Ø-mode	$S_{11,\emptyset}$	n/a	-18.5	dB
Return loss, π-mode	$S_{11,\pi}$	n/a	-15.7	dB
π-mode quality factor	$Q_{o,\pi}$	23601	22215	
Shunt impedance	Z'	24.418	18.6	MΩ/m

Table 9.1: Table of predicted and measured RF properties for the gun.

assumption significantly violated in this case.

Coupling of the destructive dipole modes to the pickup loops was also determined to understand what information about beam wakes and possible long range wakefield amplitudes could be learnt from the probes. Figure 9.13 show transmission measurements made by inserting an electric dipole antenna into the cavity through the beam tube and observing the signal from the pickup loops.

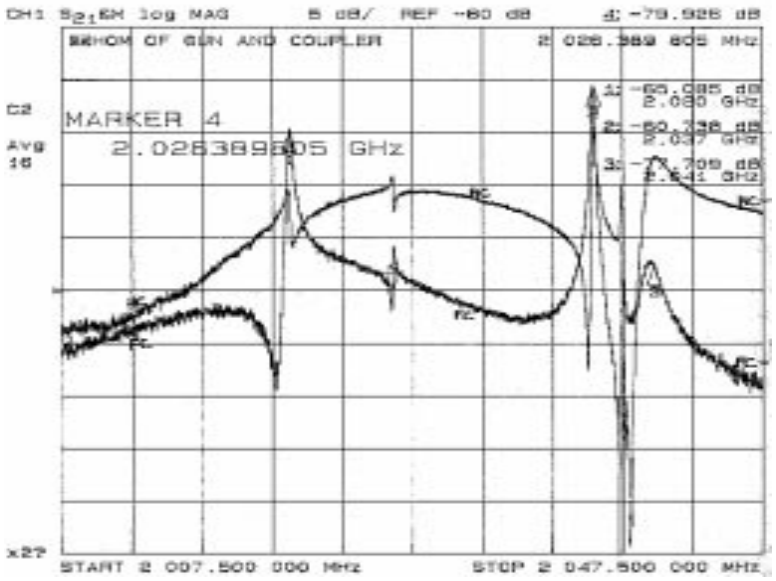

Figure 9.13: Dipole mode coupling to pickup loops: upper trace is half cell loop, lower is full cell

Field profiles were measured with a standard perturbative technique, the bead pull. A perturbing object (dielectric, conductive, or permeable) is introduced into the cavity and the frequency shift recorded. From Slater's Theorem [132], the fractional frequency shift Δf is the ratio of the displaced field energy in the perturbed volume V to the total stored field energy U in the structure:

$$\frac{\Delta f}{f_o} = \frac{(\int_V \vec{H} \cdot \vec{B} dV - \int_V \vec{D} \cdot \vec{E} dV)}{U} \tag{9.2}$$

Thus a unit-permeability dielectric bead will produce frequency shifts proportional to E^2 and a unit-permittivity permeable bead will produce frequency shifts proportional to B^2. A macroscopic conductor expels electric and magnetic field lines (since its dimensions are generally many skin depths of the RF) and will produce frequency shifts dependent on both the local E and B field strengths, requiring a separate measurement with a dielectric bead to disentangle the B and E contributions.

Care must be taken to ensure that the perturbing object is small enough to not significantly alter the resonant characteristics of of the structure. In particular, the bead should give a frequency shift which is very small compared to the passband width of the structure, in this case, 2.596 MHz. A 4.72 mm diameter plastic bead giving no more than 40 kHz total frequency shift was chosen. The diameter of the bead also sets the spatial resolution of the measurement. The finite bead diameter is the reason the measured field value does not fall to zero at the field null between the half and full cell. It is also interesting to note the sudden rise in the measured field profile as the bead approaches the cathode. This does not signify a real increase in the field amplitude, rather it is the cathode boundary condition adding an "image bead" to the system.

Longitudinal bead pulls (a direct measure of $E_z(z)$) of the structure were made to establish the longitudinal field profile, field balance characteristics and spatial mode content (by Fourier analysis). A longitudinal bead pull of the gun is shown in figure 9.14 below, together with the Superfish simulation result.

A transverse bead pull of the structure was performed to estimate the coupler-induced mode shift. A bead was drawn across the diameter of the full cell starting at the tuning plunger and ending in the quarter-wave transformer. A second order fit to the data near the beam axis was term-matched with a second order expansion about $(r = r_o)$ of the transverse mode profile $(\propto J_o(k_{01}\rho/R))$ to yield an estimated 1.1 mm shift from geometric center, somewhat larger than the HFSS prediction, 0.4 mm.

A "bead rotation" (a measure of $E_z(\theta)$, when a dielectric bead is made to make small radius revolutions at the mid-plane of the cavity where $E_r(r, z) \approx 0$) was used to estimate the dipole field component induced by the input coupler iris. This coupler-

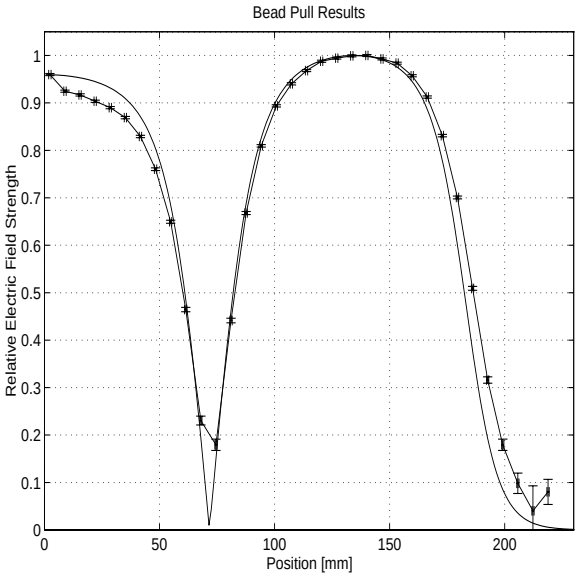

Figure 9.14: Longitudinal bead pull of symmetric gun structure

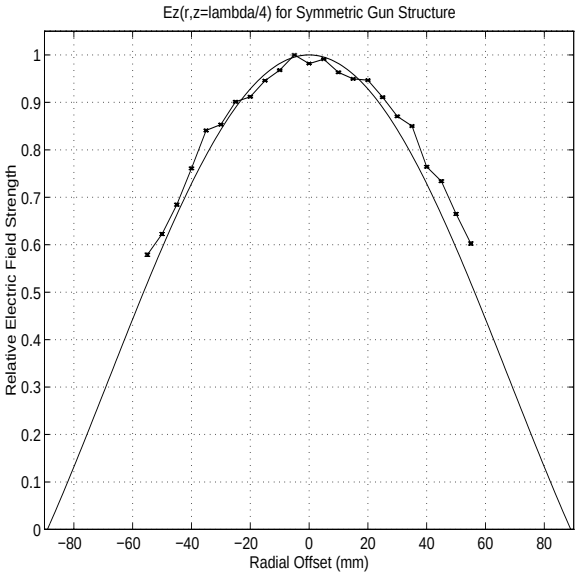

Figure 9.15: Transverse bead pull of the full cell

perturbed field has the form:

$$\begin{aligned} E_z(r,\theta,z) = \quad & E_0(\quad a_0 J_0(k_{01} r/R) sin(k_0 z) \\ & + \quad a_1 J_1(k_{11} r/R) e^{i\theta} sin(k_1 z) \\ & + \quad a_2 J_2(k_{21} r/R) e^{i2\theta} sin(k_2 z) + \cdots) \end{aligned} \tag{9.3}$$

where $k_n = \sqrt{\frac{\omega^2}{c^2} - \frac{k_{n1}^2}{R^2}}$ and is real only for the synchronous (m=0) space harmonic. The dipole and quadrupole terms are important for their potential to dilute the emittance. Figure 9.16 below shows the results of the bead rotation in the full cell, with the dipole term reaching 1.6×10^{-3} of the fundamental. Analogous measurements made on the (unsymmetrized) BNL/SLAC/UCLA RF gun [which has very similar geometry but operates at 2856 MHz] yield $\approx a_1/a_0 \approx 10^{-3}$ [75].

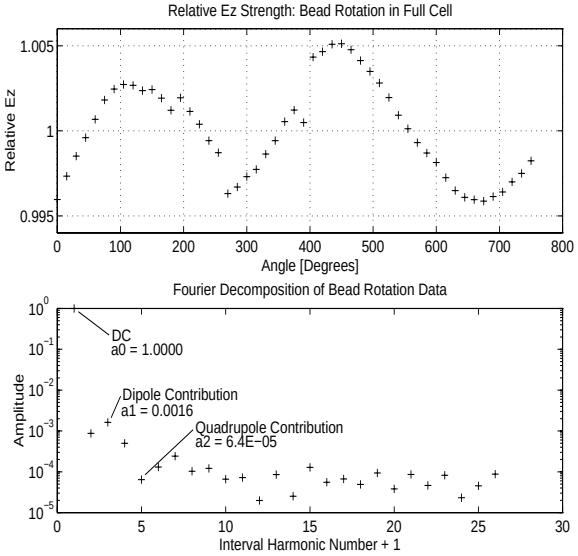

Figure 9.16: Bead rotation data and analysis

RF conditioning of the gun proceeded with the AWA RF system with short (4 μs flat top pulses) pulses at low repetition rate (1 Hz), to allow vacuum to recover

adequately between RF pulses in the event of an arc. Sample traces of the forward, reverse, half cell and full cell coupled powers are shown below in figure 9.17.

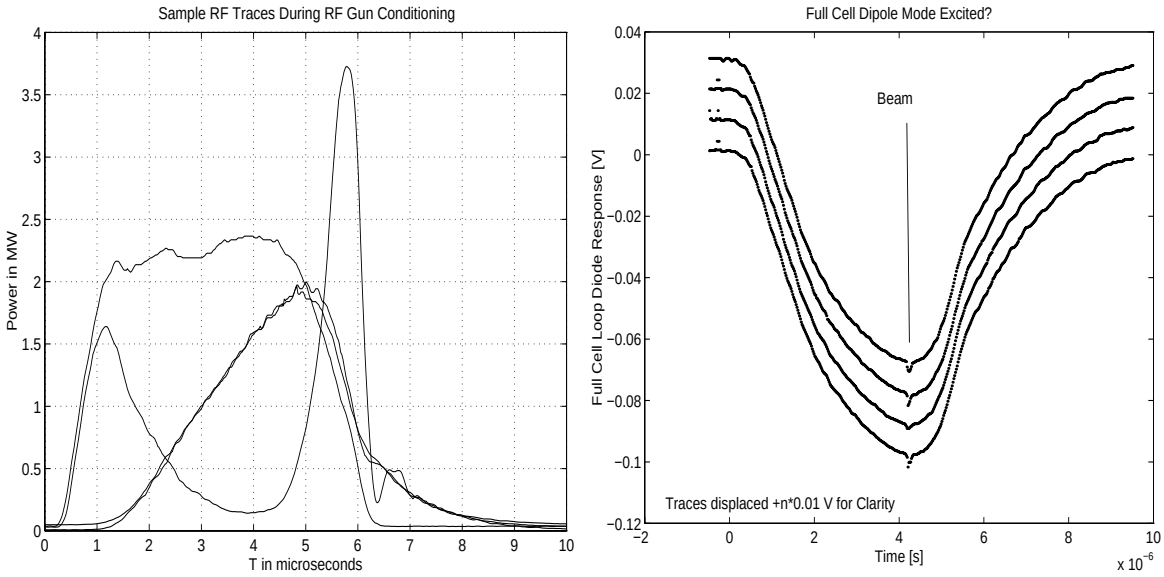

Figure 9.17: RF power traces from the gun during conditioning

For normal operation, the amplitude of the electric field in the half and full cell should be equal. Experimental determination of the field balance from the loop pickup signals is possible, but determination of sub-decibel power differences makes the measurement subject to sizeable error, given the limited accuracy of knowledge about the net transfer function from pickup loop to oscilloscope. Additionally, the RF loops used were found to be of poor mechanical quality, with the connector (and hence the underlying pickup probe) rotating slightly if moderate torque was applied to tighten an RF connector. For this reason, loop signals were not trusted to give usable field balance information.

An additional signal was detected on the full cell loop of the gun, which is interpreted to be the dipole mode, driven by the beam. The "bump" present at

the time of the beam crossing on the traces in figure 9.17 below was observed only when the laser was triggered, and not observed when the RF was pulsed alone. If it is simply an electronic artifact, it is not produced by the electrically extremely noisy modulator, but by the smaller power supplies in the laser system. Earlier measurement of the dipole mode frequency show that the four dipole modes (two eigenmodes, the zero and π, with two polarizations each, with mode degeneracy broken by the input coupler) have frequencies $\{TM_{110x,o}, TM_{110y,o}, TM_{110x,\pi}, TM_{110y,\pi}\}$-$=\{2020.5, 2026.4, 2037.8, 2039.5\}$ MHz, of which the modes polarized such that the magnetic field cuts diametrically across the cavity horizontally couple at almost the same strength (-65.1 dB vs. -60 dB) as the accelerating mode. The RF detector diodes used to convert the RF loop signals are flat in the 1-2 GHz range, with response still excellent at 2.04 GHz.

The integrated Dark current from the gun was measured to be 150 pC using the in-beamline Faraday cup. Focussing of the dark current spot was explored, with a clear annular pattern (see figure 9.18 below) emerging with several particularly bright spots, suggesting the cathode choke spring as the source of the dark current.

9.5 Characterization of the Linac RF Properties

The linac passband response, as determined with a coaxial drive antenna, is shown in figure 9.19 below, giving clear evidence of the close spacing of the $\frac{8}{9}\pi$ and π modes. It is interesting to note that the input coupler drives the fifth cell of the nine cell cavity, making coupling to the even modes (the $\frac{2}{9}\pi, \frac{4}{9}\pi, \frac{6}{9}\pi$, and $\frac{8}{9}\pi$) impossible, as all even modes have zero field in the fifth cell.

Longitudinal bead pull data for the linac after final tuning of the coupling slot is

Figure 9.18: Phosphor screen focussed image of dark current from gun

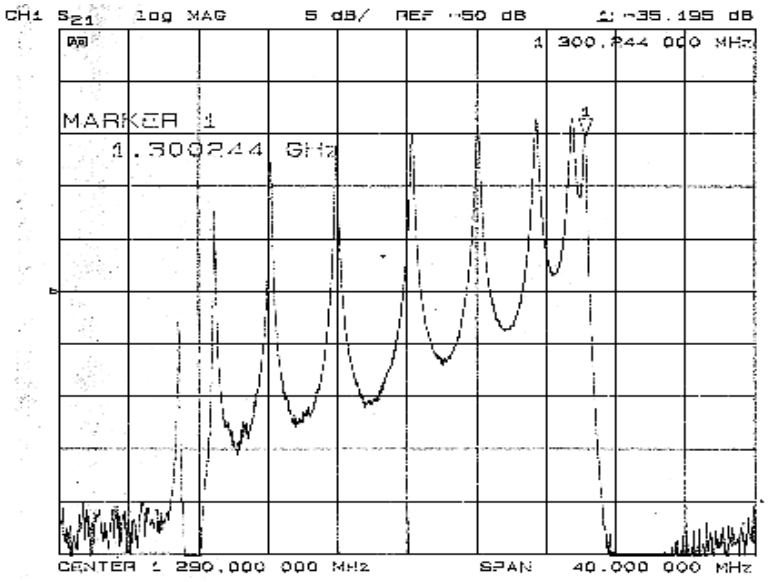

Figure 9.19: Linac cavity passband structure (complete)

shown in figure 9.20 below.

The frequency depression of the coupled cell is evidently far from being fully

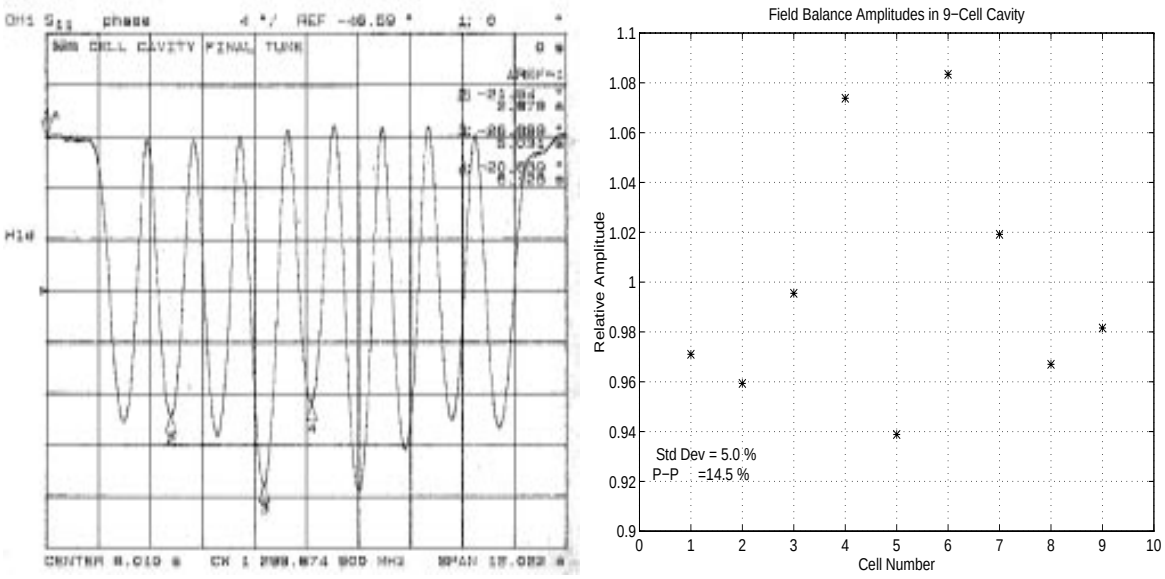

Figure 9.20: Field balance of 9-cell copper linac structure after final tuning

compensated by the clamp ring tuning assembly used. Also, the mechanically coupled nature of the tuning method guaranteed that stresses imparted on the detuned cell would be transmitted to the adjacent cells, causing opposite detunings, as is evident from bead pull data. A minimum-to-maximum amplitude field imbalance of 14.5 % (5.0 % RMS) relative to the average results.

Pickup probes, composed of trimmed lengths of .125" diameter rigid coax, where inserted through vacuum feedthrough flanges into the entrance and exit beampipes of the linac to measure the field amplitudes in the first and last cells. The capacitive probes were trimmed until couplings were approximately 70 dB down, as shown in figure 9.21 below.

Thermal tuning was established for the linac structure (as it was for the gun, but is not shown), and is displayed in figure 9.22 below.

Simple linear expansion theory applied to a pillbox estimates a detuning of the

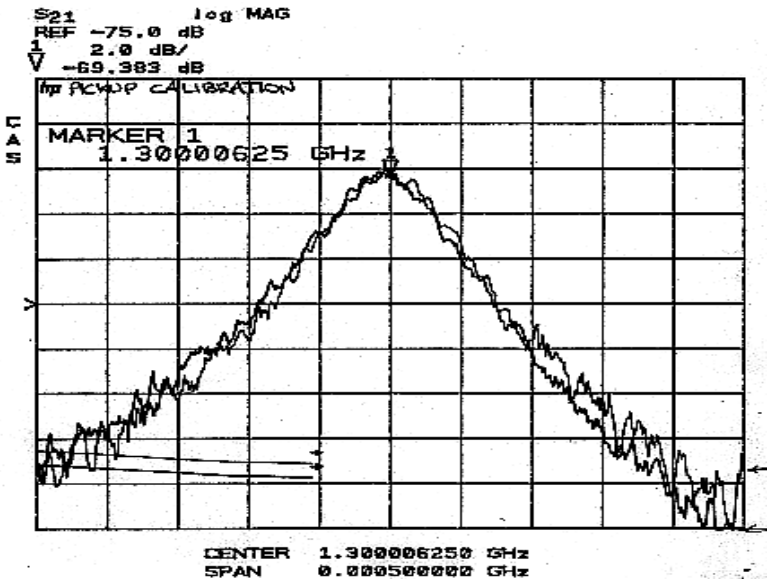

Figure 9.21: Calibration curves for linac capacitive probes

TM_{010} mode to occur (see eq 5.10) at $df/dT = 21.8kHz/K$, with a simple fit to the data here yielding a tuning slope of 22.3 kHz/K, in good agreement.

9.6 Characterization of Magnet Properties

Multipole content of the primary solenoid field was quantified by measuring $B_x(\theta)$ with a hall probe on a translating stage, and Fourier decomposing the result. Two openings in the return leg of the yoke were opened, one to accommodate the conductor terminations, the second a mirror image of the first to give a quadrupole, not a dipole component as the leading error term. Twenty revolutions ($\Delta\theta = 40\pi$ radian) were acquired at a revolution frequency of 20.7 mHz, with Fourier analysis and display occurring on an HP54512B oscilloscope. Figure 9.23 below displays the resultant data.

The primary solenoid and its bucking coil were aligned initially geometrically, by

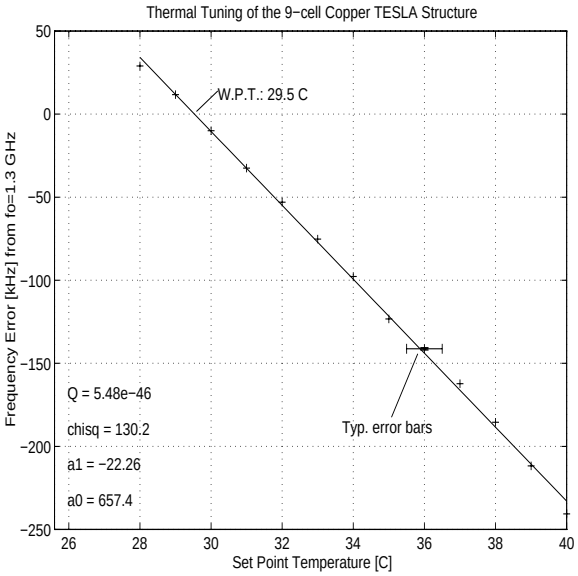

Figure 9.22: Thermal tuning curve for linac structure

autocorrelating a He-Ne laser beam of a mirror mounted on one face of the yoke, and surveying the incoming laser beam to be parallel to the beam line over a 20 foot interval. Nonperpendicularity of the yoke face, of course, will limit the accuracy of this procedure.

Subsequent alignment was performed magnetically. A fixture which mounted to the vacuum flange on the cathode end of the gun was fitted with a Hall Effect probe and revolved about the flange to measure $B_r(\theta)$. The flange location was controlled by tight machining tolerances relative to the cathode center, and was felt to be a reasonable fiducial. Figure 9.24 below shows the obvious dipole moment of the displaced solenoid and its subsequent reduction to the noise level of the measurement. Flux leakage through the permeable optical table top pulled the solenoid mode slightly downward, on the order of a millimeter, requiring additional shimming to compensate. Although substantial multipole pollution was introduced by the magnetically

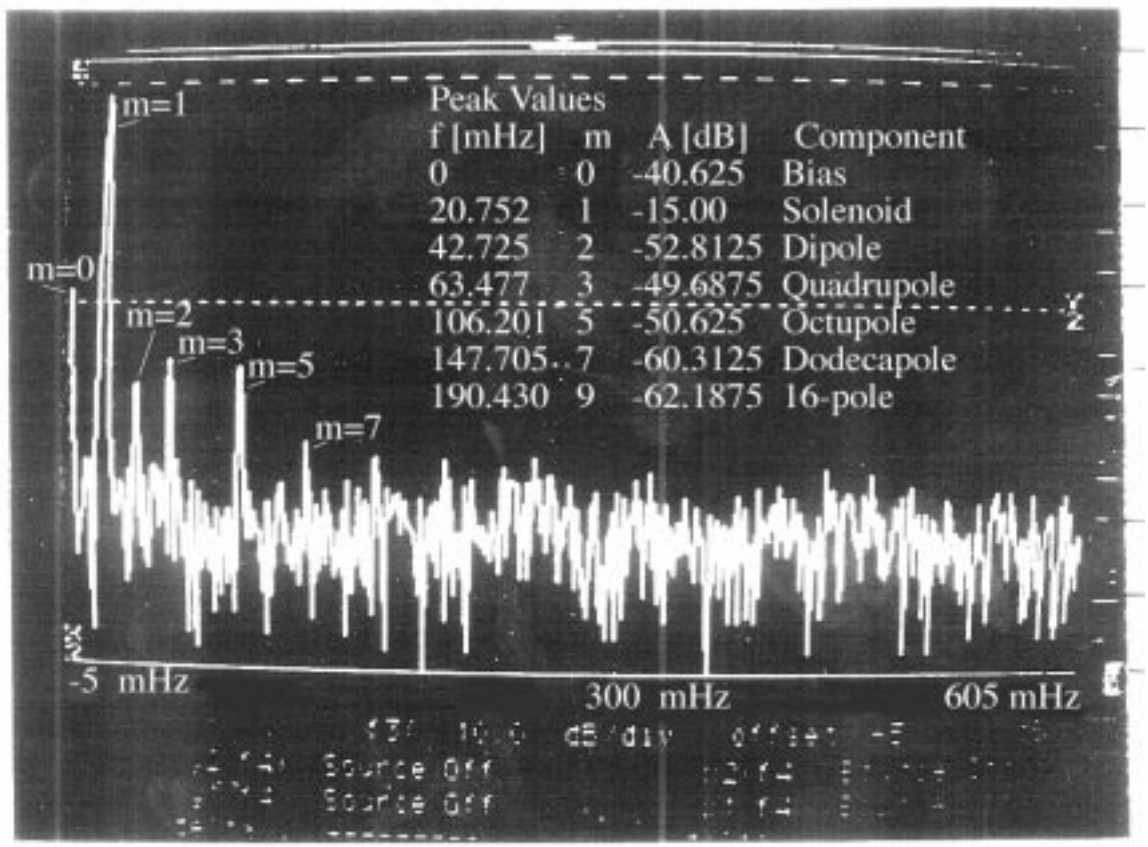

Figure 9.23: Fourier decomposition of primary solenoid field $B_x(\theta)$

conducting boundary condition at the table top the multipole content at the beamline axis was observed to be free of substantial multipole error except for the shift in the lowest order multipole, as is always expected in the far field. Martensitic (case-hardened steel) alignment rods and a nearby cable tray also provided minor distortions to the solenoid field, but again were far from the beamline axis.

The compressor dipole fields were measured as a function of current to establish the necessary current mappings to correct for differing yoke reluctances. It was found that series drive of the four dipoles resulted in wild steering of the beam due to the varying magnet yoke reluctances. Figure 9.25 below shows $B_y - \langle B_y \rangle$ versus current

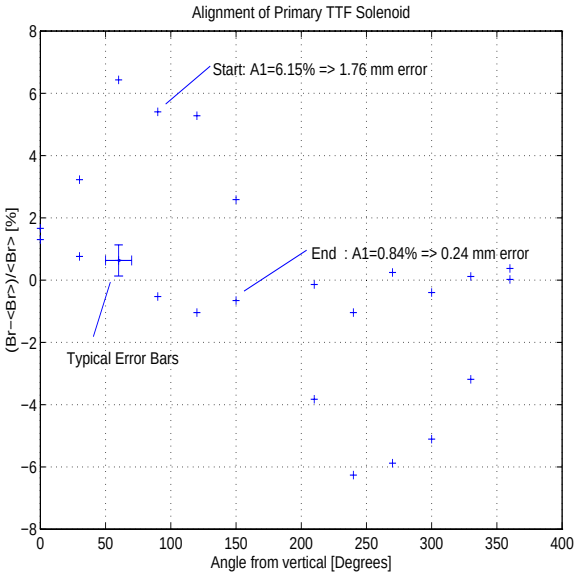

Figure 9.24: Primary solenoid magnetic alignment curves.

for the four magnets. Full magnet de-Gaussing and standard current programming (three cycles in the half-plane of the set point desired to maximum current, ending with a descent from maximum current to the required set point) was used for each data point to reduce hysteresis effects.

The measured B versus I curves for the small bore (35 mm) quadrupoles used in the beamline are shown in figure 9.26 below. The quadrupole was de-Gaussed, then cycled three times from zero to maximum field before reducing the current to the desired setting, and accounts for the absence of obvious hysteresis effects in the plotted data. Error bars are $\pm 3\%$, from the specification of the F.W. Bell hall probe. Some additional systematic error is present owing to (1) the distance between the pole tip and Hall effect sensor imposed by the sensor's protective coating, and (2) any inhomgeneities in the magnetic field close to the probe that result from variations in the pole tip iron permeability and machined surface features. Measured gradient

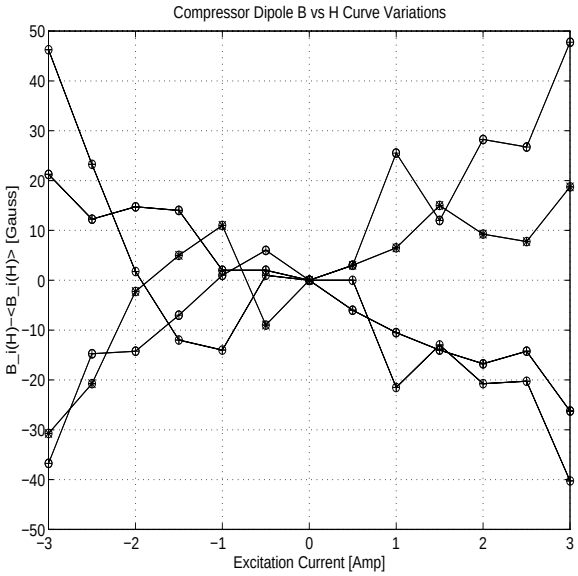

Figure 9.25: Measurement of B vs. I curves for the compressor dipoles

(4.6 T/m) agrees fairly well with the manufacturer's claim of 5 T/m gradient for 10 A excitation current.

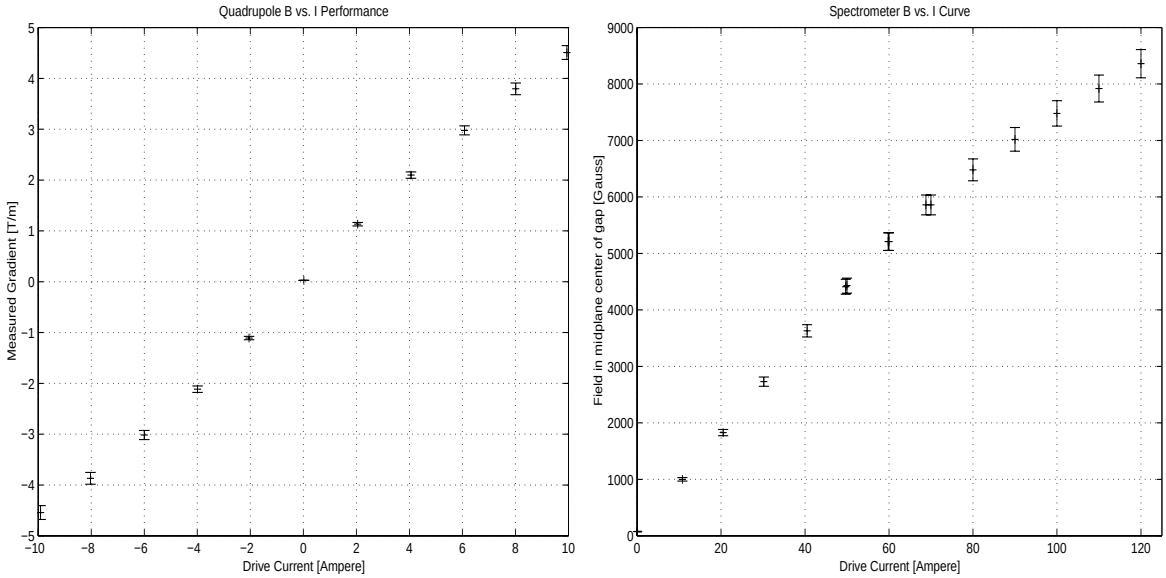

Figure 9.26: B vs. I curves for a representative quadrupole and the spectrometer magnet.

The measured B versus I curve for the spectrometer used to make energy and energy spread measurements of the beam is shown in figure 9.26 above. Unlike the measurements on the quadrupoles, the spectrometer was not de-Gaussed prior to cycling, owing to a unipolar power supply and the consistent bending direction used. Hysteresis effects are therefore expected to have entered these measurements.

Similarly B vs. I curves were measured for the spectrometer magnet, quadrupoles, and steering magnets, and used to derive bending and focal strengths. All magnetic field measurements were done with either a Bell 610 or 615 Gaussmeter with 3% accuracy probes.

The small steering dipoles were never formally calibrated. Brief examination of the basic strength ($\sim$ 50 G at 10 A) and field extent ($\sim g/2 \approx 4.5$ cm) were made to establish the approximate $\int \vec{B} \cdot \vec{dl}$ value, 560 G-cm, yielding a kick of $\approx$ 8 mr for 20 MeV electrons. As these are correction dipoles set to a given strength by direct beam position observation, the ability to dead-reckon the field strength from the drive current was not felt necessary, and hence no further studies were performed.

9.7 Other Calibrations

Most basic of the calibrations is the loss factor associated with patch cables used to transmit diagnostic signals (video, ICT and Faraday cup) from the shielding enclosure to the control room. 75 and 50 Ω cables ran for 33 meters from a central panel to the control room, and thus the loss factors associated with the signals of interest were measured. A 100 MHz scope and a sweep oscillator formed the "network analyzer" used to make S_{11} measurements in the control room with the far end of each cable shorted. Figure 9.27 below shows the result, plotted as S_{11}^{-1}. The "knee" plainly

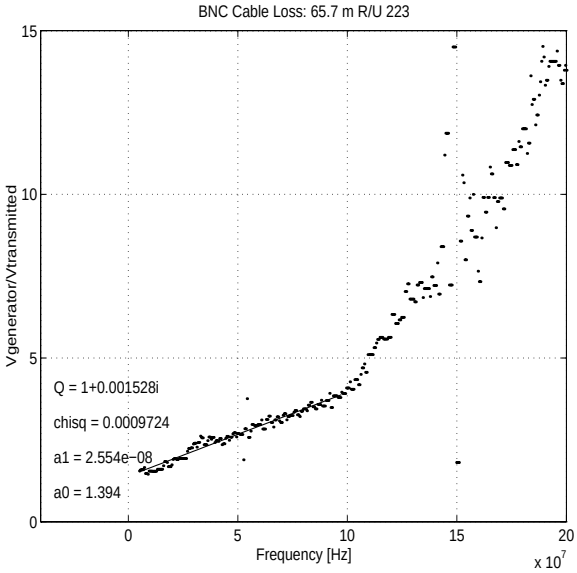

Figure 9.27: Cable loss factor in typical strand of feedthrough bundle.

visible at 100 MHz is from the oscilloscope. A simple fit to the data shows that the transfer function is:

$$H(f) \approx \sqrt{\frac{1}{1.394 + 0.0255 f[MHz]}} \tag{9.4}$$

and manifests the expected $f^{-1/2}$ scaling. In practical terms, this meant that the loss factor associated with the ∼50 MHz ICT signal was around 20%, and required correction.

9.8 Beam Measurements

As described in chapter 8, the experimental period divided into two parts. During the first period, the gun was tested using a short beamline with only charge, spot, emittance, and energy diagnostics. During the second period, testing was carried out on the full injector. Data are presented below according to period.

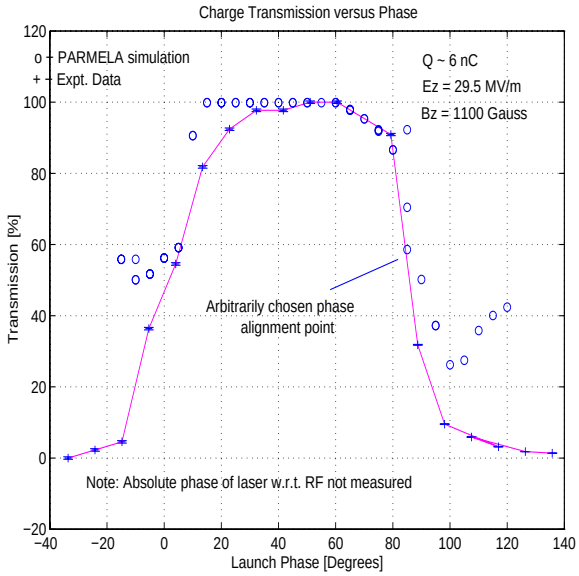

Figure 9.28: Beam charge transmission out of the gun versus launch phase

9.8.1 Gun Test Phase

Beam Charge Transmission

The charge transmission window, or range of bunch launch phase ϕ_o over which charge is accelerated from the gun was measured, and is shown in figure 9.28, together with prediction from PARMELA. No absolute phase information is available for ϕ_o, only relative shifts, thus the measured and simulation curves have been *artificially* aligned at approximately 85^o, where the slope of the curve is greatest.

Solenoid Steering

The final alignment of the solenoid was to have been beam-based, with the solenoids being shimmed until no beam steering took place, and the transverse emittances were optimized. Beam steering was reduced to within the noise of the measurement, as seen in figure 9.29.

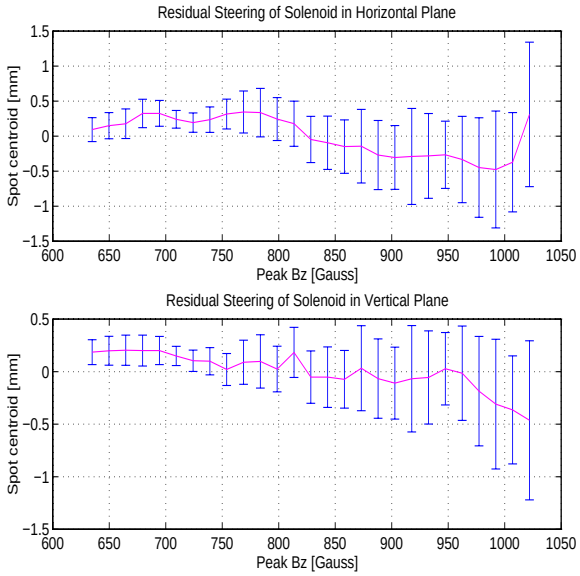

Figure 9.29: Residual solenoid steering after magnetic alignment.

As the yoke saturates progressively more at higher field levels, the degree of mode pull imposed by the permeable table top will also increase, meaning that the solenoid will effectively move out of alignment as the field is varied. Thus, alignment was attempted at what was believed to be the nominal working strength of the solenoids, with the recognition that experiments calling for variations in the field strength of the solenoid would be subject to solenoid steering effects.

Solenoid Focussing

With the solenoid steering measurement came a basic check in the strength of the solenoid focussing field to compare with simulation. Figure 9.30 show the variation in the horizontal and vertical spot size as a function of solenoid strength, "gated" for bunch charges $Q \in [9.5, 10.5]$ nC.

Clear asymmetry in the focal strengths required to create a beam waist at the

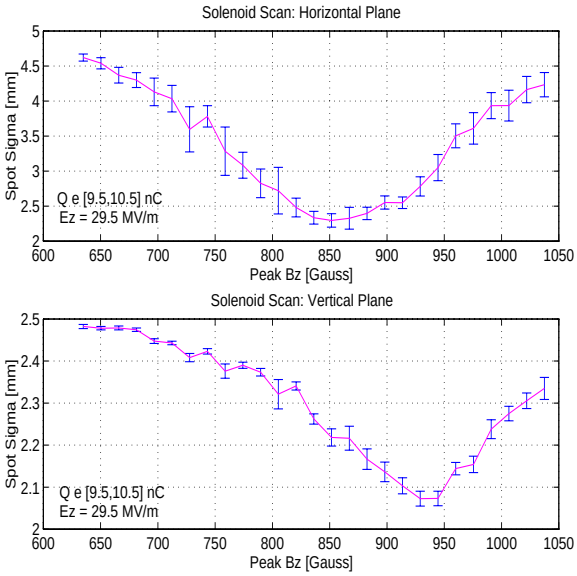

Figure 9.30: Spot after magnetic alignment

screen location point to significant spatial non-uniformity in the electron beam, and hence in the laser spot.

Gun Emittance

Measurement of gun emittance as a function of the integrated solenoid strength (varying all solenoids in constant proportion so as to vary the emittance compensating lens strength, but not its location) was the first experiment of interest. Figure 9.31 show the result. Plus signs mark the results of each recorded shot, with open circles representing PARMELA simulation under more idealized conditions. It is interesting to note that despite significantly different launch conditions (i.e. spatially highly nonuniform bunch, Gaussian rather than uniform pulse), the focal strengths at which the emittance minimum occurs are consistent with the simulation to within 7%, good agreement given the calibration uncertainties of the gun gradient and solenoid

strength, and the variation in bunch charge, the three factors influencing this measurement.

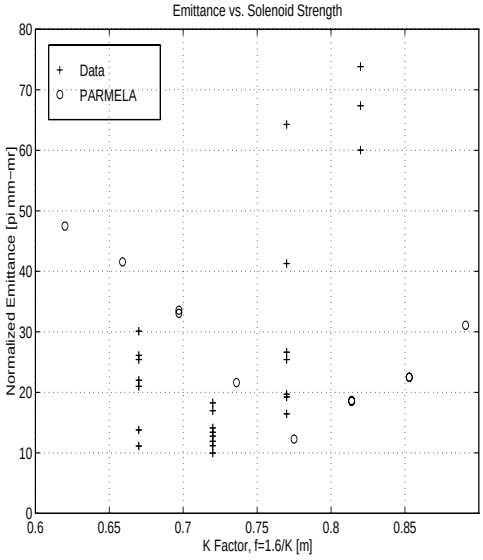

Figure 9.31: Gun emittance vs. solenoid field setting.

The relatively good correspondence between the simulated and measured performance provides evidence that the basic emittance compensation process is rather insensitive to small and moderate-scale charge inhomogeneities within the bunch. It is suspected that the above data, taken with the 10μ wide slits, is contaminated by significant scraping of the phase space. The narrow acceptance angle (1.6 mr) of the slits and broad divergence of the beam ($\geq$ 1 mr) increase the likelihood that scraping of the halo particles (which carry most of the emittance) has taken place. The end result is that the basic emittance compensation process (which takes place in the core of the beam) is still observed, but that the emittance value itself is under estimated significantly. It was this measurement which provided the impetus to shim the slits to increase the width to 35μ for the subsequent measurements.

Energy Spectra

Measurements of the beam energy and energy spread were conducted with the spectrometer located at the end of the test beamline. Figure 9.32 below shows the result.

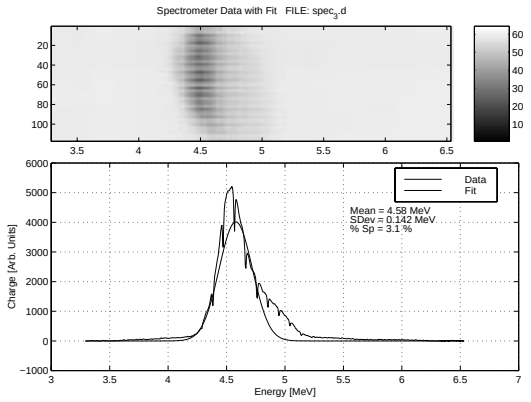

Figure 9.32: Gun energy spectrum measurement for 8 nC bunch.

Vertical streaks in the data are from a calibrating mask placed over the phosphor. The presence of a high energy shoulder in the distribution indicates substantial space charge damage to the longitudinal phase space.

9.8.2 Injector Test Phase

Gun/Linac Phasing Studies

The first commissioning task of the completed injector, following RF conditioning of the structures, was to map out calibration curves for the phase shifters and power splitters used to divide power from the klystron to feed both structures, and to understand what effects the very different thermal characteristics of the gun and linac would have on maintaining their respective RF phases.

Thermal control provided the means of tuning the structures to resonate at 1.3 GHz, and was accomplished with two independent, closed-loop systems. Cooling and heating were done by two commercial refrigeration/heating units that rejected heat to the air, rather than to a common water system which would have coupled the systems. The thermal pickup for both systems was mounted in a reservoir within the heating/cooling unit, not on the RF structure itself, which was foreseen and observed to cause both slow transient response and thermal wander under varying heat load conditions.

It was not surprising, then, to find that changes in heat load in the RF structures caused their relative phases to wander. The implication being that changes in pulse repetition rate, or peak power level would have to be accompanied by a re-tuning of the phases. Figure 9.33 below shows the relative phase of the gun and linac (obtained by mixing the inductive loop pickup of the half cell of the gun with the capacitive pickup on the upstream end of the linac) which remain quite stable over a period of many minutes, the large steps representing deliberate changes in the relative phase.

Bunch Length and Pulse Compression

Measurements of bunch compression were attempted using the aerojel Čerenkov radiator located immediately upstream of the spectrometer and the streak camera. Variations in the chicane temporal compression ratio R_{56} by varying the field strength (and hence the bending angle) in the chicane and the beam longitudinal energy correlation α_ϕ by varying the phases of the gun and linac. Pulse compression was measured over a wide range of bunch charge, with the charge recorded for each shot.

A sample streak camera image on the 1 nS/15 mm scale of the streak camera,

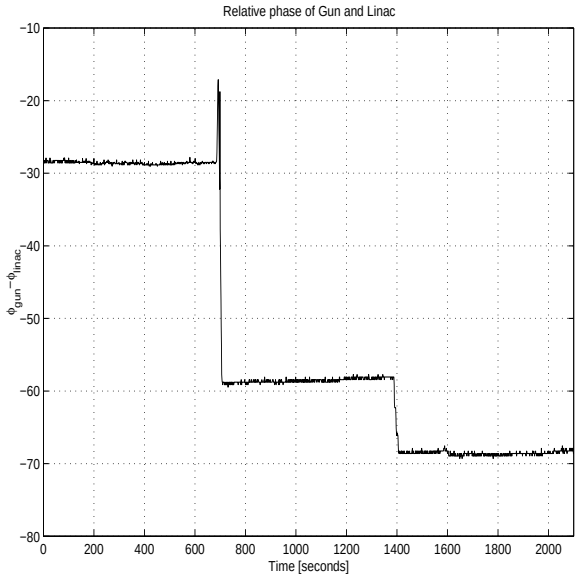

Figure 9.33: Relative phase of gun and linac over a period of 35 minutes.

is shown on the left in figure 9.34 below. The image is analyzed with the region outlined, with x- and y-projections with Gaussian fits shown on the right.

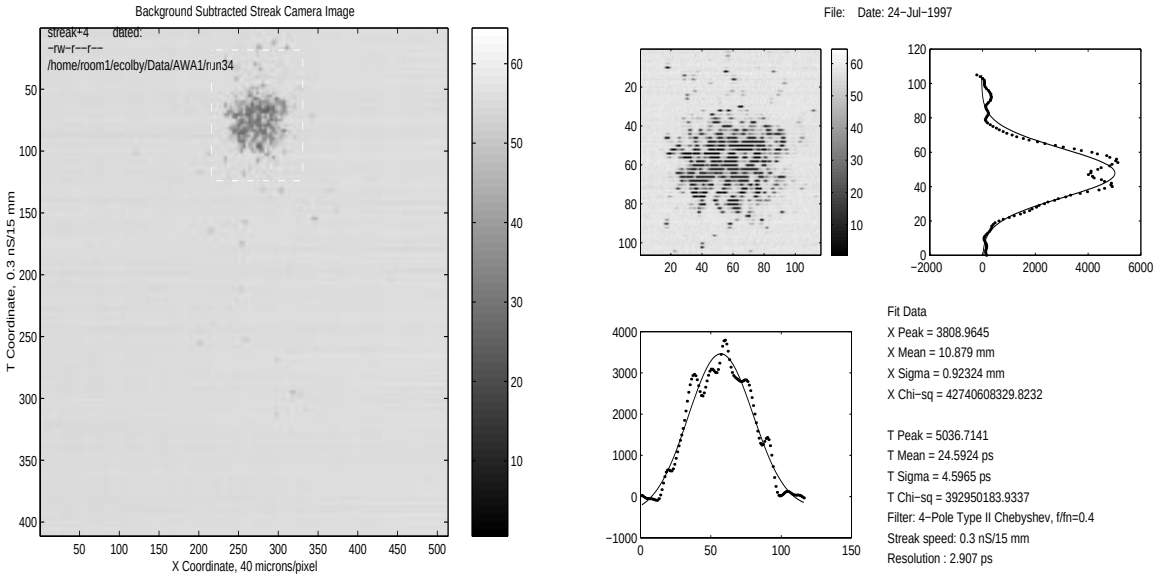

Figure 9.34: Sample beam Čerenkov light streak image (left) and ROI analysis (right).

Figure 9.35 below shows the variation of the measured bunch length as a function of temporal compression ratio R_{56} (left) and bunch correlation α_ϕ (right), with relatively little functional dependence evident. The data shown are those that survived both a χ^2 cut and a charge gating, and yet only the vaguest evidence of a dependence on R_{56} is visible. The variation of the bunch length with the gun and linac phases (right) shows relatively little variation, and disturbingly shows bunch compression for $\phi_L > 0^o$, the decompressing case.

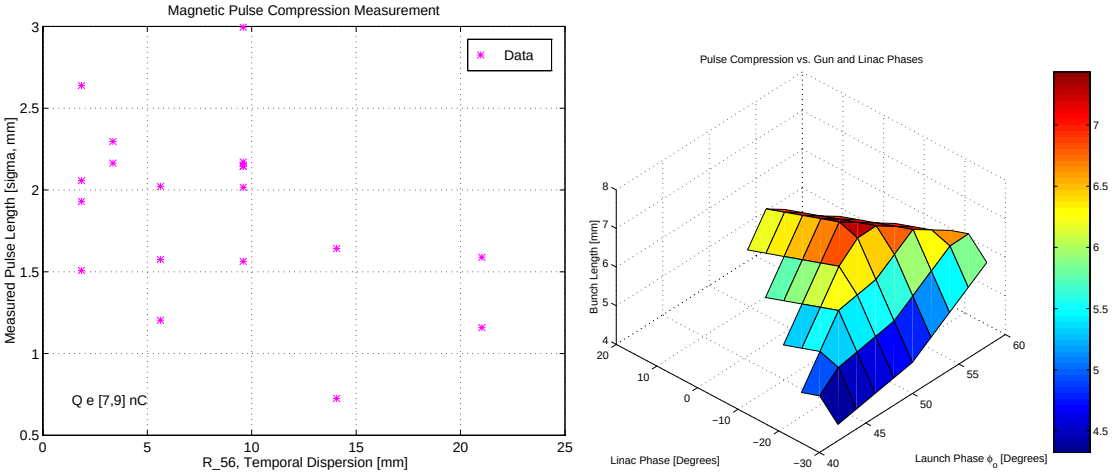

Figure 9.35: Bunch compression measurements versus R_{56} (left) gun and linac phase (right).

Wide variation in the launch charge, leading to varying degrees of scraping, and wide variation in longitudinal wakefield forces are the supposed reasons for the ambiguity of this measurement.

Emittance

Three separate emittance measurement methods were employed to understand the transverse emittance of the accelerated, uncompressed beam. The emittance slit in

cross 3, imaged in cross 5 (separation $\Delta z = 1080$ mm) was used for slit measurements in the horizontal plane, quadrupole scans were attempted between the first quadrupole of the first triplet and the screen in cross 5, (separation $\Delta z = 359$ mm), and a pepper pot [49] placed in cross 6, and imaged in cross 7 (separation $\Delta z = 595$ mm) was used to measure both transverse emittances simultaneously.

A sample beam image of a slit masked beam, made at 16.5 MeV, and its analysis are shown in figure 9.36 below.

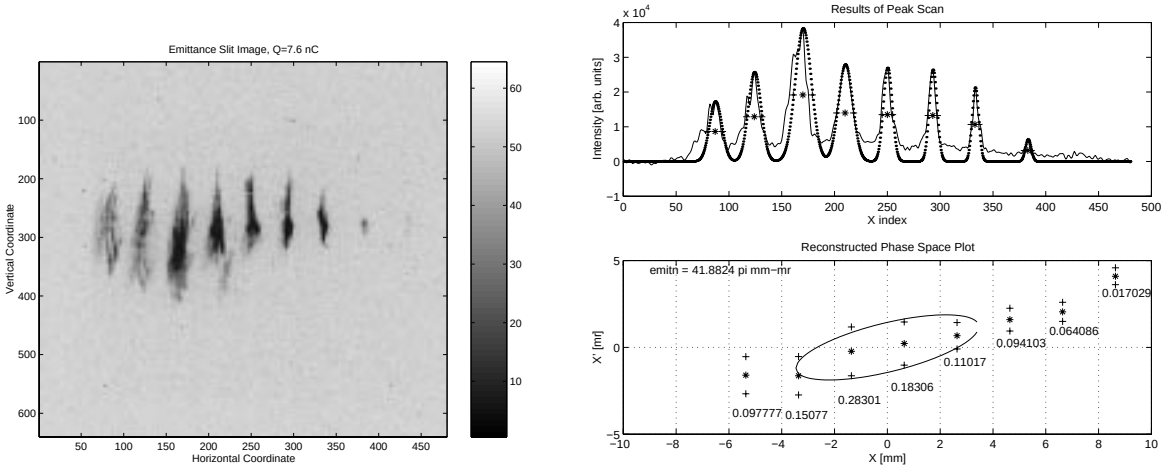

Figure 9.36: Sample beam slit image (left) and computer analysis (right), showing vertical projection, Gaussian peak fitting, and reconstructed phase space.

Slit emittance measurements were made as a function of the solenoid focal length (left) and launch phase (right) in figure 9.37 below for beam charges in the range 3-14 nC. Error bars are from sample variances, with 10 samples per data point, and are clearly affected by the wide charge variation.

Quadrupole scan emittance measurements were attempted, in full view of the substantial space charge pollution the measurement would carry. Given the theoretical grounds for rejecting this measurement technique (space charge effects are *not* neg-

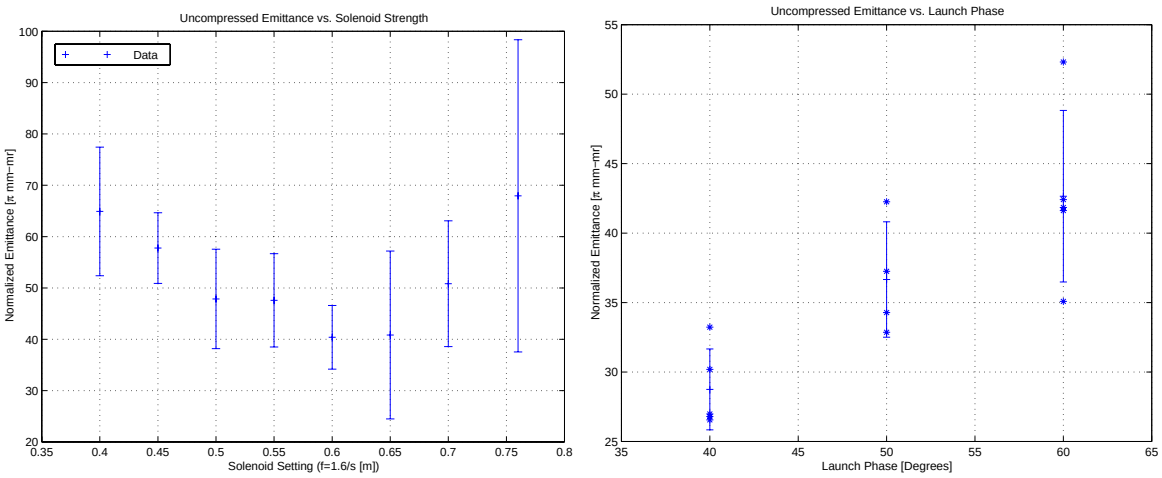

Figure 9.37: Slit emittance measurements at 16.5 MeV versus solenoid strength (left) and launch phase (right).

ligible, as discussed in section 7.3.4) and the experimental grounds for rejecting this technique (shot-to-shot stability is not good), the results are not reproduced here.

A pepper pot was placed in cross 5 after the compressor at z=5470mm, and the resultant beamlets imaged on a phosphor in cross 6, 33.6 cm downstream. Figure 9.38 below shows the phosphor image under nominal solenoid focussing conditions (left) and over focussing conditions (right), with very clear degradation of the beam resulting.

The emittances for the beams in the two images are, respectively, $\varepsilon_x^N = 22.6\pi$ mm-mr $\times\varepsilon_y^N = 24.2\pi$ mm-mr and $\varepsilon_x^N = 58.7\pi$ mm-mr $\times\varepsilon_y^N = 49.5\pi$ mm-mr. The over focussed beam has clearly filamented yielding multiple spot images from each pepper pot hole. Even the nominally focussed beam shows signs of wakefield effects, with the "comet tail" like structures giving evidence of variation in the mean divergences $\mu_{x'}(z)$ and $\mu_{y'}(z)$ along the bunch.

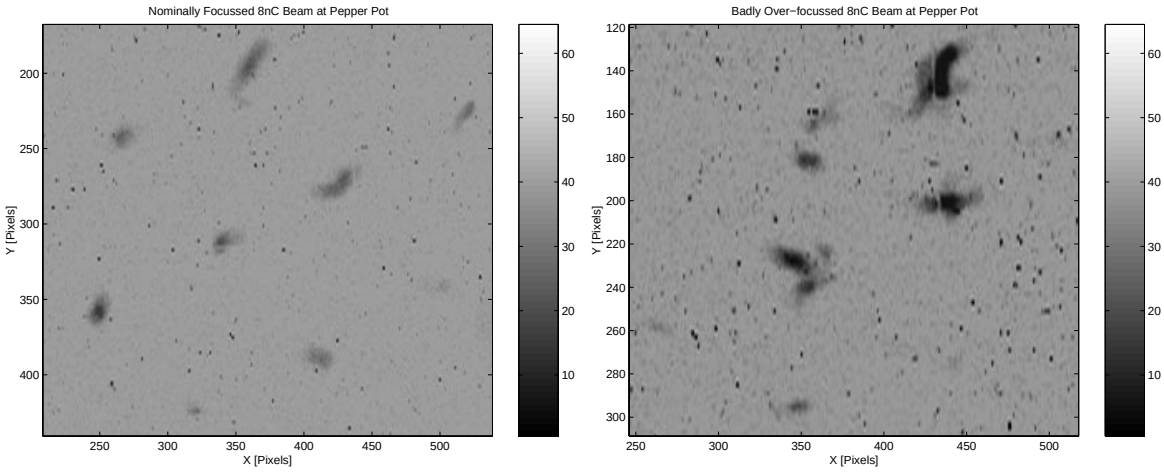

Figure 9.38: Pepper pot images of nominally-focussed (left) and over-focussed (right) 8 nC beam. Calibration: 232 pixels/cm

Energy Spectra

The energy spectrum of the bunch was measured for the uncompressed case using the same spectrometer and screen arrangement described earlier for the gun-only measurements. Peak bending fields were raised from typically 1 kG to 4.4 kG to give adequate dispersion of the higher energy beam. Figure 9.39 below shows the spectrometer image, its projection, and a Gaussian fit to the projection. The apparent curvature (i.e. correlation of energy with the non-dispersed coordinate, y) is not corrected for in the fit, resulting in a slight over-estimate of the energy spread.

The fraction of the bunch population present in the non-Gaussian tails of the distribution ($< 5\%$) giving evidence of space charge and potentially wakefield damage to the longitudinal phase space. Given the inconclusive nature of the pulse compression measurements, no measurement of the compressed pulse energy spectrum is presented here.

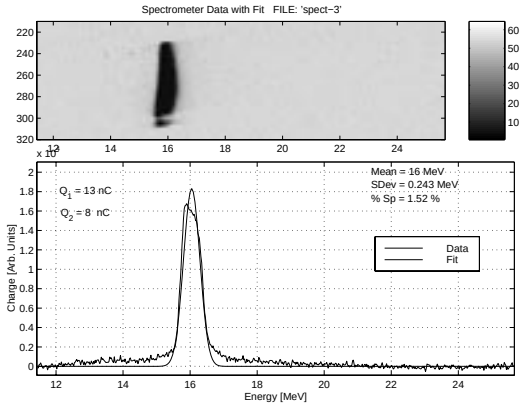

Figure 9.39: Uncompressed 8nC bunch energy spectrum at end of injector (z=6579 mm).

Chapter 10

Comparison with Simulation

10.1 Simulation Using Measured Parameters

Many departures from the idealized design parameters are known to have occurred during the prototype test experiment, and several have been quantified. To establish agreement between simulation and experiment, it is necessary to simulate the experimental conditions as accurately as possible. To that end, PARMELA has been modified to permit modelling of the experimental conditions in greater detail.

10.1.1 Laser Spot Profile

Laser spot transverse profile inhomogeneity induces substantial structure within the bunch which raises the stored electrostatic potential energy of the distribution relative to the uniform case. As a result, the charge distribution will evolve toward the lower energy case, converting potential energy into kinetic energy in an essentially irreversible manner, resulting in emittance growth. Wangler et al [133] and Lapostolle [134] have independently, explicitly shown this for matched, space-charge

dominated continuous beams:

$$\varepsilon_f^2 \approx \varepsilon_i^2 + \frac{1}{2}\left(\frac{K\beta c}{\nu_o}\right)^2\left(\frac{W - W_u}{w_o}\right) \tag{10.1}$$

where the perveance $K \equiv eI/2\pi\epsilon_o mv^3\gamma^3$, zero-charge betatron frequency ν_o, electrostatic energy of the beam distribution $W \equiv \pi\epsilon_o \int_0^\infty rE_r^2 dr$ and of a uniform distribution $W_u = w_o(1 + 4\ln(b/\sigma))$ are defined, with the constant $w_o \equiv \lambda^2/16\pi\epsilon_o$, and λ the line charge density.

As a result, spatial profile variations contribute to the emittance in proportion to the length scale associated with the variations. Very small scale variations, with length scales an order of magnitude or more below the beam size, do not appreciably alter either the potential energy of the charge distribution or the emittance. Conversely, large length-scale variations modify the stored energy appreciably, and result in significant changes in the emittance.

Modelling of arbitrary transverse laser intensity patterns was added to PARMELA, with standard rejection techniques begin applied to video image data to produce the launched macroparticles distributions. At the disassembly of the prototype experiment, laser profile data were recorded with the cathode removed (see figure 9.1). This video image of the laser spot is used as a selection function $\mathcal{F}(x, y)$. Random triplets (x_i, y_i, S_i) are generated, and retained in the bunch distribution if $S_i < \mathcal{F}(x_i, y_i)$, and rejected otherwise. Nonuniform QE effects were not folded into the distribution in light of the reasonable uniformity seen in figure 9.10.

10.1.2 Non-uniform Longitudinal Profile

Linear space charge emittance compensation is most effective when the transverse space charge strength $K_{SC}(z)$ is not rapidly varying, as is the case for longitudinally

uniform distributions (see figure 3.4). For non-uniform distributions the range of variation in $K_{SC}(z)$ is larger, requiring the stationary phase-advance condition (eq. (3.104)) to remain valid over a wider range of currents. In general this is not possible, and the emittance compensation is incomplete as a result. Gaussian beam and multi-mode profiles induced by either poorly mode-locked laser operation (see section 9.2) or cathode space charge effects will degrade the transverse emittance.

Modelling of both Gaussian profile beams and multi-mode beams have been done to estimate the resultant emittance dilutions for each. Appendix D has studies of emittance growth versus the lowest bunch harmonics (i.e. $k_z = n\pi/2\sigma_z$, $n = 0...6$), with the $n = 3$ case reproduced in the summary table in this chapter.

The σ_z^3 scaling (eq. (3.68)) of the RF contribution to the longitudinal emittance indicates that the change of bunch distribution from the ideal, uniform case (10 ps flat top, $\sigma_t = 2.88$ ps) to a Gaussian of shorter pulse length ($\sigma_t = 1.96$ ps) should decrease the longitudinal RF emittance contribution by a factor of roughly 3, resulting in significantly lower longitudinal emittance, and commensurately higher transverse emittances.

10.1.3 Laser Misalignment

Given the very gradual variation of the gun solenoidal field $B_z(r, z)$ with radius, a laser misalignment is essentially equivalent to a gun RF structure translation plus a small dipole kick from the "misaligned" solenoid. Variation in launched spot location was performed in both coordinate planes to understand this contribution. Up to the compressor, the injector is almost completely axisymmetric, with the symmetry being weakly broken by the multipole errors in the RF and solenoid fields, and in the

wakefields associated with the laser mirror holders (which appear to the beam as a wide vertical slit).

10.1.4 RF Field Imbalance

At the conclusion of the prototype test phase, the RF properties of the gun were re-measured to establish the running condition. The gun was found to be unbalanced with $\alpha \equiv E_{HC}/E_{FC} = 0.83$, implying that the extraction field on the cathode was reduced relative to the full cell peak field. The implications of this error are several, with the lower extraction field causing (1) greater space charge distortion of the bunch and consequently more emittance growth in all planes, (2) RF focussing at the exit of the half cell is exacerbated, causing a larger RF emittance contribution.

Owing to a lack of any readily moved tuners and very strong inter-cell coupling, the linac field balance was presumed unchanged from its originally measured condition of 5.0 % RMS field imbalance.

Approximate modelling of the imbalance condition is done by changing the field in each cell individually to correspond to the measured values. Given the method used to derive fields for each cell, this will replace the "bulging" of the higher cell's fields into the lower cell with a discrete jump in the RF amplitude at the cell boundary.

10.1.5 Wakefield Effects

As discussed in the Modelling chapter, provisions for modelling wakefield effects in a non-self-consistent manner have recently been added to PARMELA. ABCI modelling [135] of wakefield kicks on a Gaussian beam of the approximate uncompressed ($\sigma_z = 2.2$ mm) and compressed ($\sigma_z = 1.0$ mm) bunch lengths was done to establish the longitudinal (monopole only) and transverse (dipole only) kicks. These kicks

were then applied after each impedance discontinuity (each cell iris, each beamtube radius change, etc.). These wakefield results, in summary, indicated that monopole longitudinal wakefield effects require a further 5-7 degree phase advance of the beam relative to the RF wave in the capture cavity to overcome the wakefield contribution. Transverse wakefield effects in a reasonably well aligned beamline were found to be negligible [135]. For further details of the wakefield modelling, the reader is referred to reference [85].

10.2 Comparison with Experiment

It is often believed that the emittances generated by PARMELA are overestimates by factors of two or more[32]. Inspection of the foregoing results would seem to lend support to this notion. A consideration of the approximations made by PARMELA (as discussed in detail in section 4.2) and of the experimental tendency for underestimating the true emittance (as discussed in section 7.3.3 make it more likely that the measurement is significantly low.

To reiterate, PARMELA does not include wakefield effects in a self-consistent manner, and is much more likely to underestimate space charge effects than overestimate. Numerical noise, if truly the source of the factors of two or three, should be detectable as an $N^{-\frac{1}{2}}$ dependence of the emittance on the number of simulation particles, when, in fact, the emittance value converges to a number insensitive to N above 10^3 simulations particles, with most simulations completed for this research involving 1.5×10^4 particles. Given that wakefield effects generally do not reduce the emittance, it is difficult to exhume an explanation for PARMELA's apparent overestimates.

By contrast, it is straightforward to establish situations in which the measured

emittance can be a significant underestimate. It is therefore my opinion that it is far more likely that the emittance is underestimated by the experimental measurement than overestimated by PARMELA.

Simulation of the solenoid variation experiment shows poor agreement due to scraping losses in the simulation, giving rise to artificially small emittances away from the emittance compensation minimum. The value of the minimum is in reasonable agreement with the measurement, given the absence of wakefield effects in the simulation. Two sets of simulation emittances are shown, the open circles represent the "100% RMS" emittance, computed by the standard statistical definition, and is strongly influenced by the halo particles. The plus signs represent the "80% FWHM" emittance, which gives a clearer measure of the core emittance of the beam. The minimum measured emittance value ($40 \pm 7\pi$ mm-mr) is within one sigma of the simulated 80% FWHM value at the same solenoid setting, 37π mm-mr. Again, the lack of emittance growth in the simulation away from the compensation minimum reflects scraping losses.

Simulation of the launch phase variation experiment shows reasonable qualitative agreement, with two of the three data points lying within one sigma of the simulated 80% FWHM emittance values. Asterisks on the measurement plot indicate the individual measurements for each phase.

Simulation of the expected uncompressed longitudinal energy spectra is shown with the measured spectra in figure 10.3. The fractional energy spreads (defined as σ_E/μ_E) are in reasonable agreement (1.3% simulated, 1.5% measured), but the presence of "shoulders" on the measured distribution points to wakefield effects unaccounted for in the simulation shown here. The source of the 2.3 MeV difference in

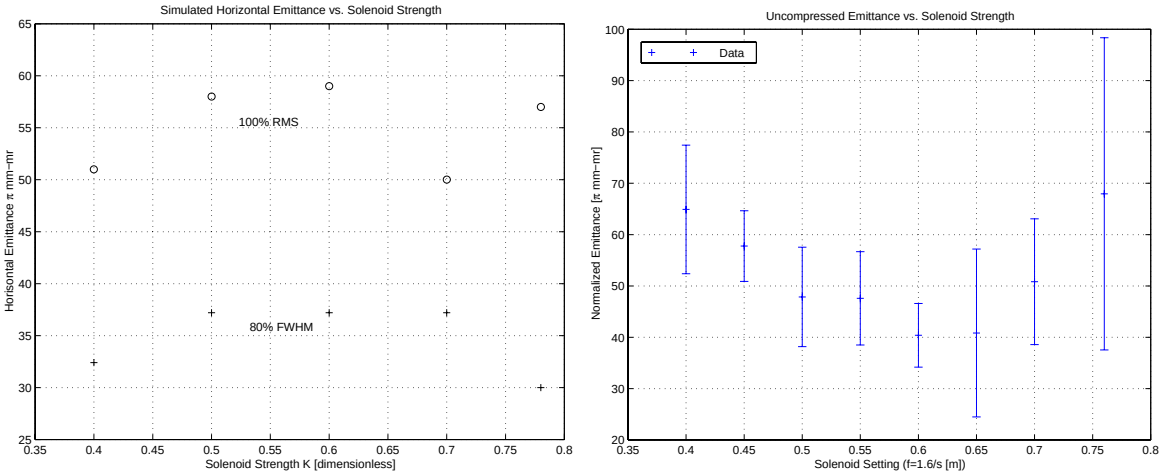

Figure 10.1: Comparison of simulated [left] and measured [right] emittance versus solenoid strength variation

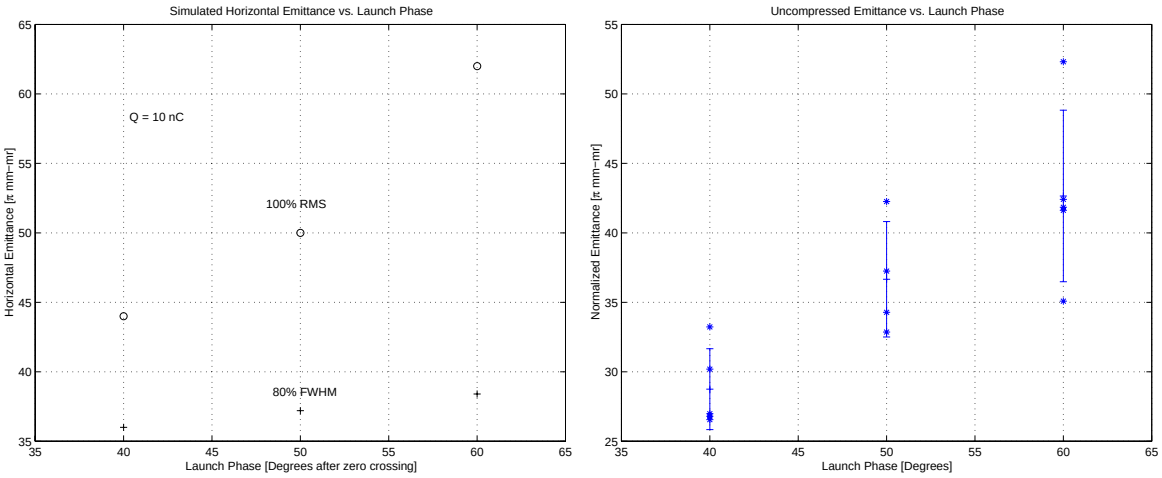

Figure 10.2: Comparison of simulated [left] and measured [right] emittance versus launch phase variation

mean energy between simulation and experiment has not been identified, but could arise from miscalibration of the spectrometer, or overestimation of the accelerating gradients in the gun and linac.

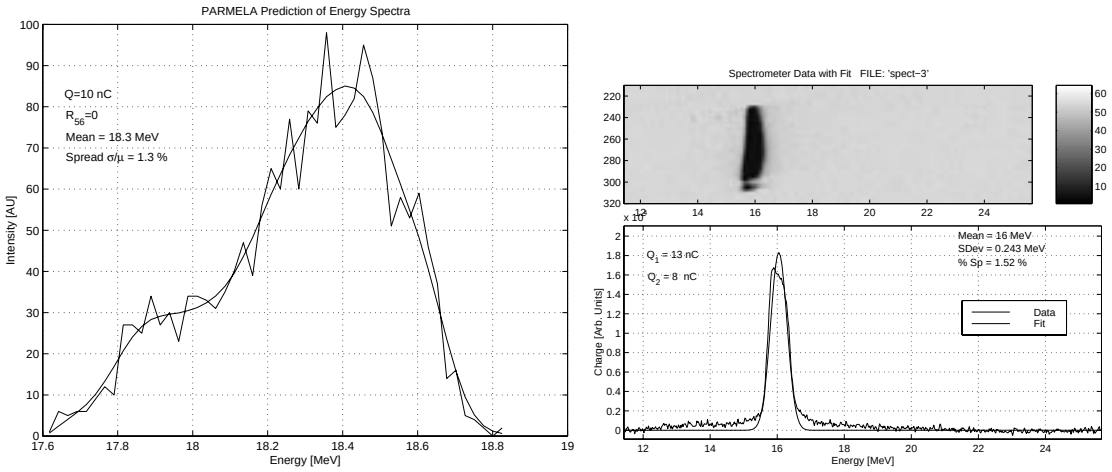

Figure 10.3: Comparison of 8 nC simulated [left] and 8 nC measured [right] energy spectra.

10.2.1 Emittance Dilution Summary

A summary of the suspected sources of emittance dilution, together with estimates of their magnitude (from simulation and direct calculation) is listed in table 10.4 on the next page. Both 100% RMS and 80% FWHM emittance values are quoted from the simulations, notated as ε_r and ε_f, respectively.

Cause	$\varepsilon_{x,N}$ After Gun $\Delta\varepsilon_r$	$\Delta\varepsilon_f$	After Linac $\Delta\varepsilon_r$	$\Delta\varepsilon_f$	$\varepsilon_{y,N}$ After Gun $\Delta\varepsilon_r$	$\Delta\varepsilon_f$	After Linac $\Delta\varepsilon_r$	$\Delta\varepsilon_f$	$\varepsilon_{z,N}$ After Gun $\Delta\varepsilon_r$	After Linac $\Delta\varepsilon_f$
LASER ERRORS	π-mm-mr								π-deg-keV	
Radial profile inhomogeneity[a]	15	8.4	13	6	17	8.4	14	1.2	-30	-30
Gaussian longitudinal profile[b]	10	4..8	15	12	12	7.2	11	15.6	-60	-80
Multi-mode noise profile[c]	5	2.4	7	4.8	4	2.4	2	3.6	-10	0
ELECTROMAGNETIC ERRORS										
Gun field imbalance[d]	10	3.6	15	6	1	6.6	13	2.4	50	45
Linac field imbalance[e]	0	0	1	0	1	1.2	-1	-1.2	10	0
MECHANICAL ERRORS										
Hor. Laser Misalignment	1	0	1	1.2	2	2.4	0	-1.2	10	0
Ver. Laser Misalignment	2	3.6	1	0	1	1.2	-1	0	10	0

[a] Using measured transverse profile, see figure 9.1.
[b] Versus ideal flat top.
[c] See discussion in section 9.2.
[d] Using measured gun field ratio, see section 9.4.
[e] Using measured linac field profile, see figure 9.20.

Figure 10.4: Summary of emittance diluting effects.

Chapter 11

Discussion

The design of an RF photoinjector with performance characteristics that are unique among the world's electron sources has been set out, realized, and tested under somewhat inauspicious circumstances. Performance characteristics, as directly measured, show that even under the unfavorable conditions examined, the photoinjector can produce beams of sufficient bunch charge, nearly sufficient peak current, and tolerable transverse emittance for use as an electron source for the TTF. That simulation of the injector under the conditions of test agrees relatively well lends some confidence to the prediction that under conditions set out in the design, the injector will perform significantly better, yielding more than ample peak current at significantly improved (if not design) transverse emittance values.

The results presented unfortunately represent significantly less than a full trial of the photoinjector's design performance. Although many of the measurements set out in the experimental design chapter have been completed, they were done so largely under circumstances not reflective of what should be expected of a high reliability electron injector for a linear collider facility. As such, Phase II, the high duty cycle test of the injector performance, will be charged will resolving a number of issues, in

addition to those set out in the introduction.

Future research will be challenged with the following additional key questions:

1. What initial focussing kick location gives optimal emittance compensation;

2. Does measured performance match original design specification under more optimal test conditions than those of the prototype experiment;

3. What wakefield corrective measures are required for the TTF photoinjector;

4. What are the degree and physical nature of emittance growth induced in low-energy chicane-based pulse compressors;

as well as the following technical challenges:

1. Direct observation of the emittance compensation process;

2. Continued development of beam diagnostics, particularly for high average beam-power applications;

3. Continued refinement of vacuum system techniques for maintaining delicate photocathode materials and superconducting cavities in a system with warm RF components.

11.1 Implications for the Next Generation Injector

The implications for a next generation injector are several. Given the emittance growth (seen in recent simulations) associated with the pulse compressor, a design eliminating the low-energy pulse compression stage is desirable. Simulations, and

evidence present in measurement, indicate that wakefield effects are of key importance not only to the basic beam quality, but especially to the bunch compression process, with simulations in reference [85] clearly indicating almost complete destruction of the phase energy correlation required for magnetic pulse compression. Further study of the wakefield effects will be required to positively establish the needed rephasing of the gun and linac to compensate the damage.

Clear evidence has been shown that quality of the transverse and longitudinal profiles of the laser pulse is of paramount importance in obtaining good electron beam quality. Careful control of shot-to-shot amplitude variation of the laser pulse energy will also be important for conducting successful experiments both on the injector beam quality, and in the broader context of operating the injector as the first stage of a superconducting accelerator.

For the same reasons as require good laser profile uniformity, the quantum efficiency of the cathode must be uniform as well, and must be ascertained by direct measurement of each cathode used to generate electron beam.

Developing diagnostics for characterizing very dense, often correlated charge distributions remains one of the most important technologically demanding tasks confronting accelerator designers. With the construction of very high duty cycle machines producing closely-spaced bunches comes the added complication of producing very fast diagnostics capable of resolving each bunch of the pulse train. The higher beam powers of modern accelerators make the development of non-intercepting and minimally intercepting diagnostics essential.

Electron injector development will likely follow two parallel, complementary trajectories, the first pursuing improved beam quality by attaining ever higher acceler-

ation gradients at the source, with LILAC and pseudo-spark sources typifying this approach, the second by compensating each of the various defects of real sources, such as the RF field asymmetries induced by input couplers, probes and tuning apparatus (the LCLS and TTF-FEL approach), the RF emittance growth itself (the CANDELA approach), or improvements to the emittance compensation process. All of the latter approaches will greatly benefit from diagnostic techniques capable of resolving the subtle cancellations sought.

11.2 Conclusions

An electron injector capable of producing bunches of the required charge and approximate beam quality for application at the TESLA Test Facility has been designed, built, and initially tested. A reasonable correspondence between simulation and experiment has been demonstrated, from which optimism arises that the injector will produce beam of suitable quality for use as a high charge injector for the next generation linear collider.

Appendix A

Design of an *A*symmetric Emittance Photoinjector

The suitability of an RF photoinjector for use as the undamped electron injector for TESLA was originally suggested by Sheffield. The necessary asymmetric beam spot and unequal transverse emittances require an injector that fully decouples the beam dynamics in the transverse planes, necessitating different beam geometry, quadrupole, rather than solenoidal focussing, and significant redesign of the RF accelerating structure. Initial simulation work on a symmetric gun cavity with quadrupole focussing and a 2D space charge algorithm was done by Rich Sheffield and Steve Russell, with sufficiently encouraging results to warrant further study.

The first issue addressed was the beam geometry. The space charge fields of a round beam are radial, causing equal emittance growth in both planes. By contrast, the fields of a sheet beam are purely normal to the surface and are lower than for a round beam of the same peak current, except near the edges of the sheet, giving rise to unequal emittance growths in the two planes. Nonlinearities in the space charge fields close at the edges of the sheet give rise to most of the emittance growth, as is clear from a plot of the electric fields, shown in figure A.1.

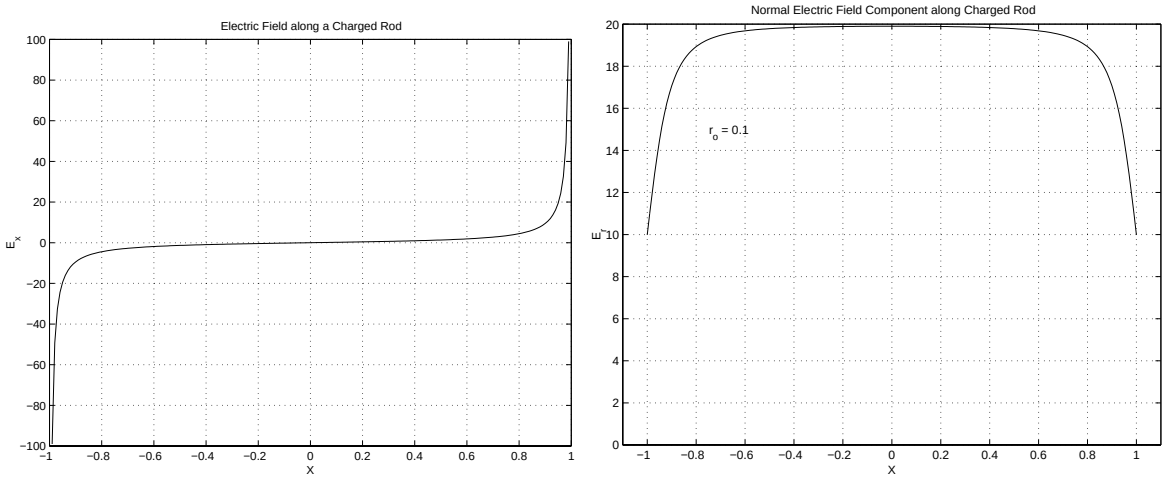

Figure A.1: Transverse space charge fields for a horizontal sheet beam as a function of the horizontal coordinate.

Thus collimation of the small fraction of "guard charge" particles subject to the most nonlinear space charge forces, and hence forming the largest contribution to the emittance, is an attractive way to achieve lower transverse emittances.

Additionally, the cathode thermal emittance is generally taken [32] to be proportional to the initial beam size:

$$\varepsilon_{therm,N} \approx \sqrt{\frac{kT_{\perp}}{m_e c^2}}\sigma \approx 1\pi\text{mm-mr}\sigma[mm] \tag{A.1}$$

where the thermal energies are generally taken to be some small fraction of the energy available to the electrons: $E = h\nu - \phi$, on the order of an electron-Volt or less. Since the thermal contribution scales with spot size, and a very small emittance is sought (1π mm-mr) in the vertical plane, the vertical spot size must be quite small to lower the thermal contribution. RF contributions to the emittance increase like σ^2, similarly requiring a small vertical spot size. As the bunch charge is quite large, and the horizontal emittance is considerably larger (20π mm-mr), the horizontal spot size can be made quite large to reduce the space charge contribution to the emittance.

The next issue addressed was the RF cavity. A circular cavity was initially considered and quickly discarded because of strong plane-coupling radial focussing forces. A "muffin tin" structure, similar in geometry (and at 1.3 GHz, in size) to a tissue box, was considered next for its simplicity. Cylindrical cavities with slot beam tubes similar to those proposed by Schnell and Wilson for CLIC[136] and measured by Kurz et al [137] were examined, not as RF quadrupoles as in the CLIC applications, but as accelerating cavities for the gun. A variant of the muffin tin cavity with elliptical cross section and slotted beam tubes was also considered. All geometries suffered from substantial field flatness problems across the broad dimension of the beam. Substantial energy variations across the horizontal dimension of the beam would result, producing unacceptable chromatic emittance contributions.

Following the recommendation of Roger Miller, a structure investigated for flat beam klystrons was examined, and is shown below in figure A.2. The cavity is made from two waveguides joined by a cutoff waveguide, similar in appearance to a ridged waveguide. In the cutoff region, the boundary conditions (E_z must vanish on upper and lower surfaces) and dispersion relation:

$$k_x^2 + k_y^2 + k_z^2 = \frac{\omega^2}{c^2} \tag{A.2}$$

requires $k_x = 0$ for the fundamental space harmonic in the cutoff region. This implies that the synchronous space harmonic has no variation across the beam horizontally. Additionally, the field geometry in the vicinity of the beam is very nearly Cartesian, with horizontal and vertical RF focussing effects having been consequently almost completely decoupled. Figure A.2 below shows a wireframe sketch and field contours of E_z of a 1.5 cell RF gun constructed from two such H-shaped cavities joined by circular beam tubes.

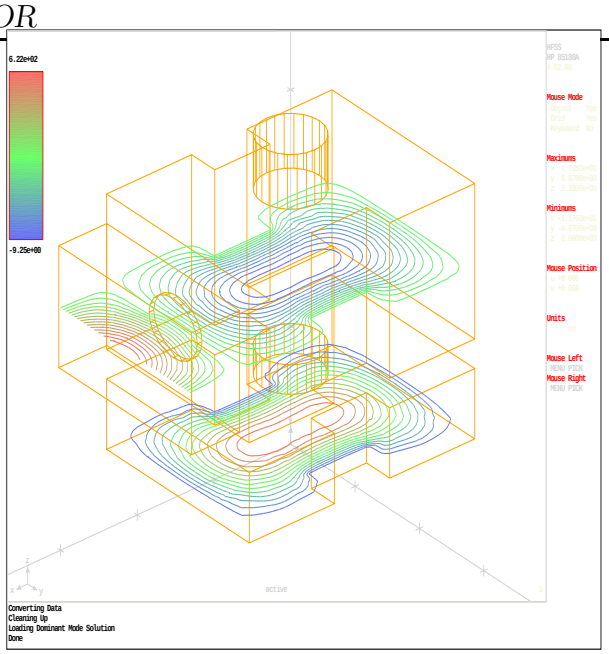

Figure A.2: Gun structure based on coupled waveguides

Field profiles in the horizontal and vertical planes show excellent field flatness, as seen in figure A.3 below.

Having chosen the beam charge distribution and RF cavity, focussing needed to be chosen next. As solenoidal focussing couples the X and Y phase planes under almost all circumstances, it is unsuitable for a flat beam injector. Decoupled focussing from a quadrupole doublet or triplet is needed instead. Given that the gun acceleration gradient is again constrained by available klystron power and considerations of dissipated power to a value similar to that of the symmetric emittance gun, focussing will need to be placed at approximately the same location, requiring the quadrupoles to surround a portion of the gun. Panofsky quads [138] of not unreasonable bore (60 cm x 30 cm) are a compact alternative that would fit tightly to the rectangular exterior of the RF structure. The relative weakness of the Panofsky quad compared with the conventional iron-dominated variety would be acceptable in view of the low

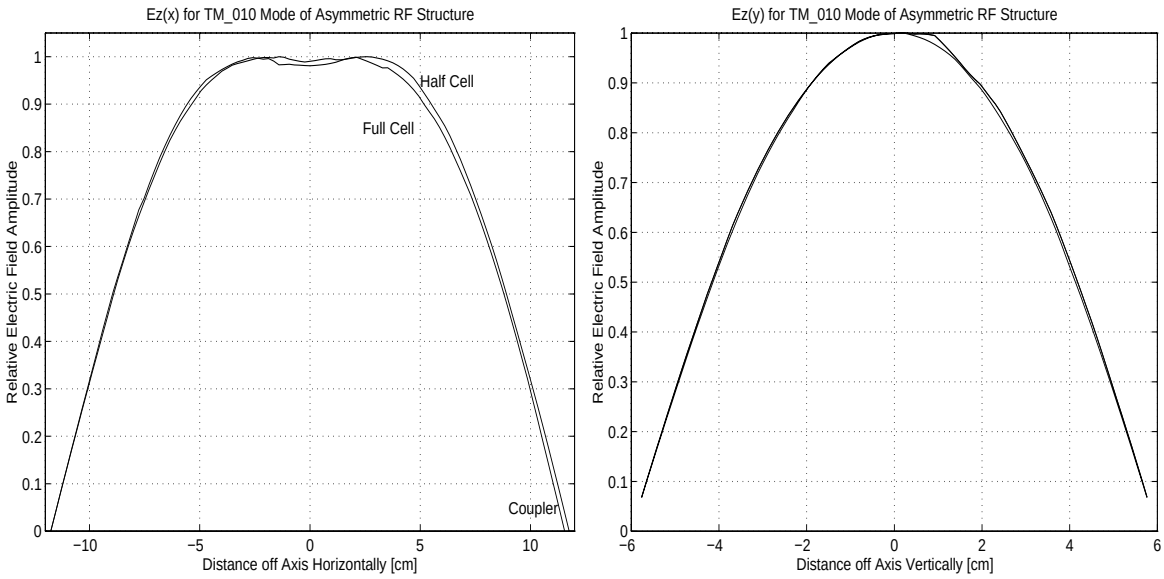

Figure A.3: Horizontal and vertical plane profiles for the accelerating mode.

beam energy and consequent low focussing fields required.

Simulations to understand the strength and required placement of the quads for optimal emittance compensation were undertaken. In all cases, numerical noise from the point-by-point algorithm used by PARMELA dominated the vertical (small-emittance plane) to an extent that made even observation of emittance compensation difficult. As a result, several alternative space charge routines were devised. A potential solver on a Cartesian mesh with the field evaluated by numerical differentiation was written, a variant of the R-Z mesh method was written that used the Green functions of horizontally infinite line charges on a 2-D yz mesh with interpolation, and an ellipsoidal generalization of the standard spherical point-by-point algorithm was written, with the third technique generally being most often used.

Continued efforts on this problem would have underscored the need for a better technique in computing the manifestly 3-D space charge fields. A 3-D finite element

space charge field solver [139] or indeed any fully 3-D technique which represents the charge distribution not as a collection of Dirac delta functions (as do all point-by-point methods), but as smooth functions constructed from an intelligently chosen basis function set, as in the current work of Gianessi [140], is a necessary development step before serious asymmetric photoinjector design work progresses.

Appendix B

Derivations, Explanations

B.1 Explanation of "Measurement Emittance"

The "measurement emittance", also called "FWHM Emittance" to distinguish it from its RMS counterpart, has as its central distinction from the traditional RMS computation of the emittance a reliance on rank statistics, rather than on RMS statistics, with increased insensitivity to outliers in the "wings" of the distributions considered [141].

Consider figure B.1 below, which shows a unipolar, unit-width, zero-mean, unit-probability Gaussian "signal" truncated at $+2 - 1.5\sigma$ with a comparable amplitude bipolar noise function added:

$$f = \{y_i | \exp(-x_i^2/2) + 2(1 - \mathcal{R}(x_i)), x_i \in [0, 1]\} \tag{B.1}$$

where $\mathcal{R}$ denotes a random function distributed uniformly in $[0, 1]$.

Computation of χ^2 for the two fits using the variance-per-point of $\sigma_i = 2/\sqrt{12}$ yields $\chi^2_{RMS} = 850$ and $\chi^2_{FWHM} = 282$, with the latter clearly better. The third method, yielding a $\chi^2 = 31$ is the Newton's method fit polisher working from a quadratic fit to the logarithm of the data. The fit polishing method is described in more detail in the next section.

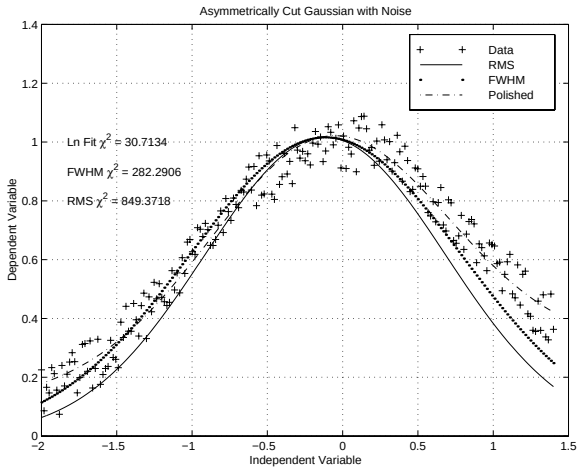

Figure B.1: Noisy Gaussian with RMS (solid), FWHM (dotted) and Polished (dot-dash) fits.

By its very nature, the slit emittance measurement often has sparse statistics and very limited dynamic range (8-bit A/D conversion limits the dynamic range to under 25 dB). Phosphor screen measurements often suffer from large backgrounds from dark current, and often are truncated well before the 2- or 3-sigma point, making the RMS calculation technique underestimate the distribution variance. As the variance is generally either a spot size or a measure of the uncorrelated portion of the emittance, it is important. Streak camera measurements generally offer poor statistics when the highest resolutions are sought from the camera. Figures 9.36 of an emittance slit image, 9.18 of dark current striking a phosphor screen, and 9.4 of a streak camera image illustrate these points.

The measurement emittance uses this FWHM technique to calculate the beam's emittance from a set of slit images. For the actual measurement, the intensity pattern from the phosphor screen is used. For the PARMELA simulations, however, statistics ($\leq 10^4$) do not allow the particles to be passed through a slit mask (which generally

passes $\sim 10^{-3}$ of the incident particles) as statistics would then be unusable. Instead, particles are binned into N_{slit} equal width bins across the beam width. Particles at the edges of the distribution are removed according to collimation fractions defined by the user on the FWHME card (see Appendix E for further detail.) The resulting collection of Gaussians (in momentum) have their mean positions computed by usual definition (eq. (3.7)), but the variances estimated by the FWHM technique.

One more observation is needed before the emittance may be computed using the extracted means and variances. N_{slit} variances and means must be combined (with weights obtained from the integrated intensity of each slit image) to yield the phase space area. The formally correct technique would be to fit a bi-Gaussian distribution in (x, x') space, yielding the Courant-Snyder parameters directly. This technique requires multidimensional, nonlinear least squares fitting, and is computing intensive. For an online emittance diagnostic, a rapid technique was sought for calculating emittances from video data, preferably at 2 Hz or more. Consider again the unit-variance, zero-mean, unit-amplitude Gaussian. With the three points $\{\mu-\Gamma/2, \mu, \mu+\Gamma/2\}$ having been obtained for each slit image, the original distribution variance is reconstructed by brute-force RMS statistics as:

$$\sigma^2 = \sum_{i=1}^{N} w_i(x_i - \mu)^2 / \sum_{i=1}^{N} w_i \tag{B.2}$$

which when applied to the mean and FWHM points using $w_i = A\exp(-(x-\mu)^2/(2\sigma^2))$ yields:

$$\sigma^2 = \frac{\frac{1}{2}(-\Gamma/2)^2 + 1(0)^2 + \frac{1}{2}(\Gamma/2)^2}{1/2 + 1 + 1/2} = \Gamma^2/8 \tag{B.3}$$

which systematically underestimates the real variance ($\sigma = \Gamma/\sqrt{8\ln(2)}$ by a factor of $1/\sqrt{\ln(2)}$. Thus the means and FWHM points (three per slit) are combined according

to (B.2), but with the necessary systematic correction of $1/\sqrt{\ln(2)} \approx 1.20$ applied. Inspection of figure 7.9 shows that the method correctly interprets input data.

As the beam halo often carries much of the emittance, collimations may be performed at user-defined ratios to establish the transverse emittance as a function of the charge, in a similar spirit to the curves of emittance versus current proposed by Lejeune and Aubert [65]. Thus "70% FWHM Emittance" specifies the one-sigma, normalized, π-exclusive emittance computed by first collimating off 30% of the particles in the particular phase plane concerned, then following the FWHM prescription above. Similarly, the "70% FWHM Bunch Length" is obtained by first collimating off 30% of the particles at the longitudinal ends of the distribution, then computing the bunch length by the FWHM procedure. Note that the collimation cuts in each phase plane remove, in general, non-overlapping sets of particles. It is often the case that the emittance compensation process produces cross-overs at the longitudinal ends of the distribution, and hence most of the transverse and longitudinal emittance arises from particles at the longitudinal extremes of the distribution.

B.2 Newton-Raphson Based Fit Polisher

Fit polishing, or further refinement of an initial trial set of fit coefficients, is useful when the data are subject to substantial noise, complicated backgrounds, or when using somewhat degenerate basis functions. As an example that occurs in beam measurements, a beam spot occurring on a round screen illuminated roughly uniformly by dark current poses the distinct challenge of fitting a Gaussian beam against a parabolic background.

The criteria for fitting is most often minimization of the χ^2 merit function. Fit functions generally have several undetermined parameters, making the problem of minimizing χ^2 a multidimensional one. Beam spot images are generally fit at minimum to Gaussians (3 parameters) or Gaussians with linear backgrounds (5 parameters). Emittance slit data shown here have up to 23 free parameters (10 loosely constrained Gaussians + a linear background). Pepper pot data can easily run to 60 free parameters (10 bi-Gaussian distributions, one per hole). Constraints, such as the regular spatial patterns expected of slit and pepper pot data, must be used to prevent fitting programs from running amok.

A substantial subset of the trial fit coefficients $\vec{a} = (a_1, a_2, ..., a_N)$ must already be evaluated, with some of the less significant parameters (e.g. relating to the background) potentially left unevaluated until the polishing step. A multidimensional fitting algorithm is then necessary to handle the minimization problem, of which a number of excellent advanced algorithms exist [130].

Minimization of χ^2 amounts to root finding for $\nabla_{\vec{a}}\chi^2 = 0$ provided the initial fit coefficients are sufficiently close to the minimum, making the Newton-Raphson method a natural choice for its simplicity, if not for its rate of convergence. Of course

this method will fail, as indeed most methods (except simulated annealing) will fail, if the χ^2 function has many local minima, or has undefined derivatives blocking the path of "modest incline" traversed by the search. In general, functions used for beam profile fitting do not manifest such bad traits, and the χ^2 function is not so geographically challenging that the fitting algorithm is apt to hang up in a local minimum. If it does, the basis functions should be checked carefully for degeneracy.

The algorithm is straightforward, with the following steps forming a single refining iteration:

1. Evaluate $\chi^2(a_1, ..., a_j + \delta a, ..., a_N)$,$\chi^2(a_1, ..., a_j, ..., a_N)$,$\chi^2(a_1, ..., a_j - \delta a, ..., a_N)$

2. Construct the three-point discrete approximations of the needed derivatives:

$$\begin{aligned}(\chi^2)'(a_j) &= \frac{1}{2\delta a}(\chi^2(a_j + \delta a) - \chi^2(a_j - \delta a)) \\ (\chi^2)''(a_j) &= \frac{1}{\delta a^2}(\chi^2(a_j + \delta a) - 2\chi^2(a_j) + \chi^2(a_j - \delta a))\end{aligned}$$

3. Advance one of the fit parameters "downhill" using the Newton-Raphson algorithm:

$$a_{j,n+1} = a_{j,n} - \frac{\partial\chi^2/\partial a_i}{\partial^2\chi^2/\partial a_i^2} \tag{B.4}$$

4. Re-evaluate χ^2 at the new point, reject step if larger

5. Continue with next fit parameter a_{j+1} until all N parameters have been advanced a step.

The Newton-Raphson method and the discrete formulæ for the derivatives are $\mathcal{O}(\delta a^2)$ [142], so this algorithm is at best quadratically convergent in step size δa.

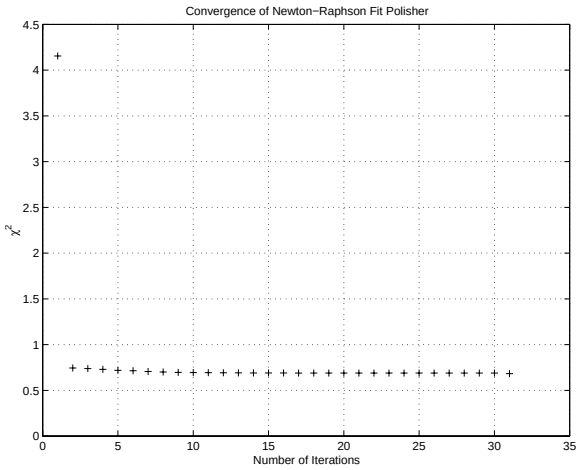

Figure B.2: Convergence of Newton-Raphson fit polisher with number of iterations.

Figure B.2 below shows the convergence of the method with number of iterations (not step size), indicating diminishing returns after about 10 iterations.

Fits for which the χ^2 merit function has numerous local minima can be handled (albeit slowly) by this method as well. Variation of the initial fit "guess" and subsequent polishings may lead to different minima. No guarantees exist that any of the minima found are the global minimum, that is left to human judgment.

Appendix C

Design of RF Tuning Paddles

Originally, the tuning of the RF gun was to have been made with RF tuning "paddles", which are simply tuning plungers with a narrow blade that protrudes normal to the plunger face. The orientation of the blade displaces differing amounts of magnetic field (for outer wall mounted tuners) depending on whether the tuner is parallel or perpendicular to the magnetic field lines, giving very fine frequency adjustment. Owing to the relative insensitivity of the gun structure to cell tuning errors, such fine adjustment was deemed unnecessary, and the paddles reduced to simple plungers. The analytic calculation of the paddle performance is believed unique, and outlined here.

Small run-time adjustments to the resonant frequency of the gun full cell (of order 1 MHz or less) are provided for by means of a tuning "paddle" placed in the outer wall, depicted schematically below. Axial motion of the paddle provides tuning in the same manner as a plunger would, while rotation of the paddle controls whether the axis of the paddle is parallel to the cavity field polarization, thereby sampling the $\cos(k_z z)$ drop off of the fields, or perpendicular, intercepting roughly constant fields, and giving the greatest frequency shift. From Slater's theorem, a perturbation

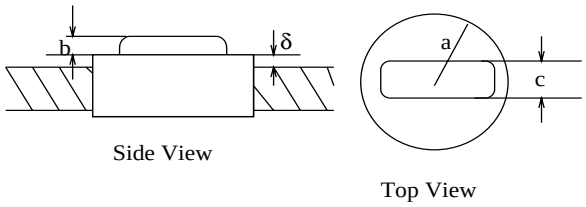

Figure C.1: Schematic Drawing of the Tuning Paddle

in the geometry of an RF cavity produces a shift in the resonance frequency that is approximately proportional to the amount of electric and magnetic field energy displaced:

$$\omega^2 = \omega_o^2(1 + \frac{1}{2U}\int_{\mathcal{V}}(\mu_o H^2 - \epsilon_o E^2)dV) \tag{C.1}$$

with U representing the total stored energy in the cavity, and $\mathcal{V}$ the volume displaced by the perturbing object. The electric and magnetic fields for the lowest space harmonic of the $TM_{010,\pi}$ mode of a pill box cavity (with on axis irises at both ends), with radius R and length L_z are approximately:

$$\begin{array}{l} E_r(\rho,\theta,z) = -E_o\frac{k_z}{k_r}J_1(k_{01}\rho/R)\cos(k_z z) \\ E_z(\rho,\theta,z) = E_o J_o(k_{01}\rho/R)\sin(k_z z) \\ H_\phi(\rho,\theta,z) = E_o\sqrt{\frac{\epsilon_o}{\mu_o}}\frac{k}{k_r}J_1(k_{01}\rho/R)\sin(k_z z) \end{array} \tag{C.2}$$

with $k_r = k_{01}/R$, $k_{01} = 2.4048...$ and $k_z = \pi/L_z$. The volume of integration may be separated into two parts, the first estimating the frequency shift due to the cylindrical portion of the paddle, the second, the shift due to the paddle itself. Assuming the boundaries follow constant coordinate surfaces for ease of integration, (reasonable only for small perturbations to the cavity geometry) both integrals are of the form:

$$\begin{aligned} \Delta W &= \int_{\mathcal{V}}(\mu_o H^2 - \epsilon_o E^2)dV \\ &= \epsilon_o E_o^2\int_{-\alpha}^{\alpha}d\theta\int_{\rho_1}^{\rho_2}\rho(\kappa^2 J_1^2(k_{01}\frac{\rho}{R}) - J_o^2(k_{01}\frac{\rho}{R}))d\rho\int_{\frac{L_z}{2}-d}^{\frac{L_z}{2}+d}\sin(k_z z)^2 dz \end{aligned} \tag{C.3}$$

where $\kappa \equiv \frac{k}{k_r}$. As the paddle is indeed a small perturbation on the exterior wall, the fields may be expanded in a Taylor series about $\rho = R$, to yield:

$$\begin{array}{l} J_o(k_{01}\rho/R) \sim -J_1(k_{01})k_{01}(\rho/R-1) + \frac{J_1(k_{01})k_{01}}{2}(\rho/R-1)^2 \\ J_1(k_{01}\rho/R) \sim J_1(k_{01}) - J_1(k_{01})(\rho/R-1) - \frac{1}{2}J_1(k_{01})(k_{01}^2-2)(\rho/R-1)^2 \end{array} \quad \text{(C.4)}$$

and the integrals evaluated (keeping terms to second order in $(\rho/R-1)$):

$$\Delta W = \epsilon_o E_o^2[2\alpha][J_1^2(k_{01})R^2\kappa^2(\rho/R-1)(1+\frac{3}{2}(\rho/R-1))\ |_{\rho_1}^{\rho_2}][d+\frac{1}{2k_z}\sin(2k_z d)] \quad \text{(C.5)}$$

where the notation ΔW is understood to mean the difference of the displaced magnetic and electric field energies $\Delta W_H - \Delta W_E$. The cylindrical portion of the paddle may be approximated by a square cross section plunger of equal cross sectional area, yielding the contribution:

$$\Delta W^c = \epsilon_o E_o^2[\frac{a\sqrt{\pi}}{R}][J_1^2(k_{01})\kappa^2\frac{\delta}{2}(-3\delta-2R)][\frac{a\sqrt{(\pi)}}{2}+\frac{1}{2k_z}\sin(a\sqrt{(\pi)}k_z)] \quad \text{(C.6)}$$

which is, of course, independent of the paddle's orientation with respect to the electric field polarization. The contribution due to the paddle when aligned with the field is:

$$\Delta W_{\parallel}^p = \epsilon_o E_o^2[\frac{c}{R}][J_1^2(k_{01})\kappa^2\frac{b}{2}(-3b-6\delta+2R)][\frac{a\sqrt{\pi}}{2}+\frac{1}{2k_z}\sin(a\sqrt{\pi}k_z)] \quad \text{(C.7)}$$

and when perpendicular to the field is:

$$\Delta W_{\perp}^p = \epsilon_o E_o^2[\frac{2a}{R}][J_1^2(k_{01})\kappa^2(-3b-6\delta+2R)][\frac{c}{2}+\frac{1}{2k_z}\sin(ck_z)] \quad \text{(C.8)}$$

where a,b,c, and δ are defined in figure C.1 above. With the total stored energy in a TM_{010} pill box field expressed as:

$$U = \frac{\epsilon_o}{4}\pi R^2 L_z(J_1^2(k_{01}) + (\frac{k_z}{k_r})^2 J_2^2(k_{01}))E_o^2 \quad \text{(C.9)}$$

the frequency perturbation due to the entire paddle may be written:

$$\begin{array}{l} \delta\omega_{\parallel} \approx \omega_o\frac{1}{4U}(\Delta W_{\parallel}^p + \Delta W^c) \\ \delta\omega_{\perp} \approx \omega_o\frac{1}{4U}(\Delta W_{\perp}^p + \Delta W^c) \end{array} \quad \text{(C.10)}$$

It is convenient to set the paddle dimensions to give a few megahertz frequency variation in 5 mm of insertion distance, and a frequency difference due to paddle rotation equal to three times the minimum settable frequency difference. By this choice, a large frequency adjustment range is available with coarse control via linear positioning and fine control via paddle rotation. Figure C.2 shows the estimated tuning performance of the paddle over the useful range of motion. The main body of the paddle is chosen to have a radius $a = 1.0$ cm, which, when taken together with an assumed linear positioning precision of 20 microns yields a minimum frequency resolution of 28.0 kHz/20 micron. Thus the paddle dimensions $b = 1.0$ cm and $c = 3.0$ mm are chosen to yield roughly 2×28.0 kHz over the 90 degree rotation of the paddle. Figure C.2 reflects these dimensional choices.

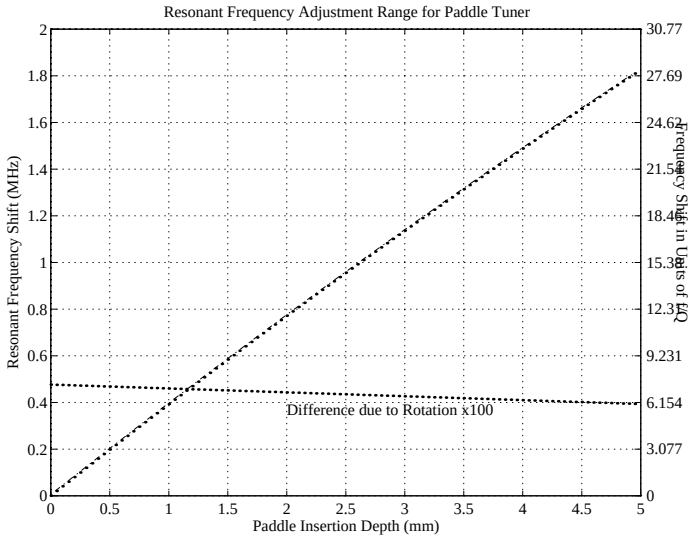

Figure C.2: Frequency Tuning Performance of Paddle-Type Tuner

Appendix D

Photocathode Excitation Laser Requirements

Although a number of different methods of producing electrons have been developed and successfully used in electron guns, the highest current densities ($> 1kA/cm^2$) possible with a laser driven photocathode are well matched to the high peak current requirements for the TTF and TESLA500 linacs. Additionally, some flexibility is available in the shaping of the charge distribution within the laser-generated beam, allowing some control over the nonlinear space charge contributions to the emittance.

A laser system suited to the requirements of the TTF and TESLA500 injectors is summarized in table D.1 below. Laser pulse energies are listed for two photocathode materials which roughly represent the two extremes of photocathode performance: a metallic cathode (Yttrium is taken as an example), with low quantum efficiency (QE), and a semiconductor photocathode (Cs_2Te) with excellent QE. Restrictions on the timing jitter arise from the need to launch the bunch at a particular time during the RF cycle to minimize the RF contribution to the emittance growth, while restrictions on the amplitude jitter are needed to ensure consistent charge per bunch, and thus consistent beam loading in the downstream linac sections.

Parameter	*Required Value*	
(Photocathode Material)	Cs_2Te	*Metallic*
(Photocathode QE)	1%	0.05%
Micropulse Energy	$> 4\mu$J	$> 80\mu$J
Wavelength	< 300 nm	
Pulse Length (Flat top)	28 ps	
Micropulse Repetition Rate	1 MHz	
Macropulse Length	$800 - 1000$ pulses	
Macropulse Repetition Rate	10 Hz	
Timing Jitter	< 1 ps	
Amplitude Jitter	$< 5\%$	
Pointing Stability	$< 100\mu$rad	

Table D.1: Laser requirements for the TTF/TESLA500 Photoinjectors

Discussions with members of industry have led to the conclusion that a laser matching the outlined requirements is technically feasible, although challenging. The conflicting requirements of high gain (for useful output pulse energy) and very long pulse trains (requiring little sag or fluctuation in the gain as subsequent pulses are amplified) will require state-of-the-art gain media, and potentially some form of closed-loop control system, as suggested by the researchers at the Max Born Institute.

Development of a laser satisfying the above parameters is underway at the Max Born Institut für Physik. A preliminary proposal [143] for a three-stage Ti:Sapphire/-LiSaF system is shown schematically in figure D.1 on the next page. Pulses from a Ti:sapphire oscillator are selected to form the required pulse train structure, stretched, then amplified in two successive LiSaF gain stages and re-compressed. For added amplitude control, a feed forward system allowing inter-pulse amplitude control surrounds the two doubling stages needed to produce the UV output.

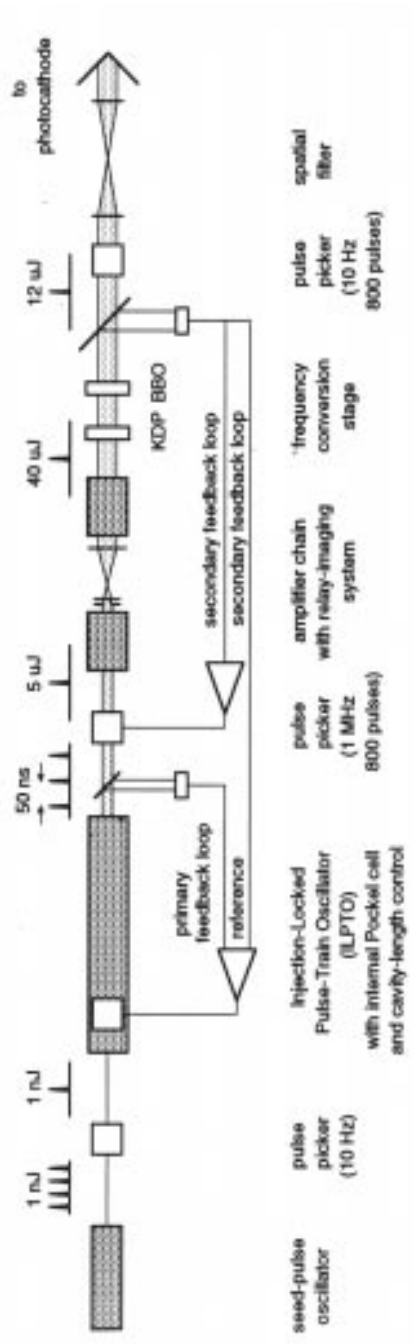

Figure D.1: Preliminary design concept of MBI laser, from I. Will, TTF/Hasylab Meeting Proceedings, DESY, May 6, 1994.

Development of another laser satisfying all but one of the parameters needs (the repetition rate, 1 Hz instead of 10 Hz.) has been designed and is in the later stages of commissioning at Fermilab in the AØ experimental hall. The University of Rochester laser is shown schematically in figure D.2.

D.1 Laser Stability Requirements

Within the course of routine operation of a laser-driven electron photoinjector random fluctuations in the laser pulse intensity, temporal and spatial profiles will result in variations of the final beam quality. Prescribing the beam quality implies a set of constraints on the amplitudes of the random variations ("jitter"). Laser parameter tolerances are derived from straightforward beam dynamics considerations, and are examined numerically for the particular case of the high brightness, high charge Injector II for the TESLA Test Facility (TTF) described elsewhere [144]. Constraints on variation in the charge and phase of each bunch arise from As the behavior of fields in a superconducting linac structure are completely dominated by beam loading effects, uniformity of loading is essential, with only very slow modulations of the average beam current permissible. This places constraints on the bunch-to-bunch ($< \pm 10\%$) and long term integrated charge variations ($< \pm 2\%$ over 100 bunches), as well as phase jitter ($< \pm 1$ps). Different constraints on the energy spread apply for general TTF machine studies or for the proposed SASE FEL. An energy jitter of $< \pm 10\%$ bunch-to-bunch (resp. $< \pm 5\%$ for the FEL), and an integrated energy jitter of $< \pm 2\%$ (resp. $< \pm 1\%$) are required.

The effects of five types of fluctuations are examined: global intensity jitter (variations in the total number of photons reaching the photocathode), phase jitter (vari-

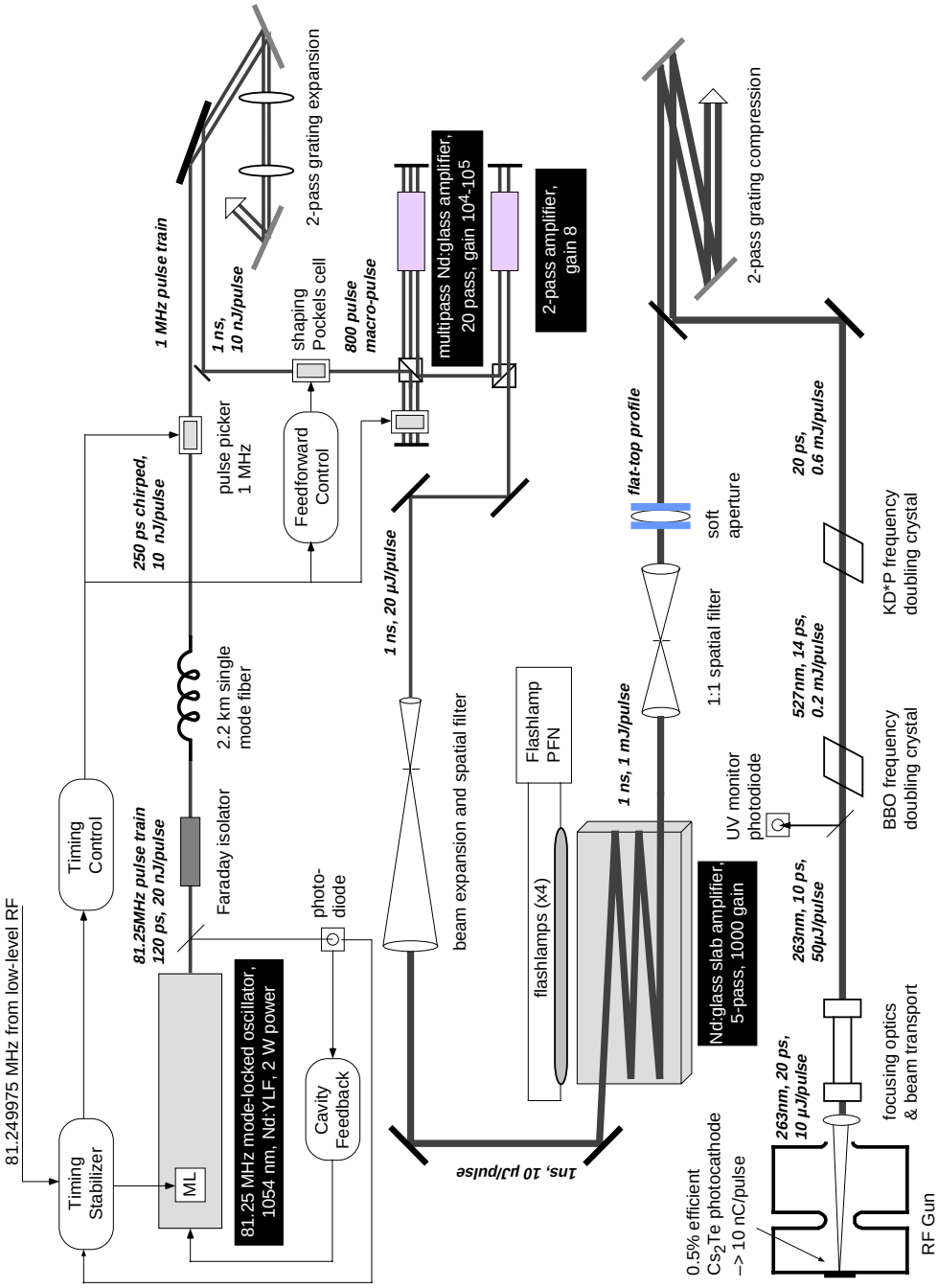

Figure D.2: A Schematic of the 1 Hz x 1 MHz UOR Laser.

ation in the temporal relationship of the laser pulse and the RF crest), spatial jitter (beam centroid motion, beam radius variation), and fluctuations of laser intensity during a single laser pulse. Simulations for each effect were carried out using the code PARMELA, which includes the effects of space charge, RF fields, static magnetic focussing fields, and image charges on a metallic cathode, but does not include any other wakefield effects. The study was carried out on a parameter-by-parameter basis, that is, it was not a factorial study, covering all the possible combinations of the five errors.

In all numerical simulations, the "design emittance" and the "perturbed emittance" were taken to occur at the same z location (305 cm downstream from the photocathode, 65 cm from the exit of the booster linac). The effects of beam compression were not included in the calculations. In simulations requiring a change in the beam size a commensurate change in the dimensions of the underlying space charge mesh dimension was made to ensure a comparable space charge field calculation. Simulations for each data set were carried out only on computers of the same architecture to avoid discrepancies arising from the slightly different computational algorithms used by different computer manufacturers.

D.1.1 Integrated Intensity Fluctuation

The space charge contributions to the transverse and longitudinal emittances for an RF photoinjector are known [69] to scale like the first power of Q in the absence of bunch volume variations (as distinct from the ideal Q-scaling case, where the bunch volume is scaled to preserve the bunch density). The RF contribution to the emittances scales as σ_r^2 and σ_z^3 for the transverse and longitudinal emittances,

respectively. As the evolution of the beam sizes are determined by the second integrals of the space charge forces ($\sim Q^1$), the RF forces ($\sim Q^0$), and the external focussing forces ($\sim Q^0$), and in general the latter two are significantly stronger than the former for physically well controlled beams, the beam sizes manifest a weak Q^1 scaling. The transverse and longitudinal RF emittances therefore manifest weak Q^4 and Q^3 scalings respectively.

Simulations were conducted assuming all other beam parameters remain constant. Figure D.3 shows the percent variation of transverse and longitudinal emittances with charge. At 11 nC and above, particle loss (greater than 5%) occurs, as is indicated by the change of plotting symbol. As the transverse emittance is dominated by space charge effects, a simple linear fit was performed, yielding $\delta\epsilon_x/\epsilon_{x,o}(\%) = 6.45\delta Q$ [nC]. The longitudinal emittance shows curvature from the RF as well as space charge growth, and thus the fit $\epsilon_z/\epsilon_{z,o}(\%) = \sqrt{83.5Q^2 + 0.0000178Q^8}$ [nC] was chosen.

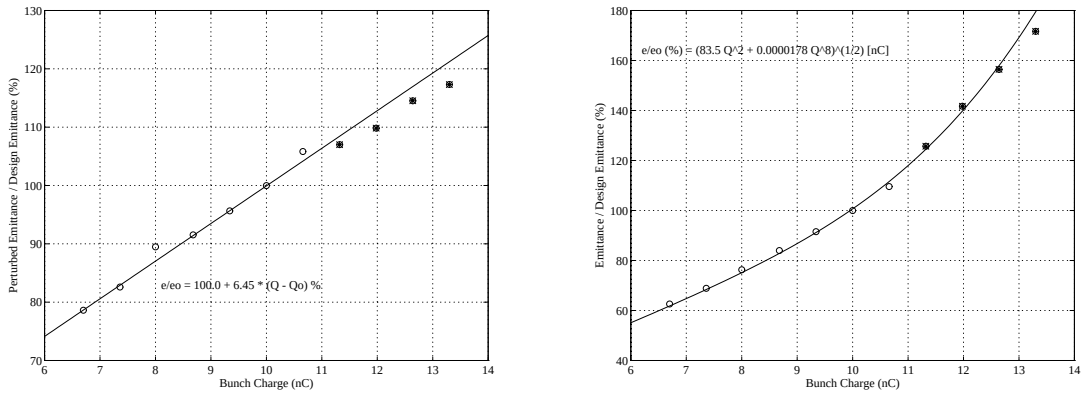

Figure D.3: Effects of integrated intensity fluctuation on transverse and longitudinal emittances

D.1.2 Spot Radius Fluctuation

Fluctuations in the radius of the laser spot on the photocathode may result from thermally-dependent lensing effects within the laser amplifier media. Such changes are expected to be slow, largely non-random, and potentially compensated for by such straightforward means as "over filling" the cathode (illuminating an area larger than the high-QE area of the cathode), but are included here for completeness.

Kim's analysis of the space charge emittance contribution leads to:

$$\epsilon_{x,z}^{SC} = \frac{\pi}{4}\frac{1}{\alpha k_{RF}}\frac{1}{\sin(\phi_o)}\frac{I}{I_A}\mu_{x,z}(A) \tag{D.1}$$

where the particulars of the charge distribution are represented by the geometrical form factor $\mu(A)$, the beam rest frame aspect ratio is $A \equiv \frac{\sigma_x}{\gamma\sigma_z}$, and $I_A = \frac{ce}{r_e}$ is the Alfven current. Kim estimates the transverse and longitudinal form factors for bi-Gaussian distributions to be well approximated by:

$$\begin{array}{l} \mu_x(A) = \frac{1}{3A+5} \\ \mu_z(A) = \frac{1}{1+4.5A+2.9A^2} \end{array} \tag{D.2}$$

For $A \ll 1$, as it is for most of the beam lifetime, the form factors imply space charge emittance contributions that scale like r^1 transversely and longitudinally.

Simulations were carried out varying the laser spot diameter, and commensurately varying the radial mesh used in the space charge calculation, to ensure an analogous computation of the space charge forces. Figure D.4 shows the results of the simulations. The transverse emittance remains dominated by the space charge contribution, and thus the increase in emittance from the RF is quite small (at the 1-2% level over the ± 10% parameter range explored). A linear fit $\delta\epsilon_x/\epsilon_{x,o}(\%) = 36.7\delta r$ [cm] was chosen for the transverse emittance, while the higher order fit $\epsilon_z/\epsilon_{z,o}(\%) = \sqrt{17530r^2 + 68.4r^{-4}}$ [cm] was chosen for the longitudinal emittance.

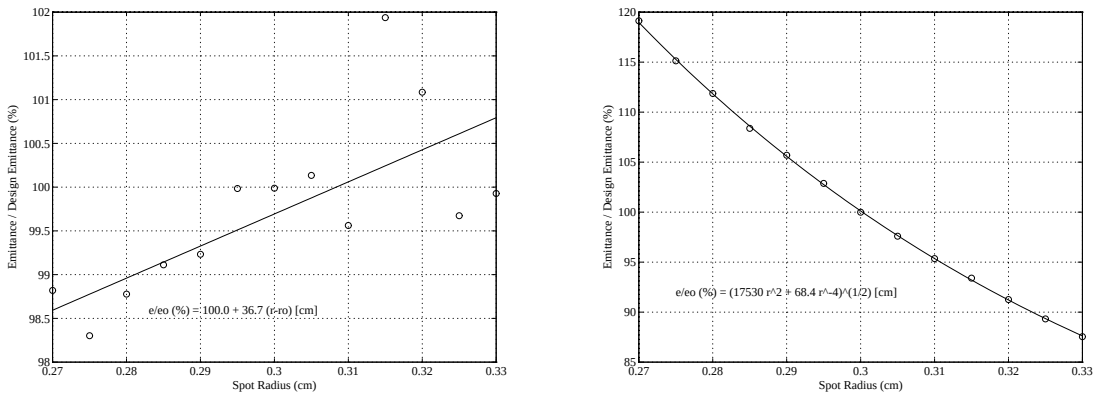

Figure D.4: Effects of spot radius fluctuation on transverse and longitudinal emittances

D.1.3 Pulse Length and Phase Fluctuation

Pulse length jitter and phase jitter may arise from instabilities in the master oscillator that seeds the laser. Phase jitter results in the launch of the electron bunch at a time other than the optimal time, causing the RF contribution to the emittance to increase.

The space charge contribution (again following Kim) to the emittances scale like σ_t^{-1} transversely and longitudinally. The RF contribution scales like σ_t^2 transversely, and σ_t^3 longitudinally.

The space charge contribution to the transverse emittance, which decreases with increasing pulse length, nearly washes out the rapid emittance growth due to the time dependent RF focussing, yielding a slight variation of the transverse emittance over the parameter range of interest. The longitudinal emittance, dominated by RF, grows rapidly with beam size. A linear fit in the transverse plane yields: $\delta\epsilon_x/\epsilon_{x,o}(\%) = 0.972\sigma_t[ps]$, while a nonlinear fit for the longitudinal emittance yields: $\epsilon_z/\epsilon_{z,o}(\%) = \sqrt{8970 - 81900\sigma_t^{-2} + 0.000180\sigma_t^6}$ [ps]. The bunch length used in the fits and on the

plots is defined to be half the flat-top pulse length. The effect of pulse length variation on the emittances are shown in figure D.5 below.

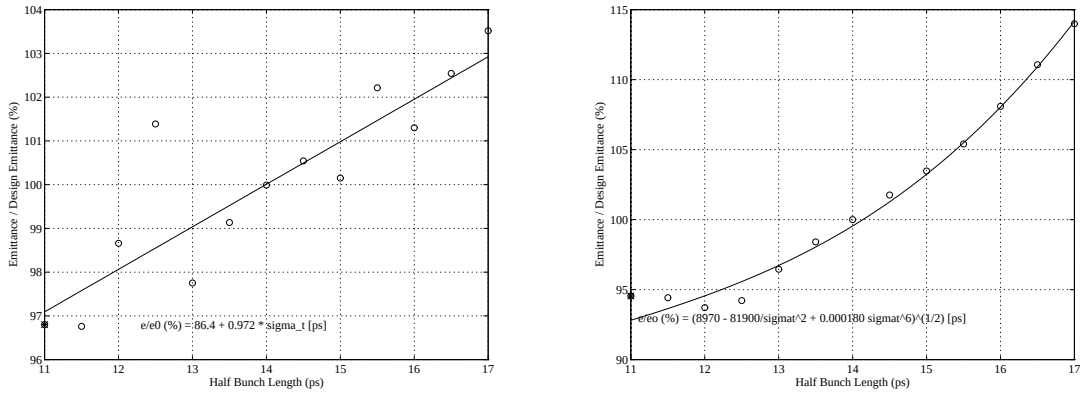

Figure D.5: Effects of pulse length fluctuation on transverse and longitudinal emittances

Jitter in the laser pulse with respective to the RF wave causes the bunch to receive a larger time-dependent defocussing kick from the RF, resulting in an increase in the RF emittance contribution. Following Kim [69] I estimate:

$$\Delta\epsilon_x^{rf} = \alpha k_{rf}\sigma_x^2\sigma_\phi \sin(\phi)\Delta\phi \sim \phi^1 \tag{D.3}$$

to leading order in ϕ for the transverse emittance, and (recalling that $\phi \sim \pi/2$ for minimal RF emittance growth):

$$\Delta\epsilon_z^{rf} = \frac{\alpha(\Delta\phi)^4}{4k_{RF}\sqrt{2\cdot 5!}}\left|\frac{3}{2}\pi\cos(\phi) - \sin(\phi)\right|\delta\phi \sim \phi^1 \tag{D.4}$$

to leading order in ϕ for the longitudinal emittance [145]. Figure D.6 manifests the expected sinusoidal behavior in both planes. The leading term in the expansion for the sine motivates the linear fits: $\delta\epsilon_x/\epsilon_{x,o}(\%) = 2.80\delta\phi$ [Degrees] for the transverse emittance, and $\delta\epsilon_z/\epsilon_{z,o}(\%) = 1.23\delta\phi$ [Degrees].

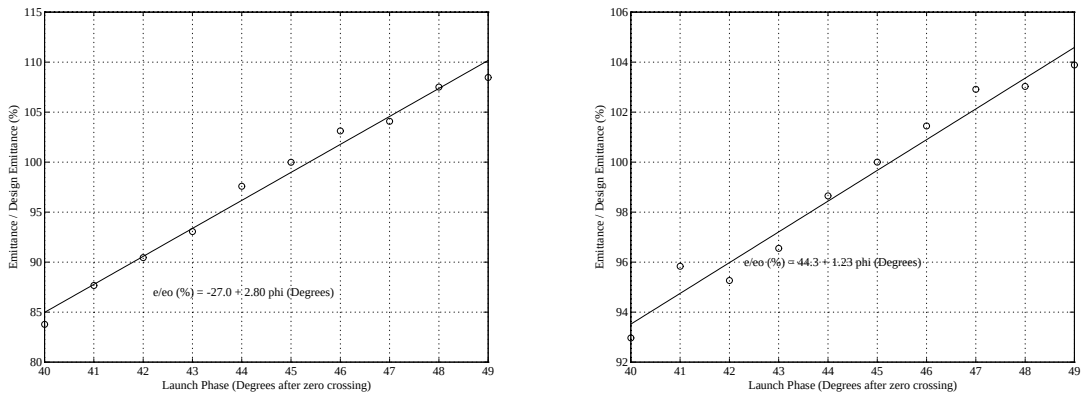

Figure D.6: Effects of phase jitter on transverse and longitudinal emittances

D.1.4 Spot Centroid Fluctuation

Laser spot centroid fluctuations give rise to a beam that is launched off the electric and magnetic axes of the gun and focussing assembly, causing the beam to experience dipole kicks from both the RF fields and from the beam wakefields, and to experience more of the nonlinear RF field variation, giving rise to fierce emittance growth and particle loss.

Simulations of both horizontal and vertical offsets were conducted, and the results cross-checked for any discrepancies. From simulation, serious beam losses are seen to occur when the beam is displaced a short distance from the axis (> 1.5 mm). Results of simulations (which exclude wakefield effects) are shown in figure D.7 below, with offsets greater than 1.0 mm resulting in substantial ($> 5\%$) particle loss, denoted on the plots by a change of plotting symbol.

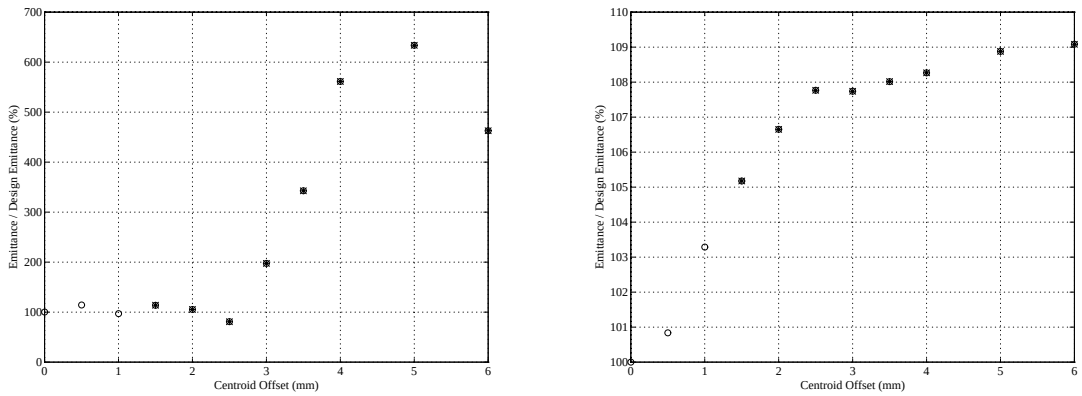

Figure D.7: Effects of centroid fluctuation on transverse and longitudinal emittances

D.1.5 Finite Risetime and Temporal Intensity Fluctuation

The effects of finite rise time and intensity fluctuation within a single laser pulse were explored by generating a flat-top distribution with a finite risetime and a sinusoidal amplitude modulation. The distribution function for study was chosen to be:

$$I(t) = I_o(1 + A_n \cos(k_n t)) \left[\tanh(k_r(t + \tau/2)) - \tanh(k_r(t - \tau/2))\right] \tag{D.5}$$

where A_n is the amplitude modulation depth, k_n is the amplitude modulation wavenumber, and $k_r = 2\tanh^{-1}(0.80)/\tau_{rise}$ sets the rise time of the pulse. Higher harmonics of the pulse length were examined up to the expected interesting limit of $k_n \approx \pi/r_o \approx 1\ \mathrm{mm}^{-1}$ set by the smallest (radial) dimension of the bunch. The limited statistics of the simulations (4000 macroparticles) resulted in distributions that only rough approximated the desired current distributions. As can be seen from figure D.8 however, the desired harmonic content of each distribution is present, despite the noise. A risetime of 5 ps was chosen for all simulations. Particle distribution traces have been separated vertically on the plot by integer multiples of 100 particles per bin for clarity.

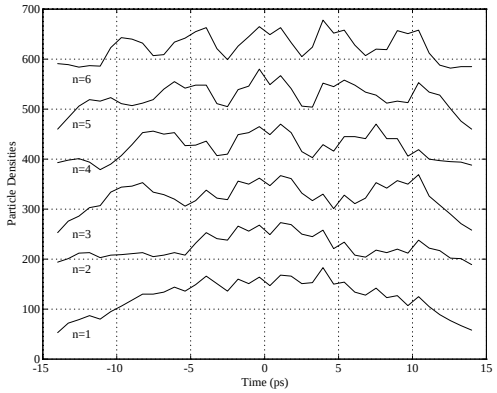

Figure D.8: Initial longitudinal distributions with 20% amplitude modulation

The effects of the six chosen perturbed longitudinal distributions is plotted in figure D.9 below. As expected, the effects of the higher harmonics result in too small a perturbation of the space charge fields to appreciably affect the transverse emittance, and negligibly affect the longitudinal emittance.

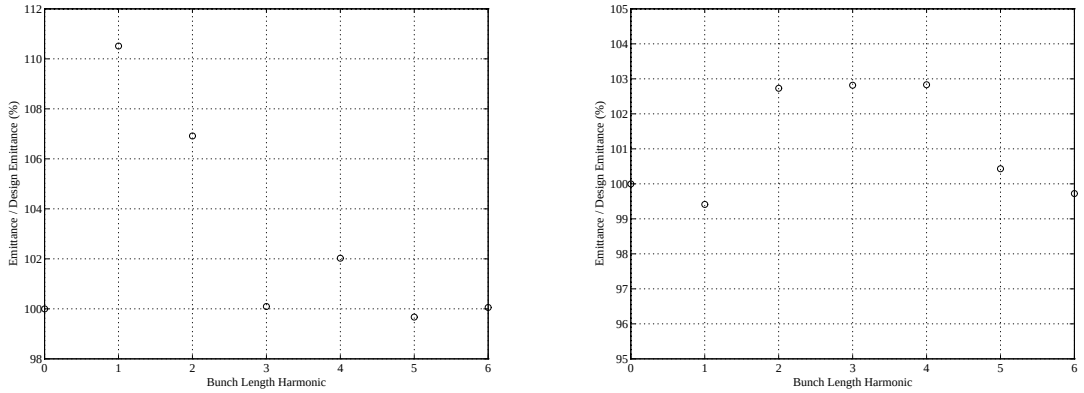

Figure D.9: Effects of intensity fluctuations on transverse and longitudinal emittances

D.1.6 Summary

The foregoing analysis may be summarized as a list of maximum fluctuations tolerable in any given parameter. In general the effects explored here are not independent, implying correlative effects that in most cases exacerbate the effects of each fluctuation. Setting a bound of $\pm 10\%$ on the fluctuations of the transverse and longitudinal emittances requires each contribution to be $\leq \pm 4.5\%$ under the optimistic assumption that correlations between effects do not appreciably add to the total emittance growth. Table D.2 below reflects these considerations.

Parameter	Nom. Value	Fluctuation Limit	Sensitivity
Phase	45.0^o	$1.6^o = 3.4$ ps	ϵ_x
Integrated Intensity[a]	2.7 μJ	66 nJ = 2.4%	ϵ_z, beam loss
Temporal Intensity Fluctuation[b]	0%	10%	ϵ_z
Centroid Offset	0.0 mm	1 mm[c]	beam loss
Pulse Length[d]	28 ps	2.6 ps = 9.3%	ϵ_z
Spot Radius	3.0 mm	72 μm = 2.7%	ϵ_z

[a] Assumes 2 % QE photocathode, 10 nC per bunch
[b] Amplitude of first harmonic only, subsequent harmonics have less stringent limits
[c] Does not reflect wakefield effects
[d] Full flat top pulse length

Table D.2: Constraints on Laser Parameter Jitter

Appendix E

New/Modified Features of PARMELA

The modified version of PARMELA detailed here is available from via anonymous ftp from the server:

`waldo.fnal.gov`

as the compressed tar file:

`/pub/outgoing/ecolby/parmela.tar.Z`.

Download the file into a new directory, `uncompress` it, execute:

```
tar xvf parmela.tar
```

and then read the enclosed `readme` file. After editing the Makefile to suit your particular computer architecture, compilation should be straightforward.

The following paragraphs detail input "cards" that have been either expanded in function or added to PARMELA. See section 4.3 for a general description of the changes embodied below.

Existing PARMELA command cards that have been modified and new PARMELA command cards are listed below, both in summary form with changes in **bold** print, and in detailed form, explaining the meaning, units, and default values for the asso-

ciated parameters.

Existing commands cards that have been modified

CONTINUE DWT NSTEPS NSC NOUT **NSLICE**

INPUT **11** NP SIGMAT MAXT SIGMAR MAXR W0 DW0 DWT **HBX HBY HBPHI HBW0 ASPECT XOFF YOFF ANOISE FNOISE**

RUN IRUN IP FREQ Z0 W0 LTYPE INTERP THRESH

SCHEFF BEAMI DRMESH DZMESH NR NZ NIP PL OPT **REMESH** RWAL POINT **SOL NCH LINEL**

START PHI0 DWT NSTEPS NSC NOUT **NSLICE NSPT**

New command cards

ASPECT AR

AUTOBUCK RI,RO,ZL,ZU

BFSETUP

BSHIFT XSHIFT,YSHIFT,XPSHIFT,YPSHIFT

BSOLENOID RI,RO,ZL,ZU,J

BZMAP SCALEF

CCELL LX LY LZ APERX APERY IOUT PHI1 PHI3 E1 E3 NC DWTMAX SYM CFREQ CTYPE BZ NFC NFC2

COLLIM TYPE LOW HIGH

FFKICK

DFILES TYPE1 NTYPE1 PAR1 PAR2 PAR3 ... TYPE2 NTYPE2 PAR1 PAR2 PAR3 ... TYPE3 NTYPE3 PAR1 PAR2 PAR3 ... -999

FWHME XCUT1 YCUT1 ZCUT1 XCUT2 YCUT2 ZCUT2 ...

MAKERS

MAPGEN NP CALX CALY SIGMAT MAXT W0 DWT

POISSON

RFSETUP

TRACE X,X'**,Y,**Y'**,**Φ**,E**

VERBOSE

WAKE wtype dumpflag scalef

NOWAKES CHARGE

In addition, the traditional 'restart' capability of PARMELA has been extended to allow a running simulation to be stopped at **any** time, with a restart file and the required change to the input deck being automatically generated. To stop a Parmela run at any time, type:`% kill -15 <pid>` at the UNIX prompt, once you have established the process id for the running PARMELA process. For large jobs, PARMELA may take up to a minute to terminate. To resume execution, simply type the command 'parmela'. The restart file, named 'parmrstrt' contains a complete description of the phase space, as well as other parameters needed for PARMELA to resume execution. The parmin6000 file is automatically modified to include the required 'restart' card after the 'run' card. Of course, if you desire to kill the process outright, do so with the usual `kill -9 <pid>`.

ASPECT AR

> This card will allow approximation of elliptic cavity modes
> by scaling the RF field components of an axisymmetric cavity

(generated with a preceding CELL card) by 1/AR in the horizontal direction and by AR in the vertical direction.

AUTOBUCK RI,RO,ZL,ZU

This card declares the physical dimensions and location of a bucking solenoid placed behind the cathode. Coordinates assume the point (r=0,z=0) to be the center of the photocathode. This card must follow the BSOLENOID cards of the solenoids whose fields are to be compensated. The required current density needed to yield Bz=0 on the photocathode is automatically calculated and applied. Up to 5 background solenoids can be handled by this routine.

RI Inside radius of bucking coil

RO Outside radius of bucking coil

ZL Lower z coordinate of coil

ZU Upper z coordinate of coil

BFSETUP

This card, when placed on the first or second line of the input file sets the number of particles to 2 and disables space charge calculations to allow rapid background solenoid field adjustment without the need to modify the SCHEFF or INPUT cards.

BSHIFT XSHIFT,YSHIFT,XPSHIFT,YPSHIFT

This card will shift the magnetic center of the background solenoid field by the vector (xshift,yshift) and the orientation of the solenoid by angles (XPSHIFT,YPSHIFT) to allow modelling of alignment errors.

BSOLENOID RI,RO,ZL,ZU,J,[Zlow,Zhigh]

This card defines a set of coils that fill the prescribed r and z coordinates with a conductor carrying a current density J. This card defines a background solenoidal field ranging from Zlow to Zhigh.

RI	Inside radius of background solenoid coil
RO	Outside radius of coil
ZL	Lower z coordinate of coil
ZU	Upper z coordinate of coil
J	Current density averaged over the entire cross section (in A/cm^2)
Zlow	(Declare with first BSOLENOID card only) lowest z location to have non-zero background field (must be > 1E-13)
Zhigh	(Declare with first BSOLENOID card only) highest z location to have non-zero background field
Notes:	This card causes an array to be loaded with 1000 on-axis B-field values ranging from Zlow to Zhigh. Setting Zhigh too far away will adversely affect the accuracy of the B-field by making the mesh

too coarse.

BZMAP SCALEF LOWZ HIGHZ
FILENAME

This card provides for direct reading of the background magnetic field strength from an external file named FILENAME.

SCALEF Scale factor to rescale fields with. (If none entered, defaults to 1.0 ⇒ use field map exactly as read in.)

LOWZ Defines the region of field information to read in from the

HIGHZ POISSON file, in POISSON coordinates.

Notes: Poisson must be run to produce the output file OUTPOI in a certain format. In particular, choose your coordinates such that the z axis corresponds to the L index (in the "y" direction) of Poisson, then use the following output option controlling CON values (enter when running Poisson):
*42 1 1 1 LMAX
where LMAX is the upper mesh index of the problem mesh. (Look in file OUTLAT for this information.)

Make sure to declare the appropriate symmetry:
*19 1 *46 1
is usually the correct choice for solenoids. See the Poisson/

Superfish reference manual for details.

CCELL LX LY LZ APERX APERY IOUT PHI1 PHI3 E1 E3 NC DWTMX SYM CFREQ CTYPE FLAG NFC NFC2

FILENAME

[**FILENAME2**]

This card is intended to introduce fully 3-D RF cavity fields by one of two methods: by the reading of a field map produced by another code, such as Superfish or HFSS, or by building the field up from a triple Fourier series expansion. Both the internal and external field maps are expressed in Cartesian coordinates. Up to 4 maps may be stored in memory for use in simulations.

LX,LY LZ — X,Y, and Z dimensions (in cm) of a rectangular cavity (Lx and Ly are only used when using Fourier series for the fields)

APERX APERY — X and Y dimensions (in cm) of the (elliptic) exit aperature (viz. the distance from the beam axis to the nearest obstruction in the given direction; not the full width of the opening)

Important note: the aperature values also declare the transverse dimensions of the internal field mesh. Choosing unreasonably large values of APERX and APERY to neglect particle loss at the exit will adversely affect the field accuracy.

IOUT Print status (Vestigial option from CELL card)

PHI1 Phase of lowest mode of cavity

PHI3 Phase of next harmonic of cavity (Defaults to PHI1) [Note: this is NOT the relative phase of the first and third harmonics]

E1 Peak Electric Field strength on axis [Ez(0,z)] (in MV/m) for fundamental mode

E3 Peak Electric Field strength on axis [Ez(0,z)] (in MV/m) for next excited harmonic. (Defaults to E1/3)

NC Cell identifier number (other cells with this number will derive their electric field structure from the same Fourier coefficients)

DWTMX Maximum temporal step in this cell (Defaults to 10 degrees)

SYM Symmetry: 1⇒upstream half, -1⇒downstream half, 0⇒full cavity

CFREQ Cell frequency in MHz (Defaults to FREQ as set on RUN card) Setting CFREQ to 0 causes a DC field of value E1 to be applied.

CTYPE Cell type code. CTYPE=1, code will assume an "ideal" rectangular cavity with only the lowest (TM000) mode excited. Type CTYPE=2 assumes an "ideal" rectangular cavity with the first and third (TM000 and TM222, respectively) modes excited in a E1:E3 amplitude ratio. CTYPE=10 (resp. 20) derive field structures for one mode (resp. two modes) from the Fourier coefficients listed in FILENAME (resp. FILENAME for fundamental, FILENAME2 for next harmonic)

CTYPE = -99,-199 ⇒ read full field map from external file

FILENAME for fundamental, and (if ctype=-199) file FILENAME2 for next harmonic. External files are overwritten on the first reading with properly interpolated field maps.

The field maps should cover the last half of the cell. For a half cell, this means a region of dimensions APERX x APERY x Lz, while for a full cell, the region APERX x APERY x Lz/2. The mesh of the external field map should not exceed the declared resolution of the internal map (40x40x100) in any dimension. The mapped fields should be normalized. (Peak field in entire map should have an absolute magnitude no greater than 1.0)

FLAG Determines which field components to turn off during the run. (Useful for separating out the contributions of RF and space charge in the emittance and examining the effects of pnderomotive focussing). Defaults to 0.

0 - Use all components (Ex,Ey,Ez,Hx,Hy,Hz)

1 - Electric focussing (Ex,Ey,Ez,0 ,0 ,0)

2 - Magnetic focussing (0 ,0 ,Ez,Hx,Hy,0)

3 - Accelerate only (0 ,0 ,Ez,0 ,0 ,0)

NFC Number of Fourier coefficients to be found in file FILENAME (Max: 10x30x30=9000). The filename (16 characters or less) must be written on the line immediately following the CCELL card.

NFC2 Number of Fourier coefficients to be found in file FILENAME2

(Max: 10x30x30=9000). The filename (16 characters or less) must be written on the line immediately following the FILENAME card.

FILENAME The file FILENAME should be in the same directory as the Parmela executable, and should list the (normalized) Fourier coefficients in the following record format:

$$IJKA_{ijk}$$

Note that since the indices of each Fourier coefficient accompany it on the same line that the ordering of the coefficients in the file need not be sequential.

The triple Fourier Series used is:

$$E_x(\vec{r},t) = \sum_{i=0}^{30}\sum_{j=0}^{30}\sum_{k=1}^{10} A_{ijk} \sin k_x x \cos k_y y \sin k_z z$$

$$E_y(\vec{r},t) = \sum_{i=0}^{30}\sum_{j=0}^{30}\sum_{k=1}^{10} A_{ijk} \cos k_x x \sin k_y y \sin k_z z$$

$$E_z(\vec{r},t) = \sum_{i=0}^{30}\sum_{j=0}^{30}\sum_{k=1}^{10} A_{ijk} \cos k_x x \cos k_y y \cos k_z z$$

$$k_x = \frac{2\pi(i+1/2)}{L_x} \quad k_y = \frac{2\pi(j+1/2)}{L_y} \quad k_z = \frac{\pi k}{L_z}$$

The origin of coordinates has been taken to be on the beam axis in the upstream opening of the cavity.

FILENAME2 This file is required only when CTYPE=20 is chosen, and should have the same structure as the other Fourier coefficient (or field map) file.

FIELD MAP INFORMATION: the field map is generated and stored in common /c3flds/ for the downstream half of the cavity only, on a 40x40x100 point mesh.

The field map file should cover the downstream half of the RF cell over the following physical dimensions:
-APERX to APERX, -APERY to APERY, Lz/2 to Lz for a full cell (SYM=0), or 0 to Lz for a half cell. (SYM=-1 or +1). Note that even if you are using the a +1 symmetry half cell, the field map must still cover the downstream half RF cell, the appropriate reflection of coordinates being done by PARMELA. The origin of coordinates is on axis in the upstream side of the map.

The ASCII file should be in the following tab- or space-delineated format:

Low-x High-x Step-x !Omit these three header lines

Low-y High-y Step-y !for the binary file

Low-z High-z Step-z

Ex(1,1,1) Ey(1,1,1) Ez(1,1,1) Hx(1,1,1) Hy(1,1,1) Hz(1,1,1)

Ex(2,1,1) Ey(2,1,1) Ez(2,1,1) Hx(2,1,1) Hy(2,1,1) Hz(2,1,1)

... ...

The first three lines give the physical mesh bounds (in [cm]) and the mesh size. (also in [cm]). PARMELA will truncate meshes larger than its own internal mesh and will interpolate meshes that are coarser than its internal mesh, but will return an error if the loaded mesh covers a physical region smaller than the internal mesh, or is finer than the internal mesh. (recompile changing the parameters NMESHX, NMESHY, and NMESHZ if you desire a finer mesh.) The E-field values must be listed at the time when the e-field is a maximum, and the H-field values must be listed at the time when the H-field is a maximum, one quarter period later. Note that the indices permute in standard FORTRAN ordering, with the leftmost index (labelling x mesh planes) incrementing the fastest, and the rightmost (labelling z mesh planes), the slowest.

SUPERFISH / OUTSHY files:

The conversion program "poi2par" will read an uneditted OUTSHY file to produce a PARMELA binary field map file. The OUTSHY file must cover a radial region $\sim$5% larger than the intended region to be used in PARMELA, and must cover one half of a cell. (i.e. If

you're mapping a full RF cavity, use OUTSHY to produce two separate files, one covering the upstream half, the other the downstream half, then process separately and include them in the PARMELA run with two separate CCELL cards.) For optimal performance, choose the Superfish mesh resolution to match the PARMELA mesh resolution: 40 x 40 x 100 mesh points.

HFSS Calculator Field Dumps:

The conversion program "hfsss" (still under development) is designed to read an HFSS space calculator dump of the E and H fields over the irregular tetrahedral mesh and produce a PARMELA binary field map. As with OUTSHY maps, full RF cells must be mapped into two separate files, and entered on two contiguous CCELL cards.

URMEL files:

A conversion program is in the works, but is not yet finished.

MAFIA files: MAFIA output files are unsupported at this time.

SOPRANO : Output from Soprano is unsupported at this time.

ARGUS : Output from Argus is unsupported at this time.

COLLIM TYPE LOW HIGH

This card provides for custom spatial filtering of the beam, as

is accomplished with a collimator.

TYPE Code to describe what type of collimator is used:

1 - vertical slit (collimates in horizontal plane)

2 - horizontal slit (collimates in vertical plane)

3 - user defined (modify the routine COLLIM)

LOW Lower coordinate bound, in [cm].

HIGH Upper coordinate bound, in [cm].

EQUAD ZSTART ZEND K XFACT YFACT

This card is designed to allow an external quad to be placed around an RF cavity. This card works only with the CCELL card.

ZSTART Starting z location of the quadrupole field, in global coords. (with the surface of the photocathode taken to be z=0) [cm].

ZEND Ending z location of the applied qudrupole field. [cm]

K Gradient, k>0 $\Rightarrow$ horizontally focussing, [Gauss/cm]

XFACT Multiplier for quad strength in horizontal plane

YFACT Multiplier for quad strength in vertical plane

FFKICK

Place this following a CCELL card to cause the transverse kick due to the fringing fields in the previous RF cavity to be calculated by a method analogous to Busch's theorem, using Rosenzweig's form for the integrated transverse kick:

$$\Delta(\gamma\beta_y) = y(\frac{eE_0}{m_e c^2})\cos(\frac{\pi x}{L_x})\sin(\omega t + \phi_0)$$

INPUT 11 NP SIGMAT MAXT SIGMAR MAXR W0 DW0 DWT HBX HBY HBPHI HBW0 ASPECT XOFF YOFF ANOISE FNOISE TANOISE TFNOISE **FILENAME**

ITYPE ITYPE=11 invokes Jerome Gonichon's "Quiet Start"

NP Number of particles

SIGMAT Temporal sigma (in picoseconds). If SIGMAT < 0, then a user-defined subroutine called LASER will be called to produce the temporal behavior of the laser pulse. See preamble to subroutine for specific instructions.
NOTE: If ANOISE is nonzero, then this is the risetime of the laser pulse in picoseconds.

MAXT Cut on temporal distribution (in picoseconds), half-length of flat top if ANOISE is nonzero.

SIGMAR Spatial sigma (in cm) = horizontal dimension of beam
If SIGMAR is negative, a user defined subroutine XSECTN will be called to produce a custom cross section shape. If SIGMAR=-666, then (X,Y) distribution will be generated by the rejection method from the image file FILENAME.

MAXR Cut on spatial distribution (also in cm) If SIGMAR=-666, then RMAX

specifies the scaling factor to use in adjusting the magnification of the input. Defaults to 1.0 .

WO Mean emission energy (in MeV)

DWO Energy spread (in MeV)

DWT Clock step size, same as DWT on START card (Degrees)

HBX Hammersley sequence base for X dist. generation (choose: 1)

HBY Hammersley sequence base for Y dist. generation (choose: 2)

HBPHI Hammersley sequence base for PHASE dist. gen. (choose: 3 for Gaussian, -3 for uniform distribution. Choosing a negative base number overrides the SIGMAT setting above)

HBW0 Hammersley sequence base for ENERGY dist. gen. (choose: 5)

Notes: In general, the base choices suggested here 1,2,3,5 can be substituted by any four prime numbers. Higher base numbers result in larger scale structure (i.e. "stripes" in the distribution) and should be avoided. DO NOT use the same base number twice, or a perfectly correlated distribution in the two parameters will result.

ASPECT Ratio of vertical to horizontal beam dimensions. (Assumed 1 if omitted) If ASPECT < 0, then beam cross section is rectangular, not elliptic.

XOFF X distance to displace laser spot from symmetry axis, [cm]

YOFF Y distance to displace laser spot from symmetry axis, [cm]

ANOISE Amplitude of intensity noise on laser pulse. (0.0 to 1.0)

FNOISE Harmonic number of intensity noise modulation applied to laser (eq. if FNOISE=10, the intensity modulation will have ten periods over the bunch length.

TANOIS Amplitude of transverse intensity noise on laser pulse. (0.0 to 1.0) (This option induces sinusoidal variations in the x-directions)

TFNOIS Harmonic number of transverse intensity noise modulation applied to laser (e.g. if TFNOISE=10, the intensity modulation will have ten periods over the bunch length.)

MAKERS

A restart file of the type generated on receiving signal 15 (SIGTERM) is generated when this card is reached, but unlike the SAVE command, execution continues.

NOWAKES CHARGE

Added anywhere before the START card, this card will supress any wakefields (all WAKE cards will be ignored), unless the optional argument CHARGE is supplied.

CHARGE Number of fundamental charges in bunch (total) = Q_{tot}/e. Used when diagnosing wakefield effects with space charge off. This value will override the value set on the SCHEFF card(s).

POISSON ZOFFSET RMULT [ZMAPL ZMAPH]
FILENAME

This card causes a POISSON field map to be read into the static B-field arrays RBFLD and ZBFLD with an offset in z given by ZOFFSET, and with a scale factor RMULT applied to every field component value. [rmult defaults to 1.0, zoffset defaults to 0.0] First POISSON card must carry start and stop coordinates of map ZMAPL, ZMAPH.

Thr program POI2PAR is available to read POISSON output files and interpolate onto the standard PARMELA mesh.

RFSETUP

This card, when placed on the first or second line of the inpt file sets the number of particles to 2 and disables space charge calculations to allow rapid RF phase adjustment runs without the need to modify the SCHEFF or INPUT cards.

SCHEFF BEAMI DRMESH DZMESH NR NZ NIP PL OPT REMESH RWAL POINT SOL NCH RMACRO

BEAMI Beam current in amps if BEAMI > 0, in number of charges otherwise

RMESH Initial mesh radius [cm] (Defaults to 5.0 cm)

ZMESH Initial mesh length [cm] (total, not half length of mesh)
(Defaults to 5.0 cm)

NR Statrting number of mesh points in radial direction. (Max:40,
default: +20) If NR is negative, remeshing will only change the
mesh dimensions, not the number of mesh points.

NZ Starting number of mesh points in logitudinal direction. (Max: 800,
default: +20) If NZ is negative, remeshing will only change the
mesh dimensions, not the number of mesh points.

NIP Number of adjacent bunches (typically just set to zero)

PL Distance between adjacent bunches
(also simply zero for single bunch case))

OPT Number of rings to use in Gaussian quadrature (typically set = 0)
If OPT>0, the BNL mesh method is used, if OPT<0, the old method
is used. If OPT=4 or 5, then image charges on a metallic cathode
are included. If OPT is an even number, binning occurs in equal
volume rings, if odd, in equal thickness rings.

REMESH Remeshing criterion: REMESH > 0 $\Rightarrow$ remesh when either the rms beam
radius or rms beam length changes by a factor of REMESH.
REMESH < 0 $\Rightarrow$ remesh when either the maximum
beam radius or maximum beam length changes by a factor of REMESH.
(Defaults to 0.05 implying a remesh when rms Rbeam or rms Zbeam
changes by 5 percent.)

REMESH = 0 ⇒ never remesh.

RWAL Radius of conducting wall. (=0 means no wall)

POINT Radius of Cloud of charge used in Point-by-Point method
If point is negative, images on cathode are included in calc.
When using ellipsoidal macroparticles, this is the distance
(expressed as a multiple of the longest semi-major axis length of
the ellipsoids) at which the fields are assumed to become the
same as those of sperical charge distribution. Defaults to 3.

SOL Point-by-point algorithm: 0-uses spheres, 1-uses "rods" composed
of NCH discrete charges of charge Q/NCH
RZ-mesh method algorithm: 0-use LANL image charge method, 1-use
LANL/UCLA hybrid method

NCH Number of charges to subdivide each charge into (obsolete)

RMACRO Size of macroparticle, expressed as a multiple of the of the
corresponding interparticle spacing. Defaults to 2.

START PHI0 DWT NSTEPS NSC NOUT NSLICE NSPT

PHI0 Launch phase of bunch w.r.t. RF [Degrees] (If set to -99,
program will use gradient of first RF cell and Kim's criteria
to calculate the proper phase [Kim's criteria yields two roots
for alpha > 0.891, this uses the root closer to 90 Degrees])

DWT Step size in degrees

NSTEPS Total number of time steps to take

NSC Mod on timestep for space charge calculation

NOUT Mod on timestep for output of RMS beam quantities; controls also the timesteps when slice emittances and trace files can be written.

NSLICE Mod on timestep for output of slice emittance data

NSPT Number of slices (even!) to take at each sample time
(Default is 14 slices)

FWHME XCUT1 YCUT1 ZCUT1 XCUT2 YCUT2 ZCUT2 ...

XCUTn Percentage of particles to include in horizontal FWHM emittance calculation. Halo is symmetrically cut off using this criterion. Specify up to five triplets of values, ending with a -999.

YCUTn Percentage of particles to include in vertical FWHM emittance calculation.

ZCUTn Percentage of particles to include in horizontal FWHM emittance calculation.

NOTE: The third set of cut values (XCUT3 YCUT3 ZCUT3) are used for the slice emittance calculation as well. (if nslice!=0)

Default: calculate 90

CONTINUE DWT NSTEPS NSC NOUT NSLICE

DWT Step size in degrees

NSTEPS Total number of time steps to take

NSC Mod on timestep for space charge calculation

NOUT Mod on timestep for output of RMS beam quantities

NSLICE Mod on timestep for output of slice emittance data

DFILES TYPE1 NTYPE1 PAR1 PAR2 PAR3 ... TYPE2 NTYPE2 PAR1 PAR2 PAR3 ... TYPE3 NTYPE3 PAR1 PAR2 PAR3 ... -999

The DFILES card should follow right after the RUN card to work properly.

TYPEn Type code for file to produce:

Type Code	**Description**	**Parameters**	**Filename**
1	Space charge impulse file	Timestep number(s)	scrz__.d sckm__.d sccc__.d
2	Phase space dump	Timestep number(s)	psd__.d
3	RZ mesh size	none	remesh.d
4	$\beta(z), \gamma(z)$	none	betag.d
5	Initial phase space	none	initps.d
6	E,B fields in RF cell	Cell number	rfc_h_.d
7	RF cell impulse dump	Timestep number(s)	rfi__.d
8	Static B-field map $B(r, z)$	none	bzmap2d.d

NTYPEn Total number of files of type TYPEn to produce (Limit: 10)

PAR1... Parameter values for plots. (e.g. timestep numbers when

PARn phase space dumps are done.)

-999 The input line is of variable length, so the -999 terminator must be included

RUN IRUN IP FREQ Z0 W0 LTYPE INTERP THRESH

IRUN User defined run number (no internal significance)

IP Print status

FREQ Global frequency declaration; is overridden by local frequency declarations by any element [MHz]

Z0 Staring z coordinate for reference particle (set to 0 for photocathode sources [cm]

W0 Energy of reference particle [MeV]

LTYPE Linac type: 1 ⇒ disk-and-washer structure
2 ⇒ side-coupled cavity
3 ⇒ RTM side-coupled cavity

INTERP Interpolation order for E,B fields : 0-NONE, 1-linear, 2-quadratic, 3-cubic. [Defaults to linear interpolation]

THRESH Acceptable particle loss threshold. If the number of particles remaining in the simulation drops below this percentage of the starting value, the simulation will stop.
(Default=0.50, or 50

TRACE X,X',Y,Y',Φ,E

The trace card is used to introduce a particle that will have a complete 6-dimensional history written to a file for subsequent analysis. Coordinate dumps occur on the same timesteps that output occurs. (See the START and CONTINUE cards for details.) This card works only with input type 11. (Photocathode with quiet start)

Up to 15 particles may be specified. The file(s) will be ptra___.d with the particle number being the suffix of the file name. The coordinates and energy must be NORMALIZED to the parameters of the rest of the distribution, while the divergences are specified in milliradians directly.

To trace a particle at the horizontal edge of the beam in the y=0 plane that is centered longitudinally, which has no transverse momentum, and the same energy as the reference particle, enter:
TRACE 1 0 0 0 0 1

The trace card(s) must precede the INPUT card.

VERBOSE

Putting this card on the first line (ahead of the title card)

causes Parmela to print information about the current task on the screen. This has limited usefulness in debugging, and should not be used in non-interactive jobs.

WAKE DUMPFLAG XOFFSET YOFFSET TSCALEF LSCALEF FILENAME

The WAKE card allows for an after-the-fact kick to be applied to the beam using data from the file FILENAME. In principle, it can be used to model any perturbative force with a dependence on the z-coordinate alone. All wake elements may be disabled by adding a NOWAKES card to the start of the input deck.

DFLAG 1-Dump map of wakefield kicks as seen by beam
0-no dump [the default] Dump file is named wakeNN.d,
with NN defined as the element number.

XOFFST Amount to offset the beam horizontally on entering the structure in [cm].

YOFFST Amount to offset the beam vertically on entering the structure in [cm].

TSCALE Scale transverse wake kicks by TSCALEFAC times the values loaded from the ABCI file. Defaults to +1.0 .

LSCALE Scale longitudinal wake kicks by TSCALEFAC times the values loaded from the ABCI file. Defaults to +1.0 .

FILENAME Name of file containing digested ABCI data. Format expected is:

line 1: Comments (column labels)

line 2: Comments (column units)

line 3: $ZW0_{\parallel,1}$ $W1_{\perp,1}$ $W1_{\parallel,1}$

...

line N: $ZW0_{parallel,N}$ $W1_{\perp,N}$ $W1_{\parallel,N}$

Where the columns are:

Z , the ABCI Z-coordinate in [m]

$W0_{\parallel}$, the monopole longitudinal wake in [V/pC]

$W1_{\perp}$, the dipole transverse wake in [V/pC/m]

$W1_{\parallel}$, the dipole longitudinal wake in [V/pC/m^2]

Bibliography

[1] D. Edwards, Editor, *TESLA Test Facility Linac - Design Report*, TESLA-95-01, 1995.

[2] *A VUV Free Electron Laser at the TESLA Test Facility at DESY - Conceptual Design Report*, TESLA-FEL 95-03, 1995.

[3] "Contributions to the FEL'96 Conference", August 26-31, 1996, Rome, Italy, TESLA-FEL 96-13, 1996.

[4] A. Fry, *Novel Pulse Train Glass Laser for RF Photoinjectors*, PhD Thesis, UR-1492, University of Rochester, 1996.

[5] J. Rosenzweig, et al, "Proposal for Staged Plasma Wake-field Accelerator Experiment at the Fermilab Test Facility", Fermilab proposal P890, 1996.

[6] P. Michelato, "INFN Photocathode Preparation System", in Proc. of TTF Collaboration Meeting, Milano, Italy, June, 1996.

[7] R. Gomer, *Field Emission and Field Ionization*, Harvard Univ. Press, Cambridge, MA, 1961.

[8] R. Miller, "Lecture Notes for the USPAS", held at U. C. L. A., Los Angeles, CA, January 1995.

[9] C. Hung, *J. Appl. Phys.*, **21**, 37, 1950.

[10] B. Leblond, *NIM*, **A317**, 365, 1992.

[11] D. Brion, J. C. Tonnerre, A. M. Shroff, *Appl. Surf. Sci.*, **16**, 55, 1983.

[12] B. C. Lamartine, J. V. Czarnecki, T. W. Haas, *Appl. Surf. Sci.*, **16**, 207, 1983.

[13] J. Lafferty, *J. Appl. Physics*, **22**, 299, 1951.

[14] S. Ordanjan, E. Nikolaeva, I. Horoshilova, E. Ostrovsky, in Proc. Sixth All-Union Conf. on High Current Electronics, vol. 1, Tomsk, Russia, 58, 1986.

[15] S. Rozhkov, O. Kultashev, A. Gugnin, in Proc. Electronics Technique, Ser. 16, vol. 2, 81, 1969.

[16] W. Schottky, *Ann. d. Physik*, **44**, 1011, 1914.

[17] H. Matsumoto, M. Akemoto, H. Hayano, T. Naito, S. Takeda, KEK Preprint 91-161, 1991.

[18] R. Fowler, L. Nordheim, *Proc. Roy. Soc. of London*, **A119**, 173, 1928.

[19] J. Halbritter, *IEEE Trans. on Elec. Insul.*, **EI-18**, No. 3, 253, 1983.

[20] J. Tan, et al, DAPNIA/SEA-93-14, 1993.

[21] R. Latham, *High Voltage Vacuum Insulation*, Acad. Press, New York, 1981.

[22] R. Latham, *IEEE Trans. Elec. Insul.*, **EI-18**, 194, 1983.

[23] R. Latham, *Vacuum*, **32**, 137, 1982.

[24] Y. Yankelevich, *Vacuum*, **30**, 97, 1980.

[25] R. Latham, in Proc. of 2nd Wkshp. on RF Superconductivity, 533, 1984.

[26] R. Miller, S. Savage, *J. Appl. Phys.*, **21**, 662, 1960.

[27] H. Gundel et al, *NIM*, **A280**, 1, 1989.

[28] H. Riege, CERN AT/95-09 (DI), 1995.

[29] K. Geissler, et al, CERN AT/95-41 (DI), 1995.

[30] H. Gundel, J. Handerek, H. Riege, *J. Appl. Phys.*, **69**, 957, 1991.

[31] W. Spicer, A Herrera-Gómez, SLAC-PUB-6306, 1993.

[32] C. Travier, LAL/RT 93-08, 1993.

[33] D. Bamford, M. Bakshi, D. Deacon, *NIM*, **A318**, 377, 1992.

[34] B. Leblond, G. Kuznetsov, M. Batazova, LAL/RT 95-06, 1995.

[35] F. Parmigiani, P. Michelato, private communication, 1995.

[36] J. Clendenin, Proc. Schwerin Sources '94 Conf., Schwerin, Germany, 91, 1994.

[37] D. Umstadter, et al, *Phys. Rev. Lett.*, **76**, 2073, 1996.

[38] X. -J. Wang, et al, in Proc. of the IEEE Part. Accel. Conf., Dallas, TX, 890, 1996.

[39] R. Yen, J. Liu, N. Bloembergen, *Optics Comm.*, **35**, 2, 1980.

[40] S. Skupsky, T. Kessler, A. Letzring, Y.-H. Chuang, *J. Appl. Phys.*, **73**, 6, 1993.

[41] M, Haner, W. Warren, *Appl. Phys. Lett.*, **52**, 18, 1988.

[42] F. Paschen, *Wied. Ann.*, **37**, 69, 1889.

[43] I. Smith, in Proc. First Int. Symp. Discharges and Elec. Insul. in Vac., MIT, Cambridge, MA, 261, 1964.

[44] S. Humphreys, *Principles of Charged Particle Acceleration*, Wiley-Interscience, New York, 1986.

[45] T. Srinivasan-Rao, J. Smedley, in Proc. of the Adv. Accel. Conc. Wkshp., Lake Tahoe, CA, 1996.

[46] F. Villa, in Proc. of the Adv. Accel. Conc. Wkshp., Lake Tahoe, CA, 1996.

[47] S. Lebedev, M. Machida, S. Moshkalyov, D. Campos, in Proc. IEEE Int. Conf. on Plasma Science, 130, 1996.

[48] Wang Mingchang, et al, *NIM*, **A375**, (1-3), 143, 1996.

[49] Pepper pot produced by N. Barov for use in diagnosing the AWA drive beam emittance.

[50] K. Ramaswamy, W. Destler, J. Rodgers, *J. Appl. Phys.*, **80**, (9), 4887, 1996.

[51] J. Rosenzweig, A. Murokh, C. Pellegrini, *Phys. Rev. Lett.*, **74**, (13), 2467, 1994.

[52] J. Fontana, R. Pantell, *J. Appl. Phys.*, **54**, 4285, 1983.

[53] P. Sprangle, E. Esarey, A. Ting, G. Joyce, *Appl. Phys. Lett.*, **53**, 2146, 1988.

[54] C. Clayton, et al, *Phys. Rev. Lett.*, **70**, 37, 1993.

[55] R. Palmer, *J. Appl. Phys.*, **43**, 3014, 1972.

[56] R. Palmer, et al, in *Laser Acceleration of Particles*, C. Joshi, T. Katsouleas, Eds., AIP Conf. Proc. 130, New York, 1985.

[57] N. Kroll, D. Smith, S. Schultz, in *Advanced Accelerator Concepts*, J. Wurtele, Ed., AIP Conf. Proc. 279, New York, 1993.

[58] N. Barov, J. Rosenzweig, *Phys. Rev. E*, **49**, (5), pt. B, 4407, 1994.

[59] X. Qiu, K. Batchelor, I. Ben-Zvi, X.-J. Wang, "Demonstration of emittance compensation through the measurement of the slice emittance of a 10 picosecond electron bunch", to be published, 1996.

[60] I. Lehrman, in Proc. of IEEE Part. Accel. Conf., Port Jefferson, NY, 3012, 1993.

[61] R. Sheffield, Proc. of TTF Coll. Mtg., Hamburg, Germany, February, 1995.

[62] B. Carlsten, *NIM*, **A380**, (3), 505, 1996.

[63] B. Dunham, M. Jablonka, "Modelling of a High Charge Injector for the TESLA Test Facility",DAPNIA/SEA internal document, 1994.

[64] P. Lapostolle, A. Septier, Editors, *Linear Accelerators*, North Holland, Amsterdam, 1970.

[65] C. Lejeune, J. Aubert, "Emittance and Brightness", in *Applied Charged Particle Optics*, A. Septier, Ed., Academic Press, New York, pp.159-259, 1980.

[66] R. Sheffield, in *Physics of Particle Accelerators*, M. Month, M. Dienes, Eds., AIP Conf. Proc. 184, New York, 1989.

[67] I. Kapchiskij, V. Vladimirskij, Proc. Int. COnf. on High Energy Accel. and Instr., CERN, 274, 1959.

[68] H. Busch, *Z. Phys.*, **81**, 974, 1926.

[69] K. J. Kim, *NIM*, **A275**, 201, 1989.

[70] L. Serafini, J. Rosenzweig, *Phys. Rev. Lett.*, **55**, 7565, 1997.

[71] L. Serafini, C. Pagani, in Proc. 1992 Linear Accel. Conf., 799, 1992.

[72] C. Travier, in Proc. EPAC92, 3rd European Part. Accel. Conf., v. 2, 1020, 1993.

[73] S. Hartman, J. Rosenzweig, *Phys. Rev. E*, **47**, no. 3, 2031-7, 1993.

[74] E. Chojnacki, C. Ho, R. Koneckny, AGN-7, 1991.

[75] D. Palmer et al, Proc. of IEEE Part. Accel. Conf., Dallas, TX, 982, 1995.

[76] L. Brillouin, *Phys. Rev.*, **67**, 260, 1945.

[77] P. Colestock, private communication, 1996.

[78] B. Carlsten, B. McVey, E. Svaton, G. Magelssen, L. Young, in Proc. IEEE Part. Accel. Conf. Washington D.C., 641, 1989.

[79] B Carlsten, et al, *Phys. Rev. E*, **53**, (3), 2072, 1996.

[80] K. Crandall, L. Young, LA-UR-90-1766, 1990.

[81] J. Rosenzweig, E. Colby, TESLA 95-04, 1995.

[82] J. Rosenzweig, N. Barov, E. Colby, *IEEE Tran. Plasma Sci.*, **24**, (2), 409, 1996.

[83] D. Carey, *The Optics of Charged Particle Beams*, Harwood Academic Publishers, New York, 1987.

[84] K. Halbach, *NIM*, **78**, 185, 1960.

[85] P. Colestock, E. Colby, H. Edwards, Wakefield Paper, to appear as a TESLA note, 1997.

[86] K. Crandall, L. Young, LA-UR-90-1766, 137, 1990.

[87] *Poisson/Superfish Reference Manual*, LA-UR-87-126, 1987.

[88] *HP 85180A High-Frequency Structure Simulator User's Reference*, Edition 1, Hewlett-Packard part no. 85180-90020, 1990.

[89] Y. Ho Chin, CERN SL/92-49 (AP), 1992.

[90] 3-D FORTRAN Monte Carlo code incorporating Bremßtrahlung and ionization losses for electrons in matter, by Nikolai Barov, written 1995.

[91] K. R. Crandall, D. P. Rusthoi, *Trace 3-D Documentation*, Second Edition, LA-UR-90-4146, 1987.

[92] ANSYS Engineering Analysis System, v. 5.1, Swanson Analysis Systems, Inc., Houston, Pa.

[93] IDEAS-VI.i, Structural Dynamics Research Corporation, Milford, OH.

[94] A. Geist et al, *PVM User's Guide*, 1994.

[95] B. E. Carlsten, *NIM*, **A285**, 313, 1989.

[96] V. Andre'ev, *Soviet Physics–Technical Physics* **13**, 1070, 1969.

[97] B. E. Carlsten, T. Raubenheimer, *Phys. Rev. E*, **51**, (2), 1453, 1995.

[98] J. B. Rosenzweig, TESLA-95-03, 1995.

[99] J. B. Rosenzweig, E. R. Colby, "Charge and Wavelength Scaling of RF Photoinjector Designs", in Proc. of Sources '94, Schwerin, Germany, 1994.

[100] M. Takabe, Y. Miyauchi, H. Sakae, M. Ogoshi, T. Komatsu and S. Mandai, *NIM*, **A318**, 367, 1992.

[101] H. Sakae, M. Takabe, M. Ogoshi, and S. Mandai, *NIM*, **A331**, 346, 1993.

[102] D. T. Palmer, SLAC-PUB-6799, 1995.

[103] Richard Sheffield, TTF/Injector II Meeting, October 5-6, 1994.

[104] J. B. Rosenzweig, E. R. Colby, G. P. Jackson, and T. Nicol, in Proc. of IEEE Part. Accel. Conf., Port Jefferson, NY, 1993.

[105] I. S. Lehrman, et al, *NIM*, **A318**, 247, 1992.

[106] J. Gao, *NIM*, **A311**, 437, 1992.

[107] J. Gao, *NIM*, **A311**, 431, 1992.

[108] H. A. Bethe, *The Physical Review*, **66**, Nos. 6 and 7, 163, 1944.

[109] T. Nicol, private communication, 1994.

[110] J. Rosenzweig, private communication, 1993.

[111] J. B. Rosenzweig, G. Travish, "Design Considerations for the UCLA PBPL Slit-Based Phase Space Measurement Systems",PBPL internal, Feb. 22, 1994.

[112] T. Kauppila, R. Carson, D. Moir, and R. Ridlon, Proc. of the 1991 IEEE Conf., San Francisco, CA, 2107, 1991.

[113] G. Baribaud, C. Bovet, R. Jung, M. Placidi, E. Rossa, Y. Solberg, Proc. of the XV^{th} Int. Conf. on High Energy Accel., 212, 1992.

[114] Goodwin, R., et al, FERMILAB-CONF-89-230, 1989.

[115] N. Barov, C code written specifically for the AWA system interface, 1995.

[116] P. Schoessow, C. Ho, J. Power, E. Chojnacki, in Proc. IEEE Conf. on Part. Accel., Port Jefferson, NY, 1844, 1993.

[117] P. Schoessow, et al, in Proc. of EPAC90, 606, 1990.

[118] W. Gai, N. Hill, C. Ho, P. Schoessow, J. Simpson, in Proc. IEEE Conf. Part. Accel., Port Jefferson, NY, 3050, 1993.

[119] E. Kahana, Proc. 3^{rd} Ann. Wkshp. on Accel. Instr., Newport News, VA, 235, 1991.

[120] E. Kahana, Y. Chung, AIP Conf. Proc. 281, Berkeley, 271, 1993.

[121] Osram Sylvania Inc., Chemical and Metallurgical Division, Technical information Bulletin for Type 2611 phosphor, 8^{th} Ed. Phosphor Reference Guide, 1994.

[122] SLAC Single Pass Collider Memo CN-290. (n.d.)

[123] P. Lapostolle, CERN report AR/Int. SG/65-15, Geneva, Switzerland, 1965.

[124] P. Oettinger, I Bursuc, R. Shefer, E. Pugh, Proc. 1987 IEEE Part. Accel. Conf., Washington D.C., 286, 1987.

[125] Y. Yamazaki, T. Kurihara, H. Kobayashi, A. Asami, *NIM A*, **322**, 139, 1992.

[126] J. Jackson, *Classical Electrodynamics*, John Wiley & Sons, Inc., New York, 1975.

[127] Initial calculations by T. Limburg, J. Roßbach, TTF Collaboration meeting, February 1995.

[128] Y. Shibata, et al, *Phys. Rev. E*, **50**, (2), 1479, 1994. Although the calculations therein are for coherent optical transition radiation, the calculation for coherent synchrotron radiation is directly analogous.

[129] Particle and Fields, *Phys. Rev. D*, **54**, third series, no. 1, 1996.

[130] W. Press, S. Teukolsky, W. Vetterling, B. Flannery, *Numerical Recipes in FORTRAN: The Art of Scientific Computing*, 2nd Ed., Cambridge University Press, New York, 1992.

[131] D. Bradley, G. New, in Proc. of IEEE, vol 62, no.3, march 1974, 313, see figure 10 in particular.

[132] J. Slater, *Microwave Electronics*, Van Nostrand, New York, 1950.

[133] T. Wangler, K. Crandall, R. Mills, M. Reiser, *IEEE Trans. Nucl. Sci.*, **32**, 2196, 1985.

[134] P. Lapostolle, *IEEE Trans. Nucl. Sci.*, **NS-18**, 1101 1971.

[135] ABCI modelling done by P. Colestock, 1996.

[136] W. Schnell, I. Wilson, Proc. of 1991 Part. Accel. Conf., San Francisco, CA, 3237, 1991.

[137] M. Kurz, P. Hülsmann, H. Klein, A. Schempp, Proc. of 1991 Part. Accel. Conf., San Francisco, CA, 3023, 1991.

[138] L. Hand, W. Panofsky, *Rev. Sci. Instr.*, **30**, 10, 927, 1959.

[139] J.F. Ostiguy, private communication, 1995.

[140] L. Gianessi, private communication, 1996.

[141] P. Rousseeuw, M. Annick, *Robust Regression and Outlier Detection*, Wiley and Sons, Inc., New York, 1987.

[142] R. Burden, J. Faires, *Numerical Analysis*, 3rd Ed., Boston: Prindle, Weber & Schmidt, Boston, MA, 1985.

[143] I. Will, P. Nickles, W. Sandner, "A Laser System for the TESLA Photo-Injector", Design Study, Max Born Insitute internal document, 1994.

[144] E. Colby, F. Ostiguy, and J. Rosenzweig, Fermilab TM-1900, 1994.

[145] L. Serafini, C. Pagani, Proc. 1992 Linear Accel. Conf., Ottowa, 1992.